



AVERTISSEMENT

Ce document est le fruit d'un long travail approuvé par le jury de soutenance et mis à disposition de l'ensemble de la communauté universitaire élargie.

Il est soumis à la propriété intellectuelle de l'auteur. Ceci implique une obligation de citation et de référencement lors de l'utilisation de ce document.

D'autre part, toute contrefaçon, plagiat, reproduction illicite encourt une poursuite pénale.

Contact : ddoc-theses-contact@univ-lorraine.fr

LIENS

Code de la Propriété Intellectuelle. articles L 122. 4

Code de la Propriété Intellectuelle. articles L 335.2- L 335.10

http://www.cfcopies.com/V2/leg/leg_droi.php

<http://www.culture.gouv.fr/culture/infos-pratiques/droits/protection.htm>



Ecole Doctorale Sciences et Ingénierie Ressources Procédés Produits Environnement.

Collège Sciences et Technologies

Thèse

Présentée pour l'obtention du titre de

Docteur de l'Université de Lorraine

Spécialité : Géosciences

Par

Stéphanie Fleurance

Métallogenèse de l'uranium associée à des processus superficiels : L'exemple de la Jordanie centrale.

Soutenance publique le 13 décembre 2012

Membres du jury :

Rapporteurs	Hani N. Houry. Professeur, Université de Jordanie, Amman. Nicolas Tribovillard. Professeur, Université de Lille 1.
Examineurs	Anne-Sylvie André-Mayer. Professeur, G2R, Université de Lorraine. Nancy. John H. Powell. Docteur, British Geological Survey, Keyworth, Angleterre.
Directeurs de thèse	Michel Cuney. Directeur de recherches CNRS, Université de Lorraine, Nancy. Fabrice Malartre. Maître de conférences ENSG, G2R, Université de Lorraine, Nancy.
Invité	Jean Reyx. Ingénieur Areva, Paris.

REMERCIEMENTS

Parce que cette thèse n'est pas seulement la concrétisation de trois années de travail mais aussi l'aboutissement d'un long parcours, et parce qu'elle ne serait rien sans les années qui l'ont précédé... je pourrais remercier beaucoup de monde mais je me contenterai cependant de remercier les personnes qui ont contribué à ce travail, mes bienfaiteurs, et ceux qui m'ont entouré pendant cette période.

Je tiens tout d'abord à remercier Michel Cuney (alias Papy Moustache, Mickael Kini), qui m'a fait confiance et qui a su m'orienter dans ce projet atypique. Merci pour ton engagement et pour tout ce que tu m'as appris.

Merci à Fabrice Malartre, qui était toujours disponible et à toujours répondu présent même pour écouter mes doutes de thésarde.

Je remercie les membres du jury qui ont accepté d'évaluer mes travaux : Nicolas Tribovillard, Hani N. Khoury, John H. Powell, Anne-Sylvie André Mayer, et Jean Reyx.

Je remercie évidemment la compagnie Areva, sans laquelle ce projet n'aurait pas été possible, ni même les rencontres qu'il a engendré...merci aux géologues français, anciens nancéens: Rémich alias le vieux petit chauve, ou petit homme (prépare le BBQ j'arrive !!!!), Cradon alias la cabine avancée, et Guigui, alias chéri-chéri, l'homme sur la brèche ou encore Jean Michel porteur d'échantillons. Cette mission n'aurait pas été la même sans vous, merci pour tout ! Merci aussi à Gilles Recoche (ancien directeur de filière) et Emmanuel Duguey (ancien chef géologue) grâce à qui j'ai pu faire cette mission et ces belles rencontres : Laith, Allam, et les autres... merci également à Jean Pierre Milesi et Marc Brouand, mes tuteurs officieux !

Merci à Patrick pour son oreille attentive, ses conseils et son professionnalisme. Merci à Laurence, Marie-Odile, Christine, pour l'administratif et pour leur gentillesse, à Roland et Vincent pour l'informatique, à Gilles pour la salle de broyage, à Cédric D., Alex, Arnaud & co pour toutes ces lames minces et pour votre disponibilité, à Pierre (Schumi pour les intimes).

Merci au service de microscopies: Alain, Sullivan, Olivier, Ludovic, et surtout Sandrine, avec qui ce fut un réel plaisir de passer du temps. Faire du meb et de la microsonde avec vous me manquera !

Merci à ceux qui ont contribué à la réalisation de mes analyses : Chantal, Karine (c'est encore décentré...), Marie-Camille (MCC Raman girl), Philippe (l'ablateur fou), Régine (tata DRX), l'équipe du SARM, ...

Merci à mes anciens professeurs, et désormais collègues voire amis, les adeptes de la cafet' qui ont parfois dû y supporter mes blagues ou ma mauvaise humeur, et j'en oublie forcément: Mr Jean, Cécile, Alex, Judith, Jérôme (mon co-thé), Cédric C, MCC, Anne-Sylvie, Laurent, Jean Louis, Poupy...

Bon courage et bonne continuation aux thésards de ma propromotion, dont certains finissent bientôt et à ceux arrivés ensuite: Vanessa, Aurélien, Christophe, Manu, Anthony, Philippe, Wilfried, Thomas et les autres.

Merci aux anciens thésards, présents, partis ou prêts à partir : Isabelle, Sandrine, Foxy, Askar, Jérémy, Rozsy, Antonin (Richhhharrrrd !!!!! et bien sûr Juliiiiieeeee, bonne continuation en Finlande), sans oublier Merca alias grande saucisse pour cette cohabitation dans la joie et presque toujours bonne humeur !! je n'aurais pas rêvé meilleur collègue de bureau !

J'ai également une pensée pour toutes ces personnes qui ont tenu un rôle important, qu'elles soient en France ou dispersées aux quatre coins du globe : merci, gracias, obrigado, thank you. Loin des yeux ne veut pas dire loin du cœur pour moi....

Je tiens à remercier plus particulièrement mes amis proches, qui ont partagé mon quotidien:

Lucille: ma plus longue relation (plus de 7 ans), qui a toujours été là dans les bons comme dans les mauvais moments, avec qui j'ai passé des moments forts et inoubliables, avec qui j'ai vécu, avec qui j'ai vaincu... Les derniers mois nous ont rapproché encore un peu plus, je me demande bien pourquoi... ;-) un grand merci pour tout, toi-même tu sais !!

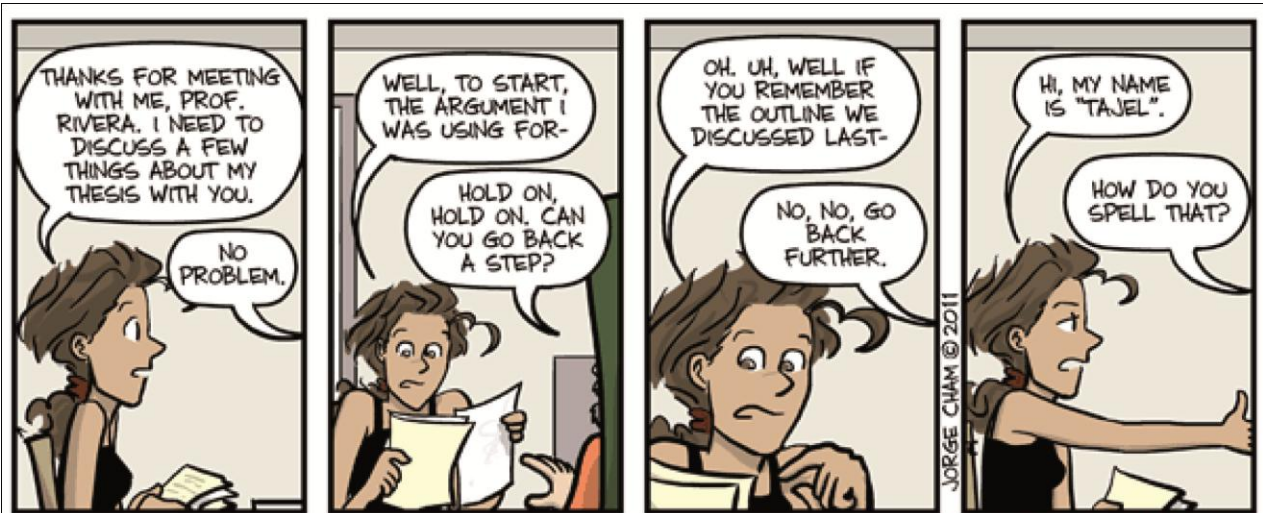
Flo & Jo: mes copcopains, ma poulette, mon double, qui partagent ma vie (non non ce n'est pas du tout excessif) depuis plus d'un an, mes partenaires de programmes télé débiles, de bons repas, de fous rires et de détente avec qui je n'ai même pas besoin de parler...

Vous me manquerez énormément tous les trois, j'espère que mon départ à l'autre bout du monde, ne sera que le moyen de mieux nous retrouver pour une nouvelle vie !

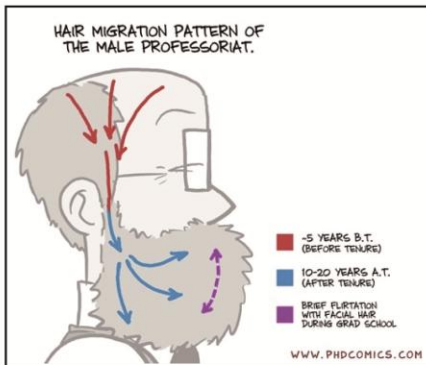
Et enfin, comment ne pas remercier celui qui me comprend mieux que quiconque, mon pilier, mes ¾, qui m'a épaulé et encouragé peut importe le pays dans le lequel il se trouvait, celui qui croit le plus en moi, celui qui me 'respecc énormément'... mille mercis à toi Guillaume. Falalel, je dirais même mieux, falafeoulche !!

Ne soyez pas vexés de ne pas tous voir votre nom, mais le cœur y est, et chacun a apporté sa pierre à l'édifice. Bonne continuation à tous !

Toute ressemblance avec des personnes existantes ne serait que fortuite :-)

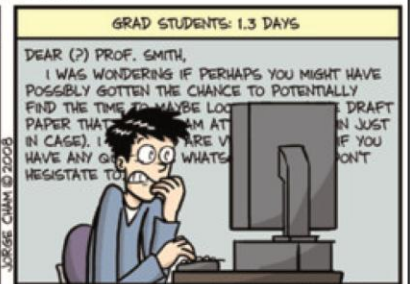


WWW.PHDCOMICS.COM

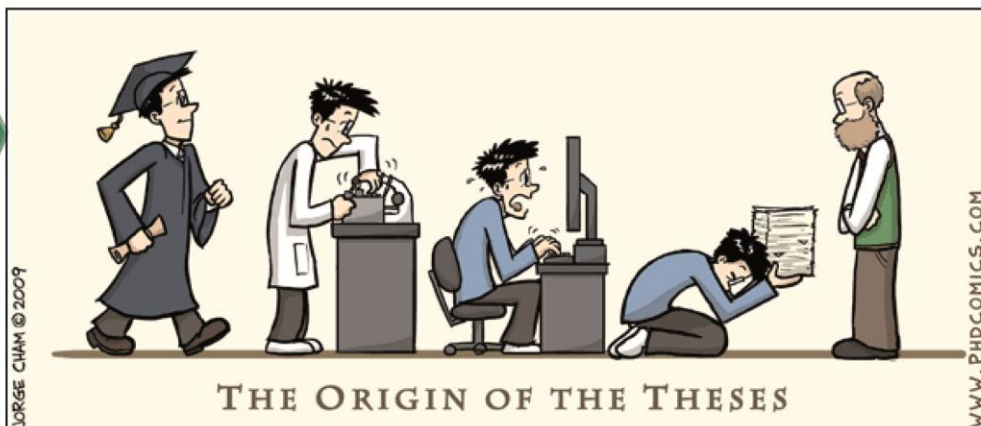
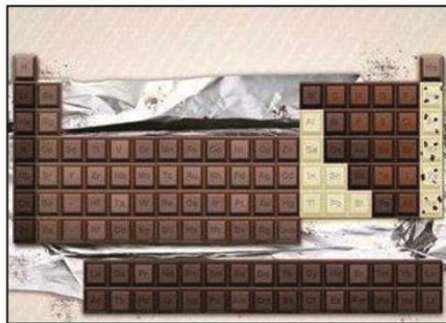


WWW.PHDCOMICS.COM

AVERAGE TIME SPENT COMPOSING ONE E-MAIL



WWW.PHDCOMICS.COM



THE ORIGIN OF THE THESES

WWW.PHDCOMICS.COM

TABLE DES MATIERES

REMERCIEMENTS.....	3
TABLE DES MATIERES	7
Bookmark.....	11

Introduction

1. CONTEXTE GEOLOGIQUE GENERAL	14
2. LES MINERALISATIONS URANIFERES SUPERGENES.....	19
3. L'EXPLORATION MINIERE EN JORDANIE	20
4. PLAN DE LA THESE	22
REFERENCES.....	23

Chapitre I

Méthodologie et Outils.....27

1. MICROSCOPIE.....	28
2. IDENTIFICATION DES FRACTIONS FINES	28
3. DETERMINATION DES COMPOSITIONS EN ELEMENTS MAJEURS, TRACES ET CHIMIE COMPLEMENTAIRE (F, S, DIOXIDE DE CARBONE TOTAL, CARBONE ORGANIQUE).....	29
4. DETERMINATION DE LA FRACTION HYDRATEE ET/OU CARBONATEE DES APATITES.....	29
5. MESURES DES TENEURS EN TERRES RARES ET EN URANIUM DES APATITES ET MINERAUX D'URANIUM	30
6. FORMULES STRUCTURALES DES PHOSPHATES.....	31
REFERENCE.....	31

Chapter II

Origin of the extreme polymetallic enrichment (Cd, Cr, Mo, Ni, U, V, Zn) of the Late Cretaceous - Early Tertiary Belqa Group, central Jordan.....33

ABSTRACT.....	35
1. INTRODUCTION.....	36
2. GEOLOGICAL SETTING.....	36
3. LITHOSTRATIGRAPHY.....	40

4. ANALYTICAL METHODS	43
5. RESULTS	43
6. DISCUSSION	59
7. CONCLUSIONS	70
ACKNOWLEDGMENTS	72
REFERENCES.....	72

Chapter III

Sedimentary, metamorphic to supergene evolution of uranium and REE in the phosphates from the Belqa Group lithologies, central Jordan.....81

ABSTRACT	83
1. INTRODUCTION.....	83
2. GEOLOGICAL SETTING.....	84
3. MATERIALS AND METHODS	86
4. HOST ROCKS	88
5. MINERALOGY AND GEOCHEMISTRY OF THE PHOSPHATES	93
6. CHEMICAL VARIABILITY.....	104
7. DISCUSSION	111
8. CONCLUSION	115
ACKNOWLEDGMENTS.....	115
REFERENCES.....	116

Chapter IV

Characterization of the pyrometamorphism123

1. INTRODUCTION.....	124
2. GENERAL POINTS	125
3. CHARACTERIZATION OF THE PYROMETAMORPHIC ROCKS IN CENTRAL JORDAN	127
4. DISCUSSION	141
5. CONCLUSIONS AND OUTLOOKS	145
REFERENCES.....	147

Chapter V

Supergene uranium mineralization155

1. SUPERGENE MINERALIZATION IN CENTRAL JORDAN	156
2. MINERALIZED LITHOLOGICAL UNITS	158
3. MINERALIZATION OF THE SUPERGENE LIMESTONES	165
4. VOLUME LOSS / MASS BALANCE.....	167
5. FORMATION PROCESS OF THE SUPERGENE MINERALIZATION	172
6. COMPARISON OF THE JORDANIAN MINERALIZATION WITH THE URANIFEROUS CALCRETES OF NAMIBIA AND AUSTRALIA.....	178
7. GLOBAL BUDGET OF URANIUM MINERALIZATION	180
8. CONCLUSIONS.....	182
REFERENCES.....	183

Conclusions générales187

Appendix

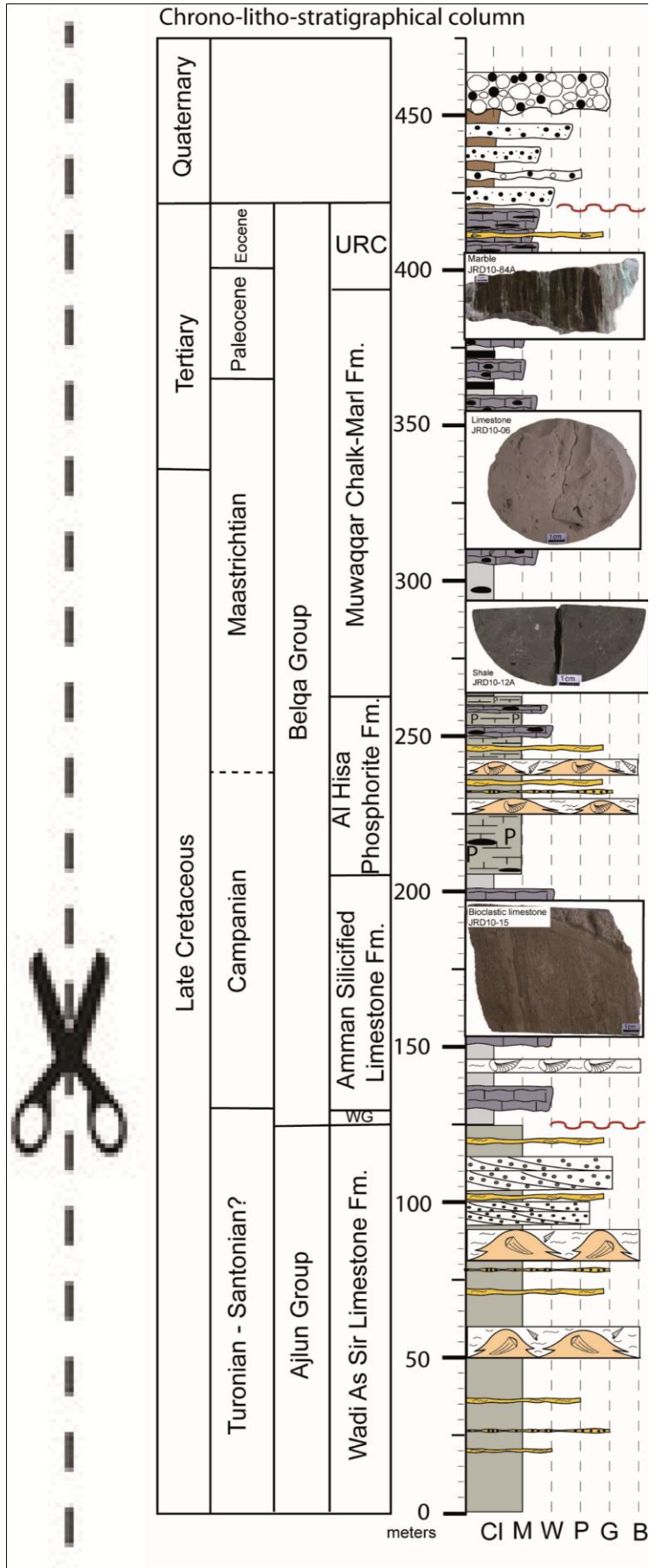
Surficial uranium mineralization of calcretes191

1. CALCRETES.....	192
2. URANIUM SURFICIAL MINERALIZATION OF AUSTRALIA AND NAMIBIA: URANIFEROUS CALCRETES	194
3. CONCLUSION	200
REFERENCES.....	202

TABLE DES FIGURES.....205

TABLE DES TABLEAUX210

Bookmark



Abbreviations

JAEC: Jordanian Atomic Energy Commission
 JERI: Jordan Energy Resources Inc.
 JFUMC: Jordan French Uranium Mining Company
 MEMR: Ministry of Energy and Mineral Resources
 NRA: Natural Resources Authority

Formations (fm.) by stratigraphic order:

URC: Umm Rijam Chert
 MCM: Muwaqqar Chalk Marl
 AHP: Al Hisa Phosphorite
 ASL: Amman Silicified Limestone
 WSL: Wadi Es Limestone

Lithologies by stratigraphic order:

	Mineralized supergene limestone	} different protolithes
	Paralava	
	Black calc-silicate rocks	
	Green calc-silicate rocks	
	Marble	
	Limestone	
	Shale	
	Bioclastic limestone	

Phosphates:

Supergene:

 newly formed Na-S-phosphates  weathered CFA

Metamorphic:

 CFA in marbles  FAp in calc-silicate rocks

Sedimentary/diagenetic:

 ( CFA in weathered lim.  CFA in shale)

Minerals:

ag: aggregate of CFA	Jn: jennite
Ap: apatite	Mel: melilite
Afw: afwillite	Mnt: montmorillonite
Bar: barite	Na-S-P: Na-sulfato-phosphate
Blf: bultfonteinite	Pmp: pumpellyite
Brw: brownmillerite	Pt: portlandite
Cal: calcite	Pw: powellite
CaSi: calcium silicate	Px: pyroxene
Cd Sp: Cd-rich sphalerite	Py: pyrite
CFA: carbonate-fluorapatite	o: ooid of CFA
Chr: chromite	OM: organic matter
CL: clay minerals	Qtz: quartz
Cl: celestine	S: sulfur
Crn: carnotite	Se: selenium
Dol: dolomite	Sk CFA: skeleton of CFA
Ett: ettringite	Spu: spurrite
FAp: fluoroapatite	Srb: srebrodolskite
Fds: feldspar	Strl: strelkinite
Fe ox: iron oxide	Tbm: tobermorite
Fe-Prv: Fe-rich perovskite	Til: tilleyite
Fl: fluorite	Tymn: tyuyamunite
Hcl: hydrocalumite	Uox: uranium oxide
Hsh: hashemite	Wo: wollastonite
Ill: illite	Zeo: zeolite



Introduction

Cette thèse est le fruit d'une collaboration entre le laboratoire G2R-CREGU et la coentreprise franco-jordanienne (JFUMC) créée par AREVA et AREVA DGS (Direction des Géosciences). Le projet s'inscrit dans le cadre de la prospection de minéralisations uranifères de subsurface découvertes dans la région de Siwaqa en Jordanie centrale. Ces gisements de faibles teneurs mais qui peuvent s'étendre sur des surfaces très importantes, sont très peu profonds et représentent un nouvel enjeu pour l'industrie minière. Ces travaux ont pour objectif de caractériser les minéralisations uranifères de la région de Siwaqa, en Jordanie centrale, de déterminer leur(s) source(s) dans les différentes lithologies du Groupe Belqa et les processus de concentration de l'uranium afin de proposer un modèle métallogénique pour ce type de gisement superficiel différent par rapport aux minéralisations de type calcrète. Au niveau des sources, un des enjeux importants était de déterminer la stabilité des phosphates uranifères en environnement superficiel et lors des événements pyrométamorphiques particulièrement bien développés dans la région. Une caractérisation fine des faciès minéralisés avait également pour objectif de définir la nature précise des phases uranifères et de leur distribution, informations fondamentale pour le développement de la méthodologie de traitement de ce minerai. La réalisation de ces objectifs a nécessité une compréhension de l'enrichissement exceptionnel en toute une série d'éléments sensibles aux conditions redox dans les différentes lithologies du Groupe Belqa et de la nature et du rôle du pyrométamorphisme sur le comportement de l'uranium dans ces mêmes lithologies.

1. CONTEXTE GEOLOGIQUE GENERAL

La plaque arabique est composée du bouclier arabique et de la plateforme arabique (Fig.1). Elle est séparée de la plaque africaine par le rift de la Mer Morte, la Mer Rouge et le golfe d'Aden. Le bouclier est principalement composé de formations endogènes précambriennes. La plateforme est constituée de roches sédimentaires déposées sur le plateau continental à partir du Cambrien inférieur. La Jordanie se situe au nord-ouest de la péninsule arabique. En Jordanie, le socle précambrien n'affleure que dans la partie sud (Picard, 1941), le reste du pays est recouvert de roches d'âges Crétacé, Paleogène, Néogène et Quaternaire.

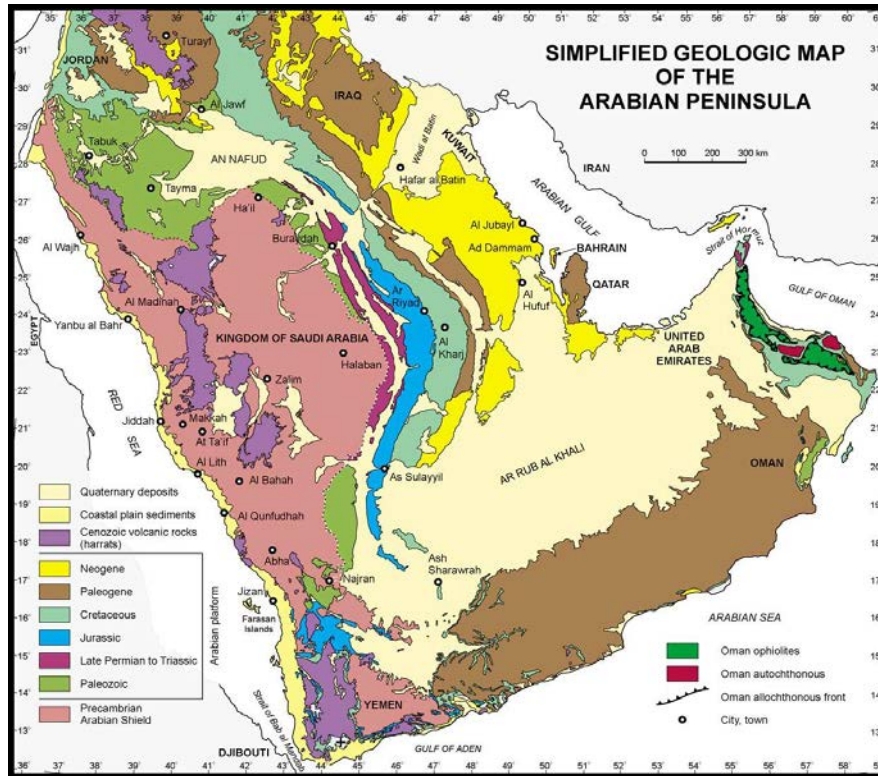


Figure 1. Carte géologique de la péninsule arabe (Le Nindre et al., 2003).

La figure 2 (synthèse d'après Harshbarger (1966), Powell (1988), Eraifej (2006), Jarra et al. (2003), Sawarieh (2005)) présente la stratigraphie générale de la Jordanie. Le socle précambrien est constitué des complexes Aqaba et Araba, respectivement composés de roches métamorphiques et plutoniques, et d'intrusions volcaniques. Les conglomérats Saramouj (du Groupe Safi) d'âge Précambrien, reposant en discordance sur les roches endogènes du massif Nubio-Arabique, sont exposés au sud-est de la Mer Morte, en particulier dans les rivières (wadi) drainant vers celle-ci. Cette formation est composée de conglomérats non métamorphiques à épimétamorphiques de couleurs variées, dérivant de granites alcalins, quartz-diorite, quartzporphyres, porphyres, gneiss et quartzites avec une matrice sablo-arkosique (Bender, 1974). Le Groupe Ram (nommé par Powell (1988), Masri (1988) pour les formations auparavant établies par Bender (1974) et Lloyd (1969)) d'âge Cambrien inférieur à Ordovicien inférieur, est composé de formations silicoclastiques et de carbonates marins. Le Groupe Khreim, d'âge Ordovicien supérieur-Silurien, est constitué de grès, argilites et shales. Ce groupe est en discordant sous le Groupe de Zarqa Ma'in d'âge triassique. Le Groupe Zarqa Ma'in est constitué de grès, calcaires, marnes et de niveau dolomitiques (Bender 1974).

Les roches recouvrant le socle précambrien et les roches Paléozoïques se sont déposées lors de plusieurs épisodes de transgression marine extensive à partir de l'Albien supérieure jusqu'à l'Eocène (Powell and Moh'd, 2011). Les Groupes Ajlun et Belqa ainsi déposés sont principalement des sédiments carbonatés (Bender, 1974). Le Crétacé inférieur est marqué par le dépôt du Groupe Kurnub constitué de facies gréseux fluviatiles, lacustres et éoliens à la base et de facies à influence marine au sommet. Le crétacé supérieur repose en discontinuité sur le crétacé inférieur. Il est divisé en deux groupes (Quennell, 1951) : le Groupe Ajlun (Cénomaniens-Turonien) et le Groupe Belqa (Santonien-Eocène). The Groupe Ajlun est lui-même divisé en plusieurs formations dont la plus jeune Wadi Es Sir Limestones (WSL) affleure dans la zone d'étude. La zone d'étude (Fig. 3) se trouve dans la région de Siwaqa à environ 80 km au sud-est de la capitale Amman. Les travaux présentés ici portent sur les roches du Groupe Belqa. Ce groupe est divisé en plusieurs formations: Wadi Umm Ghudran (WUG), Amman Silicified Limestone (ASL), Al Hisa Phosphorite (AHP), Muwaqqar Chalk Marl (MCM) et Umm Rijam Chert (URC) (Powell, 1989a,b). Les formations sont décrites plus précisément dans le Chapitre 2.

Des dépôts quaternaires non conformes recouvrent le Groupe Belqa : sédiments lacustres, fluviatiles, alluvions et travertins. Bender (1975) propose trois grandes périodes d'activités volcaniques en Jordanie : cambrien inférieur, jurassique supérieur-néocomien et néogène-quaternaire. Au nord de la Jordanie, les roches sédimentaires sont recouvertes par une épaisse série de basaltes (100 m) (Alsharhan and Nairn, 2003) déposée au miocène-pléistocène. Différents systèmes de filons ont été identifiés. La volcanostratigraphie et la datation K-Ar a permis de dater plusieurs événements: basaltes tholéiitiques miocènes (23 à 21 Ma), basaltes alcalins miocènes (12 à 8 Ma) et des basanites du pliocène supérieur-pléistocène (3 to 1.5 Ma) (Ibrahim et al., 2006). Les basaltes de Karak (Fig.3), à l'est de la Mer Morte, se sont mis en place au Pléistocène (Heimbach and Huseibeh, 1975 ; Steinitz and Batrov, 1992).

La Mer Morte est un bassin en pull-apart formé au Miocène suite à des mouvements décrochants sénestres des failles Wadi Araba et Jordan Valley (Fig. 3). Les principales structures tectoniques dans la zone d'étude sont les failles de Siwaqa et de Zarqa Ma'in orientées E-W. Ces failles sont associées au système de failles transformantes de la Mer Morte (DST system) (Fig. 3) qui a été initié au Miocène et réactivé pendant le rifting de la Mer Morte au Miocène-Pléistocène (Diabat and Masri, 2002).

Era	Period	Epoch-age	Group	Formation	Lithological description	
Cenozoic	Quatern.	Recent		Alluvium	gravel, sand, clay	
		Pleistocene		Lisan/Samra	calcareous clay, gravels	
	Tertiary	Miocene		Neogene	conglomerates	
		Oligocene		Dana (Volcanic)	basalt and conglomerates	
		Eocene Paleocene		Umm Rijam Chert	limestone, chert, marl, chalk, shale	
Mesozoic	Upper Cretaceous	Maastrichtian	Belqa	Muwaqqar Chalk Marl	chalky marl, bituminous marl, limestone, marls	
				Al hisa phosphorite	phosphates, bioclastic limestones, chert, chalk, marl	
		Campanian		Amman Silicified Limestone	limestone, silicified limestone, chert, marl	
		Santonian		Wadi Umm Ghudran	chalk, phosphate, limetone, sandstone	
		Turonian		Wadi Es Sir	marl, limestone	
				Cenomanian	Ajlun	Shueib
	Hummar	dolomite, limestone				
	Fuheis	marl, chalk, limestone				
	Na'ur	limestones, marl, chalk dolomitic limestone, marl				
	Upper Jurassic-Lower Cretaceous		Kurnub	Kurnub	sandstones	
	Triassic		Zarqa Ma'in	Zarqa	limestones, dolomite, sandstone shale, gypsum, marl	
	Paleozoic	Upper Ordovician-Silurian		Khreim	Khreim	fine-grained sandstone, mudstone, shale
		Upper Cambrian-Lower Ordovician	Ram	Disi	sandstones	
Umm ishrin				sandstones		
Cambrian		Burj		dolomite shale		
	Salib	bedded arkosic sandstone				
Pre-Cambrian		Safi	Saramouj conglomerates	conglomerates		
		Basement	Araba	alkaline, rhyolitic lavas and subvolcanic intrusions		
			Aqaba	sequence of schistose and gneissic metamorphic remnants and plutonic igneous rocks		

Figure 2. Colonne stratigraphique de Jordanie (d'après Harshbarger (1966), Powell (1988), Eraifej (2006), Jarra et al. (2003), Sawarieh (2005)).

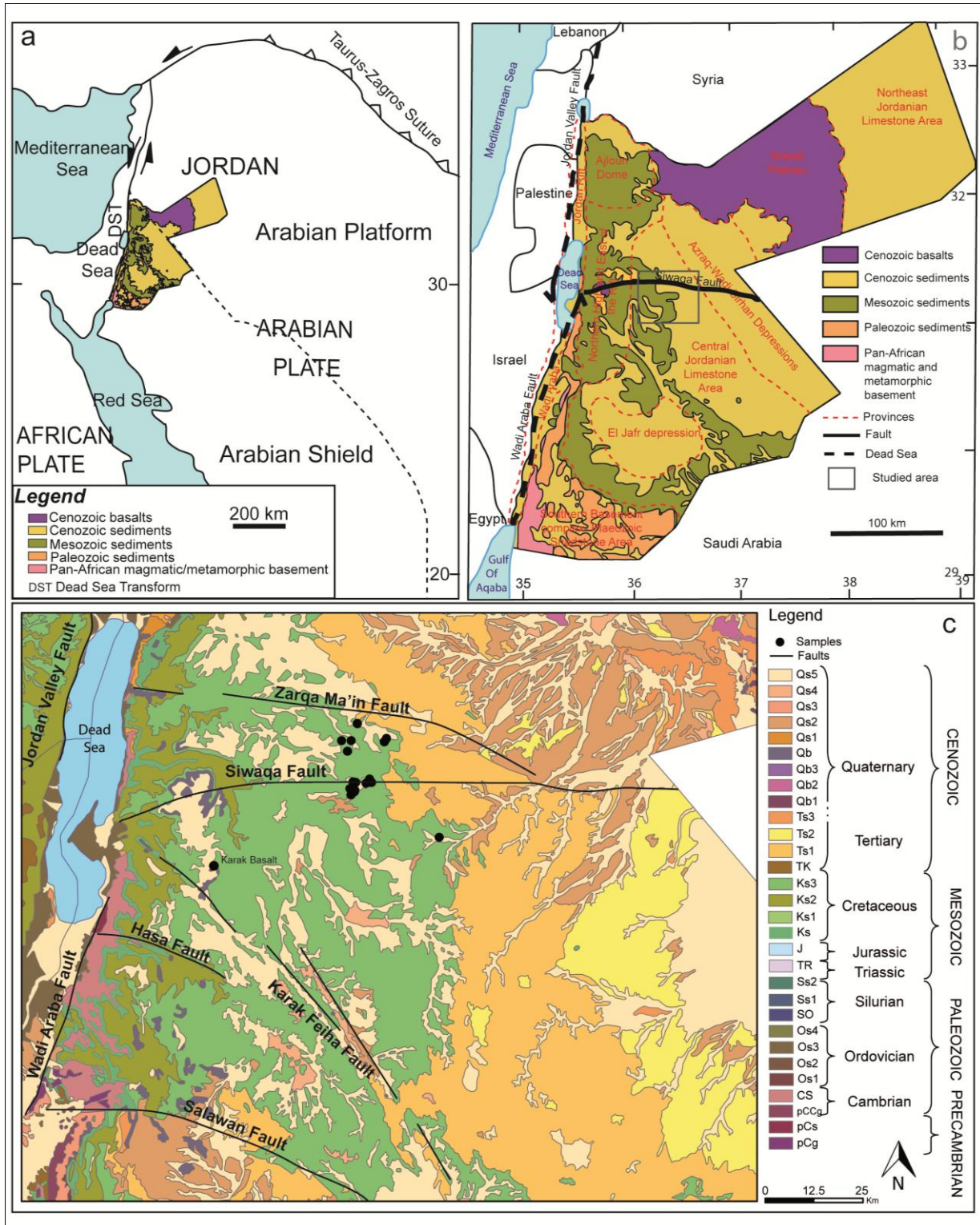


Figure 3. Cartes géologiques de la Jordanie. La carte a situe la Jordanie dans la péninsule arabique. La carte b présente les différentes provinces et la zone d'étude, la carte c présente un zoom avec la localisation des échantillonnages (d'après Alsharhan and Nairn, 2003; Bender, 1975; Förster et al., 2010; Parlak and Roberston, 2004, Sawarieh, 2005).

2. LES MINÉRALISATIONS URANIFÈRES SUPERGÈNES

Les minéralisations uranifères les plus connues en Jordanie sont associées aux formations phosphatées (Moh'd and Powell, 2010). Dill (2011) a présenté différents types de minéralisations en Jordanie: (1) magmatiques (au sud), (2) de type filonien (sud ouest), (3) dans les sables (sud de la Mer Morte), (4) les placers, (5) les black shales (sud est), (6) les phosphorites, (7) dans les calcaires et (8) superficielles (les trois dernières catégories s'étendent de la Jordanie centrale au sud est du pays). Des vanadates d'uranium, carnotite ($K_2(UO_2)_2(VO_4)_2 \cdot 3H_2O$) et tyuyamunite ($K_2(UO_2)_2(VO_4)_2 \cdot 3H_2O$) ont été décrits dans les phosphorites de Ruseifa et Al-Hasa (Zereini 1985, Coppens et al. 1977).

Les dépôts d'uranium superficiels sont définis comme des minéralisations jeunes (Tertiaire à Actuel), proches de la surface, dans des sédiments ou des sols (Toens and Hambleton-Jones, 1984). Parmi celles-ci, les minéralisations de types calcrètes sont les plus courantes. Les calcrètes sont des conglomérats à ciment carbonaté, des accumulations de carbonates authigènes développées en milieu continental sur une roche hôte à partir de l'introduction et cimentation de carbonates lors de processus d'évapotranspiration et de variations de nappes d'eau souterraines. On distingue les calcrètes d'origine pédogénétique et les calcrètes non pédogénétiques. Les calcrètes pédogénétiques se forment en zones vadoses par des processus verticaux de perte d' H_2O et CO_2 , et sont ainsi constituées d'un ciment authigène. Les calcrètes non pédogénétiques se forment à partir de l'altération de roches endogènes et d'un transport latéral des éléments, qui se différencie donc d'un système évaporitique classique avec distribution verticale des éléments. Ca, Mg, U, V sont apportés par transport latéral, U et V sont transportés et précipités en environnement oxydant avec U hexavalent (forme très soluble). La composition et la texture de ces deux types de calcrètes sont cependant souvent très similaires (Carlisle, 1983).

Les sources d'uranium les plus courantes sont les granites riches en U soumis à de fortes altérations en climat aride à semi-aride. L'uranium est transporté sous forme de carbonate d'uranyl (U6) par des fluides oxydants acides devenant alcalins au cours de la percolation (Mann & Deutscher, 1978). Ces fluides permettent l'oxydation du vanadium 4 en vanadium 5. U6 et V5 sont des formes très solubles. Les complexes CO_3-U sont dissociés. La minéralisation se dépose par remontée des eaux chargées en U et V et évapotranspiration. La carnotite, vanadates d'uranyl peu soluble, est le minéral qui précipite le plus souvent.

3. L'EXPLORATION MINIÈRE EN JORDANIE

3.1. Administration

L'Autorité des Ressources Naturelles (NRA) a été fondée en 1965. Les tâches, responsabilités et gestions de la NRA ont été régulées en 1968 par la loi n°12. Depuis 1985, le Ministère de l'Énergie et des Ressources Minérales (MEMR) gère la présidence de la NRA. Cette agence a différentes responsabilités (source: NRA):

- Gestion du développement et de l'exploitation des ressources minérales et énergétiques,
- Etudes économiques, techniques, géochimiques, géophysique et géologiques,
- Administration et régulation des lois,
- Distribution des certificats miniers, permis et licences de prospections et explorations de mines et carrières,
- Coordination de coopérations avec des entités internationales,
- Supervision des activités pétrolières incluant l'octroi de concessions, l'exploration, l'exploitation et les accords internationaux,
- Autres devoirs, assignés par le conseil des ministres, comme la promotion de l'investissement dans l'activité minière.

La Commission d'Énergie Atomique Jordanienne (JAEC), établie en 2008, est l'entité officielle en charge du développement et de l'exécution du programme nucléaire (U, Th, Zr, V) en Jordanie (Xoubi, IAEA 2008). La commission 'Nuclear Fuel Cycle' est en charge du développement de tous les aspects du cycle de combustion nucléaire incluant l'exploration, l'extraction et la production d'uranium, de la garantie de l'apport en carburant, de la gestion de la combustion nucléaire et des déchets radioactifs. Pour permettre le développement de l'économie minière et attirer des investisseurs, la JAEC a créé la compagnie JERI (Jordan Energy Resources Inc.).

3.2. Evolution des campagnes d'exploration, économie minière et contexte géopolitique

Les premières campagnes d'exploration ont commencé à la fin des années 70, par des missions de surveillances aéroportées qui ont révélé douzes zones radioactives correspondant

pour la plupart à des zones très phosphatées (Xoubi, IAEA 2008). Six de ces zones présentent un potentiel: Mafraq, Ruwaished, Haranah, Jordanie centrale, Wadi Bahiyyah, Wadi Ashb Elabiadh, et ont fait l'objet de nombreuses études menées par la NRA dans les années 80-90. Ces études (tranchées, forages, mesures de radioactivité gamma, échantillonnages) ont principalement été concentrées en Jordanie centrale et ont montré que les minéralisations d'U étaient principalement superficielles avec des teneurs de 200 à 2700 ppm U. La NRA déclarait alors que la Jordanie centrale était la région la plus riche en uranium avec 37000 t, valeur révisée à la hausse en 2007 avec plus de 64000 t U₃O₈.

En effet, les années 2000 ont vu des compagnies minières internationales investir dans cette région. En 2008, la JAEC a signé un accord d'exploration avec AREVA. La compagnie minière franco-jordanienne (JFUMC) est alors créée pour développer les activités d'explorations des ressources de Jordanie centrale. Un programme d'exploration a été développé sur une surface de 1400 km² et une production a été envisagée à partir de 2012. JFUMC a annoncé en 2011, la présence de 12300 t d'uranium potentiel pour une zone de 18 km². Après une campagne de 3500 forages, une ressource de près de 70000 tU a été annoncée (Khaled Toukan, Chaire de la JAEC, communiqué dans « World Information Service on Energy » et le « Jordan Times » du 15 décembre 2010). En février 2010, la Jordanie signait un accord avec la compagnie AREVA pour l'exploitation des ressources en U en Jordanie centrale, avec le droit d'exploiter pendant les 25 années suivantes (AREVA, 21 Février 2010). Le Ministère de l'Energie et des Ressources Minérales a déclaré que le royaume de Jordanie serait prêt à débiter les activités minières en 2013. L'accord signé avec AREVA comprendrait la construction d'une mine à ciel ouvert en Jordanie centrale à environ 50 km au sud de la capitale Amman, dans une zone contenant au moins 65000-70000 t de minerais U exploitables (Jordan Times, 23 septembre 2011). Depuis, le Jordan Times (6 juin 2012) a déclaré que JFUMC a révélé la présence de plus de 20000 tU pour 72 km². Des études de faisabilités techniques et économiques (2012) pour mettre en place un programme d'extraction ont alors été lancées. En mai 2012, la JAEC a également commencé des négociations avec AREVA –Mitsubishi Heavy Industries and Atomstroyexport (Russie) pour choisir qui fournira le réacteur nucléaire (i-nuclear, 2 mai 2012). Le 24 octobre 2012 (AFP), la Jordanie annonce la fin de la licence d'exploitation de la compagnie AREVA qui ne démarrera pas de production.

Depuis 2008, d'autres zones à potentiel uranifère sont étudiées par des compagnies internationales. Maфраq et Wadi Bahiyyah (U dans facies altérés du MCM et dans des sédiments quaternaires) sont explorées par les chinois qui ont signés un MoU (memorandum of understanding) en 2008. Le Royaume Uni a signé un MoU pour mettre à disposition son expertise pour l'exploration et l'exploitation des gisements uranifères jordaniens (The Earthtimes, 29 juin 2008). La Jordanie a également signé un MoU avec la Roumanie pour assister et gérer le futur réacteur nucléaire jordanien (Petra, 14 novembre 2008). Fin 2008-début 2009, la JAEC a passé un accord avec Rio-Tinto pour trois zones d'exploration (Al-Bahiyyah, Wadi Sahb, Rewashid). Cette entreprise s'est finalement retirée du projet. Des négociations avec le Canada (SNC-Lavalin International) ont été évoquées pour l'exploitation des ressources uranifères des phosphates qui constitueraient un dépôt d'environ 130000 t (Khaled Toukan, Jordan Times, 16 mai 2008).

4. PLAN DE LA THESE

L'objectif de ces travaux est (i) de présenter les différentes occurrences uranifères rencontrées dans le district de Siwaqa en Jordanie centrale, (ii) de mettre en évidence leurs sources, les modes de transport et de dépôts conduisant à ces minéralisations proches de la surface, et enfin (iii) de comparer avec les minéralisations superficielles de types calcrètes. La Jordanie centrale présente des formations géologiques carbonatées enrichies en métaux et en phosphates perturbées par des phénomènes métamorphiques particuliers et très localisés. Le manuscrit s'articule ainsi autour de cinq axes principaux :

- Présentation des différentes techniques utilisées pour mener à bien les objectifs de ce travail,
- L'enrichissement polymétallique (Co, Cr, Cu, Mo, Ni, U, V, Zn) synsédimentaire des lithologies du Groupe Belqa, qui a fait l'objet d'un article accepté (en date du 18 octobre 2012) dans la revue *Palaeogeography, Palaeoclimatology, Palaeoecology*.
- L'évolution sédimentaire, métamorphique et supergènes des teneurs en uranium et en terres rares dans les différents phosphates du Groupe Belqa qui fait l'objet d'un second article en préparation,
- La caractérisation du pyrométamorphisme,
- Les minéralisations uranifères secondaires superficielles.

REFERENCES

- Alsharhan, A.S., Nairn, A.E.M., 2003. Sedimentary basins and petroleum geology of the Middle East, Elsevier Ed., 942 p.
- Bender, F., 1974. Geology of Jordan. Contribution of the Regional Geology of the Earth. *Gebriüder Borntraeger*, 196 p.
- Bender, F., 1975 a. Geological map. 1:500000. Gov. of Jordan and Geol. Survey of Fed. Rep. Germ.
- Bender, F., 1975 b. Geology of the Arabian Peninsula: Jordan: U.S. Geol. Surv. Proff. Paper 560-1, 36 p.
- Carlisle, D., 1983. Concentration of uranium and vanadium in calcretes and gypcretes. Geol. Soc. London. Spec. Publ. 11, 185-195.
- Coppens, R., Bashir, S., Ritchard, P., 1977. Radioactivity of El-Hisa phosphates, a preliminary study. *Mineral. Deposita*, 12. 189-196.
- Diabat, A., Masri, A., 2002. Structural framework of central Jordan. Geothermal project of central Jordan. Geol. Mapping div., Geol. Directorate. NRA. Amman.
- Dill, H.G., 2011. A comparative study of uranium-thorium accumulation at the western edge of the Arabian Peninsula and mineral deposits worldwide. *Arab. J. Geosci.* 4, 1, 123-146.
- Eraifej, N., 2006. Gas Geochemistry and Isotopic Signatures in the deep Thermal waters in Jordan. *FOG - Freiberg Online Geology* 16, 1-256.
- Föster, H.-J., Föster, A., Oberhänsli, R., Stromeyer, D. 2010. Lithospheric composition and thermal structure of the Arabian Shield in Jordan. *Technophysics*, 481, 1-4, 29-37.
- Harshbarger, 1966. In *Managing Water for Peace in the Middle East: Alternative Strategies* by Murakami, Masahiro. The United Nations University. 319 p. 1995.
- Heimbach, W., Huseibeh, M., 1975. The geological and hydrogeological surveys in the area between the Hejaz Railway Qatrana-El Hasa and the eastern border of Jordan, unpublished report and maps, NRA, Jordan.

Ibrahim, K.M., Al-Malabeh, A., 2006. Geochemistry and volcanic features of Harrat El Fahda: A Young volcanic field in northwest Arabia, Jordan. *J. Asian Earth Sci.* 27, 147-154.

Jarra, G., Stern, R.J., Saffarini, G., Al-Zubi, H., 2003. Late- and post-orogenic Neoproterozoic intrusions of Jordan: implications for crustal growth in northernmost segment of the East African Orogen. *Precamb. Research* 123, 295-319.

Le Nindre, Y.-M., Vaslet, D., Le Métour, J., Bertran, J., Halawani, M., 2003. Subsidence modelling of the Arabian Platform from Permian to Paleogene outcrops. *Sedim. Geol.* 156, 263-285.

Lloyd, J.W., 1969. The hydrogeology of the southern Desert of Jordan. UNDP/FAO 212. Technical report 1. Project 'Investigation of the sandstone aquifers of east Jordan' F.A.O. Rome.

Mann, A.W., Deutscher, R.L., 1978. Genesis principles for the precipitation of carnotite in calcrete drainages in western Australia. *Econ. Geol.* 73, 1724-1737.

Masri, A., 1988. Halat Ammar and Al Mudawwara map sheet nos. 3248 III. 3248 IV: Jordan, Natural Resources Authority, Geol. Div., *Geol. Bull* 13, scale 1:50,000.

Moh'd, B.K., Powell, J.H., 2010. Uranium distribution in the Upper Cretaceous-Tertiary Beqa Group, Yarmouk Valley, northwest Jordan. *Jord. J. Earth Env. Sci.* 3, 1, 49-62.

Parlak, O., Robertson, A., 2004. The ophiolite-related Mersin Melange, southern Turkey: its role in the tectonic-sedimentary setting of Tethys in the Eastern Mediterranean region. *Geol. Mag.* 141, 257-286.

Picard, L., 1941. The Precambrian of the north Arabian-Nubian massif: Hebrew Univ., Jerusalem, *Geol. Dept. Bull.*, 3, 3-4, 30 p.

Powell, J.H., 1988. The geology of Karak; Map sheet No 3152 III, *Bull.* 8, Geol. Directorate, NRA, Amman.

Powell, J.H., 1989 a. Stratigraphy and sedimentation of the Phanerozoic rocks in central and south Jordan. Part A: Ram and Khreim Groups: Jordan, Natural Resources Authority, Geol. Div., *Geol., Bull.* 11, 72 p.

Powell, J.H., 1989 b. Stratigraphy and sedimentology of the Phanerozoic rocks in central and southern Jordan. Bulletin 11, Geology Directorate, Natural Resources Authority (Ministry of Energy and Mineral resources) Amman, Part B: Kurnub, Ajlun and Belqa group, 161 p.

Powell, J.H., Moh'd, B.K., 2011. Evolution of Cretaceous to Eocene alluvial and carbonate platform sequences in central and south Jordan. *GeoArabia* 16, 4, 29-82.

Quennell, A.M., 1951. The geology and mineral resources of (former) Transjordan: Colonial Geology and Mineral Resources, 2, 2, 85-115.

Sawarieh, A., 2005. Geothermal water in Jordan. Workshop for decision makers on direct heating use of geothermal resources in Asia, UNU-GTP, TBLRREM and TBGMED, in Tianjin, China, May 2008.

Steinitz, G., Bartov, Y., 1992. The Miocene-Pleistocene history of the Dead Sea segment of the Rift in light of K-Ar ages of basalts. *Isr. J. Earth Sci.* 40, 199-208.

Toens, P.D., Hambleton-Jones, B.B., 1984. Definition and classification of surficial uranium deposits. IAEA, Vienna, 322, 9-14.

Xoubi, N., 2008. Recent developments of uranium exploration in Jordan. IAEA Technical Meeting on "uranium exploration and mining methods", Nov. 2008, Amman, Jordan.

Zereini, F., 1985. Sedimentpetrographie und Chemismus der Gesteine in der Phosphoritstufe (Maastricht, Oberkreide) der Phosphat-Lagerstätte von Ruseifa/Jordanien mit besonderer Berücksichtigung ihrer Uranführung. *Frankfurter Geowissenschaftliche Abhandlungen C5.* 1-116.

Chapitre I

Méthodologie et Outils

Les échantillons ont suivis un parcours d'analyses classique avec une description macroscopique, microscopique (microscope optique, microscope électronique à balayage, et à transmission), microsonde électronique, analyses par Diffraction des Rayons X, par spectrométrie RAMAN, et par ablation laser couplée à un ICP-MS. Les échantillons ont été broyés et porphyrisés afin d'être analysés par ICP-MS et AES au SARM-CRPG. Les analyses géochimiques ont été traitées avec différents diagrammes et logiciels de géochimie (lithogeochemistry et sigmaplot).

1. MICROSCOPIE

Les microscopes optiques utilisés en lumière transmise et réfléchi pour cette étude sont des Olympus BX51 et BH2. Les analyses semi-quantitatives ont été réalisées au Service Commun de Microscopies Electroniques et de Microanalyses X (Vandœuvre-lès-Nancy), par microscopie électronique à balayage avec des MEB à effet de champ Hitachi S-4800 (émission froide) et JEOL J7600F (cathode chaude), couplés à un spectromètre EDS qui permet de recueillir les photons en fonction de leur énergie. Le JEOL est combiné à un spectromètre EDS de type SDD et un spectromètre WDS Oxford Wave qui permet de recueillir les photons en fonction de leur longueur d'onde. Un MEB Tungstène XL 30 Philips, équipé d'une diode EDS KEVEX sigma, a également été utilisé. La microsonde électronique CAMECA SX100 est un microscope électronique couplé à cinq spectromètres à dispersion de longueur d'onde WDS et un régulateur de courant (SCMEM, Vandœuvre-lès-Nancy).

La nature complexe de certains échantillons a nécessité différentes méthodes d'analyses additionnelles décrites ci-dessous.

2. IDENTIFICATION DES FRACTIONS FINES

Les facies carbonatés, préalablement broyés, ont été décarbonatés par attaque acide (HCl) pour séparer la fraction fine. Ensuite, ils ont subi plusieurs lessivages à l'eau distillée en centrifugeuse, et ont enfin été déposés sur des lames minces. Les lames minces ont été analysées en trois phases :

- analyse à température ambiante ;

- analyse après saturation à l'éthylène glycol, qui permet de vérifier la présence de phases gonflantes ;
- analyse avec chauffage (550°C).

Les diffractogrammes ont été acquis au LEM par Régine Mosser Ruck (Laboratoire Environnement et Minéralurgie de Vandoeuvre-lès-Nancy).

3. DETERMINATION DES COMPOSITIONS EN ELEMENTS MAJEURS, TRACES ET CHIMIE COMPLEMENTAIRE (F, S, DIOXIDE DE CARBONE TOTAL, CARBONE ORGANIQUE)

Les roches sont finement broyées puis analysées par méthodes multi-élémentaires pour les éléments majeurs (ICP-AES) et traces (ICP-MS pour 42 éléments), et par méthodes mono-élémentaires pour des éléments complémentaires comme le fluor, le soufre (Stot), le dioxyde de carbone total (CO₂ totale) et carbone organique (Corg). Les éléments majeurs et traces sont analysés par spectromètre d'émission et spectromètre de masse. Les concentrations en fluor sont mesurées par fusion alcaline. Les poudres sont mélangées avec du carbonate de sodium et de l'eau, puis chauffées à 990°C. Le fluor est directement mesuré avec des électrodes de fluorure. CO₂ totale, Corg et Stot sont mesurés par calcination à 1400°C (Leco SC 144DR). CO₂ et SO₂ formés pendant la calcination sont quantifiés par un détecteur infrarouge. Le carbone organique est mesuré après la destruction des carbonates par HCl.

Les analyses ont été réalisées par le SARM (Service d'Analyse des Roches et des Minéraux, au CRPG à Vandoeuvre-lès-Nancy).

4. DETERMINATION DE LA FRACTION HYDRATEE ET/OU CARBONATEE DES APATITES

Les phases hydratées et/ou carbonatées n'étant pas discernables avec les techniques microscopiques classiques, la microspectrométrie Raman est indispensable pour compléter l'étude des apatites.

La microspectrométrie Raman est une technique non destructive classiquement utilisée pour analyser les espèces présentes dans les inclusions fluides et leurs chlorinités.

Un laser monochromatique (vert) est envoyé sur l'échantillon (lame mince ou épaisse, sans colle, ni métallisation). Les photons réagissent avec le minéral et la lumière diffusée est envoyée à un monochromateur qui mesure son intensité. Le spectre RAMAN correspond aux différentes longueurs d'ondes du rayonnement diffusé (polychromatique) après interaction du rayonnement laser monochromatique avec les liaisons moléculaires du minéral analysé. Cette interaction conduit à une excitation des liaisons moléculaires provoquant une perte en énergie du rayonnement photonique incident dont la longueur d'onde est caractéristique de l'espèce moléculaire excitée et son intensité proportionnelle à l'abondance de cette molécule. Les analyses ont été réalisées grâce à l'aide de Marie-Camille Caumon au laboratoire G2R, avec un LabRAM et un LabRAM HR HoribaJobinYvon avec un laser Ar⁺ à 541.5 nm couplé à un microscope optique Olympus BX51.

5. MESURES DES TENEURS EN TERRES RARES ET EN URANIUM DES APATITES ET MINERAUX D'URANIUM

L'ablation laser couplée à un spectromètre par torche à plasma (LA-ICP-MS) est une technique destructive. Ce dispositif a permis de mesurer les teneurs en terres rares et en uranium des phosphates et des minéralisations uranifères secondaires. Cette technique consiste à vaporiser une certaine quantité de matière sur un volume très petit d'un échantillon avec un laser de longueur d'onde fixe. Le diamètre du faisceau laser incident peut être réglé en fonction des besoins analytiques (16 à 32 µm). La matière est vaporisée, transformée en aérosol puis transportée vers une torche à plasma (ICP) par l'intermédiaire d'un gaz. Dans le plasma les éléments sont ionisés et sont ensuite envoyés vers le spectromètre de masse à collecteur unique (MS) qui analyse les ions en fonction de leur rapport charge/masse. L'instrument utilisé (au G2R, avec l'aide de Philippe Lach, Chantal Peiffert et Marie-Christine Boiron) consiste en un laser GeoLas excimer (ArF, 193, Microlas, Göttingen, Allemagne), et un ICPMS Agilent 7500c quadrupole équipé d'une cellule de collision à He et une cellule de réaction octopole à H₂. L'échantillon (lame mince, plot) est placé dans la chambre d'ablation reliée à un système motorisé X-Y d'un microscope optique (Olympus

BX-41). Le matériel ablaté est transporté par de l'hélium puis mélangé avec de l'argon pour enfin entrer dans la torche à plasma (Leisen et al., 2012).

6. FORMULES STRUCTURALES DES PHOSPHATES

L'étude des phosphates et leur caractérisation définitive passe le calcul de leurs formules structurales et l'évaluation quantitative de la teneur en CO₂ des carbonate-fluorapatites. Cette méthode est détaillée dans le chapitre 3.

REFERENCE

Leisen, M., Dubessy, J., Boiron, M.C., Lach, P., 2012. Improvement of the determination of element concentrations in quartz-hosted fluid inclusions by LA-ICP-MS and Pitzer thermodynamic model of ice melting temperature. *Geochim. Cosmochim. Acta* 90, 110-125.

Chapter II

Origin of the extreme polymetallic enrichment (Cd, Cr, Mo, Ni, U, V, Zn) of the Late Cretaceous - Early Tertiary Belqa Group, central Jordan.

Origin of the extreme polymetallic enrichment (Cd, Cr, Mo, Ni, U, V, Zn) of the Late Cretaceous - Early Tertiary Belqa Group, central Jordan.

Stéphanie FLEURANCE^{1}, Michel CUNEY¹, Fabrice MALARTRE¹⁻², Jean REYX³*

¹ G2R, Université de Lorraine, Faculté des Sciences, UMR 7566 CNRS, CREGU, Boulevard des Aiguillettes B.P. 239, 54506 Vandoeuvre-lès-Nancy cedex, France.

² G2R, Université de Lorraine, Ecole Nationale Supérieure de Géologie, UMR 7566 CNRS, Rue du doyen Marcel-Roubault, BP 40, 54501 Vandoeuvre-lès-Nancy cedex, France.

³ AREVA Mines, Geosciences Department, Place Jean Millier, 92400 Courbevoie, France.

Accepted manuscript for publication in:

Palaeogeography, Palaeoclimatology, Palaeoecology, Volume 369, 1 January 2013, Pages 201-219

Impact Factor: 2,392.

Elsevier Ed.

*Corresponding author: Stéphanie Fleurance.

stephanie.fleurance@g2r.uhp-nancy.fr

ABSTRACT

The sedimentary formations of the Late Cretaceous to Early Tertiary Belqa Group correspond to pure to slightly clayey limestones and minor black shales characterized by a remarkable enrichment in phosphorous and various redox sensitive elements (Cd, Cr, Mo, Ni, U, V, Zn). Phosphorous enrichment is related to the great phosphorite deposition event that has occurred at the southern margin of the Tethys Ocean during this period. The very low organic matter contents in the limestones, despite their strong enrichment in redox sensitive elements, is attributed to a deposition in anoxic water but under shallow water conditions permitting the bacterial degradation of a large part of the organic matter. Most of the elements constituting the Belqa Group sediments have been deposited from the sea water either directly by chemical precipitation (most Ca and redox sensitive elements) or indirectly through biogenic activity (P, part of Ca and U), except for the minor detrital contribution presents in some limestones and more significantly in the shales. Such an origin is also supported by the REE patterns of the limestones which are similar to that of the present sea water. The anomalously high concentrations of some redox sensitive trace metals (Cr, Ni and probably Cd) compared to worldwide black shales is explained by an exogenic metal flux, corresponding to the leaching of the huge amounts of ophiolites obducted during the collision between the African-Arabian and Eurasian plates at the same time as the deposition of the Belqa Group sediments. Uranium is substituted for calcium in biogenic apatite in the limestones, but was also directly precipitated from sea water in the black shales in relation with the suboxic environment with the periodic anoxia developed during their deposition in restricted deeper basins.

The pyrometamorphism resulting from the burning of organic-rich levels in clayey limestones has created a further enrichment of redox sensitive elements in the resulting marbles by a volume loss resulting from decarbonation reactions and the combustion of the organic matter.

KEYWORDS: Jordan; Belqa Group; major elements; redox sensitive elements; paleoenvironments; syngenic enrichment; exogenic metal flux.

1. INTRODUCTION

The present paper examines the lower part of the Belqa Group of central Jordan, which was deposited from the Late Cretaceous to Early Tertiary. This period is particularly well known for the extensive deposition of phosphorites variably enriched in uranium along the same paleolatitude (8° - 15° N), on carbonate platforms, at the southern margin of the Tethys Ocean, from Turkey to Morocco, through Israel, Jordan, Syria, Iraq, Saudi Arabia, Egypt, Tunisia, Algeria, and beyond the Atlantic to Colombia and Venezuela (Parish and Curtis, 1982; Soudry et al., 2004). Elevated metallic element contents in the Late Cretaceous to Early Tertiary black shales have been already reported in Jordan and Israel (Bentor et al., 1963), but the Belqa Group of Central Jordan of similar age is characterized by remarkable enrichment in a series of redox sensitive elements of most lithologies either organic-rich or not. The origin of such an extreme metal enrichment of the Upper Cretaceous to Early Tertiary formations at the south-eastern part of the Tethys Ocean is not completely understood, but a new hypothesis is proposed in this paper.

The main aim of the present paper is to report on the exceptional geochemical characteristics of Maastrichtian to Paleocene Belqa Group in central Jordan, to describe the ore-bearing mineral association and to discuss the origin of such a remarkable metal enrichment, which does not appear to be simply correlated with the presence of organic matter as in classical black shales (Holland 1979; Pasava, 1993). The Belqa Group lithologies also illustrate the evolution of sedimentation during a major global warming event and during a major geotectonic event, which occurred at the southeastern margin of the Tethys Ocean.

2. GEOLOGICAL SETTING

Jordan is situated to the north west of the Arabian Peninsula, separated from Israel and Palestine by the Dead Sea Rift Valley (Dead Sea Transform) occupied by the Jordan River. The study area is located in central Jordan, approximately 80 km south-east of Amman (Fig.II.1).

From Cambrian to early Cretaceous, Jordan was located the northern margin of the Gondwana super-continent. The area was relatively tectonically stable during the Palaeozoic with a dominantly continental sedimentation, and minor but widespread marine incursions. These

conditions of sedimentation continued into the early Triassic but by the Late Triassic to early Jurassic the area became increasingly more marine with an open sea lying to the northwest (Ziegler, 2001).

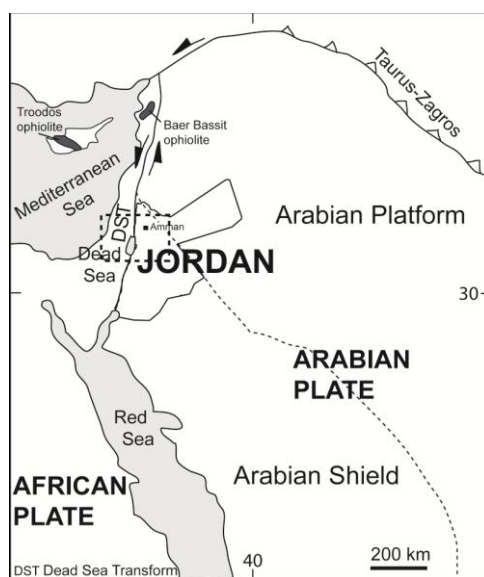


Figure II. 1. Schematic structural map of the western Arabian Plate. The dotted frame marks the figure II.2. (after Föster et al., 2010; Parlak and Roberston, 2004).

During the Late Cretaceous, subduction of the oceanic lithosphere was initiated to the north and resulted in the collision of the Arabian platform with the European continent, associated with folding and obduction of ophiolites (Lovelock, 1984). After this compression event, extension within the Arabian plate during the Late Cretaceous to early Tertiary caused the formation of a series of northwest-trending basins (Bender, 1974; Lovelock, 1984). Later left-lateral strike-slip faulting along the Dead Sea Transform in the Neogene led to the development of well defined pull-apart basins such as the Dead Sea Basin. From the Late Cretaceous to Eocene Jordan was covered by an extensive marine transgression from Cenomanian time, in relation with a global warming event, which resulted in the deposition of the Ajlun and Belqa groups (mostly calcareous sediments) (Bender, 1974; Powell and Moh'd, 2011). During the Late Eocene, a regression led to a period of folding, uplift and erosion. This period is also characterized by a left lateral transtensional event which was responsible for the Dead Sea rifting, extensive basalt flows mainly in north-east Jordan, but which extend to Syria and Saudi Arabia, and by localized lacustrine and fluvial deposits in the Azraq and Jafr basins (depressions, respectively located at the northeast and southeast of the study area).

Our study concerns specifically the sedimentary units deposited from Late Cretaceous to early Tertiary and belonging to the Belqa Group in the central part of Jordan (Fig.II.2). A lithostratigraphical scheme has been established by Bender (1974), Powell (1989), Alsharhan and Nairn (2003), Pufahl et al. (2003), Powell and Moh'd (2011) to correlate the sedimentary units in Jordan and adjacent areas (especially Israel, Egypt and Saudi Arabia). The main lithostratigraphical units are briefly summarized in Table 1.

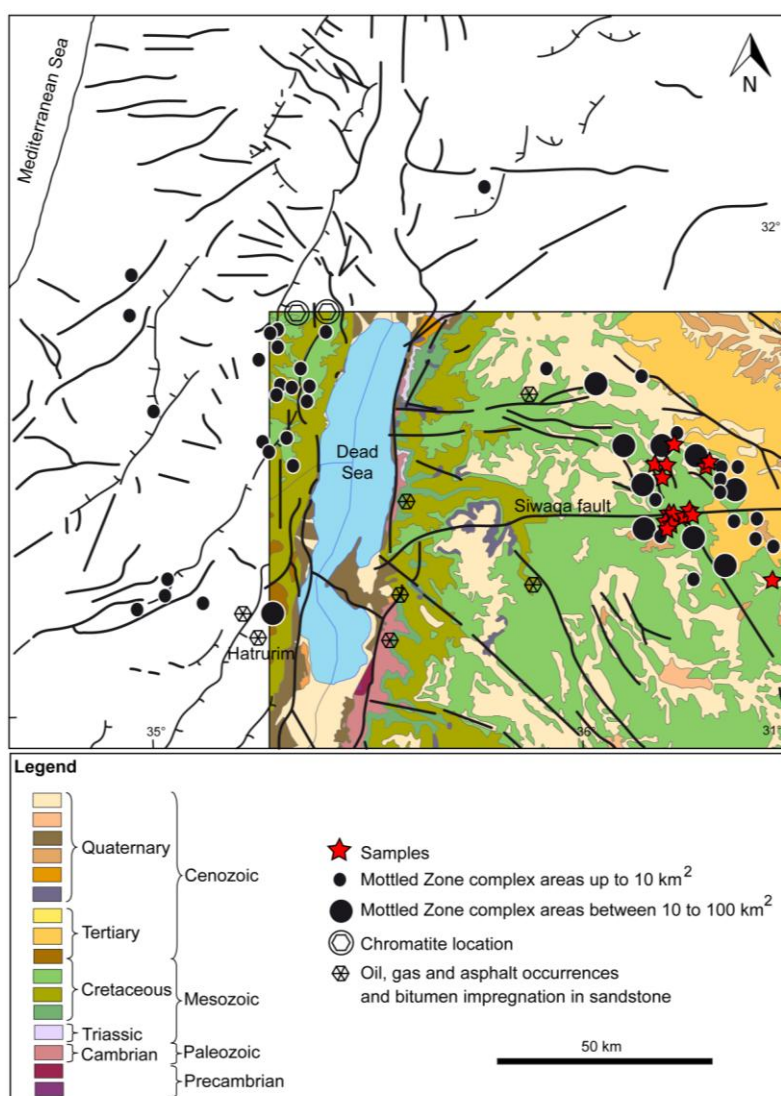


Figure II. 2. Generalized geology of the Dead Sea Transform area (modified after Sokol et al., 2011), and geological detailed map (after Bender, 1975) of the studied area, with location of samples and outcrops of the Mottled Zone Complexes in Jordan and Israel.

The Belqa Group consists mainly of limestone, chalk, marl, phosphorite and shale. The sedimentary succession was deposited during pulsatory phases of marine onlap southward and eastward across the Arabian Craton (Powell and Moh'd, 2011). This group is divided into six formations, which are in stratigraphic order: Wadi Umm Ghudran (Coniacian-Santonian), Amman Silicified Limestone (Campanian), Al Hisa Phosphorite (Upper Campanian-Lower Maastrichtian), Muwaqqar Chalk Marl (Maastrichtian-Paleocene), Umm Rijam Chert-Limestone and Wadi Shallala Chalk formations (Table II.1). This Cretaceous to Paleogene sedimentary sequence records an overall trend of progressive coastal onlap, punctuated by brief regressive, low stand sequences, bounded by burrowed condensed horizons during periods of depositional hiatus, during a globally warm greenhouse climatic regime (Powell and Moh'd, 2011).

Chronostratigraphy		Lithostratigraphy (Thickness)		Lithology (Fossils)	Depositional environments
Quaternary	Holocene			Rounded to well-rounded gravels, sands and silts	Recent alluvial, wadi sediments (present day drainage network)
	Pleistocene			Travertine, poorly sorted angular to rounded clasts gravels (mainly cherts), sands and silts	«Hot-spring», alluvial, mudfats
Tertiary	Eocene	Umm Rijam Chert-Limestone Fm. (30-45 m)		Chalky limestone, thin-bedded chert, packstone, grainstone, sparse phosphate (Fish fragments, gastropods, nummulites, calcareous nanoplankton, silicoflagellates)	Deep-water pelagic, locally hypersaline, locally shallow lagoons
	Palaeocene	Muwaqqar Chalk-Marl Fm. (100-300 m)		Chalk, bituminous -organic-rich (more than 1% TOC)- chalky marl, limestone and chert concretions (Bivalves, ammonites, gastropods, fish fragments, calcareous nanoplankton)	Deep-water pelagic ramp (locally small anoxic basins with density stratified water column)
Cretaceous	Maastrichtian				
	Campanian	Belqa Group	Qatrana Phosphorite Mb.	Phosphate, chert, chalk, chalky marl, oyster-rich coquina and bioherms (Bivalves including large oysters, gastropods, fish and reptile fragments, ammonites, silicoflagellates, radiolaria, calcareous nanoplankton, foraminifera)	Shallow-water pelagic ramp, oyster bioherms on inner ramp, stagnant bottom: winnovated phosphorite
			Bahiyya Coquina Mb.		
			Sultani Phosphorite Mb.		
			Amman Silicified Limestone Fm. (80-100 m)	Chert, microcrystalline limestone, chalky marl, sparse phosphorite, oyster-rich coquina (Bivalves including oysters, sparse ammonites, fish and reptiles fragments, silicoflagellates, radiolaria)	Shallow-water, pelagic inner ramp
			Wadi Umm Ghudran Fm. (0-3 m)	Chalk, thin-bedded chert, sparse phosphate, dolomitic grainstone (Bivalves, gastropods, fish fragments, calcareous nanoplankton)	Pelagic ramp (mid- to inner), shallow shoreline
Turonian	Ajlun Group	Wadi As Sir Limestone Fm. (80-125 m)	Micrite, wackestone, packstone, sparse ooidal grainstone, chert nodules (Bivalves, rudists, gastropods, foraminifera)	Rimmed shallow carbonate shelf, rudist patch reefs, shoaling inner shelf	

Table II. 1. Synthetic stratigraphic nomenclature: lithostratigraphy, lithology and depositional environments of the studied area. Fm.: Formation, Mb: Member. (Compiled data from Abed, 1982; Abed and Kraishan, 1991; Powell and Moh'd, 2011; Pufahl et al., 2003).

The architecture of the Late Cretaceous shallow water carbonate platforms existing at the northern margin of the Arabian plate, to which the study area belongs, is characterized by the presence of intrashelf basins. These intrashelf basins are depressions of varying sizes and shapes that occur within tectonically passive and regionally extensive carbonate shelves. They are separated from the open marine basin by the shelf margin, and are largely filled by fine-grained sediments having attributes of deeper water sedimentation (lime mud, argillaceous carbonates, shales and organic shales). This particular palaeogeographical setting is known in other locations within the Arabian plate (i.e. Oman, Iran) during the Late Cretaceous (Van Buchem et al., 2002a; Grélaud et al., 2006), but also at other time intervals such as Lower Cretaceous (Van Buchem et al., 2002b).

Neogene and Quaternary terrestrial and lacustrine deposits in Jordan reflect marine regression as a result of continuous uplift associated extensive mafic volcanic activity (Al-Zoubi and Ben-Avraham, 2002, Ibrahim et al., 2003).

3. LITHOSTRATIGRAPHY

The upper part of the carbonate platform (rimmed carbonate shelf) represented by the Turonian Wadi Es-Sir Limestone (WSL) is unconformably overlain by the Belqa Group (Fig.II.3). The Belqa Group dominantly consists of chalk, chert and phosphorite and pelagic limestone (Alsharhan and Nairn, 2003; Powell and Moh'd, 2011). Its base is represented by the Santonian Wadi Umm Ghudran Formation (WG) which is overlain by the Campanian Amman Silicified Limestone Formation (ASL) exposed along the Siwaqa Fault (Fig. II.2). The overlying Upper Campanian to Lower Maestrichtian Al Hisa Phosphorite Formation (AHP) is subdivided into three members from bottom to top: the Sultani Phosphorite, the Bahiya Coquina, and the Qatrana Phosphorite (Powell, 1989). The AHP consists of phosphorite, chert, marl, and limestone deposited on the mid to inner parts of the broad sea shelf, enriched in organic matter derived from nektonic fauna and phytoplankton. The high phosphorous content results from the high organic productivity which has occurred at the southern margin of the Tethys Ocean as that time (Alsharhan and Nairn, 2003). In the study area the phosphate enrichment of these units remains moderate and does not reach the level observed in the phosphate mining areas located to the south and north of the study area. The overlying Maestrichtian to Paleocene Muwaqqar Chalk Marl Formation (MCM) is the most extensively

exposed rock unit in the study area. The MCM consists of marl, chalk, limestone and shale. The basal and, locally, the upper part of the MCM is rich in organic matter locally known as 'oil shales'. The MCM formation was deposited in an inner to outer shelf environment, and basal bituminous horizons were accumulated in local anoxic basins which were bounded by extensional faults (Powell and Moh'd, 2011). The upper part of the MCM Formation is represented by recrystallized limestones termed marbles. Narrow basaltic like dykes and sills are injected all over the area in the MCM formation. The unconformably overlying Eocene Um Rijam Chert Limestone Formation (URC) is also locally recrystallized and contains organic-rich rocks in its lower part. The URC was deposited in an outer shelf, deeper water and more pelagic environment and represents the uppermost formation of the Belqa Group in the area. The upper most sedimentary units consist in unconformable Pleistocene travertine, and fluvial to lacustrine deposits, and finally by Holocene to present-day alluvium.

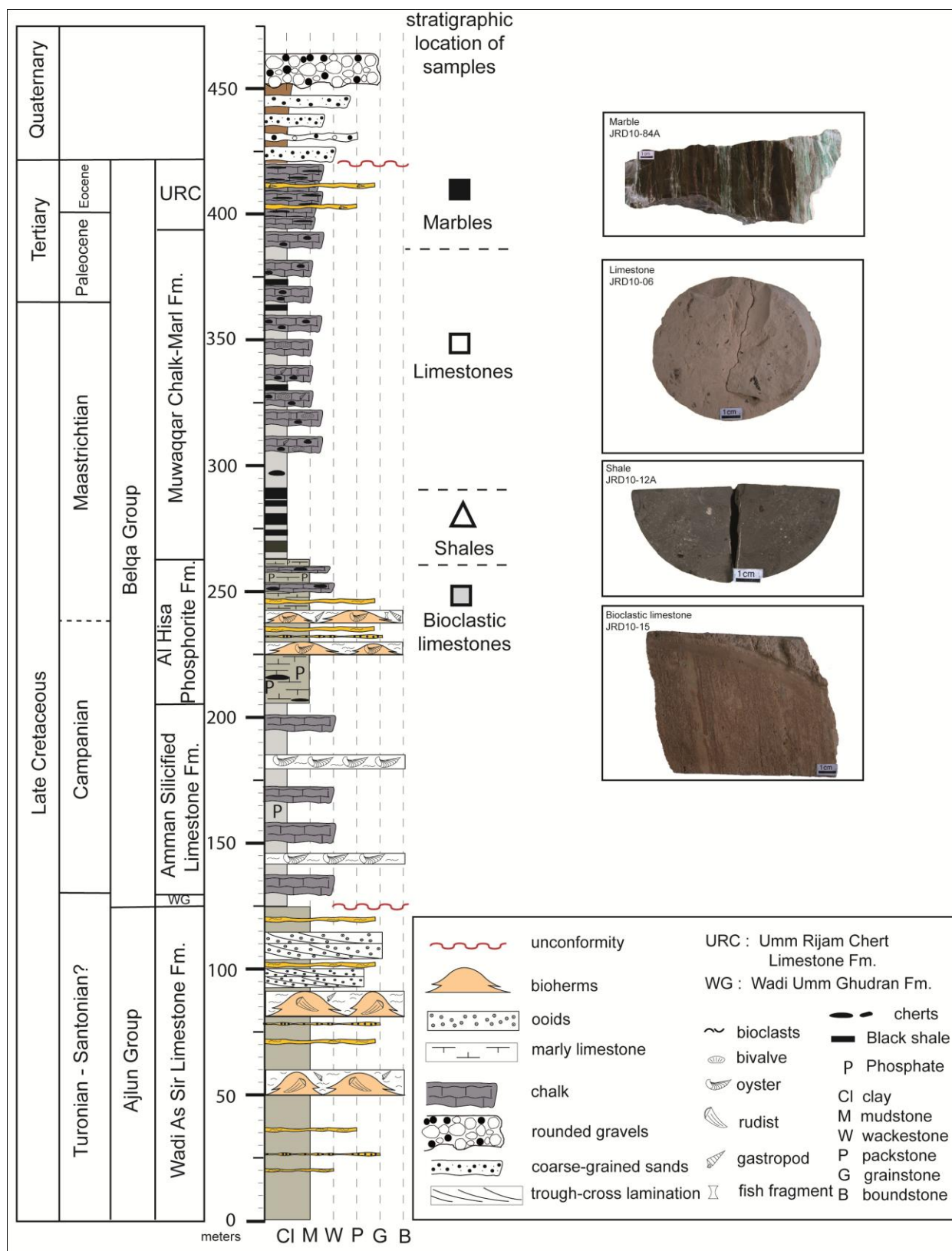


Figure II. 3. Chrono-lithostratigraphic column of central Jordan, with stratigraphic location of samples, and macrophotos of one of each lithologic group.

4. ANALYTICAL METHODS

36 samples (3 bioclastic limestones, 5 shales, 18 limestones, 10 marbles) have been selected from outcrops, trenches and exploration drilling of JORDAN AREVA RESOURCES in the Al Hisa Phosphorite (AHP), the Muwaqar Chalk Marl (MCM) and the lower part of the Umm Rijam Chert-Limestone (URC) Formations of the Belqa Group (Maastrichtian – Lower Paleocene) (Fig.3).

Polished thin sections have been studied by transmitted and reflected optical microscopy, Scanning Electron Microscopy (SEM) coupled with an Energy Dispersion Spectrometer (EDS) (Hitachi S-4800, JEOL J7600F), by Transmitted Electron Microscopy (FEI CM 20 TEM), and by a CAMECA SX100 electron microprobe at the Service Commun de Microscopies Electroniques et de Microanalyses X, Université de Lorraine, Vandoeuvre-lès-Nancy. Whole rocks were analyzed by ICP-AES for major elements, ICP-MS for 42 trace elements, and total sulphur, organic carbon, total carbon dioxide and fluor at the Service d'Analyse des Roches et des Minéraux (SARM), CNRS-CRPG, Nancy. CO₂tot, Corg and Stot are measured by calcination at 1400°C (Leco SC 144DR). CO₂ and SO₂ formed during calcination were estimated with an Infrared detector. Corg is measured after carbonate destruction with HCl. Fluor concentrations were measured by alkaline fusion. The powdered sample was mixed with sodium carbonate and water, and then was fused at 990°C. The fluor is directly measured with a fluoride selective electrode. Shales and calcium-rich lithologies have been analyzed by X-Ray Diffraction to determine complex mineral phases. Samples were decarbonated with hydrochloric acid, washed by centrifugation and lastly deposited on thin sections. They were finally analyzed by three ways: at room temperature, heated at 550°, and with ethylene glycol saturation to determine the presence of expansive clays.

5. RESULTS

5.1. Materials

5.1.1. Al Hisa Phosphorite Formation

The bioclastic limestones of the AHP formation correspond to wackestone-packstone facies. They contain abundant biogenic phosphates occurring as skeletal fragments (several

millimeter long), aggregates (up to 5 mm in diameter), ooids (up to 400 μm), and nodules (up to 300 μm) (Fig.II.4a). These phosphates are dominantly orange-brown colored, rarely colorless. These elements are embedded within a micritic mud except for the bioclastic oolitic grainstone (9502-18) which shows sedimentary laminations, alternating beds of chert and beds of microsparrite (Fig.II.4a). Besides biogenic phosphates, this limestone presents siliceous bioclastic fragments (micro grains of quartz and fibrous quartz) and silicophosphated aggregates. Some micro grains of quartz are observed within the muddy matrix. A bioclastic limestone (JRD10-15 packstone) contains a great diversity of well-preserved benthic foraminifera (up to 1 mm), and biogenic phosphates as skeleton fragments (several millimeters), and aggregates (up to 2 mm) embedded in a micrite mud. Mn-Ba oxide, romanechite ($(\text{Ba},\text{H}_2\text{O})_2(\text{Mn}_5\text{O}_{10})$), occurs as aggregates of microcrystals between the calcite crystals. Secondary uranium vanadates have been observed along a calcite vein as aggregates of microcrystals and filling spaces (50 μm) between calcite crystals in one sample (9502-17).

5.1.2. Oil shales of the lower Muwaqqar Chalk Marl Formation

Oil shales occurring at the base of the MCM Formation are laminated, fine-grained grey clayey marls with shells clasts and rare woody fragments. Discrete, isolated lamina disruptions suggest weak bioturbation. Within the shales, rare parallel orientated bivalves clasts suggest lamination. Some samples show a large numbers of foraminifera (mainly planktonic species, related to Globigerinidae). The shales consist of fine admixture of clay minerals (smectite, illite) organic matter, quartz, cristobalite and calcite. Fluorapatite occurs as skeleton fragments and irregular nodules, oriented along the laminations. The matrix of the shales contains disseminated framboidal pyrite (5 μm) and Cd-rich sphalerite crystals (up to 30 μm large aggregates and 1 μm large microcrystals) underlining the stratification (Fig.II.4b). The sphalerite microcrystals are associated with organic matter, or are included in phosphates. Uranium oxide micrograins (rounded crystals $\leq 1\mu\text{m}$) are heterogeneously distributed in the matrix of the shales. Two of the samples (JRD10-12A, B) are crosscut by a nearly vertical calcite vein. Vugs in the calcite veins are filled by 'sphalerite balls'. Hawleyite (CdS) coats the sphalerite balls. At the margin of the vein various sulfides are associated with small fibrous uranium oxide crystals ($< 1\mu\text{m}$) (Fig.II.4c) probably recrystallized from the shale matrix during the percolation of the fluids that led to the crystallization of the calcite in the veins. Zeolites (heulandite, clinoptilolite) have been determined in the shale matrix by MET analysis.

5.1.3. Limestones of the Muwaqqar Chalk Marl Formation

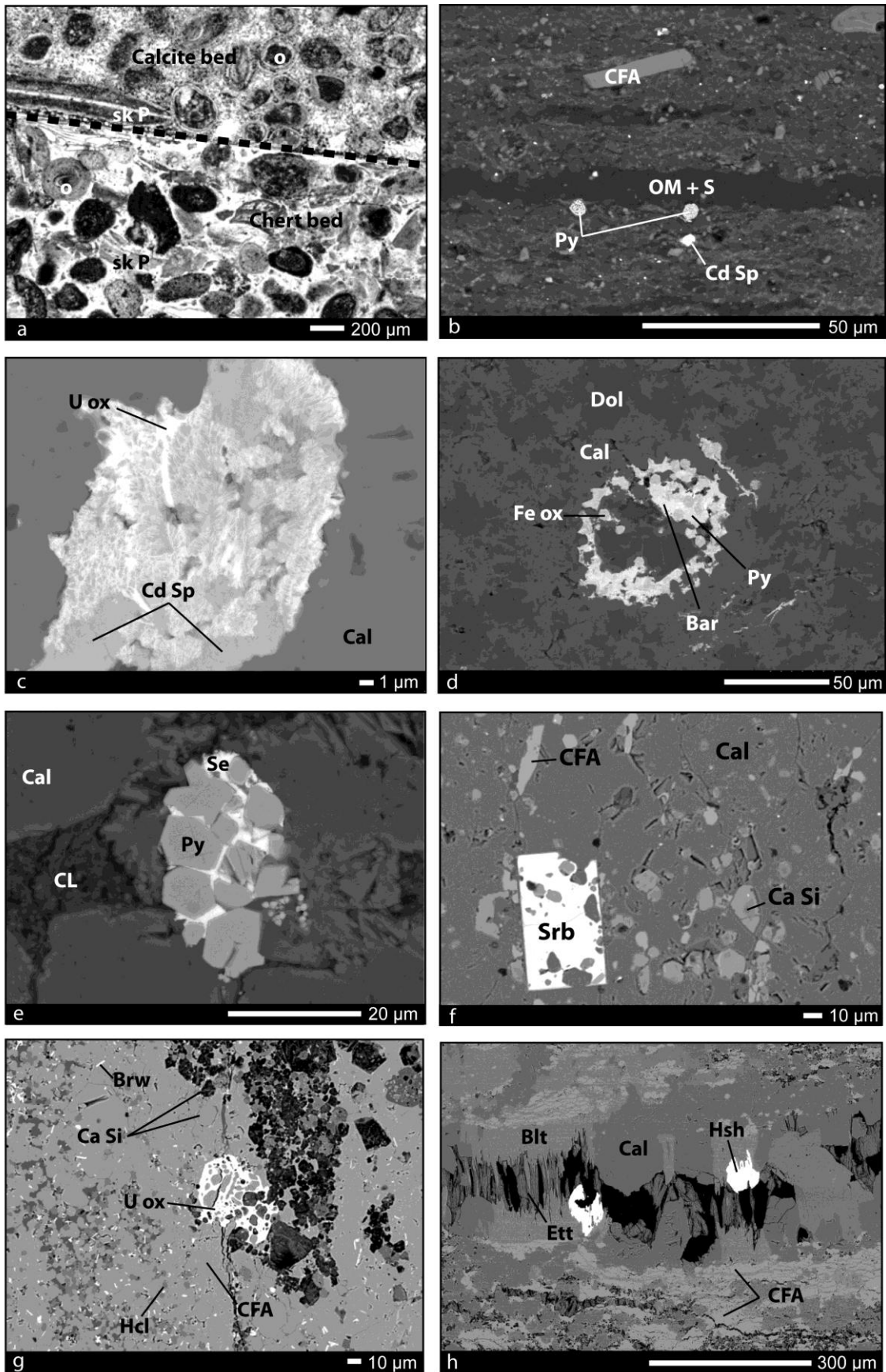
Limestones of the MCM Formation have variable colors (beige, pink-beige, pink-brown, grey, to black). There are two types: non recrystallized limestones, and recrystallized limestone. Non recrystallized limestones consist of a micritic matrix, rounded foraminifera (up to 1mm) and biogenic phosphates (up to 2mm). One of them (JRD10-08) consists of a micritic matrix between microsiliceous nodules (500 μm) and biogenic phosphates (up to 2 mm). There is porosity within the bioclasts which may represent evidence of a diagenetic replacement of initial calcite by silica. It appears as small areas that consist of cloudy zones of radial-fibrous quartz. Locally there is fracture porosity (late diagenesis ?) that cuts across the fabric elements of the rock. Within the available space, large sparitic crystals developed. The initial internal structure of foraminifera is totally destroyed by silica replacement (development of a “ghost” texture). In diagenetic recrystallized limestones, the rock consists of a mosaic of euhedral calcite rhombohedron (50 μm) clay minerals (Mg-smectite type) located between the calcite crystals. One limestone (JRD10-22) presents some dolomite crystals (Fig.II.4d). Pyrite framboids are most commonly associated with clays minerals and organic matter between the calcite grains, and sometimes with native selenium (Fig.II.4e), and with siliceous algae. Pyrite, together with barite and iron oxide may, also replace the foraminifera and others microorganisms. Sr-rich barite and native selenium crystals (micrometric aggregates) occur as inclusions in calcite crystals (up to 100 μm) in association with pyrite or clays minerals and organic matter. The foraminiferal black limestone (JRD10-19) shows some uranium vanadates adjacent to late calcite veins.

5.1.4. Marbles of the upper Muwaqqar Chalk Marl and lower Umm Rijam Chert-Limestone Formations

Marbles of the top of the MCM Formations and at the base of the URC Formation are varicolored (brown, black, pink, red, and green). They dominantly consist of calcite, carbonate-fluorapatite and calcium silicates. Calcite appears as xenomorphic elongated grains (up to 200 μm). Phosphates occur as micrograins (up to 1 mm) coating the elongated calcite grains. A series of high-temperature, sub-idiomorphic to idiomorphic (50 μm , up to 1 mm long) carbonated calcium silicates (spurrite, jennite-afwillite-tilleyite type) and oxides (brownmillerite, srebrodolskite, perovskite, hydrocalumite, mayenite) (Fig.II.4f) are

disseminated between the calcite and carbonate-fluorapatite minerals within the matrix of the marbles. Ba is hosted by barite, sometimes with powellite (CaMoO_4) around calcite grains. The marbles are rich in a variety of metallic minerals: Se-Zn-Ni sulfides like millerite, and sphalerite, pyrite and native copper disseminated in the matrix, uranium oxides occurring as poikilitic grains (up to $70\mu\text{m}$) (Fig.II.4g), and as inframetric (up to $10\mu\text{m}$) inclusions in the phosphates, complex non-identified mineral phases containing S-Fe-Ni-Cu-Se-Cr-Zn-Mo-Ba found as micro-inclusions in the phosphates, together with microcrystals of barite, Ni-Se sulfides (makinenite) and Zn-Se sulfides (stilleite). Veins filled by calcium silicates (kumtyubeite) are associated with bultfonteinite (F-silicate). These secondary Ca-silicates are associated with sulfides like Cd-rich sphalerite and gersdorffite (NiAs) and sulfates like ettringite ($\text{Ca}_6\text{Al}_2(\text{SO}_4)_3(\text{OH})_{12}\cdot 26\text{H}_2\text{O}$), hashemite ($\text{Ba}(\text{Cr,S})\text{O}_4$) (Fig.II.4h).

Figure II. 4. a) Microphotograph, Plane Polarized Light. Bioclastic limestones 9502-18; SEM images: b) shale JRD10-14A; c) shale JRD10-12B; d) limestone JRD10-22; e) limestone JRD10-09; f) marble JRD10-44; g) marble JRD10-47; h) marble JRD10-84A. Bar: barite, Blt: bultfonteinite, Brw: brownmillerite, Cal: calcite, CaSi: calcium silicate, Cd Sp: cadmium-rich sphalerite, CFA: carbonate-fluorapatite, CL: clay mineral, Dol: dolomite, Ett: ettringite, Fe ox: iron oxide, Hcl: hydrocalumite, Hsh: Hashemite, o: ooid of phosphate, OM: organic matter, Py: pyrite, S: sulfur, Se: selenium, Srb: srebrodolskite, sk P: phosphate skeleton, Uox: uranium oxide.



5.2. Major element geochemistry

Whole rock major element analyses are given in table II.2. Carbonate is quantitatively the most significant component over most of the Belqa group lithologies, with a mean content of 62.71 wt% CaCO₃. However, the concentrations are highly variable (from 3.64 to 96.92 wt% CaCO₃, Table II.2). The clay mineral abundance is low in most lithologies (0.05 < wt% Al₂O₃ < 3.12) and remains moderate in the shales (3.62 < wt% Al₂O₃ < 6.18) (Table II.2).

The **bioclastic limestones** (AHP) present large variation of Ca (13.64 < CaO < 48.67 wt%), carbonate (5.28 < CaCO₃ < 85.77 wt%) and silica (9.06 < SiO₂ < 72.41 wt%) contents reflecting the variable proportions of syndepositional silica, mostly of biogenic origin with a Ge/Si ratio (Ge/Si $0.36 \cdot 10^{-6} - 2.36 \cdot 10^{-6}$) inferior to those of the clastic ratio of the land-derived clastic supply (Tribouillard et al., 2011). Mg contents is very low (0.11 < MgO < 0.43 wt%) indicating the absence of dolomite and of magnesian clay minerals. The variable phosphate content (1.19 < P₂O₅ < 7.58 wt%) reflects the abundance of phosphates clasts and nodules. The silica-rich limestones have the highest phosphate content.

The limestone of the AHP Formation tend to have lower minor element contents (Al, Fe, Mg, Ti) than those of the MCM Formation indicating an extremely low contribution of detrital material. Its phosphate content is higher (up to 7.58 wt% P₂O₅) and one sample is extremely rich in silica (9502-18). Their total organic carbon (TOC) and total sulfur (TS) contents are very low (Table II.2).

The **shales**, overlaying the AHP bioclastic limestone, have low Al₂O₃ contents (3.62 < Al₂O₃ < 6.18 wt%) indicating low clay mineral content for shales, but high and very variable silica (26.31 < SiO₂ < 51.61 wt%) and carbonate (3.64 < CaCO₃ < 36.48 wt%) contents. The samples with the highest carbonate contents correspond to marls. Their high ignition loss (27.15 < I.L. < 39.11 wt%) reflect the presence of large amounts of organic matter (TOC) (9.39 < TOC < 16.79 wt%) and to a lesser extent of carbonates, sulfur (2.53 < TS < 4.29 wt%), and water from clay minerals. Their phosphate content is moderate (1.13 < P₂O₅ < 2.56 wt%).

The **limestones** of the MCM Formation present a large variation of carbonate (39.88 < CaCO₃ < 96.92 wt%) and silica (1.86 < SiO₂ < 32.16 wt%) contents reflecting the variable abundance of rounded siliceous nodules (chert, replacement of calcium carbonate by silica) dispersed within a micritic matrix. Variable Mg contents (0.16 < MgO < 7.01 wt%)

indicate dolomitisation of some limestone (JRD10-22) and the presence of magnesian clays minerals. The MCM limestones are poorer in phosphate ($0.20 < P_2O_5 < 3.07$ wt%) than underlying bioclastic limestones. Their organic carbon content is also generally very low (12 samples among 18 have $TOC < 0.06$ wt%), except two samples with 1.19 and 1.27 wt% TOC. Their sulfur content is also generally very low (11 samples among 18 have $TS < 0.07$ wt%), except four samples with 0.39 to 0.66 wt% TS. The sample with the highest sulfur content (JRD10-73) is poor in organic carbon.

The **marbles**, have high Ca contents ($50 < CaO < 55$ wt%), but relatively low carbonate contents ($9.31 < CO_2 < 39.43$ wt%) indicating the presence of other Ca-bearing minerals than carbonates. Calcium also enters in the structure of the phosphates ($3.42 < P_2O_5 < 20.17$ wt%) and in the silicates ($0.64 < SiO_2 < 10.21$ wt%). Their low Mg ($0.27 < MgO < 0.77$ wt%), Fe ($0.07 < Fe_2O_3 < 1.34$ wt%), and alumina contents ($0.17 < Al_2O_3 < 3.21$ wt%) indicate the low proportion of dolomite and clay minerals in the initial sediments. Their organic carbon ($< 0.02 < TOC < 0.04$ wt%) content is extremely low but their sulfur content ($0.05 < TS < 1.11$ wt%) is significant. This indicates that the dark color of the marbles is not related to the presence of organic matter, but mostly to the presence of finely disseminated sulfides.

Table II. 2. Concentrations of major, minor, trace and rare earth elements of the Belqa Group lithologies.

Formation	AHP	AHP	AHP	MCM	MCM	MCM	MCM	MCM	MCM	MCM	MCM	MCM	MCM
Lithology	bl	bl	bl*	s*	s*	s*	s*	s*	l*	l*	l*	l*	l*
Samples	9502-17	9502-18	JRD10-15	JRD10-14	JRD10-12E	JRD10-12D	JRD10-12B	JRD10-12A	JRD10-10	JRD10-09	JRD10-08	JRD10-06	JRD10-02
<i>Major and minor elements (wt%)</i>													
SiO ₂	21.03	72.41	9.06	26.31	50.66	51.61	50.00	48.79	4.83	11.39	32.16	2.63	7.78
Al ₂ O ₃	0.05	0.18	0.77	4.33	3.62	6.18	4.97	5.56	1.12	2.14	0.45	0.74	1.86
TiO ₂	0.00	0.01	0.03	0.20	0.18	0.30	0.24	0.27	0.06	0.10	0.02	0.03	0.09
Fe ₂ O ₃	0.04	0.13	0.13	1.14	2.09	2.24	1.56	1.79	0.47	0.85	0.15	0.20	1.14
K ₂ O	0.00	0.02	0.05	0.33	0.27	0.41	0.36	0.40	0.05	0.09	0.02	0.06	0.12
MgO	0.19	0.11	0.43	0.82	0.58	0.97	0.78	0.86	1.84	1.16	0.16	0.28	0.72
MnO	0.00	0.00	0.00	0.00	0.00	0.00	0.00	0.00	0.01	0.01	0.00	0.00	0.04
CaO	43.61	13.64	48.67	24.29	12.32	4.48	6.04	5.42	48.47	44.39	36.91	52.01	47.79
Na ₂ O	0.09	0.29	0.08	0.24	0.26	0.32	0.33	0.32	0.04	0.08	0.10	0.16	0.19
P ₂ O ₅	6.13	7.58	1.19	2.56	1.13	1.85	1.70	1.75	0.30	0.59	3.07	0.33	0.56
PF	28.47	4.61	38.94	39.11	27.15	30.91	32.61	33.25	42.00	39.16	26.49	42.95	39.89
Total	99.60	98.98	99.37	99.35	98.26	99.27	98.60	98.42	99.19	99.95	99.53	99.39	100.17
CO ₂ tot	28.21	2.43	38.08	64.15	41.73	56.38	62.44	63.23	44.37	39.88	25.51	41.58	36.91
TOC	0.03	0.03	0.10	13.13	9.36	14.95	16.34	16.79	1.27	1.19	0.04	0.20	0.03
TS	0.03	0.03	0.04	2.53	3.35	4.18	4.02	4.29	0.43	0.39	0.06	0.06	0.04
F	0.62	0.83	0.16	0.37	0.19	0.32	0.28	0.07	0.12	0.41	0.29	0.24	0.13
CaCO ₃	63.91	5.28	85.77	36.48	16.91	3.64	5.84	3.89	90.32	80.78	57.68	92.90	83.69
TOC/TS	1.00	1.00	2.50	5.19	2.79	3.58	4.06	3.91	2.95	3.05	0.67	3.33	0.75
<i>Trace elements (ppm)</i>													
As	4.80	4.49	0.00	21.98	145.20	50.45	74.81	75.45	7.92	14.54	8.13	3.26	24.55
Ba	93.55	67.33	16.12	43.14	40.52	49.69	46.75	49.35	8.74	429.90	158.10	31.58	398.80
Bi	0.00	0.00	0.00	0.11	0.00	0.13	0.11	0.12	0.00	0.00	0.00	0.00	0.13
Cd	41.21	41.00	6.39	85.34	98.27	349.30	110.40	342.40	15.40	9.97	468.20	55.78	0.86
Co	0.55	0.00	0.96	5.12	9.68	12.20	9.92	11.53	3.03	2.53	1.00	0.87	3.31
Cr	27.91	81.95	166.80	451.50	265.90	483.20	429.90	461.40	58.80	112.50	88.83	379.60	64.92
Cu	26.06	18.11	75.91	77.92	50.04	66.34	61.95	60.01	7.39	53.59	9.46	86.81	34.46
Mo	1.72	3.08	1.27	950.70	802.80	175.20	299.10	256.20	10.77	14.83	4.05	1.21	9.30
Ni	17.49	16.21	25.75	182.00	335.30	501.10	504.40	716.90	73.92	87.36	33.57	81.81	113.20
Pb	0.00	2.57	1.18	6.94	5.53	10.74	7.66	8.96	1.28	4.32	2.57	3.08	2.71
Sb	0.25	0.67	0.25	6.93	18.74	7.40	11.83	11.61	0.70	1.77	1.52	0.45	1.10
Sr	411.80	353.70	672.00	691.50	462.10	361.50	389.90	385.80	251.90	239.30	507.00	1491.00	471.80
Th	0.04	0.18	0.36	2.23	1.79	3.14	2.46	2.82	0.54	1.03	0.44	0.47	1.03
U	16.03	58.53	7.44	455.00	134.40	551.70	3839.00	5899.00	4.78	6.23	23.71	11.11	4.10
V	35.03	162.60	75.39	337.60	498.50	1041.00	720.20	1037.00	197.00	357.50	77.32	223.20	89.84
Zn	225.40	95.98	71.99	427.60	2321.00	4800.00	6876.00	9048.00	691.30	300.90	249.00	266.70	169.50
Cd/Zn	0.18	0.43	0.09	0.20	0.04	0.07	0.02	0.04	0.02	0.03	1.88	0.21	0.01
Cr/Th	797.43	460.39	462.05	202.65	148.71	153.74	174.47	163.68	109.29	109.76	200.07	816.34	63.09
<i>Rare Earth elements (ppm)</i>													
Ce	0.38	2.67	3.50	17.47	12.87	22.85	18.56	20.10	4.03	7.66	6.23	3.69	9.37
Dy	0.13	1.08	0.63	1.93	1.13	1.98	1.71	1.83	0.31	0.64	1.27	0.72	2.53
Er	0.13	0.96	0.48	1.30	0.73	1.24	1.13	1.22	0.20	0.39	0.92	0.49	1.77
Eu	0.02	0.18	0.13	0.46	0.30	0.54	0.46	0.49	0.10	0.18	0.27	0.15	0.54
Gd	0.11	0.96	0.61	1.92	1.18	2.10	1.79	1.91	0.35	0.67	1.19	0.68	2.48
Ho	0.04	0.29	0.15	0.42	0.24	0.42	0.37	0.40	0.07	0.13	0.30	0.16	0.59
La	0.82	6.27	3.23	11.16	7.30	12.56	10.46	11.24	2.25	4.25	5.99	3.27	13.65
Lu	0.04	0.19	0.09	0.22	0.13	0.21	0.20	0.21	0.03	0.07	0.17	0.10	0.32
Nd	0.35	3.28	2.49	9.40	6.29	11.25	9.36	10.03	1.99	3.78	4.83	2.90	9.73
Pr	0.08	0.74	0.60	2.40	1.64	2.88	2.38	2.58	0.51	0.97	1.13	0.70	2.33
Sm	0.07	0.63	0.50	1.87	1.27	2.26	1.90	2.00	0.39	0.73	0.98	0.62	1.99
Tb	0.02	0.15	0.09	0.30	0.18	0.32	0.28	0.30	0.06	0.11	0.18	0.11	0.37
Tm	0.02	0.15	0.08	0.19	0.11	0.19	0.17	0.18	0.03	0.06	0.15	0.08	0.27
Yb	0.17	1.03	0.52	1.34	0.76	1.31	1.20	1.29	0.21	0.41	0.99	0.55	1.86
ΣREE	2.38	18.56	13.10	50.39	34.13	60.10	49.95	53.78	10.52	20.04	24.60	14.19	47.80
LuN/LaN	3.90	2.68	2.51	1.76	1.53	1.48	1.66	1.67	1.29	1.41	2.53	2.56	2.04
Ce/Ce*	0.33	0.29	0.58	0.78	0.86	0.88	0.86	0.86	0.87	0.87	0.55	0.56	0.38

(bm: bioclastic limestone; s: shale, l: limestone; m: marble; *: samples of the same drilling, **: samples of another drilling)

Chapter II. Origin of the extreme polymetallic enrichment of the Late Cretaceous-Early Tertiary Belqa Group lithologies, central Jordan.

Table II.2. (Continued)

Formation	MCM	MCM											
Lithology	I**	I**	I**	I	I	I	I	I	I	I	I	I	I
Samples	JRD10-74	JRD10-73	JRD10-72	JRD10-16	JRD10-19	JRD10-21	JRD10-22	JRD10-23	JRD10-25	JRD10-40	JRD10-58	JRD10-59	9502-28
<i>Major and minor elements (wt%)</i>													
SiO ₂	25.65	6.58	20.21	2.88	3.50	2.63	2.61	7.01	1.86	2.36	5.56	20.23	2.64
Al ₂ O ₃	1.78	1.09	1.11	1.18	1.11	0.81	0.87	2.27	0.30	0.88	1.34	3.80	0.84
TiO ₂	0.08	0.05	0.05	0.05	0.05	0.03	0.04	0.09	0.02	0.04	0.05	0.16	0.04
Fe ₂ O ₃	0.68	0.47	0.46	0.57	0.52	0.32	0.33	0.75	0.12	0.31	0.41	1.22	0.38
K ₂ O	0.48	0.00	0.00	0.00	0.00	0.00	0.04	0.00	0.00	0.06	0.00	0.00	0.00
MgO	0.41	0.99	0.42	1.34	1.27	3.10	7.01	0.79	0.46	0.64	3.53	1.75	0.55
MnO	0.00	0.00	0.00	0.00	0.00	0.01	0.01	0.00	0.01	0.01	0.01	0.00	0.00
CaO	42.05	49.97	49.14	50.48	50.71	50.46	44.50	48.08	53.39	52.00	46.90	36.57	52.68
Na ₂ O	0.16	0.00	0.00	0.21	0.15	0.10	0.07	0.41	0.07	0.00	0.16	0.82	0.06
P ₂ O ₅	1.70	1.75	1.56	1.00	0.55	0.45	0.20	0.84	0.40	0.49	0.65	1.87	0.52
PF	27.33	37.35	25.91	41.38	41.78	40.84	43.25	39.54	42.43	41.88	40.07	33.92	41.82
Total	100.32	98.25	98.87	99.10	99.65	98.73	98.91	99.78	99.05	98.67	98.69	100.34	99.52
CO ₂ tot	19.33	31.78	21.22	39.23	39.49	39.43	43.13	36.22	42.01	42.09	37.15	25.30	41.03
TOC	0.49	0.09	0.02	0.05	0.06	0.01	0.14	0.03	0.06	0.20	0.01	0.04	0.05
TS	0.05	0.66	0.43	0.07	0.02	0.12	0.03	0.07	0.05	0.16	0.04	0.12	0.05
F	0.41	0.22	0.15	0.16	0.14	0.17	0.12	0.18	0.08	0.10	0.14	0.31	0.17
CaCO ₃	39.88	71.52	48.09	88.80	89.31	89.51	96.92	82.12	95.04	94.05	84.32	57.20	92.89
TOC/TS	9.80	0.14	0.05	0.71	3.00	0.08	4.67	0.43	1.20	1.25	0.25	0.33	1.00
<i>Trace elements (ppm)</i>													
As	23.18	11.98	12.74	9.45	12.55	10.57	2.94	8.87	5.34	7.22	11.24	17.74	7.71
Ba	57.38	171.90	7.87	57.49	205.10	539.90	45.53	81.69	9.35	85.58	190.50	32.15	786.20
Bi	0.00	0.00	0.00	0.00	0.00	0.00	0.00	0.00	0.00	0.00	0.00	0.25	0.00
Cd	53.53	13.45	4.70	1.54	4.05	3.29	6.21	14.96	3.08	62.92	9.85	26.85	3.94
Co	1.94	1.63	1.56	1.45	1.53	1.37	0.97	2.33	0.86	0.95	1.50	3.20	1.26
Cr	502.10	480.10	106.00	325.90	65.65	61.20	46.70	59.54	337.90	65.91	43.24	97.41	89.50
Cu	56.99	36.58	36.03	32.43	22.73	25.89	5.52	39.03	10.69	9.57	19.08	52.35	24.86
Mo	5.94	17.64	32.05	2.20	2.66	4.16	3.86	3.54	1.33	17.70	5.40	14.64	1.33
Ni	163.60	87.59	84.87	86.81	58.65	44.70	16.56	96.25	38.89	42.87	65.43	151.00	62.91
Pb	3.35	1.92	1.94	1.42	1.71	0.00	0.91	2.45	0.00	0.92	1.39	3.49	3.11
Sb	2.98	1.00	1.56	0.94	1.11	0.88	0.17	0.93	0.35	0.25	1.13	2.16	0.59
Sr	814.00	553.10	378.50	490.60	343.90	718.80	457.70	632.90	506.10	434.80	438.60	727.90	463.60
Th	0.86	0.59	0.62	0.62	0.69	0.39	0.41	1.04	0.20	0.40	0.65	1.79	0.49
U	12.87	10.78	14.34	18.47	51.11	3.78	1.31	13.36	4.35	5.42	7.11	23.14	8.19
V	209.80	74.11	167.10	237.00	176.80	118.20	30.60	87.79	28.96	67.35	154.00	344.70	38.31
Zn	895.90	282.10	214.00	190.90	298.30	217.80	53.17	291.60	160.80	349.20	428.50	399.90	254.70
Cd/Zn	0.06	0.05	0.02	0.01	0.01	0.02	0.12	0.05	0.02	0.18	0.02	0.07	0.02
Cr/Th	585.20	819.28	171.24	525.65	94.73	156.92	112.80	57.47	1664.53	163.55	67.04	54.30	181.17
<i>Rare Earth elements (ppm)</i>													
Ce	6.90	5.51	5.99	5.34	4.59	2.93	3.06	9.12	1.86	3.41	5.38	14.65	3.32
Dy	0.98	0.86	1.09	0.99	0.60	0.41	0.24	1.22	0.35	0.40	0.61	1.86	0.54
Er	0.68	0.65	0.82	0.74	0.43	0.28	0.15	0.85	0.26	0.27	0.43	1.27	0.40
Eu	0.23	0.19	0.24	0.21	0.14	0.09	0.07	0.28	0.07	0.09	0.15	0.46	0.13
Gd	0.96	0.83	1.05	0.94	0.57	0.40	0.26	1.22	0.32	0.39	0.63	1.86	0.50
Ho	0.22	0.21	0.26	0.24	0.14	0.09	0.05	0.28	0.08	0.09	0.14	0.42	0.13
La	5.32	4.74	5.53	5.03	3.51	2.27	1.64	6.43	1.74	2.32	3.76	10.38	2.99
Lu	0.12	0.12	0.15	0.15	0.08	0.05	0.02	0.16	0.05	0.05	0.08	0.22	0.07
Nd	4.30	3.61	4.32	3.89	2.69	1.78	1.44	5.38	1.36	1.93	3.00	8.85	2.17
Pr	1.06	0.89	1.06	0.93	0.68	0.45	0.38	1.34	0.33	0.49	0.77	2.19	0.55
Sm	0.87	0.76	0.89	0.77	0.54	0.37	0.31	1.11	0.27	0.39	0.60	1.80	0.45
Tb	0.15	0.13	0.16	0.15	0.09	0.06	0.04	0.19	0.05	0.06	0.10	0.28	0.08
Tm	0.10	0.10	0.12	0.12	0.07	0.05	0.02	0.13	0.04	0.04	0.07	0.19	0.06
Yb	0.71	0.69	0.85	0.81	0.46	0.30	0.15	0.91	0.27	0.27	0.44	1.30	0.41
ΣREE	22.58	19.28	22.53	20.28	14.59	9.53	7.83	28.61	7.03	10.19	16.15	45.72	11.79
LuN/LaN	1.97	2.19	2.36	2.56	2.01	2.06	1.24	2.14	2.44	1.79	1.76	1.85	2.10
Ce/Ce*	0.67	0.62	0.57	0.57	0.68	0.67	0.89	0.72	0.57	0.74	0.73	0.71	0.60

Chapter II. Origin of the extreme polymetallic enrichment of the Late Cretaceous-Early Tertiary Belqa Group lithologies, central Jordan.

Table II.2. (Continued)

Formation	MCM	MCM	MCM	MCM	MCM	MCM/URC	MCM/URC	URC	URC	AHP	MCM	MCM	MCM/URC	
Lithology	m	m	m	m	m	m	m	m	m	m	average bl	average s	average l	average m
Samples	JRD10-62	JRD10-64	JRD10-84A	9502-22	9510-15	JRD10-39A	JRD10-39B	JRD10-44	JRD10-46	JRD10-47				
<i>Major and minor elements (wt%)</i>														
SiO ₂	0.64	3.98	10.21	6.28	7.88	7.68	4.68	4.75	2.72	4.98	34.17	45.48	9.03	5.38
Al ₂ O ₃	0.17	1.01	3.09	2.61	3.21	3.12	1.71	0.54	0.95	1.57	0.33	4.93	1.32	1.80
TiO ₂	0.01	0.04	0.13	0.11	0.12	0.12	0.07	0.03	0.04	0.07	0.02	0.24	0.06	0.07
Fe ₂ O ₃	0.07	0.36	0.93	0.88	1.34	0.81	0.64	0.30	0.38	0.48	0.10	1.77	0.52	0.62
K ₂ O	0.00	0.00	0.03	0.00	0.00	0.04	0.04	0.00	0.00	0.02	0.02	0.36	0.05	0.01
MgO	0.98	0.47	0.77	0.65	0.69	0.54	0.47	0.27	0.52	0.64	0.24	0.80	1.47	0.60
MnO	0.00	0.00	0.00	0.01	0.01	0.01	0.00	0.00	0.00	0.00	0.00	0.00	0.01	0.00
CaO	54.10	53.82	52.47	53.20	50.04	54.19	55.29	55.14	54.19	54.21	35.31	10.51	47.58	53.66
Na ₂ O	0.00	0.08	0.16	0.05	0.07	0.12	0.11	0.00	0.06	0.11	0.15	0.30	0.15	0.08
P ₂ O ₅	2.82	20.17	13.92	2.52	3.96	5.09	3.94	0.95	3.42	7.76	4.97	1.80	0.93	6.46
PF	39.26	14.44	12.71	32.19	nd	26.50	31.53	36.83	35.33	26.58	24.01	32.61	38.22	28.37
Total	98.04	94.37	94.43	98.49	67.32	98.22	98.49	98.81	97.61	96.42	99.32	98.78	99.34	94.22
CO ₂ tot	39.43	14.09	9.31	28.01	23.52	23.61	30.96	36.00	34.55	25.47	22.91	57.59	35.87	26.50
TOC	0.01	0.01	0.01	0.01	0.02	0.04	0.02	0.01	0.01	0.01	0.05	14.11	0.25	0.02
TS	0.05	0.23	0.48	0.45	1.11	0.17	0.15	0.05	0.19	0.30	0.03	3.67	0.16	0.32
F	0.34	2.35	1.77	0.30	0.45	0.76	0.57	0.11	0.46	0.97	0.54	0.25	0.20	0.81
CaCO ₃	89.51	31.88	21.01	63.62	53.32	53.36	70.24	81.70	78.41	57.76	51.65	13.35	79.72	60.08
TOC/TS	0.20	0.04	0.02	0.02	0.02	0.24	0.13	0.20	0.05	0.03	1.60	3.84	1.56	0.05
<i>Trace elements (ppm)</i>														
As	20.10	68.69	22.09	16.75	113.90	9.64	21.34	2.94	8.83	7.80	3.10	73.58	11.11	29.21
Ba	25.36	868.90	269.70	2362.00	242.00	330.80	206.90	84.06	59.09	193.20	59.00	45.89	183.21	464.20
Bi	0.00	0.00	0.58	0.00	0.00	0.00	0.27	0.00	0.00	0.29	0.00	0.09	0.02	0.11
Cd	101.30	136.90	406.60	0.17	1.57	5.93	46.18	0.30	35.70	563.30	29.53	197.14	42.14	129.80
Co	0.80	1.59	2.77	2.63	6.65	3.03	1.75	1.17	1.21	1.62	0.50	9.69	1.74	2.32
Cr	119.90	1069.00	2019.00	702.80	900.30	818.60	951.70	156.10	618.00	1236.00	92.22	418.38	165.88	859.14
Cu	17.77	67.86	277.50	69.47	130.60	85.10	87.16	36.39	84.64	137.30	40.03	63.25	31.30	99.38
Mo	5.53	13.17	30.77	9.03	426.40	63.88	17.32	0.00	9.89	13.14	2.02	496.80	8.48	58.91
Ni	37.97	375.80	456.60	179.10	584.70	365.00	252.70	78.11	229.30	323.40	19.82	447.94	77.22	288.27
Pb	0.90	7.35	16.68	2.11	4.21	0.94	9.97	0.00	0.00	14.09	1.25	7.97	2.03	5.62
Sb	0.52	4.85	7.72	1.26	3.15	1.86	1.89	0.38	3.76	2.89	0.39	11.30	1.09	2.83
Sr	941.60	1707.00	1381.00	1682.00	1569.00	1449.00	1533.00	1055.00	1337.00	1586.00	479.17	458.16	551.19	1424.06
Th	0.13	0.75	3.67	1.54	1.76	1.77	1.14	0.32	0.68	1.01	0.19	2.49	0.68	1.28
U	7.90	67.58	133.60	25.16	104.80	57.33	34.61	3.00	33.18	39.99	27.33	2175.82	12.45	50.72
V	107.70	687.50	706.00	154.90	980.40	189.80	235.90	34.39	247.70	304.10	91.01	726.86	148.87	364.84
Zn	263.00	1878.00	2351.00	514.10	2344.00	1134.00	806.40	154.30	854.30	1260.00	131.12	4694.52	317.46	1155.91
Cd/Zn	0.39	0.07	0.17	0.00	0.00	0.01	0.06	0.00	0.04	0.45	0.23	0.07	0.15	0.12
Cr/Th	944.09	1429.14	550.29	457.25	512.99	463.01	837.03	493.99	906.16	1220.14	573.29	168.65	330.69	781.41
<i>Rare Earth elements (ppm)</i>														
Ce	2.11	11.78	35.45	12.80	15.00	15.56	10.59	2.35	6.11	10.72	2.18	18.37	5.72	12.25
Dy	0.93	5.13	12.40	3.05	3.04	3.23	3.66	0.77	1.60	3.53	0.61	1.72	0.87	3.73
Er	0.81	4.37	9.81	2.40	2.42	2.60	2.95	0.63	1.40	3.09	0.52	1.12	0.61	3.05
Eu	0.16	0.91	2.41	0.64	0.63	0.67	0.68	0.14	0.31	0.64	0.11	0.45	0.20	0.72
Gd	0.82	4.61	11.60	2.87	2.76	2.97	3.30	0.71	1.46	3.07	0.56	1.78	0.85	3.42
Ho	0.25	1.35	3.08	0.76	0.75	0.81	0.94	0.20	0.42	0.93	0.16	0.37	0.20	0.95
La	5.44	30.22	65.65	18.02	18.56	17.87	20.45	4.27	8.68	18.14	3.44	10.54	4.73	20.73
Lu	0.14	0.74	1.73	0.40	0.41	0.46	0.51	0.12	0.26	0.57	0.11	0.19	0.11	0.53
Nd	3.05	17.43	43.09	11.57	12.02	12.39	12.70	2.55	5.71	11.64	2.04	9.27	3.77	13.21
Pr	0.71	4.05	10.13	2.84	2.95	3.03	3.02	0.62	1.38	2.73	0.47	2.38	0.93	3.15
Sm	0.60	3.31	9.01	2.34	2.35	2.51	2.58	0.53	1.16	2.37	0.40	1.86	0.77	2.67
Tb	0.13	0.71	1.78	0.44	0.43	0.47	0.51	0.11	0.23	0.49	0.09	0.28	0.13	0.53
Tm	0.12	0.67	1.48	0.36	0.37	0.40	0.44	0.10	0.22	0.48	0.08	0.17	0.09	0.46
Yb	0.81	4.39	10.19	2.44	2.46	2.71	2.98	0.67	1.49	3.26	0.58	1.18	0.64	3.14
ΣREE	16.08	89.67	217.81	60.92	64.14	65.68	65.31	13.78	30.41	61.66	11.35	49.67	19.63	68.55
LuN/LaN	2.25	2.16	2.32	1.97	1.93	2.29	2.18	2.42	2.59	2.78	3.03	1.62	2.02	2.29
Ce/Ce*	0.25	0.25	0.32	0.41	0.47	0.49	0.31	0.33	0.41	0.35	0.40	0.85	0.66	0.36

The variation of the proportion of the major rock-forming minerals in the various lithologies of the Belqa Group is illustrated by a series of ternary diagrams (Fig.II.5a to II.5c). In the $\text{CaO-SiO}_2\text{-}5\text{Al}_2\text{O}_3$ diagram (Fig.II.5a) most of the limestones represent a mixture between carbonate, and a pole of a clay (montmorillonite-illite type) with minor quartz contribution. In contrast the silica-rich limestones are very poor in clay minerals and plot outside the trend defined by the other limestones. Hence, silicification cannot represent a late event, because a dilution trend between the Si-poor and Si-rich limestones is not observed. If the process of Si-enrichment would be silicification, in figure II.5a, the silica-rich samples should plot on a dilution trend between the field defined by the silica poor limestone which has variable clay content, and the silica pole. In fact the silica-richest samples plot on the CaO-SiO_2 side with no clay minerals, they are nearly devoid of detrital contribution. The Si-enrichment of some limestones has to correspond to a synsedimentary-diagenetic feature. The amount of detrital clay minerals and quartz being minor, silica most probably results from deposition of siliceous plankton, and/or eventually from a pure chemical precipitation. In the $\text{CaO-}10\text{P}_2\text{O}_5\text{-SiO}_2$ diagram (Fig.II.5b), the enrichment in phosphates is nearly proportional to the silica enrichment except for a few samples. This correlation is interpreted as a concomitant precipitation of silica and phosphorous, both of organic origin, together with the carbonates in the limestones. In the $\text{CaO-CO}_{2\text{tot}}\text{-SiO}_2$ diagram (Fig.II.5c) some samples are richer in CO_2 than calcite reflecting the presence of organic carbon (up to 1.27 wt% TOC) and some other are richer in Ca than calcite because of their enrichment in phosphates (up to 7.58 wt %). In the marbles most of the silica was initially bound to the clay minerals as indicated by their nearly constant Si/Al ratio (Fig.II.5a). The marbles are the richest in phosphate, but poor in silica (Fig.II.5b). In the $\text{CaO-CO}_{2\text{tot}}\text{-SiO}_2$ diagram increasing CaO/CO_2 ratios indicates not only the enrichment of the samples in phosphates, but also the decarbonation reactions which results from the development of the high temperature Ca-silicate phases observed during the mineralogical study. The shales are characterized by a high proportion of silica for a relatively low clay content, high carbonates contents (Fig.II.5a) and relatively low phosphorus content (Fig.II.5b). They are richer in organic carbon with carbon contents well above the quantity required for calcite (Fig.II.5c).

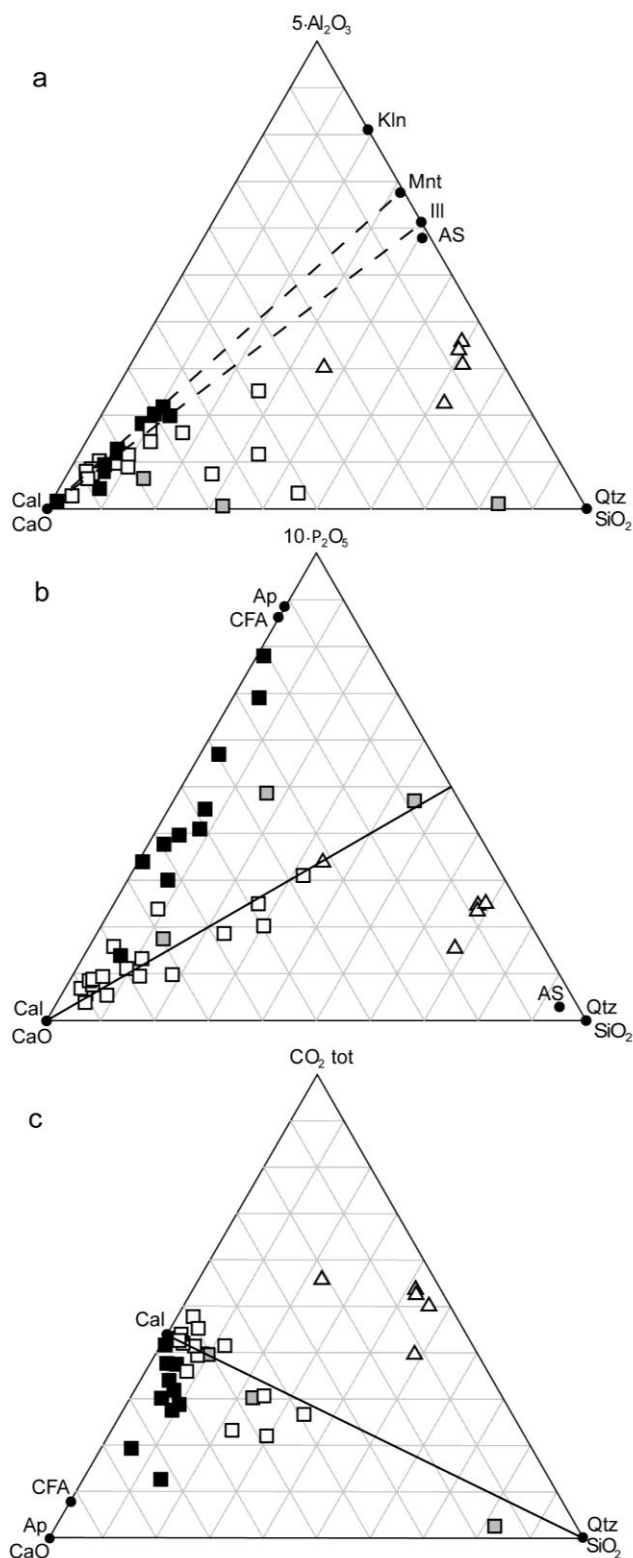


Figure II. 5. Ternary diagrams: a) $\text{CaO-SiO}_2\text{-}5\text{Al}_2\text{O}_3$; b) $\text{CaO-SiO}_2\text{-}10\text{P}_2\text{O}_5$; c) $\text{CaO-SiO}_2\text{-CO}_2\text{total}$. Grey square: bioclastic limestones, triangle: shales, white square: limestones, black square: marbles. Ap: apatite, AS: average shale (Wedepohl, 1971, 1991), Cal: calcite, CFA: carbonate-fluorapatite, Ill: illite, Kln: kaolinite, Mnt: montmorillonite, Qtz: quartz.

5.3. Redox sensitive element geochemistry

Trace elements contents are presented in table II.2 and figure II.6. All the lithologies of the Belqa Group are anomalously enriched in redox sensitive elements. The redox sensitive trace elements are much more enriched than in most organic-rich sediment occurring in the world in absolute concentration and even more when normalized to the Al content of the rock (Fig.II.6). The shales are the most enriched in zinc (427-9048 ppm), uranium (134-5899 ppm), vanadium (337-1037 ppm), molybdenum (175-951 ppm), nickel (182-717 ppm), strontium (361- 692 ppm), chromium (265- 483 ppm), and cadmium (85-349 ppm).

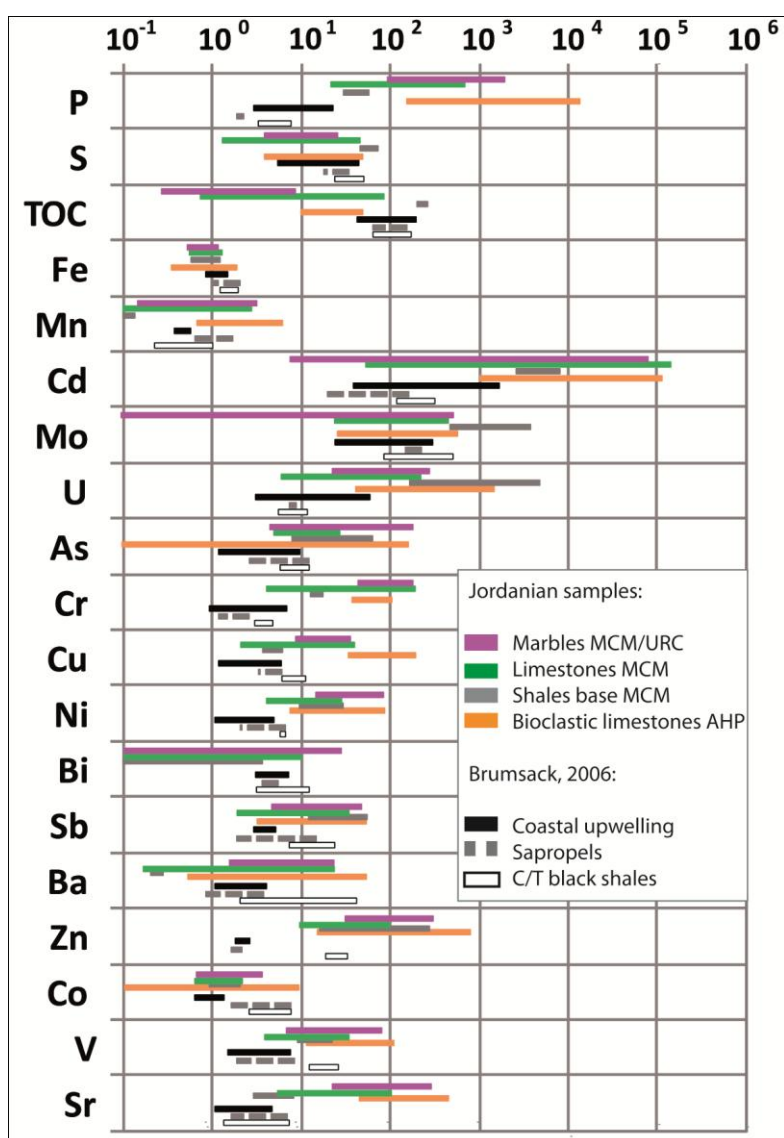


Figure II. 6. Enrichment factor (EF) of major, minor, and trace elements of each lithologic group, and OC-rich sediments (modified after Brumsack, 2006).

The limestones of the MCM and of the AHP formations, despite their lower trace element enrichment compared to other lithologies, are characterized by high concentrations of redox sensitive elements compared to common limestones: As ($0 < \text{As} < 25$ ppm, $\text{mean}(m) = 10$ ppm), Cd ($0.86 < \text{Cd} < 468$ ppm, $m = 40$ ppm), Cr ($28 < \text{Cr} < 502$ ppm, $m = 155$ ppm), Cu ($6 < \text{Cu} < 87$, $m = 33$ ppm), Ni ($16 < \text{Ni} < 164$ ppm, $m = 69$ ppm), Mo ($1 < \text{Mo} < 32$ ppm, $m = 8$ ppm), U ($4 < \text{U} < 59$ ppm, $m = 15$ ppm), V ($29 < \text{V} < 358$ ppm, $m = 141$ ppm). Zn and Cd are hosted both by sphalerite with hawleyite or its dimorph greenockite (both CdS) reflecting the high Cd/Zn of some samples (i.e. $\text{Cd}/\text{Zn} \approx 2$ in JRD10-08). As, Cu, Mo and Ni also occur as sulfides. The good correlation between U and P indicates that U is dominantly hosted by apatite, except in the U richest limestone (JRD10-19 with 51 ppm U) which is one of the poorest in phosphates (0.55 wt% P_2O_5) and where uranium is hosted in secondary uranyl vanadates observed along fractures. Some other elements, non redox sensitives like Ba ($8 < \text{Ba} < 790$ ppm, $m = 165$ ppm) and Sr ($239 < \text{Sr} < 1491$ ppm, $m = 541$ ppm) are also enriched. Ba occurs as barite and hashemite, and Sr is mainly substituted in calcite.

The marbles have still higher concentrations in many of these trace elements already enriched in the limestones (Table II.2 and Fig.II.6).

Rare earth elements

All the lithologies of the Belqa Group are poorer in REE than the Post-Archean Australian Shale (PAAS) (McLennan, 1989) and present a different global fractionation trend (Fig.II.7a). Lower REE contents reflect a lower initial clay content of these lithologies with a maximum of 6.2 wt% Al_2O_3 against 16.7 wt% for the Average Shale (Wedepohl, 1971, 1991). They tend to be richer in the heaviest REE relatively to the lightest ones. The REE patterns are also characterized by cerium negative anomalies ($0.36 < \text{Ce}/\text{Ce}^*_{\text{mean}} < 0.85$) relatively to the PAAS. The reverse fractionation of the REE and this anomaly are the strongest for the marbles and the weakest for the shales. These characteristics are similar to those of sea water (Fig.II.7a) (Zhang and Nozaki, 1998) reflecting their origin indirectly through their incorporation in biogenic carbonates and/or eventually by direct chemical precipitation from sea water with the carbonates. Seawater patterns, with the negative cerium anomalies, result of the direct incorporation of REE from seawater, or from pore water after early-burial diagenetic remobilization of REE from a REE carrier which has itself incorporated REE's directly from

seawater.

REE may be incorporated from seawater, or from occluded and associated biogenic or clastic debris via remobilization into pore water (McArthur and Walsh, 1984/1985).

The marbles are the richest in REE (ΣREE mean =69 ppm, ΣREE maximum=218 ppm), probably in relation with their higher phosphate content and the relative enrichment resulting from the volume loss as discussed hereafter. The limestones are the poorest in REE (ΣREE mean =20 ppm) because they have low phosphate and detrital particule contents. The diagram Al+P versus REE (Fig.II.8) shows the positive correlation between the abundance of REE and that of phosphate and detrital particules given by the amount of Al.

Individual REE patterns of the limestones (AHP and MCM fm.) show a great variation of REE abundance and of the negative Ce anomaly intensity ($0.29 < \text{Ce}/\text{Ce}^* < 0.95$) with increasing reverse fractionation ($0.94 < \text{LuN}/\text{LaN} < 3.90$) with decreasing REE contents (Fig.II.7c, 7e) reflecting the variable proportions of REE derived from sea water and from detrital particules. However, two bioclastic limestones have anomalously high (Al+P)/REE ratios. Their REE content is nearly only associated with the phosphates because their alumina content is extremely low (Table II.2).

The marbles (Fig.II.7b) show weaker variability of their REE patterns ($1.93 < \text{LuN}/\text{LaN} < 2.78$), a great variation of REE abundance ($13.78 < \Sigma\text{REE} < 217.81$ ppm) and an intense Ce anomaly (Ce/Ce^* mean = 0.36 ppm) reflecting their variable clay and biogenic phosphate content. The highest REE content is observed for the marble JRD10-84A which is the second richest in phosphorous and was also rich in clay minerals as reflected by its high alumina content (Fig.II.8). With the lowest in CO_2 content it also represents the most decarbonated sample. This marble is richer in REE than the PAAS except for cerium.

The shales present similar REE abundances and fractionation except one sample with lower REE content (JRD10-12E) which has the lowest clay content (lowest in alumina). The weak fractionation of their REE patterns ($1.48 < \text{LuN}/\text{LaN} < 1.76$) and the weak Ce anomalies (Ce/Ce^* mean = 0.85) reflect the predominance of REEs associated with the detrital mineral fraction as in the average shale and a much weaker contribution from sea water.

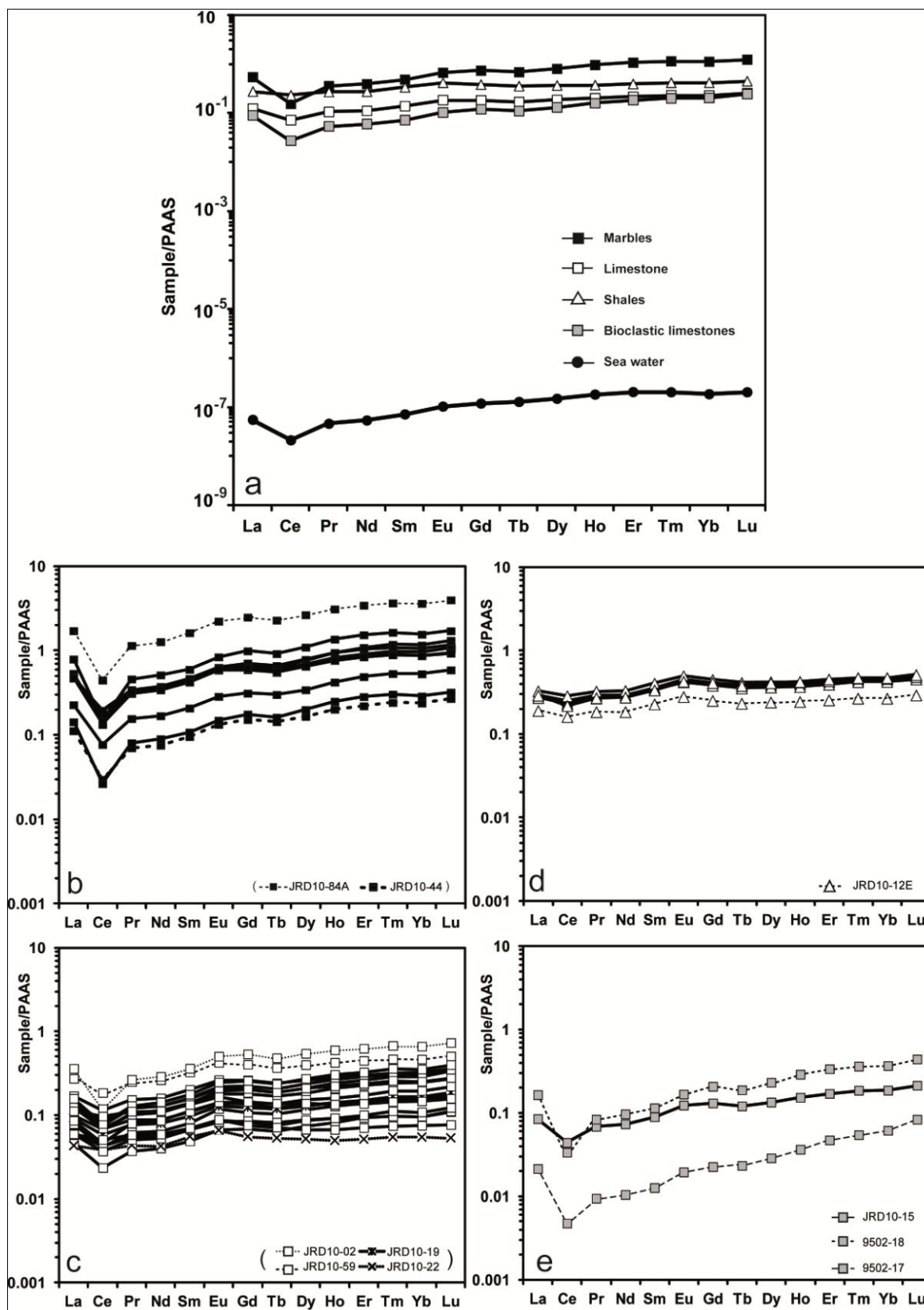


Figure II. 7. PAAS-normalized (McLennan, 1989) rare earth elements patterns of the Belqa Group lithologies: a) average REE patterns of each lithologic group; b) REE patterns of the marbles; c) REE patterns of the limestones; d) REE patterns of the shales; e) REE patterns of the bioclastic limestones.

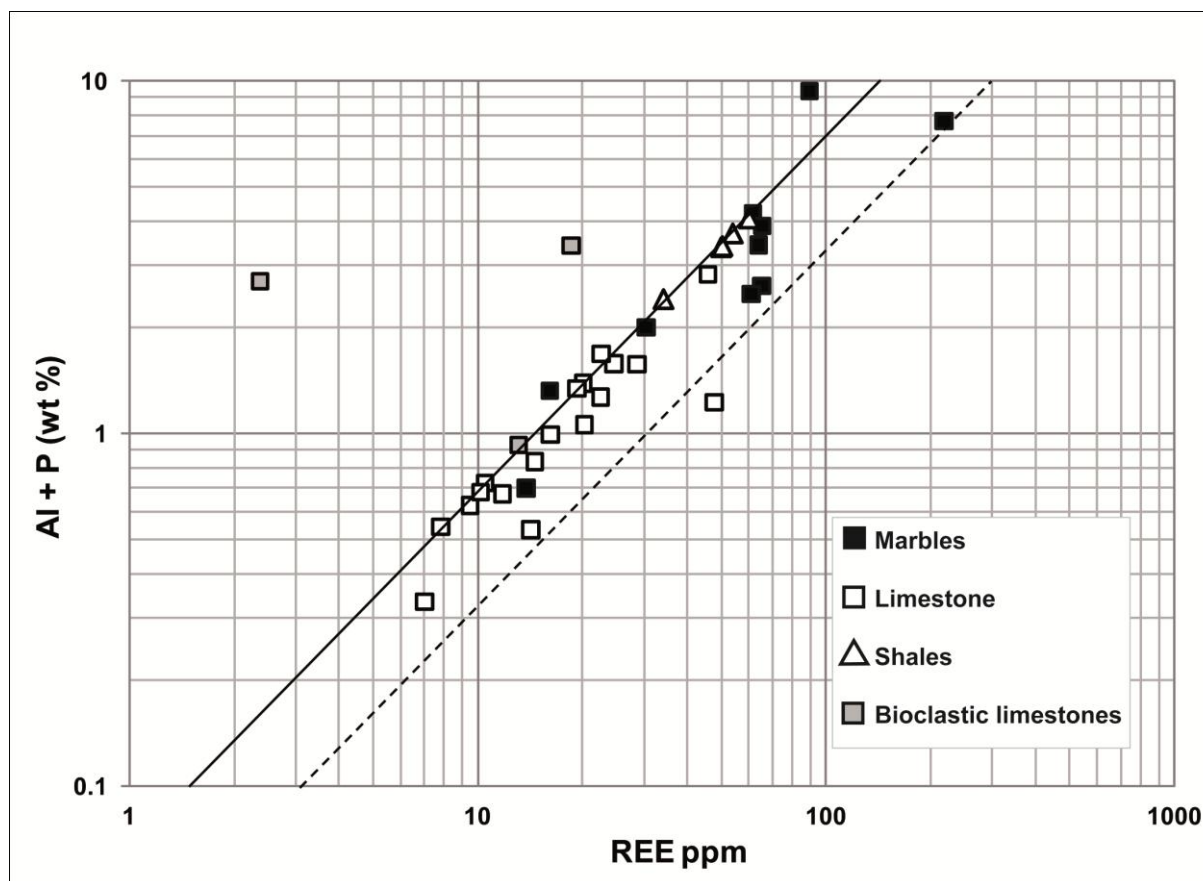


Figure II. 8. Al+P – REE diagram.

6. DISCUSSION

6.1. Redox conditions during sedimentation

All the sediments of the Belqa Group were deposited from the Late Cretaceous to early Tertiary after the major Cenomanian/Turonian (C/T) “Oceanic Anoxic Event” (OAE 2), which was associated with strong enrichments of redox-sensitive elements in organic carbon-rich sediments, well characterized by Brumsack (2006). These enrichments are usually related to anoxic bottom waters. Under reducing conditions, the elements are either directly precipitated as sulphides, co-precipitated with iron sulphides, or bound to organic matter (e.g. Breit and Wanty, 1991; Piper, 1994; Nijenhuis et al., 1998). The total amount of organic carbon preserved in sediments is mainly controlled by three factors: organic matter production, microbial decomposition, and dilution by the rate of sedimentation (Sageman et al., 2003). Most Belqa Group sediments, except the black shales and two limestones have

TOC contents below the average content of open-ocean sediment (0.3 wt% TOC) (Stein, 1990), the origin of which will be discussed below.

The relation between total organic carbon (TOC) and total sulfur (TS) of the sedimentary rock has been used by various authors to evaluate the redox conditions existing during sedimentation in the water column above the sediments and at the level of the sediment/water interface (see for example Berner, 1983, and references therein). In the Belqa Group, the shale is the only lithological unit significantly enriched in organic matter (Fig.II.9). The high TOC/TS ratios (2.79 to 5.19) of the shales is slightly lower than the average ratio of normal marine sediments beneath oxygenated water (Berner, 1983) indicating that the conditions of sedimentation of the shales were suboxic with anoxic events, a result which is surprising with regards to the very high redox sensitive metal content of these rocks (Fig.II.9). Similar conditions are obtained for about one third of the limestone samples. The main part of the limestones and the marbles with very low TOC contents (below 0.1 wt%) have low TOC/TS ratios and plot in the anoxic water – anoxic sedimentation field despite their high content in redox sensitive metals which suggest strong anoxia and even guinea. If the low TOC/TS ratios of the marbles can be easily explained by the consumption of their initial organic carbon content (necessary for the development of the combustion) during their alteration by pyrometamorphism (see later discussion).

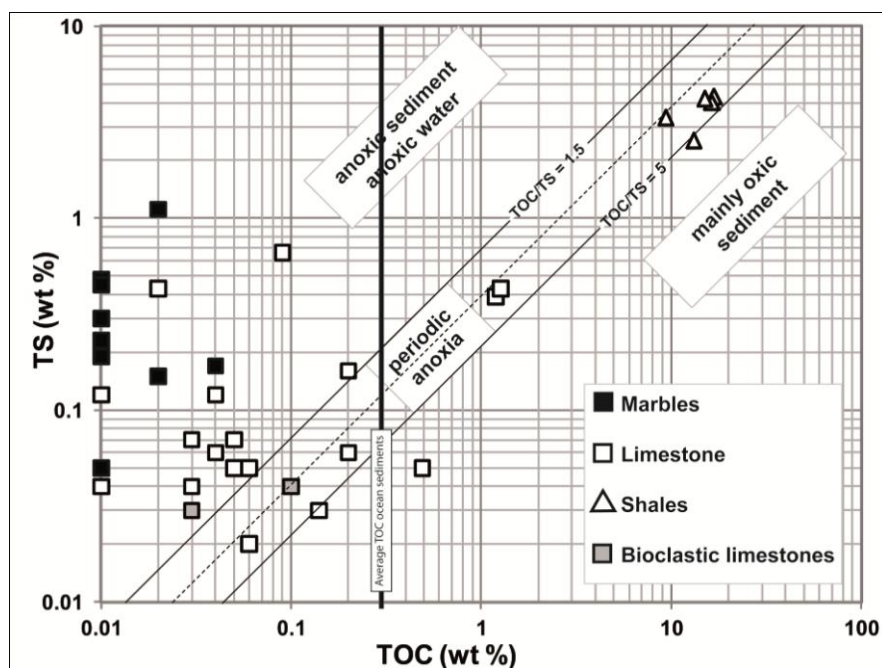


Figure II. 9. TS-TOC diagram. The dashed line represents the average S/C ratio of normal marine sediments (2.8) beneath oxygenated seawater. (Berner, 1982, 1983).

The low Al content (<3.8 wt% Al₂O₃) and the high carbonate content of the limestones indicate a very low rate of dilution by detrital particulates. The dilution may also result from the deposition of biogenic fragments and may explain at least part of explain the low TOC content of these sediments. However, the exceptionally high content in redox sensitive elements in the sediments, even in those poor in organic matter, requires the existence of a least transient anoxic conditions created by the presence of organic matter on the sea floor. The development of anoxia has been also favored by the global warming event occurring at that time which decreases the average oxygen level of oceanic waters (Meyer and Kump, 2008). The low TOC content of the limestones is a normal characteristic for carbonates. For having such low organic matter content in the limestone (despite high content of redox sensitive elements), the primary organic matter productivity should have been low, and/or the produced organic matter has been poorly preserved. However, the degradation mechanism which may have decreased the initial amount of organic matter deposited on the sea floor, has to prevent the re-oxidation of the redox sensitive elements and their removal from the sediments. Consequently, anoxic conditions of degradation are necessary (Fig.II.10). Such conditions can only result from anaerobic bacterial activity at the sea floor. Under oxygen deficiency (or suboxic conditions as defined above) denitrification and Mn and Fe reduction reactions dominates for the degradation of organic matter (Jørgensen, 2006). Also, during the transient anoxic conditions the activity of sulfate reducing bacteria occurred as shown by the existence of framboidal pyrite in the limestones JRD10-09 and 10. The different redox reactions proposed above, may explain the degradation of a large part of the organic matter initially deposited leading to the low TOC/TS ratios observed in most of the limestones.

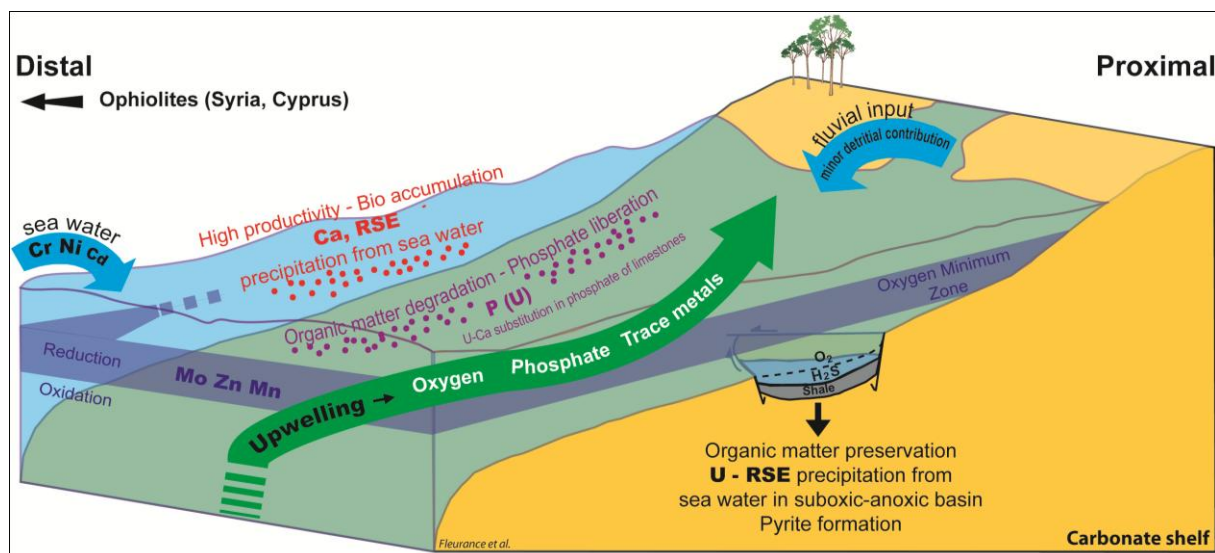


Figure II. 10. Schematic diagram of the sedimentation conditions and the chemical processes on the shelf. Without scale. (RSE: redox sensitive elements).

6.2. Origin of the phosphate enrichment

Many of the Belqa Group lithologies of Late Cretaceous-early Tertiary age are characterized by a significant but highly variable enrichment in phosphates. Enriched phosphate deposition occurred at that time over much of the southern margin of the Tethys Ocean due to a series of exceptional paleogeographic and paleoclimatic conditions (Soudry et al., 2004). More specifically, in central and south Jordan, Powell and Moh'd (2011) have related the high phosphate content of the Belqa Group:

- (i) a high organic productivity on the oyster banks that produced abundant carbonate clasts which were preferentially phosphatised off-bank, but phosphate concentrations of our samples of the phosphorite formation (AHP) do not reach the level of the phosphorites known in this region (Abed et al., 2005);
- (ii) winnowing and concentration of nektonic skeletal fragments and phosphatized grains in a shallow water environment;
- (iii) relatively low subsidence rate and low pelagic sedimentation rate resulting in a series of condensed sequences in this facies.

Most of the limestones have phosphate content below 1 wt% P_2O_5 , except five samples, with 1.6 to 3.1 wt% P_2O_5 , which tend to have the highest silica contents (up to 32 wt% SiO_2). Similarly, the bioclastic limestones which are richer in phosphates (up to 7.6 wt% P_2O_5), are also very rich in silica (up to 72 wt% SiO_2). As no detrital quartz has been observed in these samples, and as indicated by the low Ge/Si ratios, most of the silica is probably of biogenic origin as the phosphates and derived from siliceous plankton. The excellent correlation observed between Si and P enrichment for the limestones, in the ternary diagram CaO- SiO_2 - $10P_2O_5$ (Fig.II.5b), further supports this interpretation. The important development of phosphorites from Late Cretaceous to Eocene all over the southern shallow marine platform of the Tethys Ocean, indicates a predominant ocean upwelling type of sedimentation over much this area (Fig.II.10).

6.3. Origin of the metal enrichment

Most of the lithologies of the Late Cretaceous to Early Tertiary Belqa Group in central Jordan, dominated by carbonate-rich lithologies, are exceptionally enriched in a large variety of trace elements, mostly redox sensitive metals. Several origins can be proposed for such an enrichment: (i) a primary precipitation of the metals from normal sea water during their deposition, (ii) a primary precipitation from sea water contaminated by an exogenic metal source deriving from hydrothermal fluids or from river waters leaching weathered rocks enriched in specific metals, (iii) a secondary deposition (epigenetic enrichment) during burial from diagenetic fluids by replacement of the carbonates as in Mississippi Valley Type (MVT) deposits. The case of the marbles with the involvement of decarbonation and burning reactions will be discussed in a separate section.

6.3.1. Epigenetic enrichment

An epigenetic metal enrichment of the Belqa Group lithologies can be easily ruled out because:

(i) the metal-bearing minerals occur as very small isolated or crystal aggregates finely disseminated within the matrix of the rocks, most commonly with a grain-size of a few micrometers or below the micrometer size, favors syndimentary deposition of these metals,

- (ii) their distribution tends locally to follow the primary sedimentary bedding, but seldom occurs in dissolution cavities or in fractures as observed classically in Mississippi Valley Type deposits (Paradis et al., 2007), except in two samples where recrystallization of some of the metals occurs at the wall of a fracture filled by calcite in the shales JRD10-12A-B),
- (iii) the strongest metal enrichment is observed in the shales with the highest organic carbon content and the lowest carbonate contents, that is, in the rocks which are less permeable and the less liable to develop dissolution cavities in which the metals can have been deposited,
- (iv) the set of enriched elements in the Belqa Group sediments is much larger than the classical one observed in MVT deposits (mainly Zn and Pb, \pm Cu, \pm Cd, \pm Ag, \pm Ni, \pm Co, never enrichments in Cr and V), but typically correspond to the set of redox sensitive elements concentrated in organic matter-rich sediments, such as black shales (Brumsack, 2006; Vine and Tourtelot, 1970; Yu et al., 2009) or organic matter rich carbonates (Tribovillard et al., 2004), whereas Pb, a major metal in all MVT deposits, is not significantly enriched.
- (v) in hydrothermal conditions, as in the MVT deposits, the Cd/Zn ratio is generally not high enough to allow the crystallization of cadmium sulfides (greenockite or hawleyite) (Schwartz, 2000), typically sphalerite contains 0.2 to 1 wt% Cd in MVT deposits (Cook et al., 2009), which is opposite to our observations in Belqa Group sediments that have a much higher whole rock Cd/Zn ratio (average Cd/Zn=0.15, up to 1.88).

6.3.2. Syndimentary enrichment

A syndimentary enrichment from average sea water appears to be the most plausible explanation for most of the metal enrichment of the Belqa Group lithologies.

Part of the enrichment of some of the elements can be first related to the high phosphate content of many samples of the different lithologies of the Belqa Group (Table II.2). A large part of the uranium enrichment, can be attributed to the high phosphorous content of Belqa group lithologies, because uranium is replacing calcium in the structure of the biogenic apatite, as shown by the correlation between P and U for the limestones and the marbles (Fig. II.11). The fluorine content is also very well correlated with phosphorous in accordance with the fluorine-rich nature of the biogenic carbonate-fluorapatite in phosphorites (McArthur,

1985; McClellan and Van Kauwenbergh, 1991). The few limestones with low P contents plotting above the correlation correspond to samples contaminated by hexavalent U vanadates along fractures as described above. The marbles tend to plot on the same U-P correlation as the limestones, but with higher U contents related to their higher phosphate contents and to their loss of volume as discussed above.

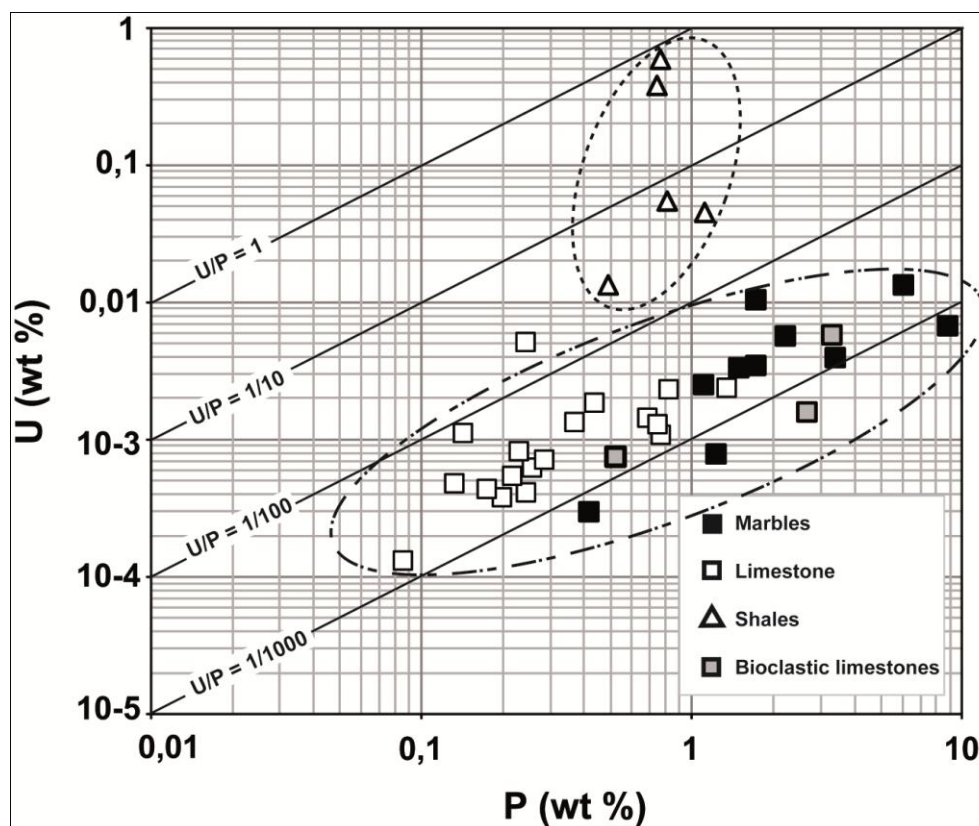


Figure II. 11. U-O diagram.

The shales are abnormally enriched in uranium relatively to their phosphate content, and part of the uranium occurs as uranium oxide microcrystals disseminated in the matrix of the shale. Such a distribution reflects a direct precipitation of uranium oxide from sea water in relation with redox conditions during the sedimentation, sufficiently reducing to permit the reduction of the uranyl ions dissolved in sea water. The quantity of precipitated uranium was exceeding the capacity of apatite to incorporate uranium. Molybdenum is also more enriched in the shales (up to 960 ppm) than in the carbonate lithologies (Table II.2, Fig.II.6), but the Mo enrichment is not correlated to the U enrichment. A number of studies (references in Piper, 1994) have shown that strong enrichments in U (Klinkhammer and Palmer, 1991) as well as

in Mo (Emerson and Husted, 1991) occur where sulfate reduction operates in the bottom oceanic waters. These observations are in agreement with the observation of framboidal pyrite in the Belqa Group shales and their relatively high TOC/TS ratios (Fig.II.9).

Besides the shales, most of the sediments of the Belqa Group are variably enriched in a large spectrum of redox sensitive metals: As, Cd, Cr, Ni, Mo, U, V, Zn, S, classically enriched in organic matter-rich sediments (Fig.II.6). However, the nature of the metal enrichment observed in the Belqa Group sediments present a series of atypical features: (i) the TOC values of most of the limestone and all the marbles is generally very low (12 limestones among 18 have TOC<0.06 wt%), but this point has been discussed for the limestones above and will be discussed for the marbles thereafter; (ii) despite these low TOC values, several of the redox sensitive trace elements are much more enriched than in most TOC-rich sediment occurring in the world in absolute concentration and even more when normalized to the Al content of the rock (Fig.II.6), and more particularly for Zn (up to 9000 ppm), Cd (up to 470 ppm) and Cr (500ppm), whereas some others are present in relatively low concentrations such as Mn, Co and Mo (Fig.II.6); (iii) a significant clastic contribution can be excluded because there is no correlation between Al and the total trace metal content for the carbonates suggesting a detrital contribution; although the shales which are the richest in alumina are the richest in trace metals, their Al/total trace metals ratio is extremely low compared to the clastic ratio of the upper crust (Rudnick and Gao, 2003), (iv) there is no relation between the TOC and TS contents and the TOC/TS ratios with the trace metal content of the rock. For example the limestone JRD10-74 relatively enriched in organic matter (0.49 wt% TOC), but with very low sulfur content (0.05 wt% TS), i.e. a low TOC/TS ratio indicating oxic deposition conditions, is the richest in most redox sensitive elements (500 ppm Cr, 60 ppm Cu, 160 ppm Ni, 210 ppm V, 900 ppm Zn), whereas sample JRD10-73 poor in organic matter (TOC=0.09 wt%), but rich in sulfur (TS=0.66 wt%) is poorer in redox sensitive elements (480 ppm Cr, 37 ppm Cu, 90 ppm Ni, 74 ppm V, 282 ppm Zn) except for Cr with a concentration which seems to be independent of that of the other redox sensitive elements. Similarly samples JRD10-09 and 10 which have close and relatively high TOC and TS and identical TOC/TS ratios have very contrasted redox sensitive elements contents (Table II.2).

The variability of phosphate, silica and trace metal concentrations in the sediments and especially in the carbonates reflects the variability of the redox conditions during the sedimentation oscillating from relatively oxic conditions when strong upwelling bring

oxygenated water in the marine environment, favoring high biogenic productivity with important phosphate accumulation from marine vertebrates, and silica from siliceous plankton, to suboxic with episodic anoxic conditions with larger accumulation of organic matter and many of the redox sensitive elements, but moderate phosphate deposition. The variability of the organic matter content of the limestone has been largely obliterated by the degradation of the organic matter by the bacterial activity, which has decreased the TOC/TS ratios of the limestones as discussed above, and which has been probably facilitated by relatively low initial rate of accumulation of the organic matter at the bottom of the relatively oxic water column. The low rate of organic matter accumulation can be explained by the shallow depths of deposition of the sediments, because degradation of the organic matter at the sediment-water interface increases with decreasing depth (Murat and Got, 2000). The role of a variable dilution of the concentration of redox sensitive elements by varying rate of supply of detrital particules has a minor important because Al contents of most of the Belqa Group sediments is very low, but biogenic carbonate supply may have represented a diluent.

Upwelling conditions during sedimentation may explain part of high Cd contents observed in Belqa Group sediments and some of their other geochemical characteristics because Cd is enriched together with P whereas Co (<3 ppm in the limestones and 12 ppm in the shales) and Mn (<0.01 wt%) are depleted in upwelling sediments (Brumsack, 2006; Delgadillo-Hinojosa et al., 2001). However, the Cd concentrations and especially the high Cd/Zn ratios observed in the Belqa Group sediments are far beyond what is observed in such depositional environments. Therefore, the origin of the extreme Cd enrichment of the Belqa Group sediments, as well as the abnormal enrichments in Cr, Zn and even Ni when normalized to the Al content of the sediments requires another explanation (Fig.II.6).

6.3.3 Exogenic metal flux

An exogenic origin for some of the trace metals in sediments has been already proposed when they reach exceptionally high concentrations. For example, if the accumulation of most trace metals in C/T black shales has been explained as deriving from seawater from balance calculations, the important accumulation of elements such as Zn has been explained by an additional metal input, possibly from hydrothermal sources (Arthur et al., 1988). For Brumsack (2006) the extreme enrichment in Ag, Cu, Ni, and Zn of the Cretaceous black

shales may require additional metals sources of possible hydrothermal origin or a different trace metal seawater composition during the Cretaceous. A hydrothermal influx from volcanic vents has also been proposed for very high Zn, Ni, Cu contents as observed in the Paleoproterozoic black shales of Talvivaara in Finland (Loukola-Ruskeeniemi and Heino, 1996). However the absence of positive Eu anomaly as observed in hydrothermally enriched plume water with elevated Mn, Fe, Zn, and Ni contents in the Teahitia and Macdonald volcanoes (Stüben et al., 1992) is not in favor of such an influx. Moreover, there is no evidence of terrestrial volcanic activity during the Late Cretaceous-Early Tertiary period in central Jordan. However, these shales despite their very high Zn contents (up to several wt% have much lower Cd (<70 ppm), lower Cr (<270 ppm), and Mo (<130 ppm) than the Belqa shales, but much higher Mn (up to several percents compared to less than 0.04 wt % in all Belqa lithologies), higher Ni (up to 5000 ppm), Cu (up to 3700 ppm), and Co (up to 560 ppm) contents, and similar V contents.

High concentrations of Cr (300 to 900 ppm) have been reported in the Pennsylvanian Shales from the USA Midcontinent (Schultz and Coveney, 1992), similar to those measured in the Belqa shales and marbles. The similarity of the Cr concentration in the Pennsylvanian shales, whatever their depositional environment was (from nearly anoxic to oxic), to the opposite to what is observed for the other redox sensitive elements in these shales, indicates that the precipitation of Cr was probably not dominantly controlled by the variations in redox conditions. Such a behavior reflects an exogenic origin of chromium for the Pennsylvanian shales, as also proposed for the Permian Bennett Shale Member in eastern Kansas (Muehleisen, 1994). More recently, Coveney (2010), considers that even the high Mo and Zn concentrations of Midwestern Pennsylvanian black shales, which are only comparable with the modern black muds directly associated with marine hydrothermal vents, result from their mineralization by hydrothermal solutions during the Pennsylvanian.

In the case of the Belqa Group sediments, their specific enrichment in Cr together with Ni and Cd may be related to the proximity of huge masses of ultrabasic rocks leached by river waters and transported to the sea. Large ophiolitic complexes are known all along the Late Cretaceous Ophiolite Belt of Southwest Asia (LCOBSWA) which stretches for 3000 km from Cyprus to Oman through Iran (Robertson, 2002; Moghadam and Stern, 2011). These ophiolites correspond to relics of the oceanic substratum of the NeoTethys which had been obducted onto the continental margin of the African-Arabian plates during continental

convergence between the Eurasian and Afro-Arabian plates in Late Cretaceous and Tertiary times as presented above. In Oman, the main obduction phase took place from Middle Turonian to Santonian (Breton et al., 2004). During Campanian to Maastrichtian, a large part of that obducted oceanic crust was emergent and was being actively eroded (Le Métour et al., 1990, Nolan et al., 1990; Alsharhan & Nasir, 1996). A similar evolution could be proposed at the scale of the LCOBSWA. The closest occurrences, presently at about 450 km from Central Jordan are those of Baer Bassit in north-western Syria and Troodos in Cyprus Island (Fig.II.1). This hypothesis is further supported by the fact that the high Cr/Th observed in the Belqa sediments ($54 < Cr/Th < 1665$, mean = 454) are only observed in the pelites of the Witwatersrand (Condie and Wronkiewicz, 1990) for which Cr deposition has been independent of the redox conditions, because the atmosphere was nearly anoxic during the Archean, and directly reflect the high Cr content of the source rocks represented at that time by the greenstone belts. An input from river waters has been already proposed to explain the high cadmium contents observed over the West European Atlantic continental shelf, with enrichment factors of the order of three to five, compared with open-ocean values (Kremling and Pohl, 1989).

6.3.4. Metamorphic enrichment of the marbles

In several localities the calcareous horizons belonging to the Muwaqqar Chalk Marl Formation (Fig.II.3) have suffered a very high temperature, very low-pressure metamorphism (named pyrometamorphism, Grapes, 2006) produced by the endogenous combustion of organic matter-rich layers resulting in the formation of marbles. The metamorphism is evidenced by the peculiar high temperature mineralogical assemblage existing in these rocks, and by their much lower carbonate content than that of limestone despite similar calcium contents (Fig.II.5c). This type of metamorphism has been observed over much of the study area and has been recorded in different part of Jordan, Syria and Israel (e.g. Bentor et al., 1963; Khoury and Nassir, 1982; Burg et al., 1999; Sokol et al., 2010) and dated to the Neogene (Gur et al., 1995) (Fig.II.2). The lithological unit in which these rocks occur is named the “Mottled Zone” or the Hatrurim Formation (in Israel) (Fig.II.2). All strata are densely veined and altered by late hydrothermal solutions. A detailed presentation of the mineralogical assemblage of these rocks, outlined above, is beyond the scope of this paper.

The decarbonation reactions and the burning of organic matter have led to a significant volume loss in the rock, and thus have created a relative enrichment of the trace metals. An excellent estimation of these effects on trace metal concentration is provided by the study of Yoffe et al. (2002) which compares the geochemistry of the Maastrichtian oil shales from the Negev desert with the corresponding ashes produced by fluidized bed combustion at 700-800°C. The Maastrichtian oil shales from the Negev desert (Ghareb Formation, Soudry, 2000) are stratigraphic equivalents of the MCM of Central Jordan (Powell and Moh'd, 2011) and evidence of pyrometamorphism of these units is also known in Israel because of their high TOC contents (up to 26 wt%). The concentration of trace elements is nearly doubled in the ash compared to the initial concentrations measured in the oil shales. This variation corresponds to a maximum enrichment factor, because many of the marbles still contain a significant amount of carbonates: 21 to 82 wt% in the marbles compared to 40 to 95 wt% in the limestones and only 4 to 37 wt% in the shales (Table II.2). However, the average enrichment factor in the marbles with respect to the carbonates is much higher (0 to 10). The trace element level of the marbles is closer to that of the shales, although the marbles are not derived from the combustion of shale type protolith because of their lower alumina content despite the volume loss resulting from the pyrometamorphism ($mAl_2O_{3shales} = 4.93wt\%$ compared to $mAl_2O_{3marbles} = 1.80wt\%$). Hence, the enhanced redox sensitive element content in the marble is due to the burning of initially high organic carbon content.

7. CONCLUSIONS

The Late Cretaceous to Early Tertiary Belqa Group lithologies were deposited in two sedimentary environments during the Maastrichtian to Paleocene. The shales and part of the limestone succession were deposited in suboxic water with periodic anoxia with relatively abundant accumulation of organic matter, and in deeper waters, within local anoxic basins bounded by extensional faults. The sedimentary protoliths of the marbles from the MCM and lower URC formations were deposited in the same conditions that allowed the deposition and preservation of abundant organic matter. Abundant organic matter must have been present in the marbles protoliths to permit the development of pyrometamorphism by combustion of organic matter, evidenced by the high temperature mineral paragenesis of these rocks. The sedimentation of the limestones with variable phosphate contents took place in areas of

upwelling with moderate to abundant organic matter production, but with its poor preservation because of the shallower depth of deposition.

The exceptional redox sensitive elements enrichment (RSE) of the Belqa Group sediments results from a series of mechanisms:

(i) The enrichment in many of the RSE (U, Cu, Co, Mo, Sb, V) are comparable to the enrichment observed in the black shales and results from a syndimentary deposition either by direct precipitation from average sea water-or through their incorporation in the marine organisms, in suboxic conditions with episodic anoxia.

(ii) Some other RSE (Cr, Ni, Cd, Zn) are much more enriched compare to in average shales (worldwide) or Upper Cretaceous black shales, generally, (Fig.II.6) and require an exogenic metal flux which we propose to be derived from enrichment these metals in sea water by river waters deriving these elements from the weathering and alteration of the huge masses of ultrabasic rocks obducted at the end of the Cretaceous. The nearest occurrences of such rocks are the ophiolites of the Troodos Massif (Cyprus Island) and Baer Bassit (North-western Syria),

(iii) Pyrometamorphism of some of the limestones which leads to the formation of marbles is responsible of further trace elements enrichment because of the large volume loss resulting from decarbonation reactions and burning of the organic matter which resulted in high-temperature combustion,

(iv) The main part of the uranium enrichment in the Belqa Group sediments is well correlated with the biogenic phosphates accumulation, except in the black shale which shows exceptional enrichment in uranium in local anoxic basins where the rate of sedimentation was extremely low.

ACKNOWLEDGMENTS

This work would not have been possible without the financial and scientific support of AREVA NC, notably the French and Jordanian geologists with whom we have selected the samples. We would like to thank the team of the lithopreparation service for the preparation of numerous thin sections; the staff of SCMEM for the access at the microprobe service, Jerome Marin and the staff of the SARM for the geochemical analysis, his availability and his patience. Also, we thank Jean Louis Vignerese and Julien Mercadier of the G2R laboratory for their helpful comments on the manuscript. The two reviewers are greatly thanked for their constructive remarks.

REFERENCES

- Abed, A.M., 1982. Microfacies and palaeoenvironment of the Wadi Sir Formation (Upper Cretaceous), north Jordan. *Facies*, 7, 1, 229-236.
- Abed, A.M., Kraishan, G.M., 1991. Evidence for shallow marine origin of a Monterey Formation type chert-phosphorite-dolomite sequence, Amman Formation (late Cretaceous), central Jordan. *Facies*, 24, 1, 25-38.
- Abed, A.M., Arouri, K.R., Boreham, C.J., 2005. Source rock potential of the phosphorite-bituminous chalk-marl sequence in Jordan. *Mar. Petrol. Geol.* 22, 413-425.
- Al-Zoubi, A. S., Ben Avraham, Z., 2002. Structure of the earth's crust in Jordan from potential field data. *Tectonophysics* 346, 45-59.
- Alsharhan, A.S., Nasir, S.J.Y., 1996. Sedimentological and geochemical interpretation of a transgressive sequence: the Late Cretaceous Qahlah Formation in the western Oman mountains, United Arab Emirates. *Sedimentary Geology* 101, 227-242.
- Alsharhan, A.S., Nairn A.E.M., 2003. Sedimentary basins and petroleum geology of the Middle East. Elsevier Ed., 942 p.
- Arthur, M.A., Jenkyns, H.C., Brumsack, H.-J., Schlanger, S.O., 1988. Stratigraphy, geochemistry, and paleoceanography of organic carbon-rich Cretaceous sequences. In: Ginsburg, R.N., Beaudoin, B. (Eds.), *Cretaceous Resources, Events and Rhythms:*

Background and Plans for Research. Kluwer Academic Publishers, Digne, France, pp. 75-119. Proc. of ARW.

Bender, F., 1974. Geology of Jordan. Contribution of the Regional Geology of the Earth. *Gebüder Borntraeger*, pp 196 .

Bender, F., 1975. Geological map. 1:500000. Gov. of Jordan and Geol. Survey of Fed. Rep. Germ.

Bentor, Y.K., Gross, S., and Heller, L., 1963. High-temperature minerals in nonmetamorphosed sediments in Israel. *Nature*, 199, 478-479.

Berner, R.A., 1982. Burial of organic carbon and pyrite sulfur in the modern ocean: its geochemical and environmental significance. *Am. J. Sci.* 282, 451-473.

Berner, R.A., 1983. Sedimentary pyrite formation: an update *Geochim. Cosmochim. Acta* 48, 605-615.

Breit, G.N., Wanty, R.B., 1991. Vanadium accumulation in carbonaceous rocks. A review of geochemical controls during deposition and diagenesis. *Chem. Geol.* 91, 83-97.

Breton, J.P., Béchenec, F., Le Métour, J., Moen-Maurel, L., Razin, P., 2004. Eoalpine (Cretaceous) evolution of the Oman Tethyan continental margin: insights from a structural field study in Jabal Akhdar (Oman mountains). *GeoArabia* 9, 41-57.

Brumsack, H-J., 2006. The trace metal content of recent organic carbon-rich sediments: implications for Cretaceous black shale formation. *Palaeogeogr.Palaeoclimatol.Palaeoecol.* 232, 344-361.

Burg, A., Kolodny, Ye., Lyakhovsky, V., 1999. Hatrurim-2000: the "Mottled Zone" revisited, forty years later. *Isr. J. Earth Sciences*, 48, 209-223.

Condie, K.C., Wronkiewicz, D.J., 1990. The Cr/Th ratio in Precambrian pelites from the Kaapvaal Craton as an index of craton evolution. *Earth Planet. Sci. Lett.* 97, 256-267.

Cook, N.J., Ciobanu, C.L., Pring, A., Skinner, W., Shimizu, M., Danyushevsky, L., Saini-Eidukatg, B., Melcherh, F., 2009. Trace and minor elements in sphalerite: A LA-ICPMS study. *Geochim. Cosmochim. Acta* 73, 16, 4761-4791.

Coveney, R.M., Jr., 2010. Metals in Pennsylvanian black shales from ore fluids not from seawater. Abstracts with Programs. Geol. Soc. Am. 42, 54.

Delgadillo-Hinojosa, F., Macías-Zamora, J.V., Segovia-Zavala, J.A., Torres-Valdés, S., 2001. Cadmium enrichment in the Gulf of California. Mar. Chem. 75, 109-122.

Diabat, A., Masri, A., 2002. The state of palaeostress along the Siwaqa Fault (central Jordan) based on fault slip data. The 15th Iraqi Geological Congress, 15-17 December, Baghdad.

Emerson, S.R., Huested, S.S., 1991. Ocean anoxia and the concentrations of molybdenum and vanadium in seawater. Mar. Chem. 34, 177-196.

Föster, H.-J., Föster, A., Oberhänsli, R., Stromeyer, D. 2010. Lithospheric composition and thermal structure of the Arabian Shield in Jordan. Technophysics, 481, 1-4, 29-37.

Grapes, R., 2006. Pyrometamorphism. Springer. 275p.

Grélaud, C., Razin, P., Homewood, P.W., Schwab, A.M., 2006. Development of incisions on a periodically emergent carbonate platform (Natih Formation, Late Cretaceous, Oman). J. Sed. Res. 76, 647-669.

Gur, D., Steinitz, G., Kolodny, Y., Starinsky, A., McWilliams, M., 1995. ⁴⁰Ar/³⁹Ar dating of combustion metamorphism ("Mottled Zone", Israel). Chem. Geol. 122, 171-184.

Holland, H.D., 1979. Metals in black shales: a reassessment. Econ. Geol. 74, 295-314.

Ibrahim, K.M., Tarawneh, K., Rabba, I., 2003. Phases of activity and geochemistry of basaltic dike systems in northeast Jordan parallel to the Red Sea. J. Asian Earth Sci. 21, 467-472.

Jørgensen, B.B., 2006. Bacteria and marine biogeochemistry. In: Schulz, H.D., Zabel, M. (Eds.), Mar. Geochem. Springer Verlag, Berlin. 169-201.

Khoury, H., Nassir, S., 1982. A discussion on the origin of Daba-Siwaqa marbles. Dirasat 9:55-66.

Klinkhammer, G., Palmer, M.R. 1991. Uranium in the oceans: where it goes and why. Geochim. Cosmochim. Acta 55, 1799-1806.

Kremling, K., Pohl, C., 1989. Studies on the spatial and seasonal variability of dissolved cadmium, copper and nickel in northeast Atlantic surface waters. Mar. Chem. 27, 43-60.

Le Métour, J., Rabu, D., Tegye, M., Béchenec, F., Beurrier, M., Villey, M., 1990. Subduction and obduction: two stages in the Eo-Alpine tectonometamorphic evolution of the Oman mountains. In: Robertson A.H.F., Searle M.P. & Ries A.C. (Eds), "The geology and tectonics of the Oman region", Geol. Soc London, Sp. Pub. 49, 327-339.

Loukola-Ruskeeniemi, K., Heino, T., 1996. Geochemistry and genesis of the black shale-hosted Ni-Cu-Zn deposit at Talvivaara, Finland. *Econ. Geol.* 91, 1, 80-110

Lovelock, P.E.R., 1984. A review of the tectonics of the northern Middle East region. *Geol. Mag.* 121, 577-587.

McArthur, J.M., Walsh, J.N., 1984/1985. Rare earth geochemistry of phosphorites. *Chem. Geol.* 47, 191-220.

McArthur, J.M., 1985. Francolite geochemistry – compositional controls during formation, diagenesis, metamorphism and weathering. *Geochim. Cosmochim. Acta* 49, 23-35.

McClellan, G.H., Van Kauwenbergh, S.J., 1991. Mineralogical and chemical variation of francolites with geological time. *J. Geol. Soc.* 148, 809-812.

McLennan, S.M., 1989. Rare earth elements in sedimentary rocks: influence of provenance and sedimentary processes. In: Lipin B.R. and McKay G.A. (Eds.), *Geochemistry and mineralogy of rare earth elements. Reviews in Mineralogy*, 21, 169-200.

Meyer, K.M., Kump, L.R., 2008. Oceanic Euxinia in Earth History: Causes and Consequences. *Annu. Rev. Earth Planet. Sci.* 36, 251-288.

Moghadam, H.S., Stern, R.J., 2011. Late Cretaceous forearc ophiolites of Iran. *Island Arc*, 20, 1-4.

Muehleisen, S.A., 1994. Trace and Rare-Earth Element Geochemistry of the Bennett Shale Member (Red Eagle Limestone) and its implications for the Depositional Environment of this unit at the Tuttle Creek Dam Spillway exposure, Eastern Kansas, U.S.A. Kansas Geological Survey, Open-file Rept. 94-36.

Murat, A., Got, H., 2000. Organic carbon variations of the eastern Mediterranean Holocene sapropel: a key for understanding formation processes. *Palaeogeogr. Palaeoclimatol. Palaeoecol.* 158, 241-257.

- Nijenhuis, I.A., Brumsack, H.-J., de Lange, G.J., 1998. The trace element budget of the eastern Mediterranean during Pliocene sapropel formation. In: Robertson, A.H.F., Emeis, K.-C., Richter, C., Camerlenghi, A. (Eds.), Proc.ODP Sci. Results, 160, 199-206.
- Nolan, S.C., Skelton, P.W., Clissold, B.P. & Smewing, J.D., 1990. Maastrichtian to early Tertiary stratigraphy and palaeogeography of the central and northern Oman mountains. In: Robertson A.H.F., Searle M.P. & Ries A.C. (Eds), "The geology and tectonics of the Oman region". Geol. Soc London, Sp. Pub. 49, 495-519.
- Paradis, S., Hannigan, P., and Dewing, K., 2007, Mississippi Valley-type lead-zinc deposits, in Goodfellow, W.D (ed). Mineral Deposits of Canada: A synthesis of major deposit types, district metallogeny, the evolution of geological provinces, and exploration methods. Geol. Assoc. of Canada, Mineral Deposits Division, Sp. Pub. No. 5, 185-203.
- Parlak, O., Robertson, A., 2004. The ophiolite-related Mersin Melange, southern Turkey: its role in the tectonic-sedimentary setting of Tethys in the Eastern Mediterranean region. Geol. Mag. 141, 257-286.
- Parish, J.T., Curtis, R.L., 1982. Atmospheric circulation, upwelling, and organic-rich rocks in the Mesozoic and Cenozoic eras. *Palaeogeogr.Palaeoclimatol.Palaeoecol.* 40, 31-66.
- Pasava, J., 1993. Anoxic sediments - an important environment for PGE: an overview. *Ore Geol. Rev.* 8, 425-445.
- Piper, D.Z., 1994. Seawater as the source of minor elements in black shales, phosphorites and other sedimentary rocks. *Chem. Geol.* 114, 95-114.
- Powell, J.H., 1989. Stratigraphy and sedimentology of the Phanerozoic rocks in central and southern Jordan. Bulletin 11, Geology Directorate, natural resources Authority (Ministry of Energy and Mineral resources) Amman, Part B: Kurnub, Ajlun and Belqa group, 161.
- Powell, J.H., Moh'd, B.K., 2011. Evolution of Cretaceous to Eocene alluvial and carbonate platform sequences in central and south Jordan. *GeoArabia*, 16, 4, 29-82.
- Pufahl, P.K., Grimm, K.A., Abed, A.M., Sadaqah, M.Y., 2003. Upper Cretaceous (Campanian) phosphorites in Jordan : implications for the formation of a south Tethyan phosphorite giant. *Sed. Geol.*, 161, 175-205.

- Robertson, A.H.F., 2002. Overview of the genesis and emplacement of Mesozoic ophiolites in the Eastern Mediterranean Tethyan region. *Lithos*, 65, 1-67.
- Rudnick, R.L., Gao, S., 2003. Composition of the continental crust. p 1-64. In *The Crust* (ed. R.L. Rudnick) vol. 3. *Treatise on Geochemistry* (eds. H.D. Holland and K.K. Turekian), Elsevier-Pergamon, Oxford.
- Sageman, B.B., Murphy, A.E., Werne, J.P., Ver Straeten, C.A., Hollander, D.J., Lyons, T.W., 2003. A tale of shales: the relative roles of production, decomposition, and dilution in the accumulation of organic-rich strata, Middle- Upper Devonian, Appalachian basin. *Chem.Geol.* 195, 229-273.
- Schultz, R.B., Coveney, R.M., Jr., 1992. Time-dependent changes for Midcontinent Pennsylvanian black shales, U.S.A. *Chem. Geol.* 99, 83-100.
- Schwartz, M.O., 2000. Cadmium in Zinc Deposits: Economic Geology of a Polluting Element. *Int. Geol. Rev.* 42, 5, 445-469.
- Sokol, E., Novikov, I., Zateeva, S., Vapnik, Ye., Shagam, R., and Kozmenko, O., 2010. Combustion metamorphic rocks as indicators of fossil mud volcanism: new implications for the origin of the Mottled Zone, Dead Sea rift area. *Basin Research*, 22, 414-438.
- Sokol, E.V., Gaskova, O.L., Kokh, S.N., Kozmenko, O.A., Seryotkin, Y.V., Vapnik, Y., Murashko, M.N., 2011. Chromatite and its Cr³⁺ - and Cr⁶⁺ -bearing precursor minerals from the Nabi Musa Mottled Zone complex, Judean desert. *Am. Mineral.* 96, 659-674.
- Soudry D., 2000. Carbonate-phosphate competition in the Negev phosphorites (southern Israël): a microstructural study. In: Glenn C.R., Prévôt-Lucas L. & Lucas J. (Eds), "Marine authigenesis: from global to microbial". *Soc. Econ. Paleont. Mineral. Sp. Pub.*, 66, 415-426.
- Soudry, D., Segal, I., Nathan, Y., Glenn, C.R., Halicz, L., Lewy, Z., VonderHaar, D.L., 2004. ⁴⁴Ca/⁴²Ca and ¹⁴³Nd/¹⁴⁴Nd isotope variation in Cretaceous-Eocene Tethyan francolites and their bearing on phosphogenesis in the southern Tethys. *Geology*, 32, 389-392.
- Stein, R., 1990. Organic carbon content/sedimentation rate relationship and its palaeoenvironmental significance for marine sediments. *Geo-Mar. Lett.* 10, 37-44.

Stüben, D., Stoffers, P., Cheminee, J-L., Hartmann, M., McMurtry, G.M., Richnow, H.H., Jenisch, A., Michaelis, W., 1992. Manganese, methane, iron, zinc, and nickel anomalies in hydrothermal plumes from Teahitia and Macdonald volcano. *Coschim. Cosmochim. Acta* 56, 3693-3704.

Tribovillard, N., Riboulleau, A., Lyon, T., Baudin, F., 2004. Enhanced trapping of molybdenum by sulfurized marine organic matter of marine origin in Mesozoic limestones and shales. *Chem. Geol.* 213, 385-401.

Tribovillard, N., Bout-Roumazeilles, V., Riboulleau, A., Baudin, F., Danelian, T., Riquier, L., 2011. Transfer of germanium to marine sediments: insights from its accumulation in radiolarites and authigenic capture under reducing conditions. Some examples through geological ages. *Chem. Geol.* 282, 120-130.

Van Buchem, F.S.P., Razin, P., Homewood, P.W., Oterdoom, H., Philip J., 2002a. Stratigraphic organization of carbonate ramps and organic-rich intrashelf basins: Natih Formation (middle Cretaceous) of northern Oman. *Amer. Assoc. Petrol. Geol. Bull.* 86, 21-53.

Van Buchem, F.S.P., Pittet, B., Hillgärtner, H., Grötsch, J., Al Mansouri, A.I., Billing, I.M., Droste, H.H.J., Oterdoom, W.H., 2002b. High-resolution sequence stratigraphic architecture of Barremian/Aptian carbonate systems in Northern Oman and United Arab Emirates (Kharai and Shu'aiba Formations). *GeoArabia* 7, 461-500.

Vine, J.D., Tourtelot, E.B., 1970. Geochemistry of black shale deposits. A summary report. *Econ. Geol.* 65, 253-272.

Wedepohl, K.H., 1971. Environmental influences on the chemical composition of shales and clays. In: Ahrens, L.H., Press, F., Runcon, S.K., Urey, H.C. (Eds), *Physics and Chemistry of the earth*, Pergamon, Oxford pp. 305-333.

Wedepohl, K.H., 1991. The composition of the upper earth's crust and the natural cycles of selected metals. Metals in natural raw materials. *Natural Resources*. In: Merian, E; (Ed.), *Metals and Their Compounds in the Environment*. VCH, Weinheim, pp 3-17.

Yoffe, O., Nathan, Y., Wolfarth, A., Cohen, S., and Shoval, S. 2002. The chemistry and mineralogy of the Negev oil shale ashes. *Fuel*, 81, 101-117.

Yu, B., Dong, H., Widom, E., Chen, J., Lin, C., 2009. Geochemistry of basal Cambrian black shales and cherts from the Northern Tarim Basin, Northwest China: Implications for depositional setting and tectonic history. *J. Asian Earth Sci.* 34, 418-436.

Zhang, J., Nozaki, Y., 1998. Behavior of rare earth elements in seawater at the ocean margin : a study along the slopes of the Sagami and Nankai troughs near Japan. *Geochim. Cosmochim. Acta* 62, 1307-1317.

Ziegler, M.A., 2001. Late Permian to Holocene paleofacies evolution of the Arabian Plate and its hydrocarbon occurrences. *GeoArabia* 6, 445-504.

Chapter III

Sedimentary, metamorphic to supergene evolution of uranium and REE in the phosphates from the Belqa Group lithologies, central Jordan.

Sedimentary, metamorphic to supergene evolution of uranium and REE in the phosphates from the Belqa Group lithologies, central Jordan.

Stéphanie FLEURANCE^{}, Michel CUNEY*

G2R, Université de Lorraine, Faculté des Sciences, UMR 7566 CNRS, CREGU, Boulevard des Aiguillettes B.P. 239, 54506 Vandoeuvre-lès-Nancy cedex, France.

In preparation.

*Corresponding author: Stéphanie Fleurance.

stephanie.fleurance@hotmail.fr

ABSTRACT

Carbonate-fluorapatite (CFA) is the most common apatite in the marine sediments and phosphorites. The CFA studied in central Jordan were formed by upwelling into relatively shallow marine settings during the important Late Cretaceous-Early Tertiary phosphogenesis event responsible of the great phosphorite belt along the southern margin of the Tethys Ocean. Uranium can enter in the CFA structure by substitution for Ca. The sedimentary-diagenetic carbonate-fluorapatites suffered local pyrometamorphism allowing the mobilization and the concentration of U to form micrometric uranium oxides hosted by CFA in marbles, which contain high uranium concentrations. Newly formed fluorapatite of other metamorphic facies (black and green calc-silicate rocks), formed from different protolithes poorer in phosphates, have been totally decarbonated and have a low uranium content. The meteoric and evaporitic alteration of the limestones led to the weathering of the carbonate-fluorapatite which lost some fluor ions to form fluorite, and gained sulphur ions inducing the crystallization of sulfato-phosphate with low uranium and REE contents.

1. INTRODUCTION

Phosphorites are widespread in Jordan and are variably enriched in uranium. They belong to one of the most extensive phosphogenic events in Earth history, the Late Cretaceous-Eocene Tethyan phosphate province, which extends from India to Columbia, and which was developed along the southern shelf of the Neo-Tethys Ocean (Abed et al., 2007; Moh'd and Powell, 2010). The sediments of the Belqa Group in central Jordan were deposited during this period were variably enriched in phosphate and, remarkably, in a series of redox sensitive elements: Cd, Cr, Mo, Ni, U, V, Zn (Chapter II, Fleurance et al., accepted). Although the phosphate concentration of the sediments of the Belqa group from the Dabba-Siwaqa are of central Jordan not reached in the ore grade commonly observed in phosphorites, this area offers the possibility to study the evolution of the chemistry of apatite through a succession of processes: sedimentation and diagenesis, pyrometamorphism and supergene alteration, leading locally to the formation of surficial uranium mineralization. Although, the uranium mineralization in this area mainly consists of uranyl vanadates, the genetic conditions leading to the formation of the uranium mineralization differs significantly from the classical calcrete-type uranium deposit model. In phosphatic rocks, apatite is generally the main host for the

uranium and the rare earth elements (REE) which can be used as tracers of petrogenetic processes. Moreover, uranium derived from apatite may represent a metal source for the genesis of uranium deposits. The aim of this work is to characterize the geochemistry of uranium and REE in the apatite crystals from the various types of lithologies of the Belqa Group in central Jordan, using Laser Ablation ICP-MS in situ analyses, and to follow their behavior through sedimentary-diagenetic, metamorphic and supergene processes until the formation of surficial uranium mineralization.

2. GEOLOGICAL SETTING

The phosphate deposition occurred during the Late Cretaceous to Eocene is related to the coincidence of four exceptional conditions (Cuney, 2010): (i) the rise in sea level during the Late Cretaceous resulted from a global warming episode, (ii) the Late Cretaceous east-west Paleotethys Ocean developed between Laurasia and Gondwana, (iii) the Neo-Tethys Ocean location in the warmest equatorial latitudes, and (iv) the upwelling of cold nutrient-rich waters along the the southern Neo-Tethys Ocean margin during the Late Campanian and Early Maastrichtian (Fig.III.1). During the Late Cretaceous to Eocene times about 29×10^9 tons of phosphate rocks have been accumulated (Jasinski, 2003, Soudry et al., 2006).

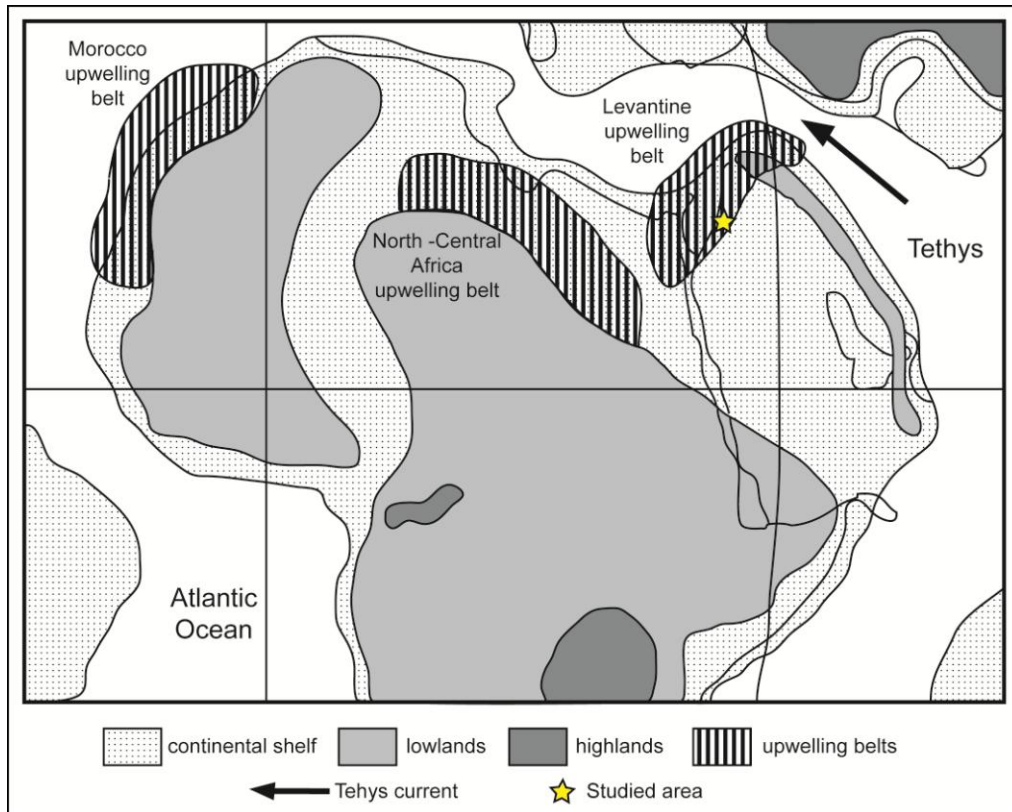


Figure III. 1. Paleogeographic map of the upwelling belt along the southern Tethys margin during the Late Campanian and Early Maastrichtian, (after Parish and Curtis 1982, Ashckenazi-Polivoda et al., 2011). Star marks the location of central Jordan.

Phosphorites of Central Jordan belong to the Late Campanian – Maastrichtian phosphate belt. Many of the lithologies of the Belqa Group appear to be rich in phosphates, but more particularly the Al Hisa Phosphorite formation (AHP fm). The Belqa Group was deposited between the Campanian to Eocene and consists mainly of carbonate rocks, divided into six formations, which are in stratigraphic order: Wadi Umm Ghudran, Amman Silicified Limestone, Al Hisa Phosphorite, Muwaqqar Chalk Marl, Umm Rijam Chert Limestone and Wadi Shallala Chalk formations deposited during pulsatory phases of marine onlap southward and eastward across the Arabian Craton during a marine transgression (Powell and Moh'd, 2011; Fleurance et al., 2013).

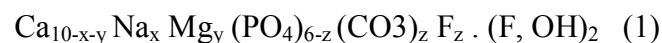
3. MATERIALS AND METHODS

15 samples were selected from the bioclastic limestones (3 samples) of the Al Hisa Phosphorites formation (AHP fm.), the bituminous shales (1 sample) of the basal Muwaqqar Chalk Marl formation (MCM fm.), the marbles (5 samples) of the upper MCM fm. and of the basal Umm Rijam Chert Limestone formation (URC fm.), the calc-silicate rocks (3 samples) of the MCM fm., and the supergene mineralized and altered limestones (3 samples) of the MCM fm.. We carried out a petrological and mineralogical study, geochemical analyses on whole rocks by ICP-AES for major elements and MS for the traces elements, and additional analyses for fluorine and total CO₂. CO₂ formed during the calcinations was estimated with an Infrared detector. Fluorine was measured by alkaline fusion: the powdered sample was mixed with sodium carbonate and water and then was fused at 990°C. F was directly measured with a fluoride selective electrode. X-Ray Diffraction analysis on decarbonated fine fractions has been used to identify the complex mineral phases and clay minerals. A semi-quantitative analysis by Scanning Electron Microscopy (JEOL J7600F) allowed the identification of complex mineral species. Quantitative analysis of the phosphates has been obtained using an electron microprobe (CAMECA SX100, composed by a scanning electronic microscope coupled with five wavelength-dispersive spectrometers and current regulation). Several parameters affect the quality of the analyses of fluorapatites, which may lead to fluorine concentrations higher than the maximum F concentrations of 3.76 wt% which can be incorporated in stoichiometric fluorapatite. The electron probe microanalytical operating conditions such as spot size, current, accelerating potential, crystal orientation, and F standard, could be responsible for analytical errors. The F content and the crystalline structure generate a unique analytical problem, namely, time-dependent variation in apatite F X-ray intensity induced by the implantation of primary beam electrons which could make permanent damages (Pyle et al., 2002). Stormer et al. (1993) and Goldoff et al. (2012) tested different operating parameters of a CAMECA SX100: accelerating potentials investigated were 7, 10, 15 kV, beam currents were 4, 10, 15 nA, and electron-beam diameter were 2, 5, 10 µm. Each possible combination was tested on several locations on each anhydrous fluorapatite crystal oriented with two possible crystal positions: c-axis parallel or perpendicular to electron beam. The time-dependent intensity (TDI) of F X-rays could be varying as function of the crystal orientation.

Stormer et al. (1993) showed important changes in the TDI of F X-rays when the c-axis of the apatite crystal is parallel to the incident electron beam, with the increase 100 % of the $K\alpha$ X-ray intensity during the first 60 to 120 seconds with the an accelerating voltage of 15 kV, a beam current of 15 nA and a spot diameter of 5 μm . While, if the c-axis is perpendicular to the electron beam, the count rate increases by only 20% during the first 300 seconds. With the following conditions: 10 kV, 4 nA, 10 μm and the c-axis oriented parallel to the electron beam, the F X-ray count rates of the apatite increase 60-70% in the first 300-500 s, to finally do not be stable. Conversely, the F X-ray count rates are constant for 600 s if the crystal c-axis is perpendicular to the electron beam with the same operating conditions. The TDI could be varying in function of the apatite composition. The variations of the F X-ray count rates are higher with an apatite-poor fluorine. The accelerating potential could be affects the F X-ray intensity variation. The natural apatite are often analyzed with an accelerating voltage of 15 kV, but the F reponse seems to be complicated, more than the others halogens. F X-ray count rate shows great variations for a 15nA beam current and is more constant for 10 and 4 nA currents. However, the use of a 15 kV accelerating voltage may helpful because robust X-ray counts for most elements analyzed, including heavier metals (Goldoff et al., 2012). A smaller beam diameter induced higher F X-ray count rates. Pyle et al. (2002) suggested that the damages created during the electron microprobe analysis are permanent. In summary, the optimal analytic conditions for measuring fluorine concentration is obtained with a beam parallel to the c-axis of the apatite crystal, a low beam current (4 nA), a low accelerating potential (10 kV), and a large spot size (10 μm). Initially, we used for our work a CAMECA SX100 electron microprobe with an accelerating voltage of 15 kV, a beam current of 12 nA, and a beam diameter of 1 μm , which are not the optimal conditions for fluorapatite analyses. Trough the identification of these potential interactions, the following elements: F, Na, Mg, Al, Si, P, S, Cl, K, Ca, Fe, Sr were analyzed under the following conditions: 15 kV accelerating voltage, 10 nA beam current, 10 μm or 1 μm beam diameter when the crystal size permitted; F standard: fluorapatite. It was however rarely possible to choose the right orientation of the apatite crystals for the analyses because the crystals are generally anhedral. We kept a 15 kV accelerating voltage, classically used for phosphates, silicates and carbonates, to have better statistics and to be sure to be above the excitation limit of emitted rays of each element. With a 15 kV accelerating voltage, a 10 nA beam current, we have an adequate counting statistic for a peak time of 10 second. The calcium concentrations obtained from electron microprobe analyses have been used as an internal standard for the Laser

Ablation inductively coupled plasma mass spectrometer (LA-ICP-MS) analyses. Calcium, uranium, REE's (La, Ce, Pr, Nd, Sm, Eu, Gd, Tb, Dy, Ho, Er, Tm, Yb, Lu), thorium, lead, vanadium concentrations in the phosphates of the different facies of the Belqa Group have been determined by LA-ICP-MS (G2R Laboratory, Université de Lorraine, France). Raman spectrometry (G2R Laboratory, LabRAM/LabRAM HR HoribaJobinYvon with a laser Ar⁺ à 541.5 nm, coupled with an optical microscope Olympus BX51) was used to identify the presence/absence of carbonate and/or hydroxyl groups in the structure of the some of the phosphates.

Several types of phosphates are described in this work: sedimentary-diagenetic, metamorphic, supergene. All these minerals are varieties of apatite. The theoretical apatite formula is $A_{10}(XO_4)_6Z_2$ where A, X and Z represent the common cations (A=Ca, X=P,Si, S, Z=F, OH, CO₃). The theoretical Carbonate-Fluorapatite (CFA) formula is: $Ca_{10} (PO_4)_5(CO_3)F_{2-3}$. Some constituents can be present by substitutions in the lattice of the apatite. CO₃²⁻ and OH⁻ are commonly calculated by difference, and the amounts are uncertain. CO₃ and F are associated and replace PO₄, McClellan (1980) suggests that 40 mole% of the structural CO₂ is accompanied by additional F to obtain the following formula: $Ca_{10-x-y} Na_x Mg_y (PO_4)_{6-z} (CO_3)_z F_{0.4z} \cdot F_2$. In the majority of works (Regnier et al., 1994) the proportion is 1 F⁻ for each CO₃²⁻, unlike McClellan (1980) which indicates a maximum proportion of 0.4 F⁻ for each 1 CO₃²⁻. Considering these problems, we used the formula established by McClellan (1980), modified by McArthur (1990) and recently used by Toledo et al. (2004):



Ions numbers of the structural formula are calculated on the basis of 10 cations (Ca, Mg, etc.) and of 26 anions (O, OH, F, Cl). Carbonate, not measured by electron microprobe, is evaluated from the number of ions of the member (PO₄).

4. HOST ROCKS

The petrographical characteristics of the bioclastic limestones, the shales, and the marbles are presented in Fleurance et al., 2013 (Chapter II). We will present here only the detailed petrographical characteristics of the phosphates.

4.1. Bioclastic limestones

Bioclastic limestones of the AHP formation consist of orange-brown to colorless biogenic phosphates occurring as skeletal fragments (several mm), ooids (up to 300 μm), aggregates and nodules (up to 2 mm) (Fig.III.2). These clastic elements are generally embedded within a micritic mud except for a bioclastic oolitic grainstone sample (9502-18) which shows sedimentary laminations, alternating beds of chert and beds of microsparite. Bioclastic limestones present a large variation of uranium contents ($7 < \text{U} < 59$ ppm) and variable phosphate content ($1.19 < \text{P}_2\text{O}_5 < 7.58$ wt%). They present the lowest REE contents ($2 < \Sigma\text{REE} < 19$ ppm) of the studied samples.

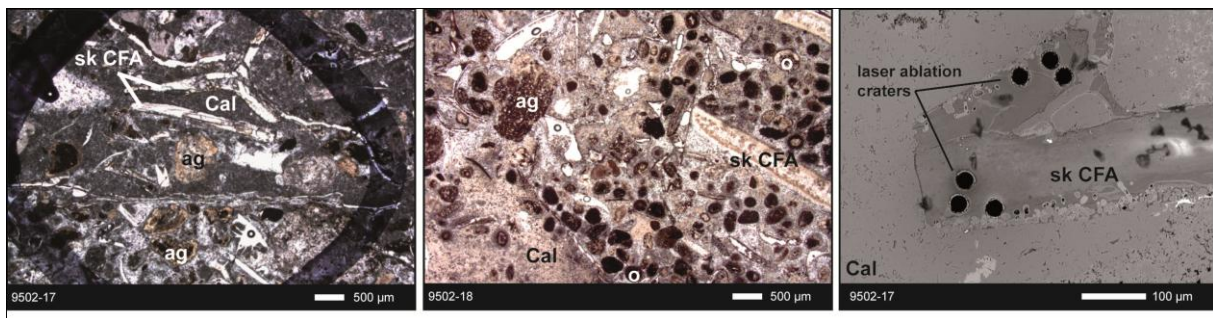


Figure III. 2. Microscopic and SEM views of the bioclastic limestones and its phosphates. ag: carbonate-fluorapatite aggregate, Cal: calcite, O: ooid of carbonate-fluorapatite, Sk CFA: skeleton of carbonate-fluorapatite.

4.2. Shales

The shales, often referred to as oil-shale, by petroleum geologists because of their bituminous potential are located in the lower part of the MCM formation. They comprise fine-grained, grey clayey and laminated marls. They consist of fine admixture of clay minerals (smectite-illite), organic matter, cristobalite and calcite. The phosphates occur as orange-brown striated and alveolar skeletal fragments and irregular nodules, oriented parallel to the laminations (Fig.III.3). Sulfides underlie the stratification. Micrograins of uranium oxides are disseminated throughout the matrix, and in addition fibrous uranium oxides crystals are associated with sulfides at the margin of a calcite vein. The shales show large variation of U ($134 < \text{U} < 5899$ ppm), and very low phosphate contents ($1.13 < \text{P}_2\text{O}_5 < 2.56$ wt%). Phosphate grains also contain inclusions of Cd-sphalerite. The REE contents of the shales is low ($34 < \Sigma\text{REE} < 60$ ppm).

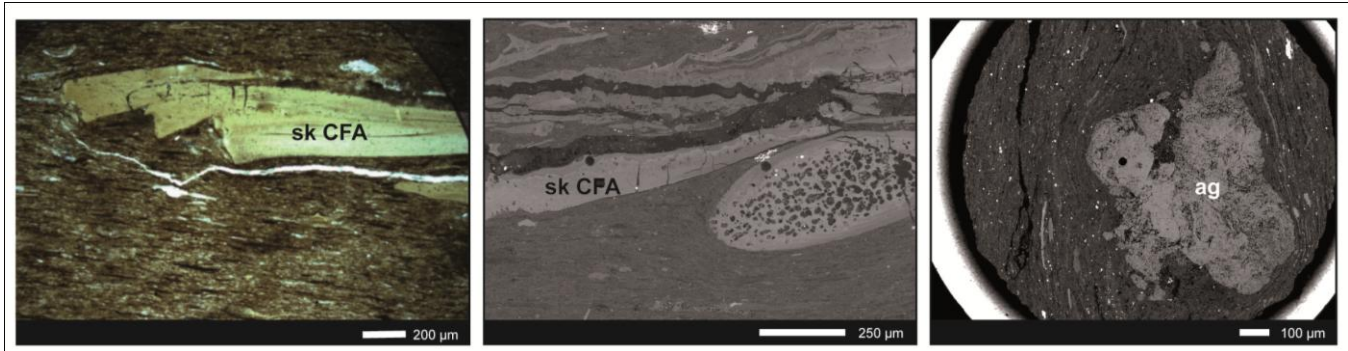


Figure III. 3. Microscopic views of the phosphates in the shale JRD10-12B. ag: CFA: aggregate, Sk CFA: skeleton of carbonate-fluorapatite.

4.3. Marbles

Marbles are varicoloured (brown, black, pink, red, yellow and green). They are mainly composed of calcite, phosphates and calcium-silicates. Phosphate occurs as micrograins ($< 50 \mu\text{m}$) coating the elongated xenomorphic calcite grains. The phosphates grains are hardly discernible, and can form relatively thick laminae (up to $500 \mu\text{m}$ of width) and include individual calcite grains and calcium silicates (Fig.III.4). Carbonated calcium silicates and oxides correspond to a series of high temperature sub-idiomorphic to idiomorphic minerals developed in the matrix of the marbles. The marbles show a large variation of uranium contents ($33 < \text{U} < 134 \text{ ppm}$) and a very large variation of phosphate contents ($0.95 < \text{P}_2\text{O}_5 < 20.17 \text{ wt\%}$). Uranium oxides occur as inframetric inclusions in the phosphates (Fig.III.4) and as poekilitic grains in association with the phosphates and the calcium silicate. They present a large variation of REE contents and the highest concentrations ($14 < \Sigma\text{REE} < 218 \text{ ppm}$).

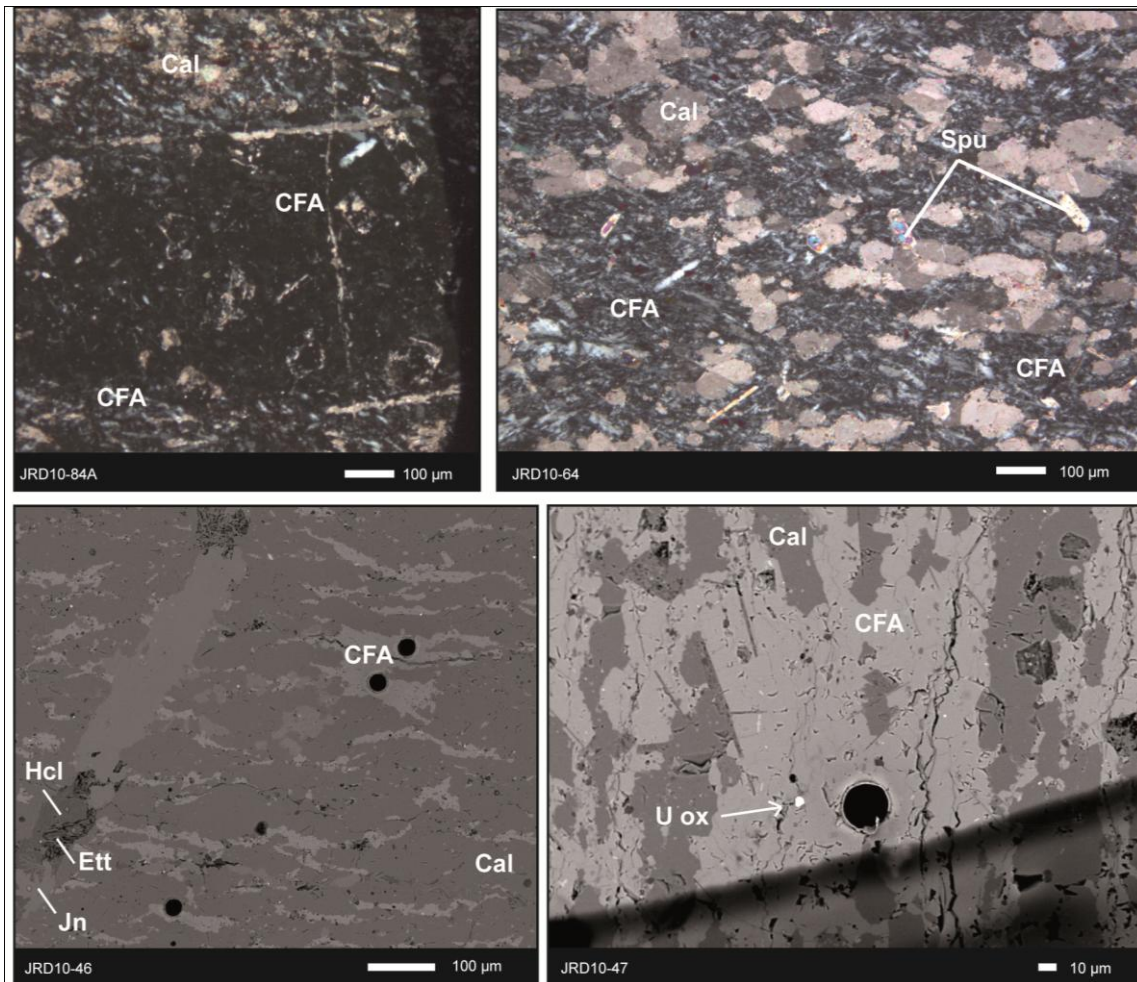


Figure III. 4. Microscopic views of the marbles and its phosphates. Cal: calcite, CFA: carbonate-fluorapatite, Ett: ettringite, Hcl: hydrocalumite, Jn: jennite, U ox: uranium oxide, Spu: spurrite.

4.4. Black and green calc-silicate rocks

These metamorphic facies are represented by two peculiar types of rocks. First, samples JRD10-54 and 55, black, mainly consisting of wollastonite crystals forming a ‘puzzle’ with an equant granular texture. Apatite forms acicular crystals (up to 600 µm) (Fig.III.5a). The second facies (JRD10-60 and 61) is a green facies with sedimentary laminations, mainly constituted by a mixing of small wollastonite and melilite grains, and cavities filled by tobermorites and zeolites. Phosphates occur as elongated groups of subidiomorphic microcrystals (Fig.III.5b). Uranium and phosphates contents of these metamorphic rocks are homogeneous ($38 < U < 45$ ppm) ($4.81 < P_2O_5 < 5.4$ wt%). These two facies may be derived from a different protolith probably more clayed such as clayey limestones and marls, and result

from a higher metamorphic grade (see Chapter 4). Their REE contents are homogeneous too ($80 < \Sigma \text{REE} < 101$ ppm).

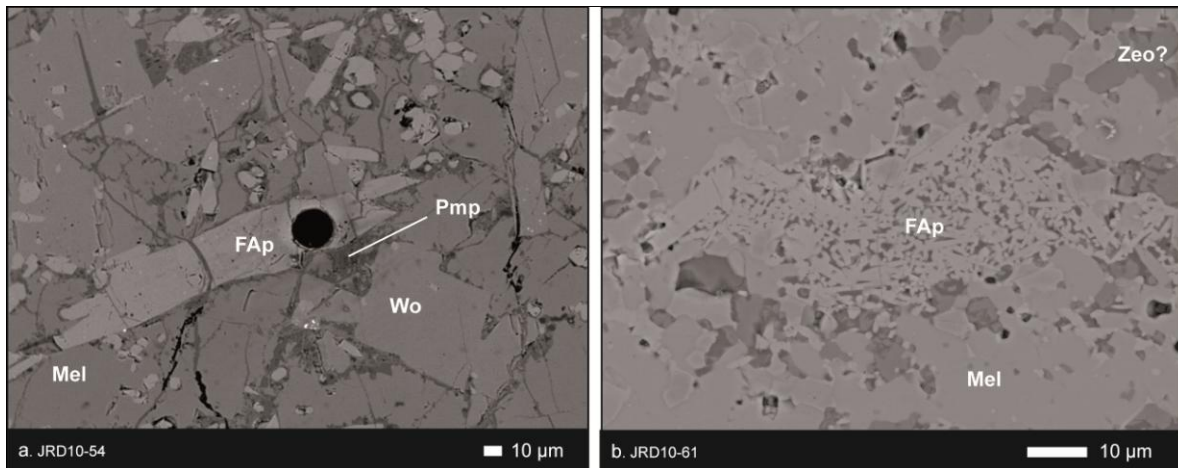


Figure III. 5. Microscopic views of the phosphates in black calc-silicate rock (a) and in green calc-silicate rock (b). FAp: fluorapatite, Mel: melilite, Pmp: pumpellyite, Wo: wollastonite.

4.5. Weathered mineralized limestones

Weathered limestones are dominantly composed by calcite, clays, fluorite, uranium vanadates and phosphates. Phosphates are altered or form new crystals (9542-5) (sub-idiomorphic to idiomorphic acicular crystals up to 200 μm). One shows detritic orange-brown phosphates (JRD10-90). The weathered limestones show a large variation of uranium contents ($10 < \text{U} < 1046$ ppm) and a moderate variation of phosphate contents ($0.31 < \text{P}_2\text{O}_5 < 3.36$ wt%). Their REE content is low ($30 < \Sigma \text{REE} < 61$ ppm). Newly formed acicular crystals of Na-sulfato phosphates form rosette (Fig. 6) and weathered phosphates are associated with clay (Fig.III.6).

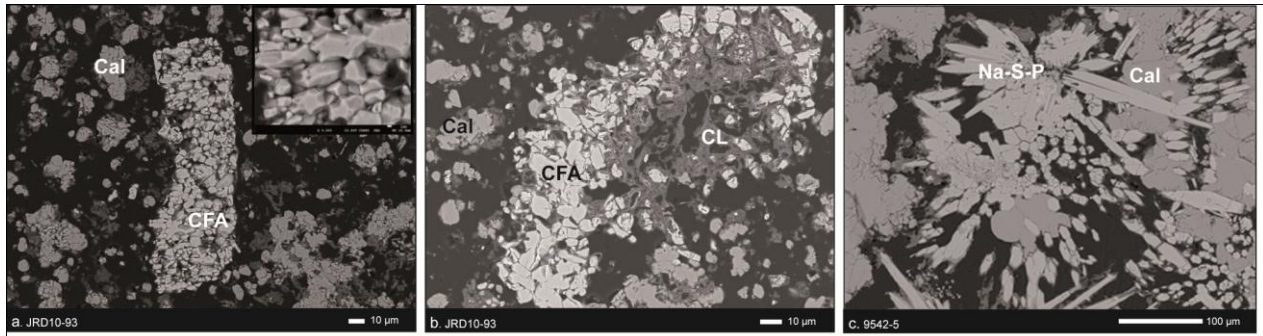


Figure III. 6. Microscopic views of the weathered phosphates (a, b) and of the newly formed supergene phosphates (c). Cal: calcite, CFA: carbonate-apatite with low fluorine content, Na-S-P: Na-sulfato phosphate.

The table III.1 summarizes the uranium, phosphate and REE contents of the different rocks of the Belqa Group.

	Uranium content (ppm)	Phosphate content (P ₂ O ₅ wt%)	ΣREE content (ppm)
Bioclastic limestones	7-59	1.19-7.58	2-19
Shales	134-5899	1.13-2.56	34-60
Marbles	33-134	0.95-20.17	14-218
Calc-silicate rocks	38-45	4.81-5.4	80-101
Weathered limestones	10-1046	0.31-3.36	30-61

Table III. 1. U, P₂O₅ and ΣREE contents of the different rocks of the Belqa Group.

5. MINERALOGY AND GEOCHEMISTRY OF THE PHOSPHATES

The different lithologies of the Belqa Group present 3 major types of apatite: i). sedimentary-diagenetic apatite mainly observed in the shales and bioclastic limestones, but some can be preserved in a supergene altered limestone (JRD10-90); ii). metamorphic phosphates in the marbles and calc-silicate rocks; iii). altered and newly formed phosphates in the mineralized limestones resulting from the supergene alteration. Chemical compositions and cation

proportions are presented in Table III.2. The corresponding structural formula illustrates the variation of composition of each apatite type. Sedimentary-diagenetic, metamorphic (only from the marbles, not from the calc-silicate rocks) and weathered supergene apatites contain a carbonate phase and/or a hydroxyl constituent. The newly formed phosphates of the weathered limestones have a sulfate group in their structure, and do not contain a carbonate constituent.

a

	wt % (electron microprobe)													ppm (LA-ICP-MS)
	CaO	P2O5	F	Na2O	MgO	Al2O3	SiO2	SO4	K2O	FeO	SrO	Cl	TOTAL	ΔU
Sedimentary/diagenetic phosphates	46.88	32.66	3.54	0.48	0.16	0.02	0.1	2.43	0.01	0.02	0.23	0.09	86.62	13-1769
Metamorphic phosphates of marbles	55.74	28.23	2.95	0.16	0.02	0.16	5.40	1.70	0.03	0.07	0.19	0.01	93.43	0-41994
Metamorphic newly formed phosphates	55.25	38.63	2.86	0.02	0.07	0.15	3.50	0.24	0.03	0.32	0.28	0.01	100.15	14-264
Weathered supergene phosphates	53.87	37.28	0.91	0.04	0.10	0.10	2.24	2.82	0.00	0.08	0.52	0.01	97.65	2-112
Newly formed supergene Na-sulfato-phosphates	44.99	25.93	1.92	5.10	0.14	0.16	0.01	16.17	0.26	0.01	0.04	0.12	94.01	2-34

b

	ion numbers							wt %	
	Ca	P	F	C	S	Na	Mg	CO3	Total + CO3
Sedimentary/diagenetic phosphates	10.1	5.5	2.2	0.5	0.4	0.2	0.05	2.31	88.93
Metamorphic phosphates of marbles	11.2	4.5	1.8	1.5	0.2	0.01	0.02	8.00	101.43
Metamorphic newly formed phosphates	10	5.5	1.5	-	0.03	0.005	0.02	-	100.15
Weathered supergene phosphates	10.2	5.6	0.5	0.4	0.2	0.013	0.028	2.52	100.17
Newly formed supergene Na-sulfato-phosphates	9.2	4.2	1.2	-	2.3	1.9	0.04	-	94.01

Table III. 2. Major elements and U contents of the different phosphates types (a), ions numbers and CO₃ contents (b).

5.1. Sedimentary-diagenetic phosphates

Sedimentary-diagenetic apatites (Fig.III.2, III.3) show an average phosphorous content of 33.66 wt%P₂O₅ (30.05 <wt% P₂O₅< 36.22). With the CO₃ calculation method (in methodology section) we can estimate the carbonate content of 2.31 wt% CO₃. However, the calculated CO₃ content is not sufficient to have a total of the analyses reaching 100%, for this type of apatite. The lacking component is certainly related to the high porosity of these sedimentary-diagenetic apatites (estimated at about 20 vol %), and/or the presence of a hydroxyl component in the mineral structure. They present a large variation of U concentrations (36 < U < 1769 ppm, U_{mean} = 192 ppm) (Table III.2).

The resulting calculated formula is: Ca_{10.1}Na_{0.2}Mg_{0.05}(PO₄)_{5.5}(CO₃)_{0.5}F_{2.2}

If we consider the theoretical structural formula (1) given in the methodology section, the resulting formula is: Ca_{10.1}Na_{0.2}Mg_{0.05}(PO₄)_{5.5}(CO₃,F)_{0.5}F_{1.7}

The theoretical fluorine content is 2+z. In the case of the sedimentary-diagenetic apatites, the F ion number is 2.2, the calculated formula is correct. OH, not measurable by electron microprobe may also contribute to the low total of these apatites together with the porosity. But the RAMAN analyzes, disturbed by an important fluorescence, do not show the presence of the OH groups.

The phosphatic particles from Ruseifa and Esh Shidiya (Jordan) have the chemical formula (Abed and Fakhouri, 1996): Ca_{9.86}Na_{0.13}Mg_{0.005}(PO₄)_{4.93}(CO₃)_{1.07}F_{2.06}. Their total, equal or very slightly higher than 100 wt%, and the stoichiometrically correct F content could be explained by analytical method used. The major elements and some traces were analysed by Atomic Absorption Spectroscopy on hand-picked phosphatic particles. P₂O₅, SO₃ and F have been analyzed by spectrophotometry, and CO₂ content were measured by acid digestion.

5.2. Phosphates from the metamorphosed rocks

Two types are distinguished here: the phosphates from the marbles, and the phosphates from the calc-silicate rocks.

Phosphates from the marbles (Fig.III.4) show an average phosphorous content of 28.23 wt% ($25.06 < \text{wt\% P}_2\text{O}_5 < 32.25$) and a carbonate fraction calculated at 8 wt% CO_3 (table 2). The presence of a carbonate component fraction is confirmed by RAMAN microspectrometric analyses. The spectrum (fig.III.7) shows the C-O bond with the peak of the carbonates at 765, 1070 and 1107 cm^{-1} . No O-H bounds have been detected in this phosphate.

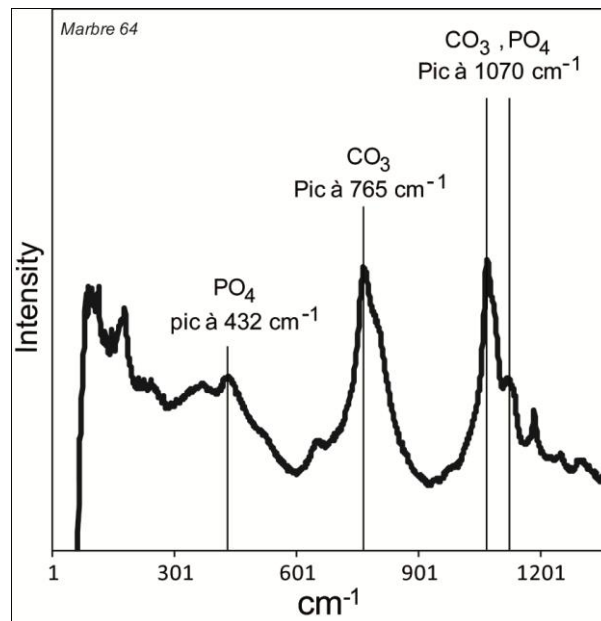


Figure III. 7. RAMAN spectrum of a carbonate-fluoroapatite hosting by a marble.

The resulting calculated structural formula is: $\text{Ca}_{11.2}\text{Na}_{0.01}\text{Mg}_{0.02}(\text{PO}_4)_{4.5}(\text{CO}_3)_{1.5}\text{F}_{1.8}$

If we consider the theoretical structural formula (1) given in the methodology section, the resulting formula is:



The total completed with CO_3 is 101,43 wt% (Table III.2). The metamorphic phosphates in the marbles are carbonate-fluorapatites.

Carbonate-fluorapatites of the marbles present the highest and most heterogeneous uranium concentrations ($0 < \text{U} < 41,994$ ppm, U median=27 ppm). In general, LA-ICP-MS spectra present a flat pattern when the mineral begins to be ablated (example in Fig.III.8a), but the spectrum of marbles phosphates are different. They present variation of uranium concentration during the ablation. In the figure III.8b the spectra show an important variation of uranium, with a minimum concentration of 607 ppm and a maximum content of 41 994

ppm. Such a variation can only be explained by the presence of submicronic inclusions of uranium oxides which are sporadically ablated during the analysis of the carbonate-fluorapatite.

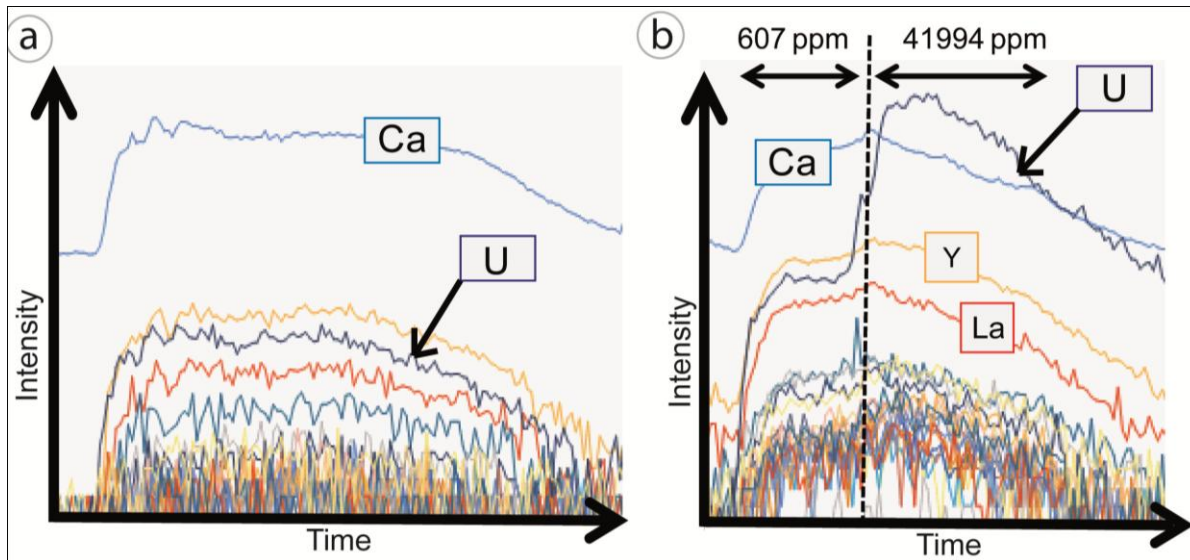


Figure III. 8. LA-ICP-MS spectrum. a: carbonate-fluorapatite (bioclastic limestone 9502-17). U=78 ppm; b: carbonate-fluorapatite (marble JRD10-84A).

Phosphates of the calc-silicate rocks (Fig.III.5) present the highest phosphate content ($37.05 < P_2O_5 < 41.93$ wt%, P_2O_5 mean =38.63 wt%). The resulting structural formula of this apatite is:



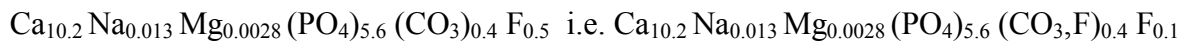
The total of this apatite is 100.15 wt%, corresponding to a fluorapatite with no carbonate component. The small fluorine deficit could be due to the presence of OH constituent in this F site.

They show a relatively large range of uranium contents ($14 < U < 352$ ppm, $U_{mean} = 182$ ppm), but with a smaller variation than in the marbles.

5.3. Phosphates from the weathered carbonates

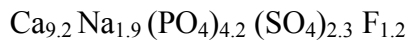
The weathered mineralized limestones show two types of phosphates (Fig.III.6): i) weathered phosphates with corroded surfaces and associated to clay minerals (JRD10-93), ii) newly formed acicular Na-sulfato-phosphates (9542-5).

i. The weathered phosphates have phosphates concentrations of 34.98 <P₂O₅<38.46 wt% (P₂O₅ mean =37.28 wt%). If we consider that this phosphate is a CFA, the formula is:



The recalculated total with the CO₃ content is 100.17 wt% (Table III.2). They have uranium content up to 112 ppm (U_{mean}= 13 ppm) very low, despite not recrystallized compared to unaltered phosphates.

ii. The newly formed Na-sulfato-phosphates in the weathered zone have a lower phosphate content than in the other lithologies (23.07 <P₂O₅<27.77 wt%, P₂O₅mean=25.93 wt%) because of its substitution by sulfates (13.51 < SO₄ < 18.52 wt%) and associated with high sodium content (Na₂O mean= 5.1 wt%). The resulting formula is:



The total is 94.01 wt%, this phosphate contains probably a hydroxyl component which should be confirmed by RAMAN microspectrometric analyses. If we consider the structure of an apatite, there is an excess of sulfates which substitute the PO₄ group (see thereafter), a small excess of sodium which substitutes the M group, and a small fluorine deficit (X group). These sulfato-phosphates have also a low uranium, slightly lower than in the weathered phosphates (1.70<U<34 ppm, U_{mean}=11 ppm).

5.4. REE contents

The sedimentary phosphates are richer in REE (ΣREE_{mean} = 274 ppm) than the Post-Archean Australian Shale (PAAS) (McLennan, 1989) (Fig.III.9). Phosphates tend to be richer in heaviest REE (0.19 <LaN/YbN < 0.99). The metamorphic phosphates show two different patterns: the metamorphic carbonate-fluorapatites of the marbles are fractionated (0.25<LaN/YbN<1.69) and present an important negative cerium anomaly (Ce/Ce*

mean=0.28), the fluor-apatite of the calc-silicate rocks have higher REE content ($\Sigma\text{REE}_{\text{mean}} = 401$ ppm) than the CFA of the marbles ($90 < \Sigma\text{REE}_{\text{mean}} < 248$ ppm) and have a lower negative cerium anomaly (Ce/Ce^* mean= 0.6). The weathered CFA of the weathered limestones show a fractionated pattern ($0.35 < \text{LaN}/\text{YbN} < 2.07$) with lower LREE and higher HREE than the CFA of the marbles for a global higher total REE ($\Sigma\text{REE}_{\text{mean}}=163$ ppm). They present a negative cerium anomaly (Ce/Ce^* mean= 0.037) and the slight negative europium anomaly (Eu/Eu^* mean= 0.71). The newly formed supergene Na-sulfato-phosphates have the lowest REE contents ($\Sigma\text{REE}_{\text{mean}}= 19$ ppm) and show a sawtooth pattern due to the lower analytical precision of the LA-ICP-MS analyses at very low REE contents, close to that of sea water for sample 9542-5.

The Jordanian phosphates of the Belqa Group have a similar pattern that the phosphorites of Morocco (Lécuyer et al., 2004) and Negev (Soudry et al., 2002) (Fig.III.9). Seawater patterns, with negative Ce anomalies, are characteristic of phosphatic carbonates (McArthur and Walsh, 1984/1985). This pattern results from an incorporation of the REE directly from seawater, or indirectly from pore water after a REE remobilization from a REE source which has itself incorporated the REE from the seawater.

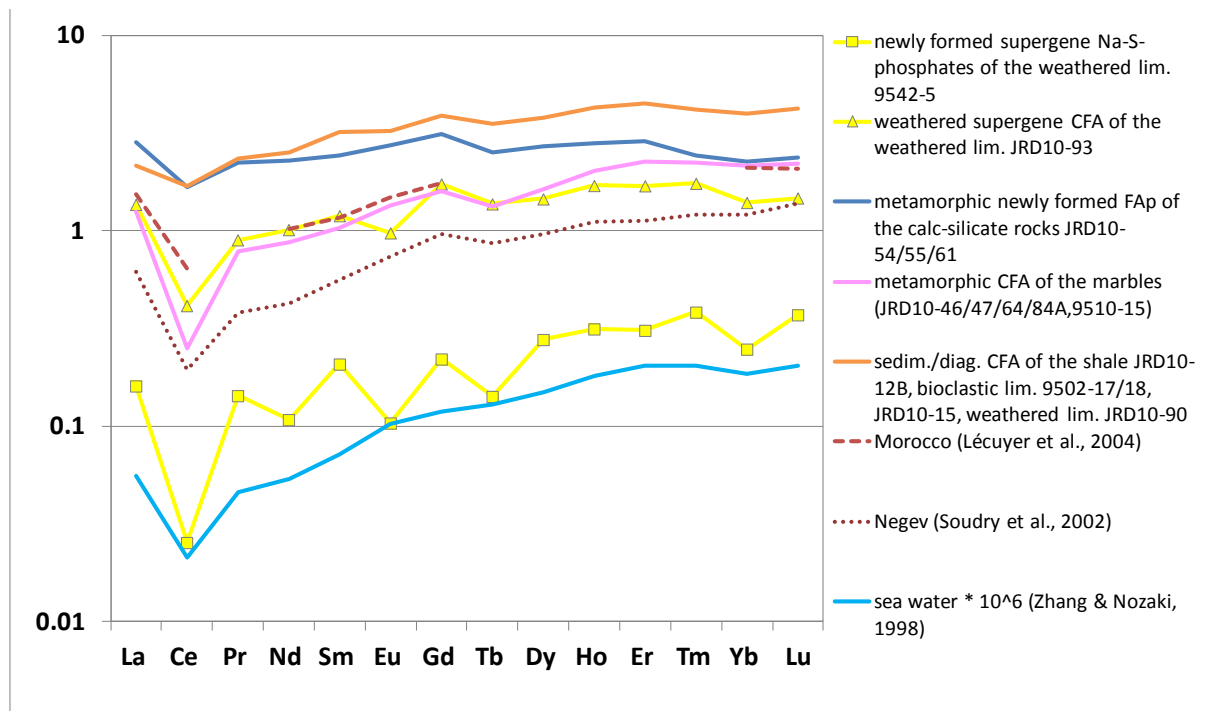


Figure III. 9. PAAS-normalized (McLennan, 1989) rare earth elements patterns of the different apatites of the lithologies of the Belqa Group.

The figure III.10 presents the whole rocks-normalized rare earth elements patterns of each apatite type of the Belqa Group. All the apatites have higher REE content than the host rocks because of the dilution by the other minerals (especially carbonates) which contain very low REE contents, except for the supergene limestone 9542-5 which could also contain some newly formed REE-rich minerals. The REE enrichment may reach a factor 16 between the phosphate and its host rock, but this comparison depends on the phosphate content of the host rocks. So, the whole rock-normalization is significant in determining if the apatites control the REE contents or if these REE contents are attributed to other minerals in the rocks.

In the figure III.10a, the sedimentary carbonate-fluorapatites of the bioclastic limestone JRD10-15 show a flat pattern in contrast with those of the shales which present a negative anomaly in Pr. Sedimentary CFA of the bioclastic limestone 9502-17 presents a negative anomaly in Tb, indicating that this element is hosted by another mineral. The sedimentary CFA of the weathered limestone JRD10-90 ($\Sigma\text{REE}_{\text{mean}} \text{ CFA} = 668 \text{ ppm}$) has a flat pattern except for Eu which shows a negative anomaly reflecting that this element is probably hosted by another mineral. This CFA has also higher REE content than the other sedimentary CFA ($\Sigma\text{REE}_{\text{mean}} = 513 \text{ ppm}$ for the CFA in the shale and $7 < \Sigma\text{REE}_{\text{mean}} < 129 \text{ ppm}$ for the CFA in the bioclastic limestones).

The CFA of the marbles (Fig. III.10b) show a large range of REE contents ($\Sigma\text{REE}_{\text{mean}} = 144 \text{ ppm}$) in comparison with the whole rocks. These CFA present flat patterns except those of the marbles JRD10-64 and 84A, which show a negative Ce anomaly indicating that cerium is hosted by other minerals such as cerianite-(Ce).

The fluorapatites (Fap) of the calc-silicate rocks are presented in figure III.10c. Fap of the calc-silicate rock JRD10-54 present a flat pattern except for Eu which is less enriched reindicating that europium is hosted by other minerals. Fap of the samples JRD10-55 and 61 are more fractionated with higher LREE contents ($0.17 < \text{LaN/YbN} < 0.36$; $0.29 < \text{LaN/YbN} < 0.33$) indicating that the HREE of the whole rocks are hosted by another mineral or that the LREE have been slightly enriched by metamorphism.

The weathered CFA (Fig. III.10d) of the weathered limestone JRD10- ($\Sigma\text{REE}_{\text{mean}} = 163 \text{ ppm}$) are fractionated with higher LREE contents ($0.20 < \text{LaN/YbN} < 1.16$) with a negative europium anomaly and a slightly negative cerium anomaly reflecting that HREE are hosted by another phase and that the presence of rare mineral of florencite (Ce phosphate) probably formed by

leaching from the upper horizons (see Chapter 5). Newly formed supergene phosphates present a pattern globally flat despite the sawtooth pattern. They are the only to have lower REE contents ($\Sigma\text{REE}_{\text{mean}} = 19 \text{ ppm}$) than the whole rock (9542-5) ($\Sigma\text{REE} = 59 \text{ ppm}$). This indicates that the main part of REE present in this weathered limestone is not hosted by the supergene phosphates.

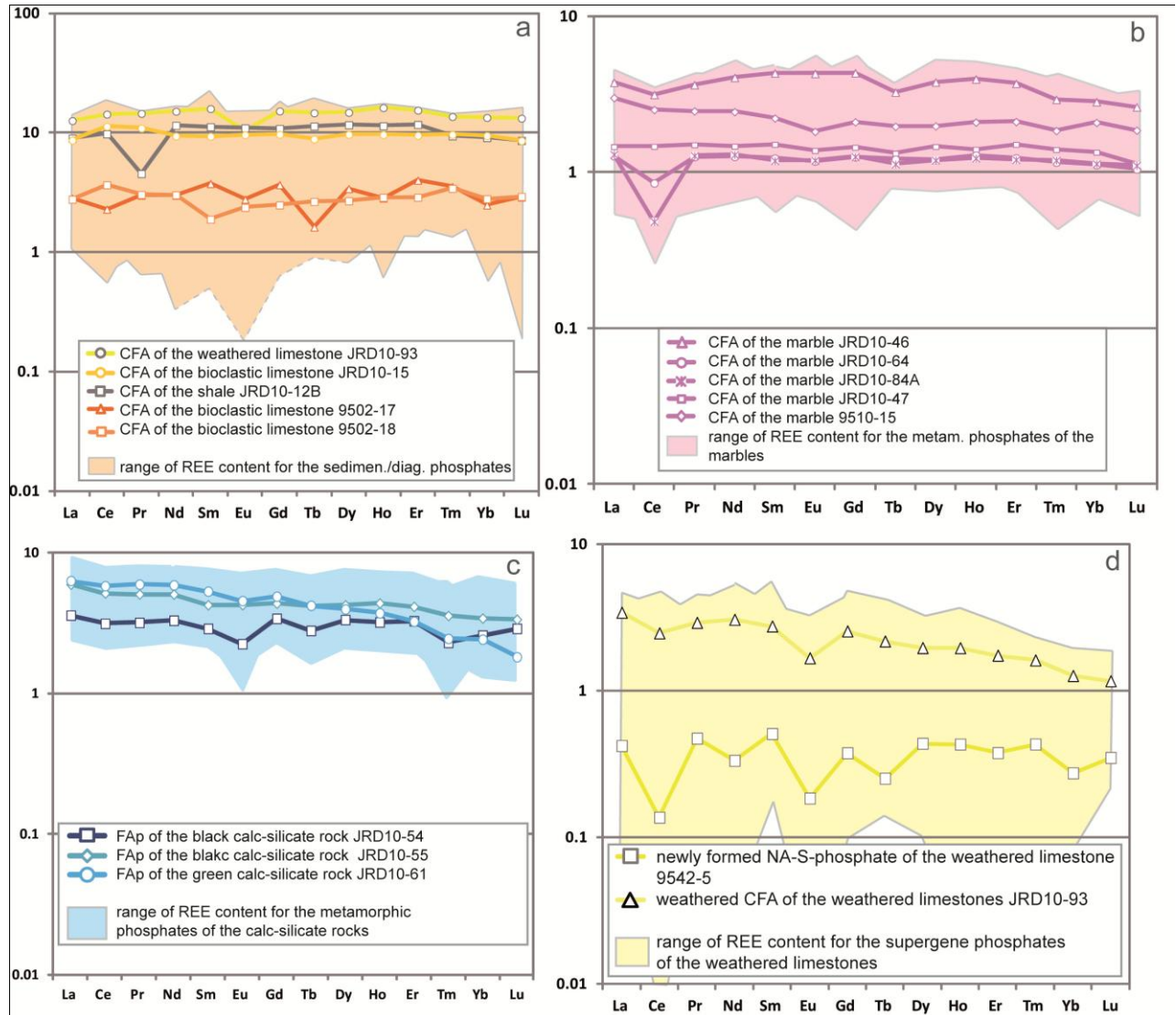


Figure III. 10. Whole rocks-normalized rare earth elements detailed for each phosphate type of each rock. a) sedimentary carbonate-fluorapatites, b) metamorphic carbonate-fluorapatites of the marbles, c) metamorphic idio to subidiomorphic fluorapatites of the calc-silicate rocks, d) weathered and newly formed supergene phosphates.

To summarize, the sedimentary carbonate-fluorapatite have flat pattern indicating that they carry the rare earth elements of the host rocks. Subsequently, the pyrometamorphism led to the destabilization of the CFA and the loss of Ce for some of the samples. The higher metamorphic grade responsible of the total decarbonation and the formation of the fluorapatite in the calc-silicate rocks (see Chapter 4) allowed a weak loss of HREE or a slightly enrichment in LREE. The alteration led to the gain of LREE in the CFA of the weathered limestone (JRD10-93) leached from the upper horizons. The new formed sulfato-phosphates of the weathered limestone have lower REE concentrations than their host rock, indicating that they are not carrier of the REE present in the rock.

The U- Σ REE diagram (Fig.III.11) presents the relation between these two elements in the different apatite types. The diagram shows the large range of U and REE contents. The sedimentary carbonates-fluorapatites (orange) show a positive correlation with higher U variations and higher REE contents for the CFA of the shales and the weathered limestone. CFA of the marbles show a weak variation of the REE contents with a large range of U concentrations illustrating the presence of micrometric inclusions. The REE concentrations of the metamorphic CFA (marbles) are higher than the CFA of the bioclastic limestones because of the pyrometamorphism process. The fluor-apatites of the calc-silicate rocks present high REE content, higher than those of the CFA of the marbles probably because of the higher metamorphic grade. Weathered phosphates of the supergene limestone JRD10-93 contain weak uranium content and do not show correlation. Newly formed sulfato-phosphates of the supergene limestone 9542-5 show a weak positive correlation with low uranium content and lower REE contents than the weathered CFA.

The rocks which are the poorest in total phosphate have phosphate grains which incorporate the highest REE contents (Fig.III.12). Marbles and calc-silicate rocks have a low REE content, probably due to the pyrometamorphism. The lower REE contents of the newly formed sulfato-phosphates of the weathered limestone 9542-5 are due to the meteoric alteration and a supergene recrystallization. This relation tends to support a diagenetic introduction of the REE in the apatite structure, at least a re-equilibration during diagenesis, when less apatite is initially present in the rock, available REE's will enter proportionally in larger amounts in the apatite structure than in the rocks with a larger quantity of apatite available in the original host rock.

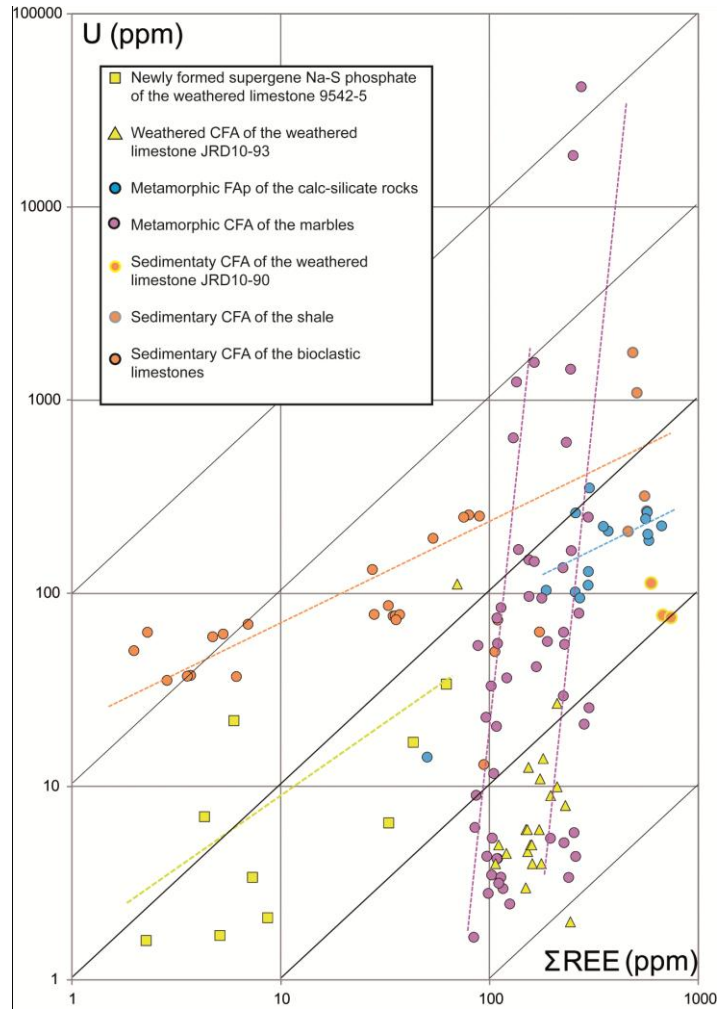


Figure III. 11. U - ΣREE.

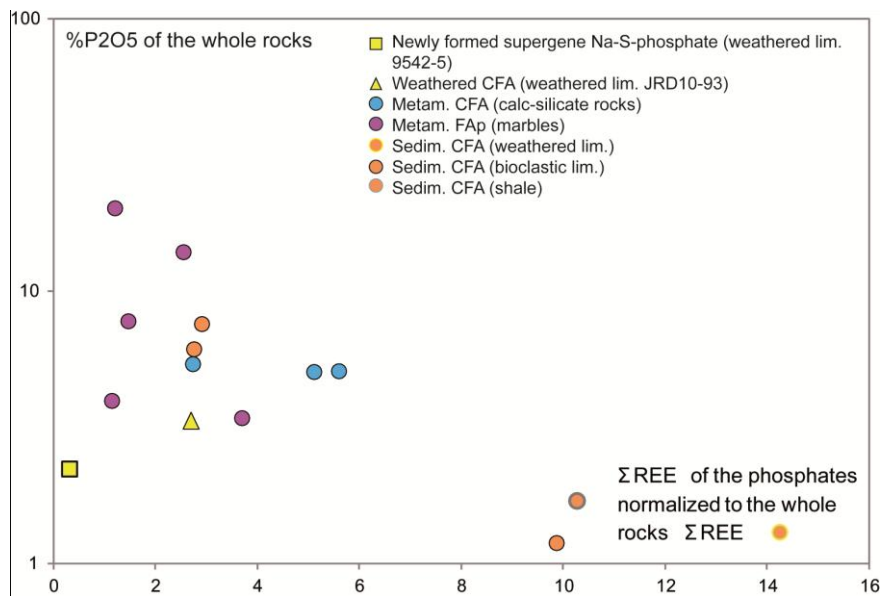


Figure III. 12. wt% P₂O₅ - ΣREE of the phosphate normalized to the whole rocks ΣREE.

6. CHEMICAL VARIABILITY

The different types of apatites show a chemical variability of their major components and of their uranium and REE contents. The laws of substitutions allow us to understand the variability of composition observed in these minerals, the mechanisms responsible for the compositional changes, and to understand the conditions of incorporation or liberation of trace elements such as uranium.

6.1. Substitutions mechanisms in apatite

The structure of the apatite ($M_{10}(ZO_4)_6X_2$) permit numerous substitutions. Various cations and anions can substitute for Ca and the PO_4^{3-} group (Pan & Fleet, 2002).

M cations

Calcium (M cations) can be substituted by various divalent cations (Pb^{2+} , Sr^{2+} , Ba^{2+} , etc), trivalent cation (REE^{3+}) and tetravalent cations U^{4+} . Uranium in the apatite lattice, most likely enters by substitutions between Ca^{2+} and U^{4+} (Altschuler et al., 1958), because of the similarity of their ionic radii. Uranium is tetravalent and Ca is divalent. Also, in the substitution 2 Ca^{2+} are replaced by one U^{4+} leaving a vacancy in the structure according to the following substitution reaction: $2Ca^{2+} \leftrightarrow U^{4+} + \square$

The diagram in figure III.13 shows the correlation between uranium and phosphorous. In most lithologies, uranium enrichment tends to be proportional to the phosphorous content of the limestones and of the metamorphic rocks ($1/1000 < U/P < 1/100$). The high uranium contents of the shales and weathered limestones cannot be attributed only to the phosphates. In the black shales, a large part of the uranium is associated with the clayey organic-rich matrix whereas in the weathered limestones, uranium is dominantly associated with vanadium to form uranyl vanadates (tyuyamunite, strelkinite). Minor amounts of secondary uraninite are also associated with sulfides in calcite veins which cut the shales. This uranium-phosphate relation is also illustrated by the diagram in figure III.14. The uranium concentrations of the shales and of the weathered supergene limestones appear clearly higher than the uranium content of the whole rocks, indicating that uranium is hosted in other U-richer bearing minerals besides the phosphates.

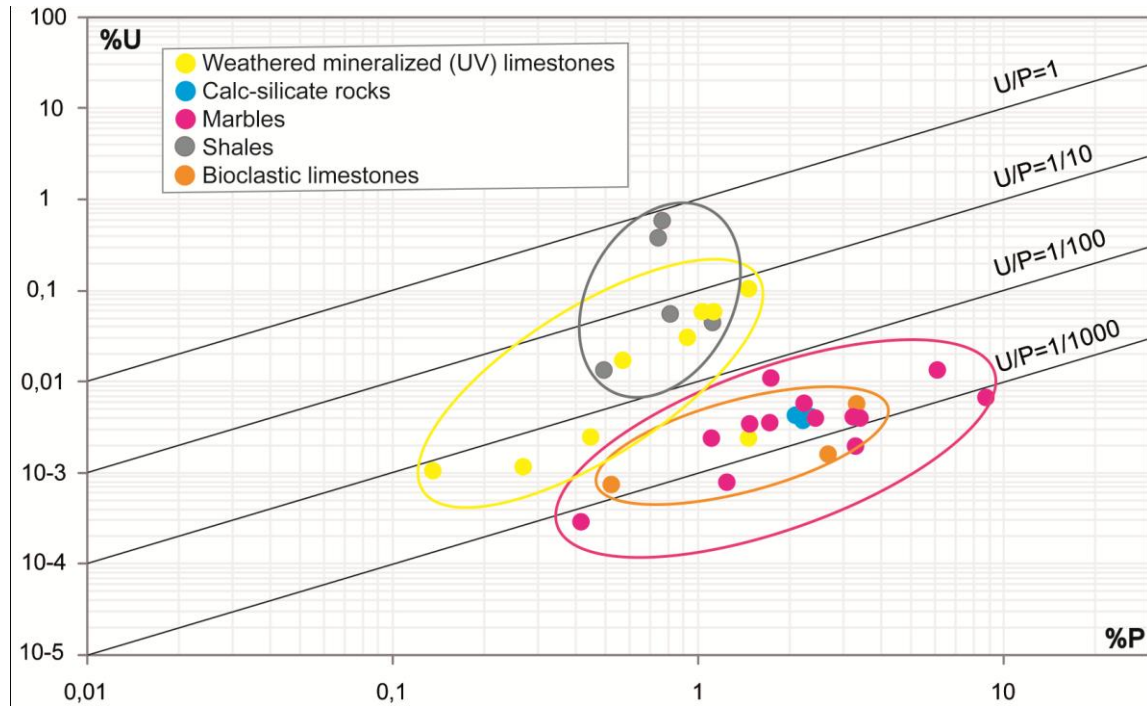


Figure III. 13. U - P diagram (after Fleurance et al., 2013; see Chapter II).

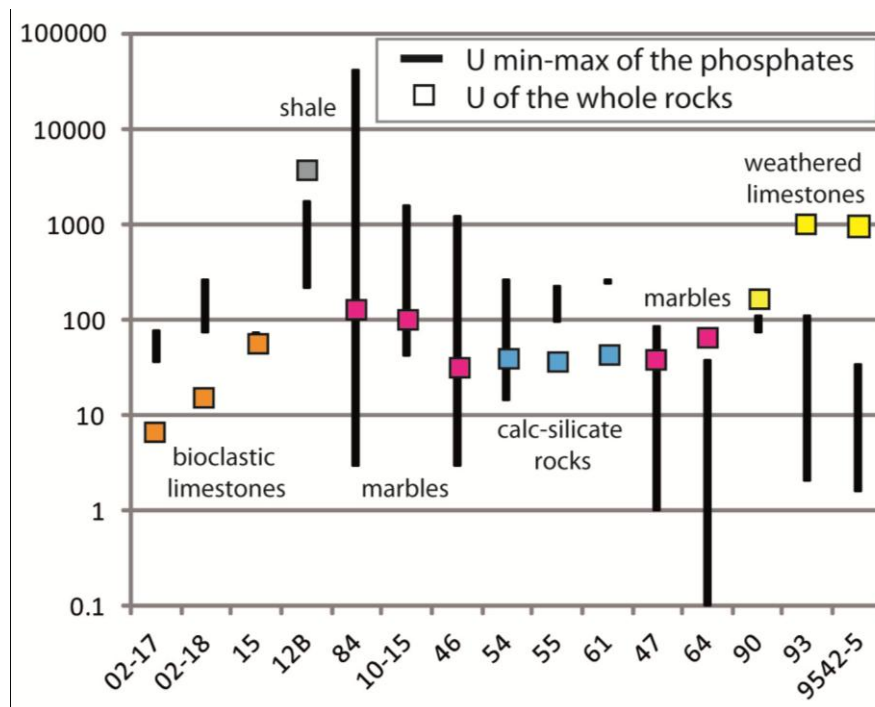


Figure III. 14. U contents of the whole rocks with the range of U content of the phosphates from each rock.

ZO₄ group

Phosphate PO₄³⁻ (ZO₄ group) can be replaced by a variety of tetrahedral anions groups such as SO₄²⁻ and CO₃²⁻. The substitutions by divalent group require a charge compensation.

The carbonate-fluorapatites of the sedimentary rocks differ of the fluor-hydroxyapatites because of substitutions of carbonate for phosphate. Several charge compensation mechanisms (Pan and Fleet, 2002) have been proposed for the incorporation of CO₃²⁻ (□ = vacancy):



The carbonate-apatites present fluorine contents higher than in the others types of apatites (McClellan and Lehr, 1969). They generally contain more fluorine than required by the formula Ca₁₀(PO₄)₆F₂. The combined substitution CO₃F³⁻ ⇔ PO₄³⁻ may explain why the sedimentary apatite contains more fluorine than the quantity which enters in the X sites. This configuration allows to keep the electroneutrality. The F excess balances the loss of negative charge resulting from the CO₃²⁻ - PO₄³⁻ substitution (McArthur, 1990). But a great controversy exists in the literature around this substitution mechanism. Borneman-Starinkevich and Belov (1953), Smith and Lehr (1966), Trueman (1966), Gulbrandsen (1966), McClellan and Lehr (1969), Bacquet et al. (1980), Binder and Troll (1989) and Regnier et al. (1994) have proposed that when a planar CO₃²⁻ ion replaces a PO₄³⁻ group, a F ion occupies the vacant O site. But the electroneutrality can be respected with other chemical simpler substitution mechanisms. Nathan (1996) evoked the positive correlation between nonstoichiometric F and CO₂. Despite, the improbable existence of a CO₃F³⁻ ion because of the too close proximity of CO₃²⁻ and F⁻ in the structure leading to great repulsion between these two anions (Elliot, 1994), Nathan (1996) concluded finally that these two facts are not contradictory.

The table III.3 summarizes the different structural formulae and the F excess calculations. As presented above (section III.3: materials and methods), the F ions number in a carbonate-fluorapatite is equal to 2+ z (z= C ions number= F ions due to the substitution). Also, we considered the case where F ions numbers is equal to 0.4z, giving the total F ions number of to 2+0.4z. Fluorine excess, generally observed in the litterature and with previous analyzes, is not observed with these phosphates and with the analytical protocol presented in the Materials

and Methods section above. This is an illustration of the importance of the electron probe microanalytical operating conditions for the phosphate analyses.

	structural formulae	F ions	C ions=z	2+z	2+0.4z	excess F _{min}	excess F _{max}
Sedimentary/diagenetic carbonate-fluorapatites	Ca _{10.1} Na _{0.2} Mg _{0.05} (PO ₄) _{5.5} (CO ₃) _{0.5} F _{2.2}	2.2	0.5	2.5	2.2	-0.3	0.0
	Ca _{10.1} Na _{0.2} Mg _{0.05} (PO ₄) _{5.5} (CO ₃ ,F) _{0.5} F _{1.7}						
Metamorphic carbonate-fluorapatites of marbles	Ca _{11.2} Na _{0.01} Mg _{0.02} (PO ₄) _{4.5} (CO ₃) _{1.5} F _{1.8}	1.8	1.5	3.5	2.6	-1.7	-0.8
	Ca _{11.2} Na _{0.01} Mg _{0.02} (PO ₄) _{4.5} (CO ₃ ,F) _{1.5} F _{0.3}						
Metamorphic newly formed fluorapatites	Ca ₁₀ Na _{0.005} Mg _{0.02} (PO ₄) _{5.5} F _{1.53}	1.5	0.0	2.0	2.0	-0.5	-0.5
Weathered supergene carbonate-fluorapatite	Ca _{10.2} Na _{0.013} Mg _{0.028} (PO ₄) _{5.6} (CO ₃) _{0.4} F _{0.5}	0.5	0.4	2.4	2.2	-1.9	-1.7
	Ca _{10.2} Na _{0.013} Mg _{0.028} (PO ₄) _{5.6} (CO ₃ ,F) _{0.4} F _{0.1}						
Newly formed supergene Na-sulfato-apatites	Ca _{9.2} Na _{1.9} Mg _{0.04} (PO ₄) _{4.2} (SO ₄) _{2.3} F _{1.2}	1.2	0.0	2.0	2.0	-0.8	-0.8

classic apatite: F=2 ions; Carbonate-fluorapatite: 2+z<F<2+0.4z

Table III. 3. Excess fluorine calculations

The sedimentary-diagenetic carbonate-fluorapatite does not present perfect correlation between F and CO₃ concentrations in contrast with the metamorphic carbonate-fluorapatite of which tend to define a good negative correlation (Fig. III.15). The phosphates of the weathered limestones seem to show positive correlations with a poor correlation coefficient of 0.45 for the weathered supergene phosphates. The relations between F and CO₃ for these four types of apatites are presented in figure III.15.

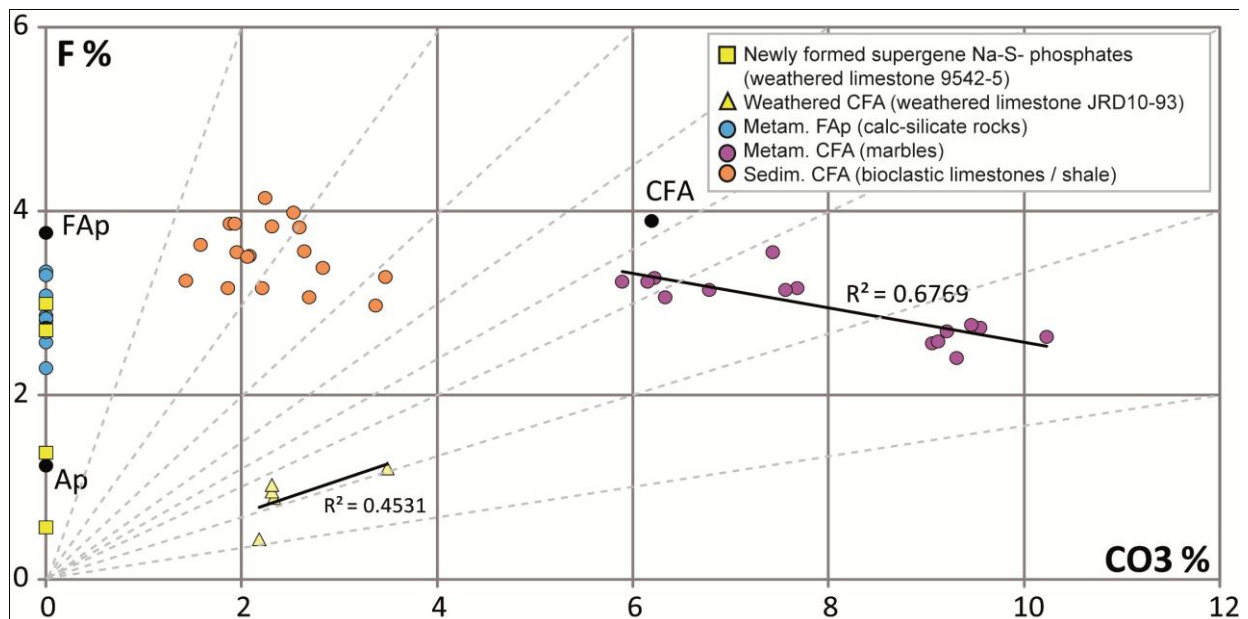


Figure III. 15. F - CO₃ diagram.

The different substitutions occurring in the apatite structure presented above can be illustrated by the following diagrams (Fig.III.16, 17, 18).

The substitution reactions $\text{CO}_3\text{F}^{3-} \Leftrightarrow \text{PO}_4^{3-}$ and $2\text{CO}_3^{2-} + \square \Leftrightarrow 2\text{PO}_4^{3-} + \text{Ca}^{2+}$ are confirmed (Fig.III.16) but not for the fluorapatites of the calc-silicates and the newly formed supergene Na-S-phosphates which do not have carbonate component. The sedimentary-diagenetic carbonate-fluorapatites are below the correlation line, probably because of the porosity of these phosphates.

Others possible substitutions are illustrated by the diagrams in figure III.17 and III.18 below.

In the diagram 2PO_4 versus $\text{CO}_3 + \text{SiO}_4$ (Fig.III.17) the fluorapatite of the calc-silicate rocks are also reversely correlated with a correlation coefficient of 0.8963. This correlation indicates that the fluorapatite of the calc-silicate rocks are controlled by a substitution $\text{CO}_3^{2-} + \text{SiO}_4^{4-} \Leftrightarrow 2\text{PO}_4^{3-}$.

The $\text{PO}_4 + \text{Ca}$ versus $\text{CO}_3 + \text{Na}$ diagram (Fig.III.18) shows a negative correlation for the newly formed Na-sulfato-phosphates of the weathered limestones 9542-5 with a correlation coefficient of 0.98. This indicates that this phosphate type is also controlled by the substitution $\text{CO}_3^{2-} + \text{Na}^+ \Leftrightarrow \text{PO}_4^{3-} + \text{Ca}^{2+}$.

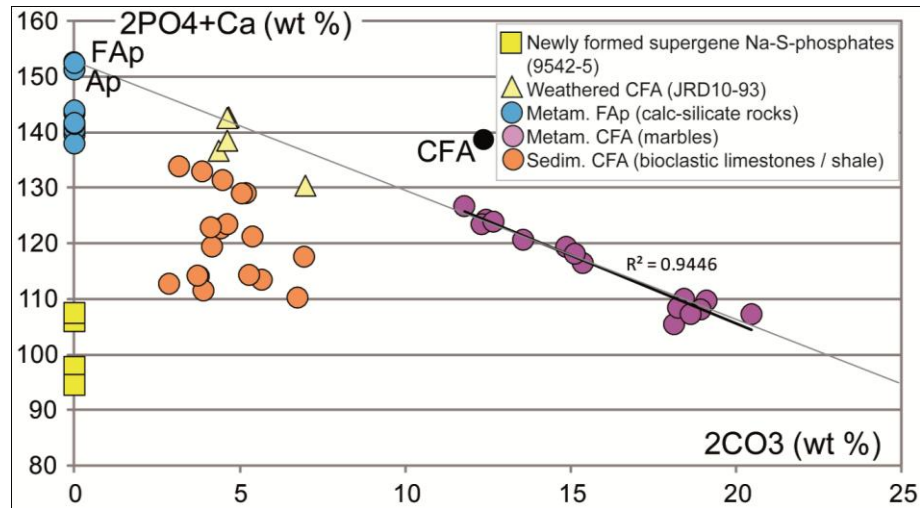


Figure III. 16. $2\text{PO}_4+\text{Ca}$ versus 2CO_3

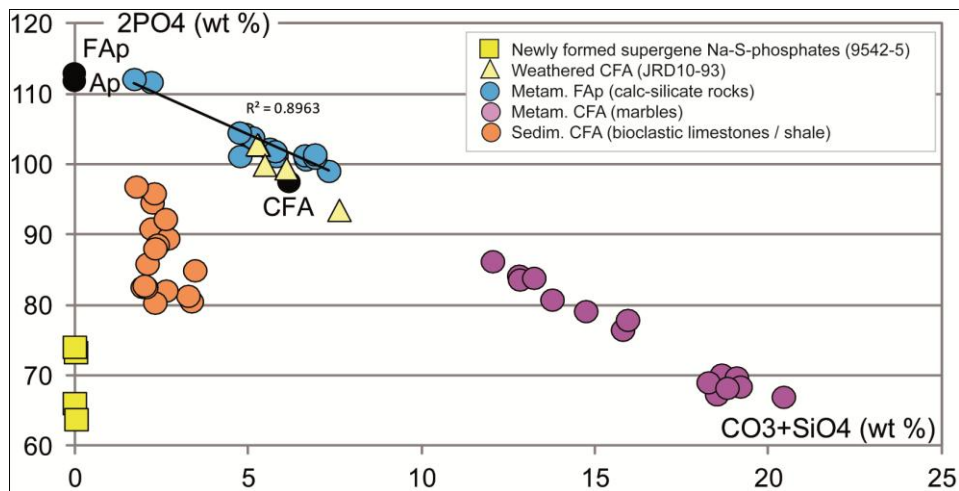


Figure III. 17. 2PO_4 versus CO_3+SiO_4 diagram.

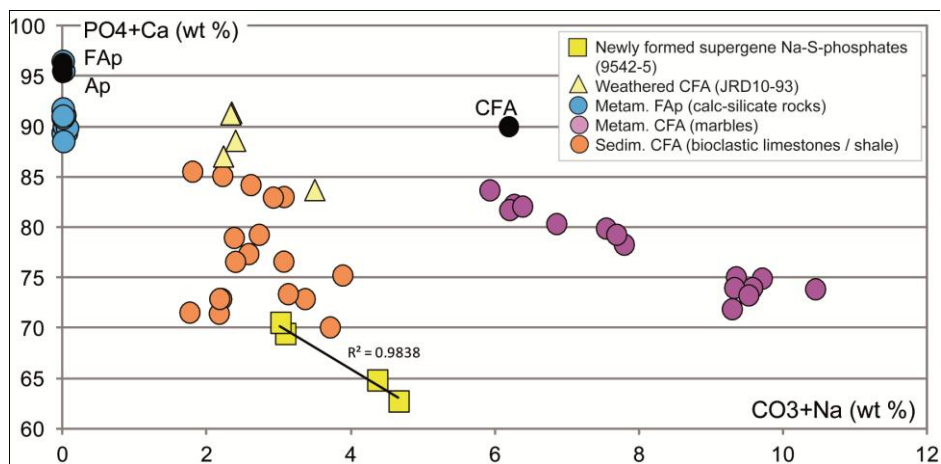


Figure III. 18. PO_4+Ca versus CO_3+Na diagram.

Also, sulfate (SO_4) can substitute PO_4 according to the substitution: $\text{SO}_4^{2-} + \text{Na}^+ = \text{PO}_4^{3-} + \text{Ca}^{2+}$ (Liu and Comodi, 1993; Peng et al., 1997). The substitution of phosphate by sulfate groups requires a partial replacement of calcium by monovalent cations such as sodium for the charge compensation (Piotrowski et al., 2004). The newly formed supergene phosphates (9542-5 square symbols) have the higher content in sulfate with an average of 16.17 wt% SO_4 . The substitution $\text{PO}_4^{3-} \rightarrow \text{SO}_4^{2-}$ is coupled with the substitution $\text{Na}^+ \rightarrow \text{Ca}^{2+}$ and illustrated by the diagram $\text{SO}_4^{2-} + \text{Na}^{2+}$ versus $\text{PO}_4^{3-} + \text{Ca}^{2+}$ (Fig.III.19) where these two elements show a negative correlation with a correlation coefficient of 0.88 for the newly formed sulfato-phosphates. Hence, the newly formed supergene Na-sulfato-phosphates are controlled by the coupled substitution of sulfate and sodium for phosphates and calcium (Fig.III.18, 19).

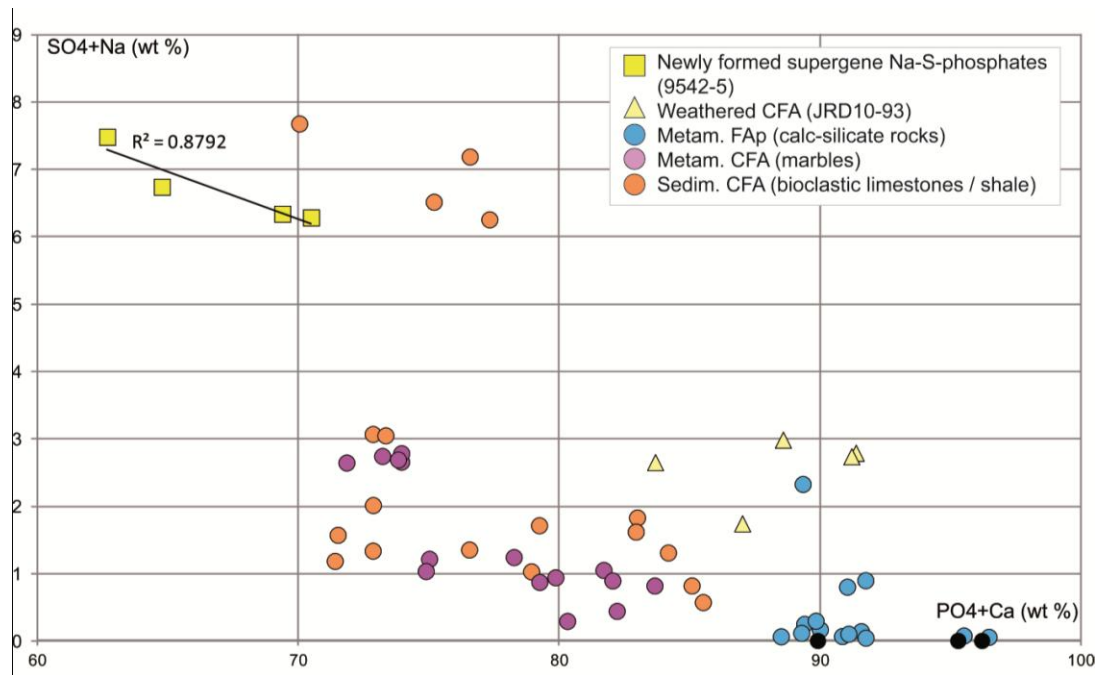


Figure III. 19. $\text{SO}_4 + \text{Na}$ versus $\text{PO}_4 + \text{Ca}$ diagram.

7. DISCUSSION

7.1. Evolution of the sedimentary-diagenetic phosphates

Phosphate ooides, nodules, aggregates and skeletal fragments in the carbonates and the shales consist of carbonate-fluorapatite. Phosphorus present in the ocean is absorbed by marine organisms and plants to be converted in organic P. Phosphate derives from these biological associations which are decomposed at the death of the organisms, and deposited it on the sea floor (Knudser and Gunter, 2002). P production is promoted by the upwelling events which are rich in nutrients and lead a high productivity (phytoplankton, zooplankton, and other marine organisms) and hence a great P fixation. The depth of formation of phosphate is located to the OMZ (oxygen minimum zone) (Föllmi, 1996) indicating the need of a reducing environment to release P. The suboxic conditions lead to the sequestration of phosphate ions and their precipitation to form CFA (Slansky, 1986; Rougerie and Jehl, 1993). CFA crystallize in the interstitial waters, when PO_4^{3-} and F^- concentration are high and the pore water alkalinity and Mg^{2+} concentration are low (Jahnke, 1984; Slansky, 1986; Froelich et al., 1988). Also, CFA can be formed by precipitation from anoxic pore-water, by replacement of carbonate (oxic process), by bacterial processes (Soudry and Champetier, 1983; McArthur, 1985), and can be also deposited as bone, teeth or shells (Carpenter, 1969; Slansky, 1986).

In phosphorites or phosphatic rocks, carbonate-fluorapatites can include a large variety of trace elements such as uranium which can be present as a separate uraninite phase (Altschuler et al., 1958), as an adsorbed or structurally incorporated as dominantly a U^{4+} replacement for Ca^{2+} because of their close ionic radii ($\text{Ca}^{2+} = 0.99\text{\AA}$ and $\text{U} = 0.97\text{\AA}$) (Altshuller, 1980; Nathan, 1984; McClellan and VanKauwenberg, 1990; Panczer et al., 1998).

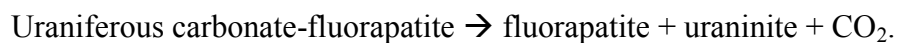
In seawater, U is present as the hexavalent uranyl ion, which is more soluble than U(IV). The enrichment of U in phosphorites may be due to the association of the latter with abundant organic matter in the depositional environment of the phosphorites (Burnett, 1990). All the sedimentary/diagenetic lithologies show a positive correlation U-P reflecting that uranium was incorporated dominantly in the apatite lattice. The apatite crystals from the sedimentary rocks have a maximum uranium concentration of 1769 ppm (in shale) and an average U content of 192 ppm. The shales and their phosphates are formed in anoxic restricted basins whereas the phosphate bioclastic limestones of the Belqa Group are mainly formed in the suboxic OMZ where the primary productivity is high.

According to McArthur (1985), the substitutions for Ca and PO₄ of the CFA reflect the composition of the solution which forms this mineral and are not influenced by redox conditions of the formation. But the tetravalent uranium concentrations become significant in acid reducing environment (Garrels, 1955). The CO₂ content of the carbonate-fluorapatite should be due to the increase of the temperature of the water from which the francolite (other name for the CFA, but not admitted by all the scientific community) formed (Gulbrandsen, 1970; Cook, 1970).

7.2. Uranium mobilization from the biogenic phosphates during pyrometamorphism

Carbonate lithologies of the Belqa Group suffered pyrometamorphism, which resulted from the combustion of organic-rich layers where oxygen was supplied (see Chapter 4). This peculiar metamorphism affected restricted zones of variable thickness, and was limited to the organic-rich protolithes, but has occurred over very large areas (up to 2 km²).

The carbonate-fluorapatites of the marbles show a great variation of uranium content during the ablation at a same point leading to peaks of concentration in the LA-ICP-MS spectra because of the presence of inframetric inclusion of U in the phosphate. The very low U median content (27 ppm) shows that the lattice of the CFA of the marbles is not rich in U. The U content of 41 994 corresponds to an U inclusion ablated during the LA-ICP-MS analysis. CFA of marbles are the only apatite type to show this specificity due to the metamorphism process which led to the recrystallization of the phosphates and the exsolution of U to form inframetric inclusions microscopically visible. The reaction allowing this uranium reconcentration is:



The phosphates of the calc-silicate rocks are fluorapatite newly formed without a carbonate or hydroxyl group. This may be due to a decarbonation reaction associated with the metamorphism as already observed by Matthews and Nathan (1977) and McClellan (1980). Uranium mobilization was possible by the temperature increase which led the destabilization of the carbonate-fluorapatite. Stein (1979) showed that the minimum temperature needed for begin the uranium migration and concentration process in the structure of the apatite is about

600-700°C. The uranium oxide is exsolved and forms microcrystals (up to 5 µm), sometimes visible by optical microscopy. These metamorphic fluorapatites have high and homogeneous uranium concentration (average U = 194 ppm). But we did not see any uranium inclusions in these calc-silicates rocks. The lack of uranium inclusions could indicate that the higher metamorphic grade has disrupted the process of U reconcentration.

7.3. New Phosphate formation and secondary uranium mineralization during the weathering of the carbonates

Altered fluorapatite (JRD10-93) and newly formed sulfato-phosphates (9542-5) of the weathered porous limestones have the lowest average uranium concentration (respectively up to 112 ppm and 34 ppm). Newly formed sulfato-phosphates form rosettes of acicular crystals in the porosity and weathered phosphates occur as aggregates of dissolved grains sometimes rounding within fibrous clay mineral. These weathered carbonates are mineralized in uranium which is associated with vanadium to form tyuyamunite ($\text{Ca}(\text{UO}_2)_2(\text{VO}_4)_2\text{H}_2\text{O}$) and strelkinite ($\text{Na}_2(\text{UO}_2)_2\text{V}_2\text{O}_8 \cdot 6\text{H}_2\text{O}$) in the matrix of the rocks. The uranyl vanadates are disseminated in the porosity of the rocks or occur as splinter thinly associated with fibrous fluorite. Also, fluorite occurs in calcite or as coating of vugs of idiomorphic calcite.

The formation of these mineralized weathered limestones is probably due to the following steps (which are presented in detail in Chapter 5):

- Supergene alteration of the carbonate-fluorapatites of the carbonated facies with liberation of U(4) oxidized in U(6),
- Concentration by water infiltration along an altered, weathered and permeable limestone profile
- Trapping of U sub-in situ because of the low vanadium concentrations of the sedimentary carbonated lithologies (U and V sources are the same lithologies, which prevent the lateral migration observed in the classic mineralized calcretes)
- Addition of U from the more metamorphosed facies of which carbonate-fluorapatite have liberated U leached by meteoric fluids leading the transport of elements (U, F, Na, S) from the more resistant marbles that form the topographical highs, to the altered facies beneath.

The weathered phosphates have been formed according to the following reaction:



The newly formed sulfato-phosphates have been formed according to the following reaction:



Na probably originates from the evaporation of surficial water in arid climate which increase its salinity. It may originate from the alteration of the limestones which contain numerous sulfides (pyrite, sphalerite, millerite, hawleyite, makienite, stilleite) and the metamorphosed limestones which contain minerals such as ettringite ($\text{Ca}_6\text{Al}_2(\text{SO}_4)_3(\text{OH})_{12} \cdot 26(\text{H}_2\text{O})$), Hashemite ($\text{Ba}(\text{Cr,S})\text{O}_4$) and sulfides. The sodium and sulfate contents reflect a high palaeosalinity during the deposition (Russell and Trueman, 1971).

7.4. REE evolution

The marine biogenic apatites from Morocco (Ypresian - Campanian) and from Negev (Late Campanian-Early Maastrichtian) (Lécuyer et al., 2004; Soudry et al., 2002) (Fig.III.9), formed at the same period and with the same paleogeographic context, present PAAS-normalized REE patterns similar to those of the Jordanian sedimentary phosphates. The negative Ce anomalies reflect the seawater pattern, and not an oxic environment during deposition.

Normalizations of the REE contents of the apatites to their host rocks (Fig.III.10) show that the sedimentary and the metamorphic carbonate-fluorapatite have flat patterns indicating that they represent the host minerals for most of the REE contained in the rocks. The preserved seawater pattern for the CFA of the marbles normalized to their host rocks shows that the pyrometamorphism did not change significantly their REE contents. This contrast with the pattern of the fluorapatite of the calc-silicate rocks which have suffered of a higher pyrometamorphic grade and present a more fractionated pattern. This is another line of evidence that the protoliths of the calc-silicate rocks are different from the parent rock of the marbles, with a flat PAAS-normalized pattern similar to that of a shale (Fig. III.9). The weathered CFA of the weathered limestone JRD10-93 have higher LREE contents and are more fractionated because of the alteration responsible for the loss of REE by leaching of the upper weathered horizons (see Chapter V).

The lower REE content of this newly-formed phosphate indicates that the REE have not been incorporated in the Na-sulfato-phosphates which have also a lower REE content than their host rock (9542-5) (Fig.III.9). However, a non REE-rich mineral has been identified in this rock, REE could have been leached toward the other weathered horizons. This hypothesis cannot be confirmed because the sample was not collected along a vertical profile.

8. CONCLUSION

The biogenic carbonate-fluorapatites deposited in calcareous sediments are enriched in uranium during sedimentation in the redox zone below the sediment-water interface. Uranium substitutes for calcium in the lattice structure of the carbonate-fluorapatite formed by seawater phosphore enrichment during the coincidence of exceptional Late Cretaceous to Eocene palaeogeography and depositional environments, promoted by a huge upwelling event in the Neo-Tethys event. P was fixed by marine organisms and plants which were deposited on the sea-floor in a redox environment that preserved the organic matter and allowed drawdown of U in the carbonate-fluorapatite. After millions years, the phosphatic limestones and bituminous shales underwent pyrometamorphism during uplift and associated faulting during the Neogene. This resulted in the mobilization and the reconcentration of the uranium in the lattice of the carbonate-fluorapatite to form uranium oxide grains. Meteoric groundwater alteration allowed the leaching of the uraniferous carbonate-fluorapatite, and the resultant evaporitic fluids led to the alteration of supergene carbonate-fluorapatites, permitting the crystallization of surficial uranium minerals (see Chapter 5), and the new formation of Na-sulfato-phosphates that are characterized by a low uranium content and by the fluorite.

ACKNOWLEDGMENTS

We thank AREVA NC for the financial and scientific support and more specially Jean Reyx to have allowed us to complete the sampling with his thin sections. We would like to thanks Philippe Lach for the LA-ICP-MS analyses, thank you to having granted us a little part of your precious PhD time. Also, we thank Marie-Camille Caumon for the help for using of the RAMAN spectrometer; Régine Mosser Ruck for the XRD analyses; the team of the lithopreparation service; Olivier Rouer and the staff of the SCMEM; and the staff of the SARM.

REFERENCES

- Abed, A.M., Fakhouri, K., 1996. On the chemical variability of phosphatic particles from the Jordanian phosphorites. *Chem. Geol.* 131, 1-13.
- Abed, A.M., Sadaqah, R., Al-Jazi, M., 2007. Sequence stratigraphy and evolution of Eshidiyya phosphorite platform, southern Jordan. *Sedim. Geol.* 198, 209-219.
- Altschuler, Z.S., Clarke, R.S. Jr., Young, E.J., 1958. Geochemistry of uranium in apatite and phosphorite. *U.S. Geol. Surv., Prof. Paper*, 314-D, 45-90.
- Altschuler, Z.S., 1980. The geochemistry of trace elements in marine phosphorites. Part II. Characteristic Abundances and enrichment, *SEPM Spec Publ* 29, 19-30.
- Ashckenazi-Polivoda, S., Abramovich, S., Almogi-Labin, A., Schneider-Mor, A., Feinstein, S., Püttmann, W., Berner, Z., 2011. Palaeoenvironments of the latest Cretaceous oil shale sequence, Southern Tethys, Israel, as an integral part of the prevailing upwelling system. *Palaeogeogr. Palaeoclimatol. Palaeoecol.* 305, 93-108.
- Bacquet, G., Vo, Q.T., Bonel, G., Vignoles, M., 1980. Résonance paramagnétique électronique du centre F dans les fluorapatites carbonatées de type B. *Journal of Solid State Chem.* 33, 189-195.
- Burnett, W.C., 1990. Phosphorite growth and sediment dynamics in the modern Peru shelf upwelling system. In *Phosphorites deposits of the world, 3. Neogene to modern phosphorites.* (Eds Burnett, W.C. & Riggs, S.), Cambridge University Press, 62-74.
- Baumer, A., Caruba, R., Ganteaume, M., 1990. Carbonate-fluorapatite: Mise en évidence de la substitution $2\text{PO}_4^{3-} \rightarrow \text{SiO}_4^{4-} + \text{SO}_4^{2-}$ par spectrométrie infrarouge. *European Journal of Mineralogy*, 2, 297-304.
- Binder, G., Troll, G., 1989. Coupled anion substitution in natural carbon-bearing apatites. *Contrib. Mineral. Petrol.* 101, 394-401.
- Borneman-Starynkevich, I.D., Belov, N.V., 1953. Carbonate-apatites. *Doklad Akad Nauk SSSR* 90, 89-92.

Carpenter, J.H., Pritchard, D.W., Whaley, R.C., 1969. Observations of eutrophication and nutrient cycles in some coastal plain estuaries, 210-221. In *Eutrophication: Causes, consequences, correctives*. Natl. Acad. Sci., Washington, DC.

Comodi, P., Liu, Y., Stoppa, F., Wooley, A.R., 1999. A multi-method analysis of Si-, S- and REE-rich apatite from a new kind of kalsilite-bearing leucitite (Abruzzi, Italy). *Mineral. Mag.* 63, 661-672.

Cook, P.J., 1970. Repeated diagenetic calcitization, phosphatization and silicification in the Phosphoria Formation. *Geol. Soc. Am. Bull.* 81, 2107-2116.

Cuney, M., 2010. Evolution of Uranium Fractionation Processes through Times: Driving the Secular Variation of Uranium Deposit Types. *Econ. Geol.* 105, 553-569.

Elliot, J.C., 1994. Structure and chemistry of the apatites and other calcium orthophosphates, 389 p. Elsevier, Amsterdam.

Fleurance, S., Cuney, M., Malartre, F., Reyx, J., 2013. Origin of the extreme polymetallic enrichment (Cd, Cr, Mo, Ni, U, V, Zn) of the Late Cretaceous – Early Tertiary Belqa Group, central Jordan. *Palaeogeogr. Palaeoclimatol. Palaeoecol.*

Föllmi, K.B., 1996. The phosphorus cycle, phosphogenesis and marine phosphate-rich deposits. *Earth Sci. Rev.* 40, 1-2, 55-124.

Froelich, P.N., Arthur, M.A., Burnett, W.C., Deakin, M., Hensley, V., Jahnke, R., Kaul, L., Kim, K.H., Roe, K., Soutar, A., Vathakanon, C., 1988. Early diagenesis of organic matter in Peru continental margin sediments: phosphorite precipitation. *Mar. Geol.* 80, 309-343.

Garrels, R.M., 1955. Some thermodynamic relations among the uranium oxides and their relation to the oxidation states of the uranium ores of the Colorado Plateau: *Am. Mineral.* 40., nos. 11 and 12, 1004-1021.

Goldoff, B., Webster J.D., Harlov, D.E., 2012. Characterization of fluor-chlorapatites by electron probe microanalysis with a focus on time-dependent intensity variation of halogens. *Am. Mineral.* 97, 1103-1115.

Guldbrandsen, R.A., 1966. Chemical composition of phosphorites of the Phosphoria Formation. *Geochim. Cosmochim. Acta* 30, 769-778.

- Gulbrandsen, R.A., 1970. Relation of carbon dioxide content of apatite of the Phosphoria Formation to regional facies. U.S. Geol. Surv., Prof. Paper, 700-B, B9-B13.
- Hughes, J.M., Drexler, J.W., 1991. Cation substitution in the apatite tetrahedral site: crystal structures of types hydroxyllestadite and type fermorite. *Neues Jahrbuch Mineral.* 327-336.
- Jahnke, R.A., 1984. The synthesis and solubility of carbonate-fluorapatite. *Am. J. Sci.* 284, 58-78.
- Jasinski, S.M., 2003. Phosphate rocks. U.S. Geol. Surv. Minerals Yearbook, 56.1-56.5.
- Knudser, A.C., Gunter, M.E., 2002. Sedimentary Phosphates- An example: Phosphoria Formation, Southeastern Idaho, U.S.A. *Rev. Mineral. Geochem.* 48, 363-390.
- Lécuyer, C., Reynard, B., Grandjean, P., 2004. Rare earth element evolution of Phanerozoic seawater record in biogenic apatites. *Chem. Geol.* 204, 63-102.
- Liu, Y., and Comodi, P., 1993. Some aspects of the crystal chemistry of apatites. *Mineral. Mag.* 57, 709-719.
- Matthews, A., Nathan, Y., 1977. The decarbonation of carbonate-fluorapatite (francolite). *Am. Mineral.* 62, 565-573.
- McArthur, J.M., 1985. Francolite geochemistry – Compositional controls during the formation, diagenesis, metamorphism and weathering. *Geochim. Cosmochim. Acta* 49, 23-35.
- McArthur, J.M., Walsh, J.N., 1984/1985. Rare-earth geochemistry of phosphorites. *Chem. Geol.* 47, 191-220.
- McArthur, J.M., 1990. Fluorine-deficient apatite. *Mineral. Mag.* 54, 508-510.
- McClellan, G.H., Lehr, J.R., 1969. Crystal chemical investigation of natural apatites. *Am. Mineral.* 54, 1374-1391.
- McClellan, G.H., 1980. Mineralogy of carbonate fluorapatites. *J. Geol. Soc. London* 137, 675-681.

- McLennan, S.M., 1989. Rare earth elements in sedimentary rocks: Influence of provenance and sedimentary processes. *Geochemistry and mineralogy of the rare earth element*. *Rev. Mineral. Geochem.* 21, 169-200.
- McClellan, G.H., Van Kauwenbergh, S.J.V., 1990. Mineralogy of sedimentary apatite. In: A.J.G. Notholt and I. Jarvis (Editors), *Phosphorite Research and Development*. Geol. Soc. London. Sp. Publ. 52, 23-31.
- Nathan, Y., 1984. The mineralogy and geochemistry of phosphorites. In: Nriagu, J.O. and Moore, P.O. (eds), *Phosphate minerals*. Springer, Berlin, 275-291.
- Nathan, Y., 1996. Mechanism of CO_3^{2-} substitution in carbonate-fluorapatite: Evidence from FTIR spectroscopy, ^{13}C NMR, and quantum mechanical calculation. *Discussion. Am. Mineral.* 81, 513-514.
- Pan, Y., Fleet, M., 2002. Compositions of the Apatite-Group Minerals: Substitution Mechanisms and Controlling Factors. *Rev. Mineral. Geochem.* 48, 13-50.
- Panczer, G., Gaft, M., Reinfeld, R., Shoval, S., Boulon, G., Champagnon, B., 1998. Luminescence of uranium in natural apatites. *J. Alloys Compounds* 275-277 :269-272.
- Parish, J.T., Curtis, R.L., 1982. Atmospheric circulation, upwelling, and organic-rich rocks in the Mesozoic and Cenozoic eras. *Palaeogeogr. Palaeoclimatol. Palaeoecol.*, 40, 31-66.
- Peng, G.Y., Juhr, J.F., McGee, J.J., 1997. Factors controlling sulfur concentrations in volcanic apatite. *Am. Mineral.* 82, 1210-1224.
- Piotrowski, A., Kahlenberg, V., Fischer, R.X., 2004. Mixed phosphate-sulfate fluor apatites as possible materials in dentral fillers. *Eur. J. Mineral.* 16, 279-284.
- Powell, J.H., Moh'd, B.K., 2011. Evolution of Cretaceous to Eocene alluvial and carbonate platform sequences in central and south Jordan. *GeoArabia* 16, 4, 29-82.
- Pyle, J.M., Spear, F.S., Wark, D.A., 2002. Electron Microprobe Analysis of REE in Apatite, Monazite and Xenotime: Protocols and Pitfalls. *Rev. Mineral. Geochem.* 48, 337-362.

- Regnier, P., Lasagna, A.C., Berner, R.A., 1994. Mechanism of CO₂- substitution in carbonate-fluorapatite: Evidence from FTIR spectroscopy, ¹³C NMR, and quantum mechanical calculations. *Am. Mineral.* 79, 809-818.
- Roeder, P.L., McArthur, D., Ma, X.P., Palmer, G.R., 1987. Cathodoluminescence and microprobe study of rare-earth elements in apatites. *Am. Mineral.* 72, 801-811.
- Ronsbo, J.G., 1989. Coupled substitution involving REEs and Na and Si in apatites in alkaline rocks from the Illimaussaq intrusions, South Greenland, and the petrological implications. *Am. Mineral.* 74, 896-901.
- Rougerie, F., Jehl, C., 1993. Le dossier phosphate revisité: Controverse et nouveau modèle. *Océanographie récifale*, Centre ORSTOM de Tahiti, 48-62. Journées de la recherche en Polynésie Française, Institut Mathilde Frébaut, 27-28 octobre 1993.
- Rouse, R.C., Dunn, P.J., 1982. A contribution to the crystal chemistry of ellestadite and the silicate sulfate apatites. *Am. Mineral.* 67, 90-96.
- Russell, R.T., Trueman, N.A., 1971. The geology of the Duchess Phosphate Deposits, Northwestern Queensland, Australia, *Econ. Geol.* 66, 1186-1214.
- Slansky, M., 1986. *Geology of Sedimentary Phosphates*. Kogan Page Ltd., London, 207 p.
- Smith, J.P., Lehr, J.R., 1966. An X-ray investigation of carbonate apatite. *J. Agr. Food Chem.* 14, 342-349.
- Soudry, D., Champetier, Y., 1983. Microbial processes in the Negev phosphorites (southern Israel). *Sedimentology*, 30, 411-423.
- Soudry, D., Ehrlich, S., Yoffe, O., Nathan, Y., 2002. Uranium oxidation state and related variations in geochemistry of phosphorites from the Negev (southern Israel). *Chem. Geol.* 189, 213-230.
- Soudry, D., Glenn, C.R., Nathan, Y., Segal, I., VonderHaar, D., 2006. Evolution of Tethyan phosphogenesis along the northern edges of the Arabian-African shield during the Cretaceous-Eocene as deduced from temporal variations of Ca and Nd isotopes and rates of P accumulation. *Earth Sci. Rev.* 78, 27-57.

Chapter III. Sedimentary, metamorphic to supergene evolution of uranium and REE in the phosphates from the Belqa Group lithologies, central Jordan.

Stein, M., 1979. Behavior of uranium during calcination of phosphate rocks. M.Sc thesis, Hebrew Univ. Jerusalem.

Stormer, J.C., Pierson, M.L., Tacker, R.C., 1993. Variation of F and Cl X-ray intensity due to anisotropic diffusion in apatite during electron microprobe analysis. *Am. Mineral.* 78, 641-648.

Toledo, M.C.M. de, Lenharo, S.L.R., Ferrari, V., Fontan, F., Parseval, P. de, Leroy, G., 2004. The compositional evolution of apatite in the weathering profile of the catalão I alkaline-carbonatitic complex, Gois, Brazil. *Can. Mineral.* 42, 1139-1158.

Trueman, N.A., 1966. Substitutions for phosphate ions in apatite. *Nature*, 210, 937-938.

Chapter IV

Characterization of the pyrometamorphism

1. INTRODUCTION

In this chapter, the aim is to present the peculiar mineralogical and geochemical characteristics of the metamorphic rocks occurring in the central Jordan (Siwaqa and Khan Azzabib zones) and to outline the process of their formation in this particular area. In the previous chapter we have shown the importance of pyrometamorphism on the mobilization of uranium from the carbonate-fluorapatite structure. The pyrometamorphism and the high temperature-low pressure rocks are known from a large part of the Levant Region (Fig.IV.1). Metamorphic complexes are located on the both sides of the Dead Sea, in Israel and at west of Jordan. Metamorphic rocks of central Jordan are a stratigraphical analogue of the ‘Mottled Zone’ (Hatrurim formation) in Israel the origin of which is attributed to pyrometamorphism (Heimbach and Rosch, 1980). Pyrometamorphic rocks have been identified also in Iran, Iraq, Czech Republic, Australia, Shanxi province in China (Grapes, 2006), and in Wyoming (Cosca et al., 1989, Clark and Peacor, 1992, Grapes et al., 2009). Two other metamorphic complexes are located in Jordan: Maqarin in the north, and Khushaym Matruk to the east of the study area (Fig.IV.1). These rocks have been intensively studied because they are considered to be comparable to the Portland/clinker cements, and thus represent a natural analogue of concrete which will be used for the storage of high level nuclear waste (Linklater et al., 1996; Mader et al., 2001; Techer et al., 2006; Fourcade et al., 2007; Elie et al., 2007; Pitty, 2009). Their mechanical and geochemical behavior during their interaction with geologic groundwater fluids over millions of years is of particular interest in this respect.

Four types of metamorphic rocks have been identified in the field (Fig.IV.1): (1) the marbles, (2) the black calc-silicate rocks, (3) the green calc-silicate rocks and (4) paralavas. The samples were collected from several outcrops in the MCM and URC formations (Maastrichtian-Palaeocene) (see general geological setting in introduction, Fig.2). The identification of the metamorphic minerals, and in particular, the calcium silicates (hydrated and/or carbonated) is complex. The determinations have been made using optical microscopy and scanning electron microscopy electron microprobe: structural formulae have also been calculated. The identification of some minerals is still uncertain and requires further study.

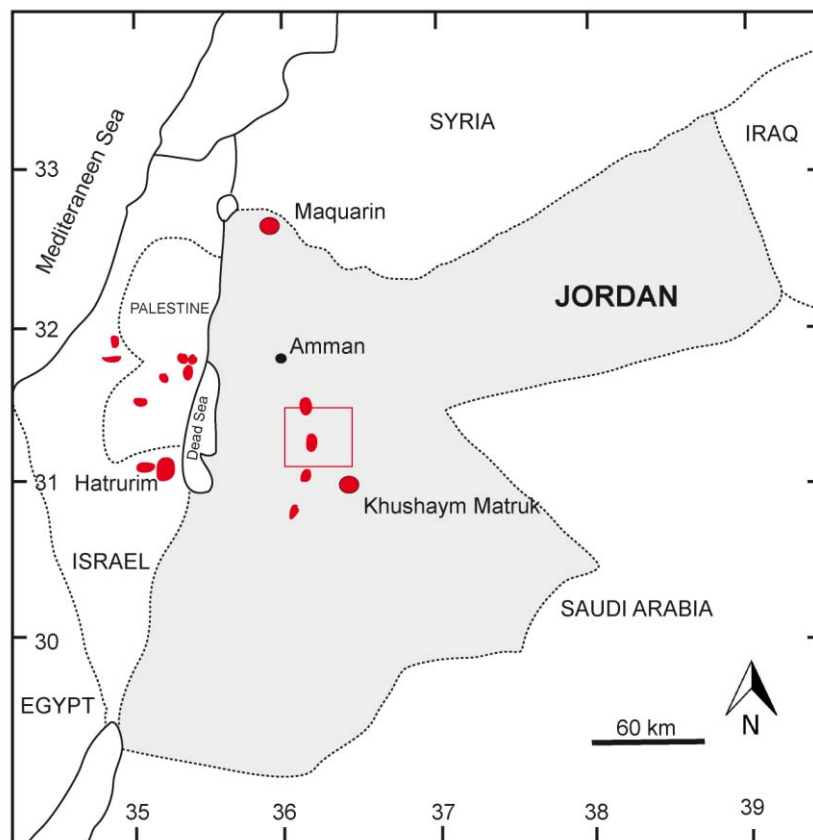


Figure IV. 1. Location of the metamorphic complexes (coloured in red) and the studied area (red square) (after Techer et al., 2006; Grapes, 2006).

2. GENERAL POINTS

2.1. Pyrometamorphism definition

The pyrometamorphism is a high temperature and very low pressure metamorphism. It is a peculiar metamorphism for which the thermal energy is provided by the combustion of organic matter-rich layers or coal (Clark and Peacor, 1992). In his book (Pyrometamorphism, Springer 2006), Rodney Grapes showed that these high temperatures could have several causes: (1) a mafic magma flow, (2) the spontaneous combustion of coal, organic-rich sediments, oil or gas, and (3) lightning strikes. The pyrometamorphism, related to mafic magma intrusion or due to organic matter combustion, results in anisotropic thermal expansion and contraction during heating/cooling in contact rocks due to reaction and melting of the mineral phases. The thermal gradient can be extremely high, but only over only a few tens of centimeters, in particular in the case of organic matter combustion. Temperatures of 400-1600°C can be reached for the pyrometamorphism resulting from the combustion of

bituminous material. The motor of the ignition is the introduction of oxygen along faults, during terrain collapse, subsidence or when the rocks are brought to the surface by erosion. The combustion reaction is: $C+O_2 = CO_2 + \text{heat}$ (94 kcal/mol).

2.2. Previous studies on pyrometamorphism in central Jordan.

A considerable number of petrographic and isotopic studies have been carried out to characterize the mineralogical assemblages of the pyrometamorphic rocks of the Levant (e.g.: Bentor et al., 1963; Gross, 1977; Matthews and Kolodny, 1978; Kolodny, 1979; Matthews and Gross, 1980; Burg et al., 1999, 1999; Khoury and Milidowski, 1992; Gur et al., 1995; Sokol and Volkova, 2007). This process affected the Upper Cretaceous (Maastrichtian)-Lower Tertiary (Palaeocene) sedimentary rocks (marls, bituminous chalks, cherts, clays, bituminous limestones, dolomites, conglomerates and phosphorites). Several areas extending over 1 to 50 km² have been identified. The 'Mottled Zone' covers a total surface of 90 by 60 km, with a thickness up to 190 m. The depth of the metamorphic horizons is 80 to 120 m. K-Ar, ⁴⁰Ar/³⁹Ar dating and fission track dating of the apatites has demonstrated several pyrometamorphic event at 2.3 and 4 Ma (Gur et al., 1995). The first stage began during the Miocene (16 Ma) (Kolodny et al., 1971; Burg, 1990) uplift that resulted in the near-surface exposure at the surface of the carbonate-rich protoliths. The metamorphic rocks of the 'Mottled Zone' are varied (fels, marbles, metamorphic conglomerates) and they contain up to sixty metamorphic minerals, mainly calcium silicates. A part of this mineralogical assemblage also testifies to the intense retrograde metamorphic process (rehydration, recarbonation, sulfatization). Strongly metamorphosed rocks make topographic highs: hills and cliffs. The process was initiated by the oxidation of the bituminous components of the sedimentary rocks near to the surface, at low pressures (≤ 25 bar) and high temperatures ($550 < T < 900^\circ\text{C}$) (Vapnik et al., 2007). Kolodny and Gross (1974) refuted the hypothesis of a contact metamorphism because of the absence of igneous rocks, and because the rocks underlying the metamorphic rocks are marine limestones and siliceous sediments without any evidence of metamorphism. Palaeomagnetic studies in Israel (Ron & Kolodny, 1992; Khesin et al., 2002; 2005, 2007) show that the magnetic anomalies in the 'Mottled Zone' can be explained by the metamorphism. The Hatrurim basin presents a great positive aeromagnetic anomaly (Folkman & Yuval, 1976). The combustion has completely changed the mineralogy and the properties

of the bituminous protolithes. These anomalies are thought to be due to the oxidation of the pyrites to magnetite giving the magnetization of the rocks. Al-Zoubi and Avraham (2002) show the presence of a thermal anomaly (by isodepth of the crystalline basement, isodepth of the Curie isotherm, isodepth of the Moho discontinuity), extended from the Dead Sea to the Al-Azraq basin, through central Jordan. In fact, the Curie isotherms (temperature for which a material loses its magnetization and becomes magnetized again at temperatures lower than the Curie temperature), determined from the heat flow data, indicate the presence of small magnetic bodies in central and west Jordan. The estimated duration of the pyrometamorphism for an area of 10m^2 is in the region of two years (Sokol et al., 2005, Grapes, 2006).

3. CHARACTERIZATION OF THE PYROMETAMORPHIC ROCKS IN CENTRAL JORDAN

3.1. Petrographic analysis

The four metamorphic facies: marbles, “black facies”, “green facies”, and paralavas do not show evidence of ductile deformation, which is to be expected for a rock fabric altered under low pressures and in the absence of tectonic stresses.

3.1.1. Marbles

The marbles correspond to metamorphosed phosphatic limestones and have varied colours. This colour change is due to the oxidation of sulphides, and to the colour change of the phosphates which became more crystalline with the green colour resulting from trace element substitutions (Fig.IV.2a, b). This phenomenon has also been noted by Matthews and Nathan (1977). These rocks are completely recrystallized and present a preferential orientation of their main minerals: calcite and carbonate-fluorapatites, inherited from the sedimentary bedding. The marbles contain a large series of metamorphic minerals such as oxides (brownmillerite, brownmillerite Ti, srebrodolskite, brownmillerite-perovskite series) (Fig.IV.2c, d, e) and primary accessory minerals such as barite (in the matrix and in inclusion in the phosphates), powellite (CaMoO_4), sulfides (Ni: millerite, Zn-Fe: sphalerite, Fe: pyrite) (Fig.IV.2d), native copper is disseminated in the matrix. Uranium oxides occur as micrometric inclusions in phosphates and poekilitic grains in the calcite-phosphate matrix (see in Chapter 3). Phosphates contain mackinawite (NiSe), stilleite (ZnSe) and barite (BaSO_4)

inclusions too. Also, marbles contain some hydrated and/or carbonated calcium silicates (spurrite/tilleyite) (Fig.IV.2c, e, f, g, h). Calcium silicate hydrate fills some veins in association with ettringite (sulfate) and hydrocalumite (oxide) (Fig.IV.2i). Bultfonteinite (Ca-F silicate), ettringite (sulfate) and calcite mostly occur in veins and cavities (Fig.IV.2j, k). Veins filled by bultfonteinite associated with Cd-sphalerites, gersdorffites (NiAsS) and Hashemite ($\text{Ba}(\text{Cr,S})\text{O}_4$) crystals (Fig. IV.2l). DRX analyses reveal some zeolites such as laumontite. Idiomorphic phases are composed of calcium silicate with high carbon content (black coloured, Fig.IV.2m, n). Some original clasts of calcite and phosphate are present, rounded by the recarbonated mineral.

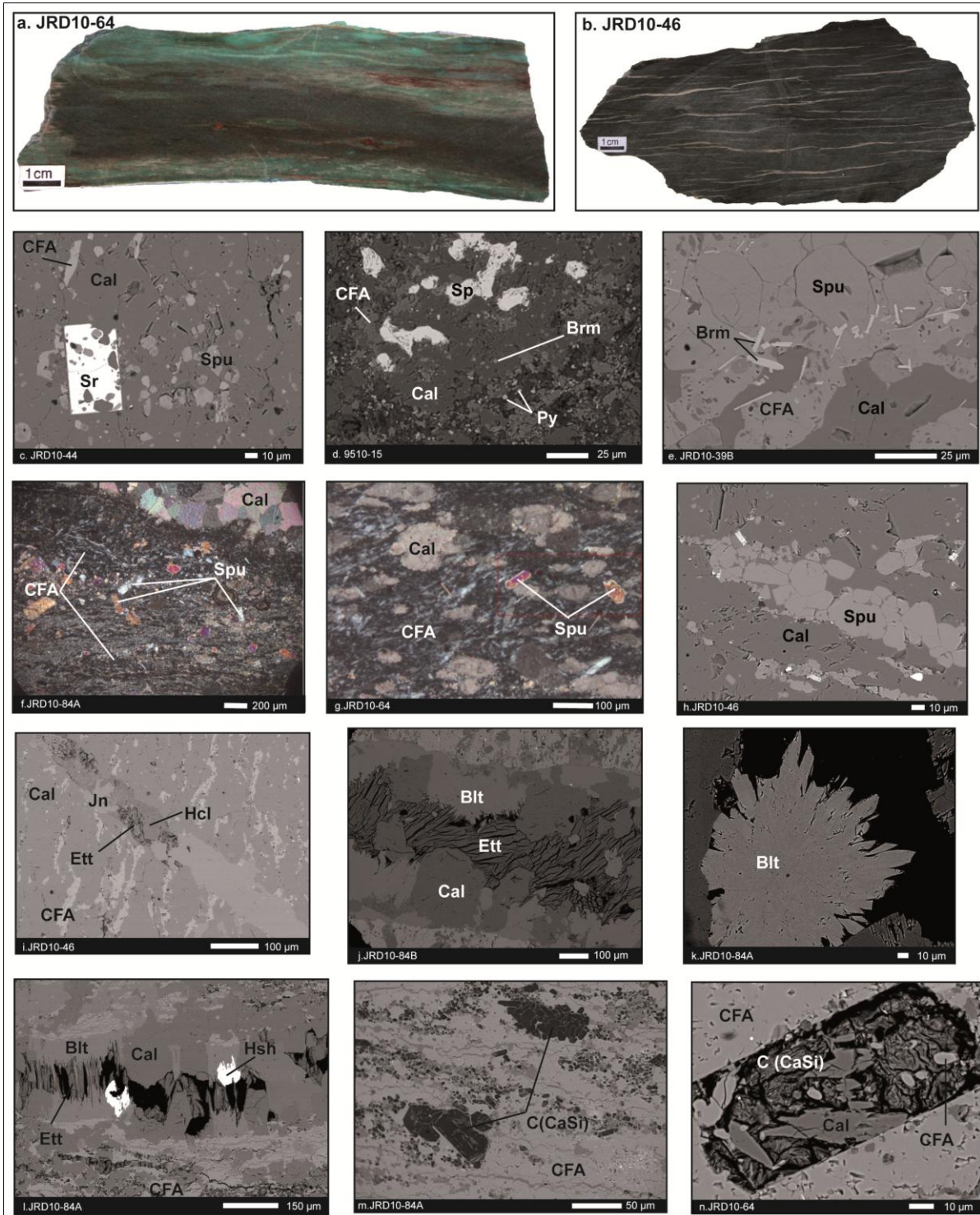


Figure IV. 2. Macroscopic (a, b) and SEM views (c to n) of the marbles. (Blt = bultfonteinite, Brm = brownmillerite, Cal = calcite, CFA = carbonate-fluorapatite, Ett = ettringite, Hcl = hydrocalumite, Hsh = hashemite, Jn = jennite, Py = pyrite, Spu = spurrite, Sr = Srebrodolskite).

3.1.2. Black calc-silicates rocks

The black calc-silicate rocks (JRD10-54/55) (Fig.IV.3a) are mainly composed by wollastonite (CaSiO_3) forming a mosaic and melilite ($(\text{Ca},\text{Na})_2(\text{Al},\text{Mg},\text{Fe}^{2+})(\text{Si},\text{Al})_2\text{O}_7$) (Fig.IV.3b). Acicular idiomorphic fluorapatites (Fig.IV.3c) are disseminated between the wollastonite and melilite frame. Subidiomorphic to idiomorphic chromite, chromatite, perovskite occur in the matrix and in the cavities. Millerite (NiS), bunsenite (Ni oxide) and iron oxide are closely associated. Fayalite, forsterite and palygorskite have been identified by DRX analyses. Between the two major components, there are tobermorite ($\text{Ca}_5\text{Si}_6\text{O}_{16}(\text{OH})_2 \cdot 4(\text{H}_2\text{O})$), pumpellyite ($\text{Ca}_2\text{M}(\text{XSiO}_7)$) group minerals and ettringite ($\text{Ca}_6\text{Al}_2(\text{SO}_4)_3(\text{OH})_{12} \cdot 26\text{H}_2\text{O}$) (Fig.IV.3c, d). Powellite occurs into tobermorite veins (Fig.IV.3e). Celestine and chromite are associated in tobermorite cavities (Fig.IV.3f). Veins of zeolites-calcite and veins of ettringite-tobermorite veins cut the calcium silicates.

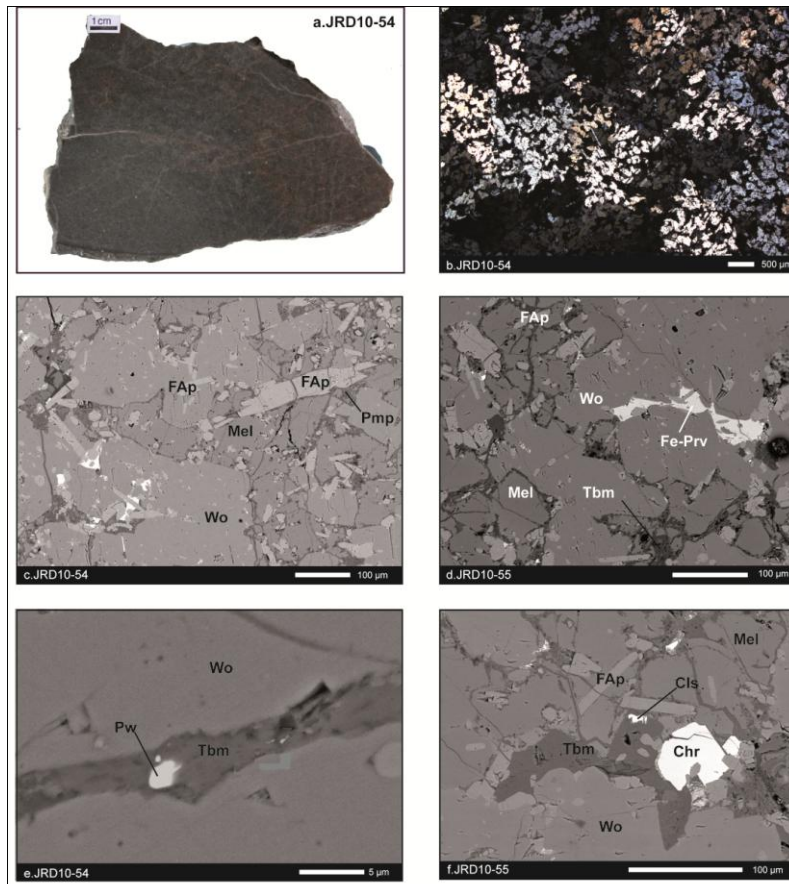


Figure IV. 3. Macroscopic and microscopic views of the black calc-silicate rocks (Chr = chromite, Cls = celestine, FAp = fluorapatite, Fe-Prv = Fe-perovskite, Mel = melilite, Pmp = pumpellyite, Pw = powellite, Tbm = tobermorite, Wo = wollastonite).

3.1.3. Green calc-silicate rocks

The green calc-silicate rocks (JRD10-60/61) present a bedding marked by levels of dark green nodules (μm - mm) and white micrograins (Fig.IV.4a). The rocks are composed of a complex assemblage of multiple minerals smaller (some twenty μm) than those of the black metamorphic facies. The principal minerals are wollastonite, anhydrous and non carbonated Al-Mg-Fe calcium silicates (melilite? augite?). Phosphates occur under cluster of subidiomorphic small elongated crystals (10 μm). Powellite grains are associated with zeolites and tobermorite is disseminated between the melilite (augite?) grains. Numerous vacuoles are filled by zeolites (general formula: $\text{Na}_{x1}\text{Ca}_{x2}\text{Mg}_{x3}\text{Ba}_{x4}\text{K}_{x5}(\text{Al}_{x6}\text{Si}_{x7}\text{O}_{x8})_{x9}\text{H}_2\text{O}$, thomsonite: $\text{NaCa}_2\text{Al}_5\text{Si}_5\text{O}_{20}\cdot 6\text{H}_2\text{O}$) tobermorite, sometimes thaumasite ($\text{Ca}_3\text{Si}(\text{CO}_3)(\text{SO}_4)(\text{OH})_6\cdot 12\text{H}_2\text{O}$), and with native copper and non-sulphurated Ni-Fe assemblages. These oriented vacuoles represent the micro nodules seen macroscopically, and indicate either the presence of gas during the cooling, or the dissolution of constitutive oriented elements. Silver micrograins and fluocerite are associated with tobermorite in some cavities. Dolomite, albite, olivine, diopside and hematite have been detected by DRX analyses.

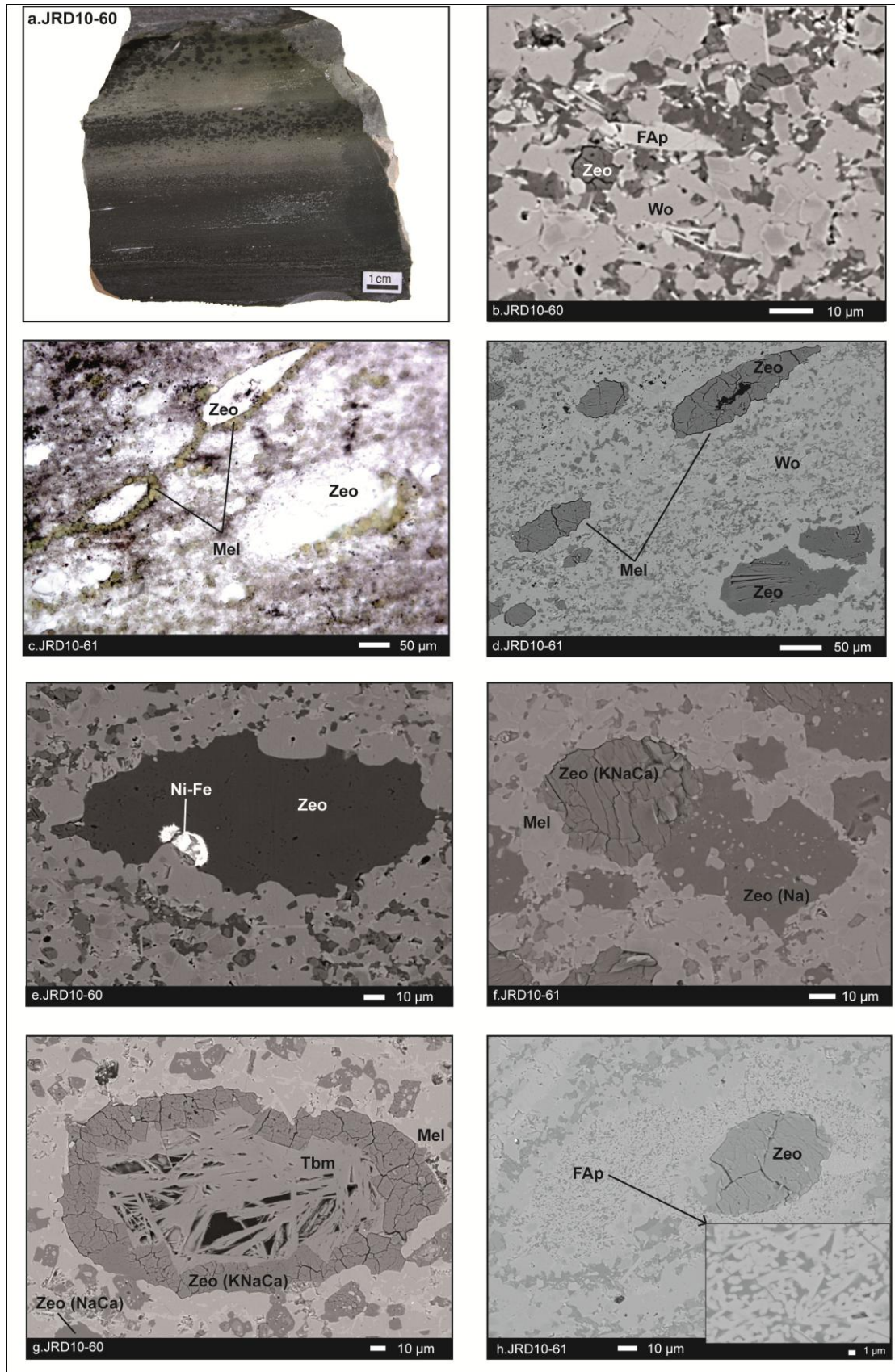


Figure IV. 4. Macroscopic and microscopic views of the green calc-silicate rocks (FAP = fluorapatite, Mel = melilite, Tbm = tobermorite, Zeo = zeolites, Wo = wollastonite).

3.1.4. Paralavas

Paralava is the term given to vesicular, aphanitic, fused shale and sandstones due to the combustion of coal, but which have the appearance of slag and igneous rock (Grapes, 2006). Three rocks (JRD10-32, 35 and 9536-22) (Fig.IV.5a, b) have been initially identified that are similar to altered basalt, but seems to be paralavas. Like the other metamorphic facies, they are present only locally, forming dike-like bodies. The microscopic study is not very advanced, but we already know that the matrix is composed of an assemblage of very small crystals with some calcite, feldspars and idiomorphic pyroxenes (Fig.IV.5c, d). The vacuoles analyzed in the sample consist of feldspars, calcite, silica and silicates Mg (Fig.IV.5e, f, g, h)

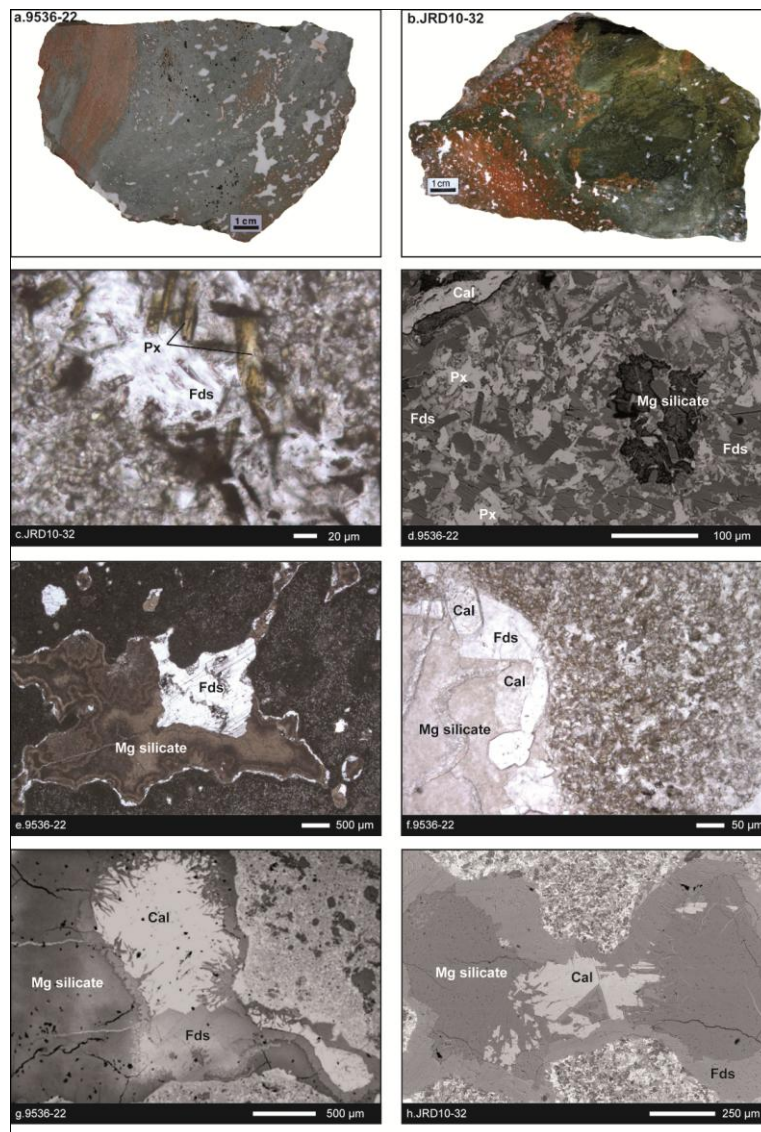


Figure IV. 5. Macroscopic and microscopic views of the paralavas (Cal = calcite, Fds = feldspar, Px = pyroxene).

3.1.4. Pyrometamorphic minerals

(*Theoretical formulae*)

3.1.4.1. Marbles

Brownmillerite ($\text{Ca}_2(\text{Al}, \text{Fe}^{3+})_2\text{O}_5$) is a typical oxide of the impure metamorphosed limestones of high temperatures. They occur as poekilitic minerals with inclusions of calcium silicates and calcite grains. It seems to that mixture perovskite-brownmillerite form Ti-brownmillerite as idiomorphic elongated microcrystals.

Srebrodolskite ($\text{Ca}_2\text{Fe}_2^{3+}\text{O}_5$) is another poekilitic idiomorphic mineral with inclusions of calcium silicates, calcite and phosphates grains.

Spurrite ($\text{Ca}_5(\text{SiO}_4)_2(\text{CO}_3)$) and **tilleyite** ($\text{Ca}_5\text{Si}_2\text{O}_7(\text{CO}_3)_2$) are carbonated calcium silicates typical of the high temperatures – low pressures thermal metamorphism. They are idiophormic and have flashy yellow-brown-grey colours in cross polarized light. They occur also as rounded to subidiomorphic crystals which cluster along the same orientation of the calcite and carbonate-fluorapatite minerals. Hydrocalumite and srebrodolskites (see below) may form inclusions in them.

Jennite ($\text{Ca}_9\text{H}_2\text{Si}_6\text{O}_{18}(\text{OH})_6 \cdot 8\text{H}_2\text{O}$) and **afwillite** ($\text{Ca}_3(\text{SiO}_3\text{OH})_2 \cdot 2\text{H}_2\text{O}$) are calcium silicate hydrates typical to the metamorphosed limestones. These minerals occur as fibrous or rounded to subidiomorphic grains in veins and cavities. They are associated with ettringite and bultfonteinite which crystallize later.

Hydrocalumite ($\text{Ca}_2\text{Al}(\text{OH})_6[\text{C}_{11-x}(\text{OH})_x] \cdot 3\text{H}_2\text{O}$) is an oxide disseminated in the matrix and in the calcium silicates. Also, this mineral occurs in association with jennite and ettringite in vein.

Tobermorite ($\text{Ca}_5\text{Si}_6(\text{O},\text{OH})_{18} \cdot 5\text{H}_2\text{O}$) is a group of calcium silicate hydrates containing some aluminium. This phase occur as subidiomorphic to idiomorphic crystals, sometimes with altered black carbonates.

Bultfonteinite ($\text{Ca}_2\text{SiO}_2(\text{OH};\text{F})_4$) is a fluor calcium silicate hydrate belonging to the afwillite group, common in the thermal metamorphosed limestones. This mineral filled cavities and veins along with ettringite (before or after, sometimes both). Also, bultfonteinite occurs as fibro-radials minerals in cavities.

Kumtyubeite ($\text{Ca}_5(\text{SiO}_4)_2\text{F}_2$) is a fluor calcium silicate typical of combusted coal. This secondary mineral occurs in the internal edge of veins in association with calcite. Subsequently, the formation of Hashemite crystals and ettringite filled the centre of the vein. Kumtyubeite occurs also as fibro radial minerals in the cavities, sometimes including a fluorapatite core.

Ettringite ($\text{Ca}_6\text{Al}_2(\text{SO}_4)_3(\text{OH})_{12} \cdot 26\text{H}_2\text{O}$) is a sulfate hydrate occurring as crackled fibrous secondary phase which filled the cavities and veins in associations with anterior bultfonteinite.

Hashemite ($\text{Ba}(\text{Cr}, \text{S})\text{O}_4$) is a sulfate which occurs as idiomorphic minerals in veins with bultfonteinite, ettringite and calcite.

3.1.4.2. Black and green calc-silicate rocks

Wollastonite (CaSiO_3) is an anhydrous calcium silicate. This mineral is the main constituent of the black metamorphic facies where it forms a mosaic of xenomorphic minerals. In the green facies, these minerals and the others constituents of the 'matrix' are smaller.

Melilite is associated with the wollastonite minerals. Some minerals of this group could be confused with augite. They are very small, it is not possible to distinguish cleavages. The melilite mineral is anhydrous and not carbonated.

Zeolites and ***tobermorite*** filled the veins, the vacuoles and the small cavities between the main constituents of the rocks and are thus clearly later than the preceding minerals.

Hydrated and/or carbonated Al-Mg-Fe-Ca-silicates (Pumpellyite type?) are disseminated between the wollastonite minerals.

In the black and green metamorphic facies, the calcium silicates show frequently black coloured alterations zone composed of carbonated phases (Fig.IV.2m, n).

3.1.4.3. Paragenetic sequences

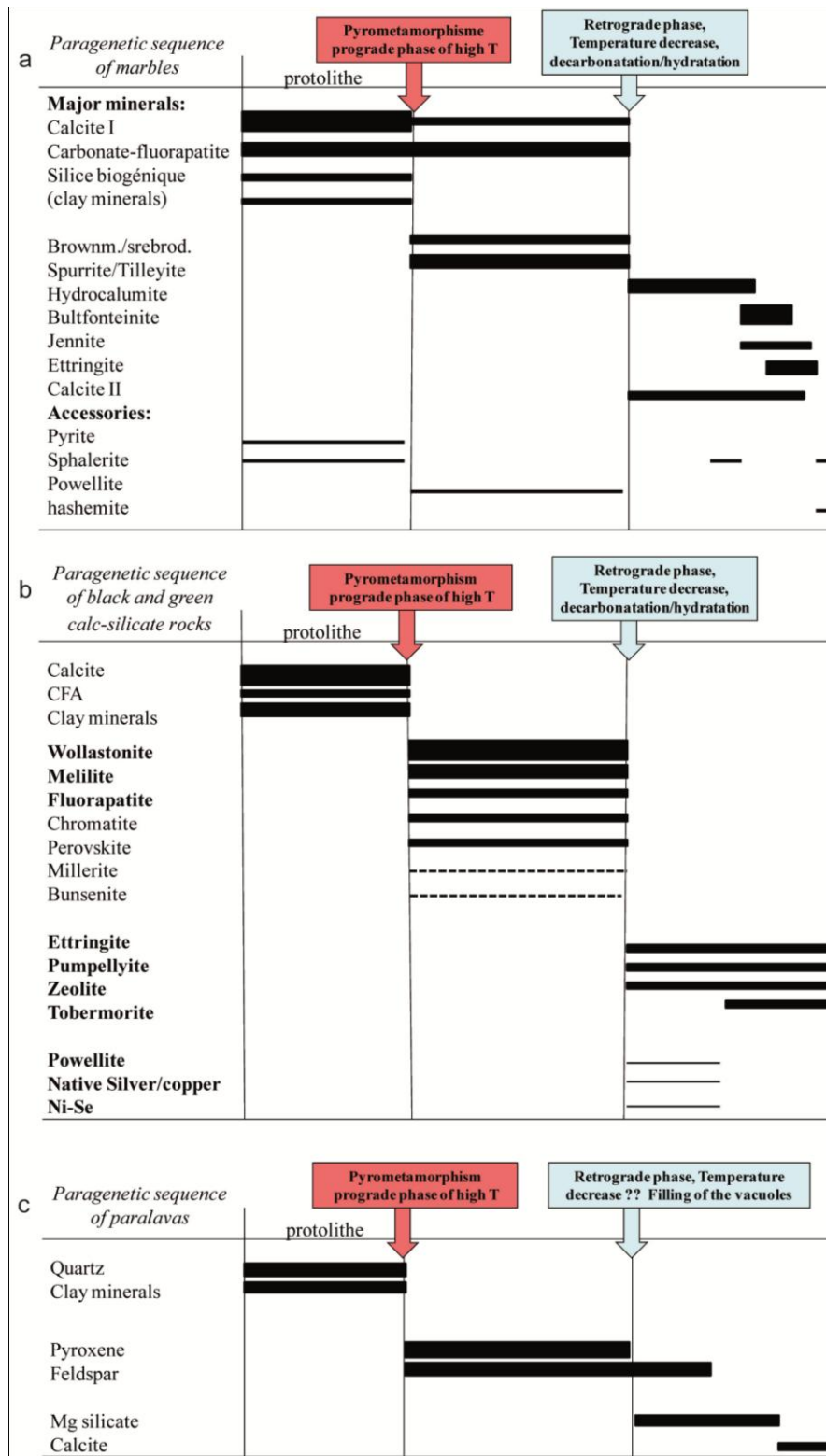


Figure IV. 6. Paragenetic sequences for the formations of the marbles (a), the calc-silicate rocks (b), and the paralavas (c).

3.2. Geochemistry

Whole rock element analyses are given in appendix IV. (p. 150).

The marbles are rich in calcium ($50 < \text{CaO} < 55$ wt %), but show an important variation of the calcium carbonate content ($21 < \text{CaCO}_3 < 90$ wt %) reflecting that Ca is also borne by other phases such as the carbonate-fluorapatites ($0.95 < \text{P}_2\text{O}_5 < 20.17$ wt %) and a large variety of the silicates described above ($0.64 < \text{SiO}_2 < 10.21$ wt %). As explained in the Chapter II, the marbles as with the non-metamorphosed limestones, are rich in redox sensitives elements.

The paralavas have the highest silica content ($51.82 < \text{SiO}_2 < 61.86$ wt%), alumina ($7.39 < \text{Al}_2\text{O}_3 < 9.18$ wt%), iron ($2.62 < \text{Fe}_2\text{O}_3 < 3.14$ wt%) and magnesium ($1.91 < \text{MgO} < 7.74$ wt%) reflect the presence of Al-Fe-Mg-silicates. The poorest calcium content ($10.55 < \text{CaO} < 13.99$ wt%) indicates a lower Ca-silicates and calcite content than the three other metamorphic facies. Paralavas show trace element concentrations lower than the other metamorphic facies (Cr, Cu, Ni, V) except for molybdenum ($40 < \text{Mo} < 949$ ppm), uranium ($23 < \text{U} < 459$ ppm), and zirconium ($41 < \text{Zr} < 74$ ppm).

The black and green calc-silicate rocks have an intermediary silica contents ($33.79 < \text{SiO}_2 < 41.33$ wt %). Given the low ignition loss ($2.85 < \text{LOI} < 5.83$ wt%) and the low total organic carbon ($0.09 < \text{TOC} < 0.38$ wt %), the high concentrations in calcium ($35.1 < \text{CaO} < 45.50$ wt%) are associated with abundant Ca-silicates and not to carbonates. The variable contents in alumina ($6.23 < \text{Al}_2\text{O}_3 < 8.61$ wt%), iron ($1.78 < \text{Fe}_2\text{O}_3 < 3.11$ wt%) and magnesium ($1.59 < \text{Mg} < 1.75$ wt%) reflect the different oxides and silicates identified above in these rocks. The phosphorus content ($4.81 < \text{P}_2\text{O}_5 < 5.40$ wt%) and fluor ($0.42 < \text{F} < 0.52$ wt%) correspond to the fluor-apatite. Fluorine is also present in fluor-calcium silicates (bultfonteinite). These rocks show trace element contents slightly lower than the marbles, but yet high for: chromium ($692 < \text{Cr} < 926$ ppm), copper ($87 < \text{Cu} < 172$ ppm), molybdenum ($154 < \text{Mo} < 268$ ppm), nickel ($196 < \text{Ni} < 392$ ppm), vanadium ($639 < \text{V} < 793$ ppm). Also, the uranium content ($38 < \text{U} < 45$ ppm) is lower than those of the marbles. They show higher zirconium concentrations $49 < \text{Zr} < 74$ ppm than the marbles ($5 < \text{Zr} < 56$ ppm) in relation with the higher detrital particles present in the initial protolith as also indicated by their higher alumina contents.

The variations of the major elements concentrations of the metamorphic rocks are illustrated in a series of diagrams in figure IV.7 and IV.8. The $(\text{SiO}_2 + \text{P}_2\text{O}_5) - (\text{Al}_2\text{O}_3 + \text{Fe}_2\text{O}_3) - (\text{CaO} + \text{MgO})$ diagram (Fig.IV.7) shows that the metamorphic rocks have varying calcium (Mg is never in

high concentration), silica and phosphorus contents. The four types of metamorphic rocks plot along a mixing line between the average Jordanian shales composition and the calcite pole. The marbles are the closest of the calcite pole, are the lowest in alumina and silica and present variable and higher phosphate contents than those of the two calc-silicate rocks. The paralavas compositions plot closer to the Jordanian shales. Black and green calc-silicate rocks compositions plot in intermediary composition, near the tobermorite pole. The Jordanian metamorphic rocks define the same trend that the Israeli metamorphic rocks of the 'Mottled Zone' (Hatrurim Fm.) (Fig.IV.1) but with lower Fe and Al contents and the presence of the marbles, a facies rich in carbonates not described in the other occurrences. The CaO-SiO₂-CO₂ diagram (Fig.IV.8a) show that the Ca/CO₂ ratios of the marbles increase compared to that of the limestone reflecting the decarbonation reactions. The calc-silicate rocks are very poor in total carbon and have the highest silica concentrations, indicating the higher content of non carbonated calcium silicates such as wollastonite. The CaO-SiO₂-Al₂O₃ diagram (Fig.IV.8b) show that the ratios Al/Si decrease from the marbles to the paralavas, and Al/Ca increase. Calc-silicate rocks have an intermediary composition between the marbles and paralavas, close to the shale JRD10-14 shale. Paralavas are closest of the shales JRD10-12A/B/D/E. The CaO-SiO₂-P₂O₅ diagram (Fig.IV.8c) illustrates the low phosphate content of the paralavas in contrast with marbles which show a large variation. The calc-silicate rocks show intermediary phosphate concentrations.

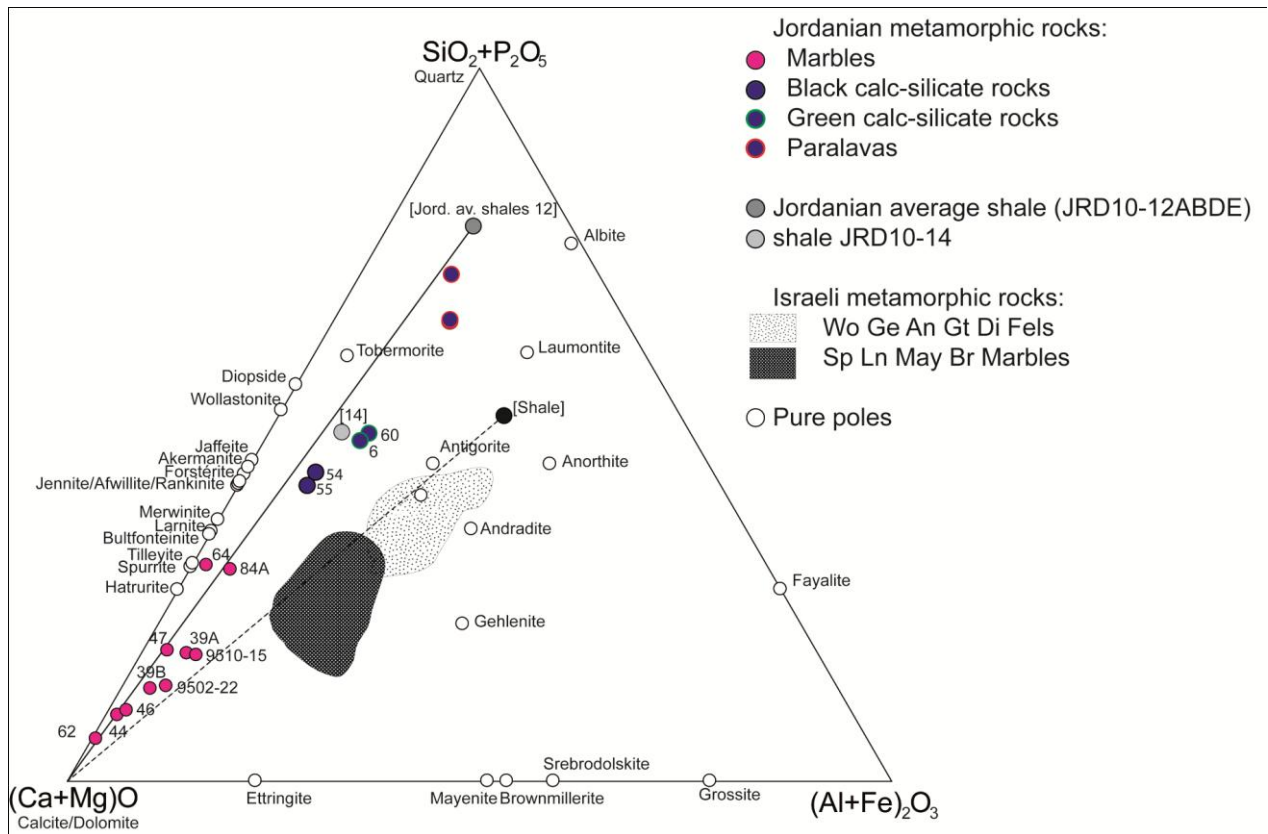


Figure IV. 7. $(SiO_2+P_2O_5)$ - $(Al_2O_3+Fe_2O_3)$ - $(CaO+MgO)$ diagram. (After the ternary diagram of Grapes (2006). However, the fields enclosed rock analyses from the Mottled Zone (Israel) have been corrected for carbonate content by substrating and amount of CaO equivalent to CO_2 (after Matthews and Gross, 1980). Our Jordanian samples have not been corrected in the same way, but it is not impact the ratio $SiO_2+P_2O_5/(Al+Fe)_2O_3$.

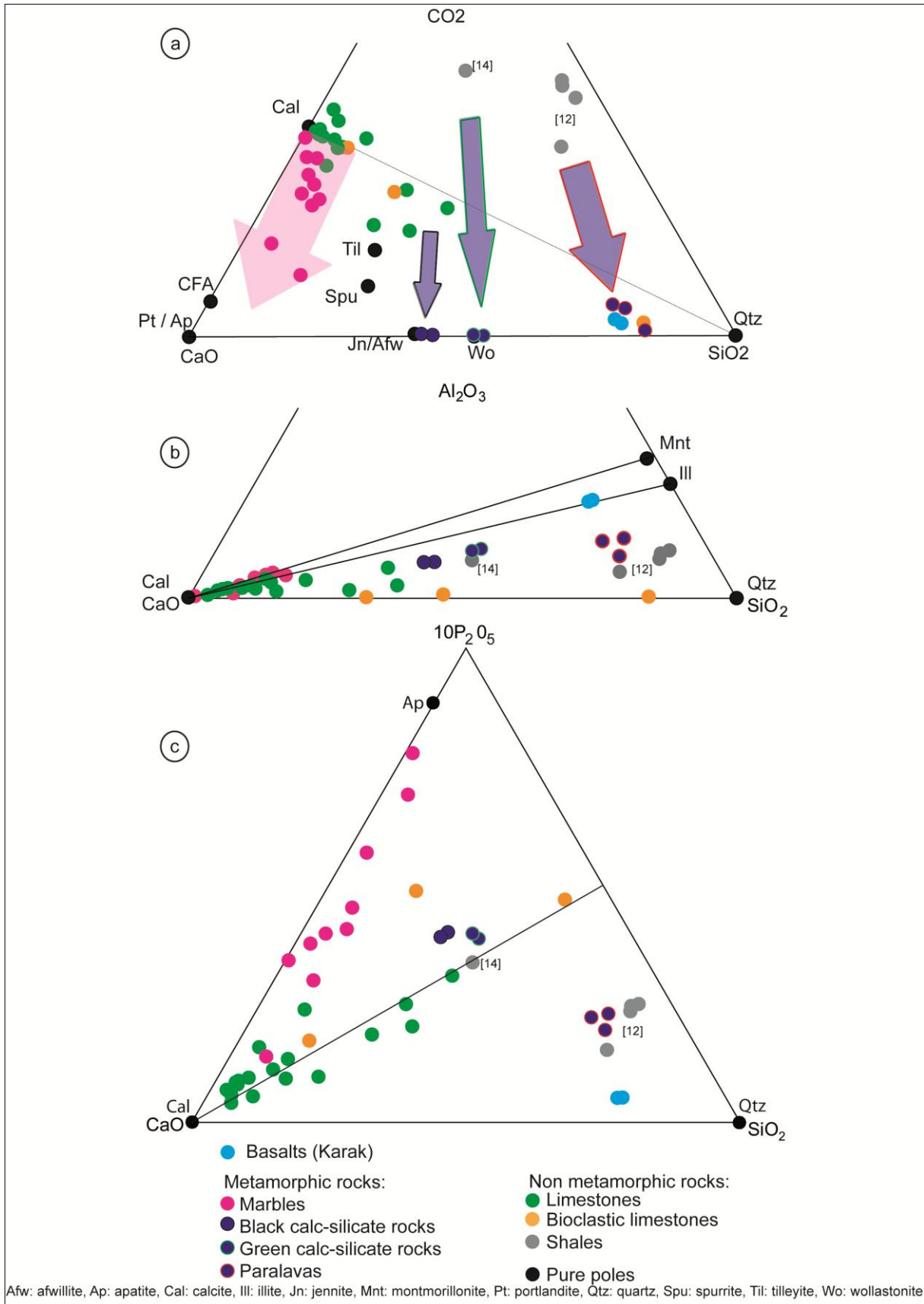


Figure IV. 8. Ternary diagrams. a: CaO-SiO₂-CO₂. b: CaO-SiO₂-Al₂O₃. c: CaO-SiO₂-P₂O₅.

4. DISCUSSION

4.1. Original and rare mineralogical assemblages

4.1.1. High temperature - low pressure prograde metamorphic assemblages

The protoliths have suffered pyrometamorphism characterized by the recrystallization of typical minerals such as calcium silicates like wollastonite, spurrite, and oxides such as brownmillerite.

4.1.2. Retrograde metamorphic assemblages

This high temperatures event was followed by retrograde event. Hydration and recarbonation led to the formation of hydrated secondary minerals such as jennite, ettringite, bultfonteinite and zeolites. During this retrograde episode the carbonation preserved the idiomorphic form of Ca-silicates, and led to the crystallization of secondary calcite.

4.2. Protolithes and conditions of formation.

The mineralogical composition of these three metamorphic facies testifies to the variable intensity of the metamorphic process affecting different parental rocks.

The **marbles** are mainly composed of oriented calcite crystals associated with carbonate-fluorapatite. Nevertheless, they contain prograde carbonated calcium silicates (spurrite/tilleyite), oxides (brownmillerite), and retrograde hydrated phases such as Ca-silicate hydrate (bultfonteinite), and sulfate hydrate (ettringite). Marbles JRD10-64>84>47 are the richest in phosphate with the respectively concentrations 20.17, 13.92, 7.76 %wt P₂O₅. The protoliths were beds of phosphatic limestone. Sample JRD10-84, the richest in silica (10.21%wt SiO₂), show abundant calcium silicates disseminated in the phosphatic matrix. Its parent rock probably contained silica rich layers. Sample JRD10-62 and 46 are the poorest in silica (0.64, 2.72 %wt SiO₂), and thus present few calcium silicates. Their mineralogy consists mainly of calcite with a low phosphate content; the parent rocks are interpreted to have been limestones with organic-rich layers. The pyrometamorphism process has not caused decarbonation of the calcium carbonate and the carbonate-fluorapatite.

The **black calc-silicite facies** is mainly constituted of wollastonite, anhydrous and non carbonated calcium silicate, and include minor retrograde phases in their cavities (tobermorite, zeolites, ettringite). The **green calc-silicate facies** is composed of a mixture of small sized minerals (wollastonite, melilite? augite?) and contain numerous oriented vacuoles filled by hydrated retrograde phases (zeolites and tobermorite). The lower Al/Si and Al/Ca ratios show that the protoliths of these two metamorphic facies were probably organic matter-rich clayey limestones or marls, with higher Al, Fe, Si contents, and lower phosphate minerals than the marbles. Green facies protoliths were probably marls such as the shale JRD10-14, in contrast with the parent rock of the black facies which mainly contain calcium silicates. Black and green facies are rich in Ca-silicates and phosphate with a low carbonate contents reflecting that the decarbonation reactions were more advanced than in the marbles, which still contain calcite. It indicates that the pyrometamorphic grade was higher than those forming the marbles, and the duration of combustion was probably longer.

The **paralavas** seems to be mainly constituted of Mg, Al silicates and their compositions in the ternary diagrams induce that their protolith was a shale (clayey marl) or a sandstone.

The rocks have been formed at very low pressure in subsurface conditions, a condition which is necessary for the introduction of oxygen needed for the burning of the organic material. The prograde mineralogical assemblages correspond to high temperature and very low pressure. The temperature increase is due to the combustion of Maastrichtian-Palaeocene organic-rich lithologies of the Belqa Group. The motor of the ignition is the atmospheric oxygen supply, various mechanisms have been proposed: by fractures and faults, by oxidizing fluid circulations, by volcanic muds (Sharygin et al., 2008 ; Vapnik et al., 2007 ; Sokol et al., 2010), or still by igneous intrusions. Some authors propose that the cracks may have been formed by earthquakes (Alexander and Smellie, 1998). Organic matter maturity indicators (TOC, hydrogen index of whole rocks, Tmax for whole rocks and isolated kerogen; Elie et al., 2007) prove that the organic matter of the metamorphic and adjacent units in the Khushaym Matruk area in central Jordan have oxidized and altered. With the absence of basic rocks nearby the studied metamorphic rocks, the pyrometamorphism was probably initiated by fractures or in areas which were exposed during rapid uplift and erosion during the Neogene. The scattered outcrops of these metamorphic complexes indicate that the protoliths were very geographically and temporally limited. The bituminous parent rocks responsible of the process were probably very limited spatially such as the restricted oils shales deposited in

small basins. The distribution of these rocks is restricted to the organic-rich areas and where the bituminous layers were ignited and where oxygen was introduced possibly via flauts and associated fractures.

The temperatures of the first appearance (T_{min}) for different minerals of the metamorphic facies are presented in table IV.1. In the marbles, idiomorphic spurrite or tilleyite have respective T_{min} of 625 and 870°C. Srebrodolskite has been crystallized at T_{min} of 815 °C, but the presence of brownmillerite which have a T_{min} of 800-980°C show that the highest temperatures responsible of the marble facies are about 800-900°C. In the black and green calc-silicate rocks, the minerals show higher T_{min} . Notably, the perovskite with T_{min} about 900°C, the chromite with T_{min} of 750-1200°C, and the melilite minerals which composed the matrix of these rocks and have a T_{min} of 1500°C.

Metamorphic facies	Mineral	T_{min} (°C)
marbles	spurrite	625 (<i>Burnham, 1959</i>)
	srebrodolskite	815 (<i>Rosa and Martin, 2010</i>)
	tilleyite	870 (<i>Harker, 1959</i>)
	brownmillerite	800-980 (<i>DeKayser, 1955</i>)
black and green calc-silicate rocks	wollastonite	270/550 (<i>Turner, 1967/Bentor et al., 1972</i>)
	powellite	630-880 (<i>Mendoza, 2010</i>)
	perovskite	900 (<i>Sharygin et al., 2008</i>)
	chromite	750-1200 (<i>Bardez, 2004</i>)
	melilite	1500 (<i>Grossman et al., 2002</i>)
T _{min} of the decarbonatation		350 (<i>Matthews and Nathan, 1977</i>)

Table IV. 1. Minimum temperatures of appearance of the minerals in the metamorphic rocks.

Marbles consist of xenomorphic carbonate-fluorapatite, and the two calc-silicate rocks contain subidiomorphic fluorapatite, which confirms the fact that the pyrometamorphism process occurred during higher temperatures for these black and green facies. The totally decarbonatation and recrystallization of fluorapatite in the calc-silicate rocks show that they suffered higher temperature increase.

The palaeomagnetic anomalies in central Jordan and Israel (presented above general points) are due to a magnetism change, provoked by a temperature increase ($T > T_{\text{Curie}}$ of 580°C) inducing a loss of magnetization, followed by a temperature decrease ($T < T_{\text{Curie}}$) allowing the remagnetization called the thermoremanance. This phenomenon is another evidence of the minimum temperature reached during the pyrometamorphism.

4.3. Redox sensitive elements enrichment

The high redox sensitive elements content of these rocks is due to the burning of the initial organic matter and the volume loss. The average enrichment factor of the marbles is much higher (0 to 10) than the carbonates. The polymetallic enrichment of the marbles is presented in Chapter II (Fleurance et al., 2013).

4.4. Role on the uranium mobilization

The phosphatic minerals of the metamorphic facies have been presented in the previous Chapter 3. The pyrometamorphism allowed the destabilization of the carbonate-fluorapatite of the marbles. Uranium in the lattice of the phosphates has been mobilized and reconcentrated to form micrometric inclusions of uranium oxides. The calcination temperature necessary for the remobilization of uranium is $600\text{-}700^{\circ}$ (Stein, 1979). The black and green facies, formed by combustion from protolithes poor in phosphate, present newly formed fluorapatites without uranium.

4.4. Pyrometamorphic complexes: natural analogues

4.4.1. Production of Clinker/Portland cements

Rocks formed by the combustion of organic matter have similar mineralogical assemblages as industrial cements. The principal process of fabrication of clinker/Portland cement is the combustion of a mix of calcium carbonates, silica and alumina at high temperatures and atmospheric pressure. This calcination leads to a deshydration, a decarbonation and the formation of calcium silicates and calcium aluminates. The product (clinker) is crushed and

mixed with gypsum and water to form Portland cement. With high temperatures of ignition, the Jordanian rocks have suffered of the similar transformations, without gypsum but with the some sulphides and sulfates (ettringite).

4.4.2. High-alkaline fluid alteration of radioactive wastes reservoirs

The recent works (Techer et al., 2006 ; Alexander et al., 1992 ; Elie et al., 2007 ; Fourcade et al., 2007 ; Khoury, 2011) considered pyrometamorphic complexes in Jordan, in the context of some studies about the storage of radioactive wastes in collaboration with ANDRA, CEA, FORPRO, etc. The areas of Khushaym Matruk (north east of our study zone), Maqarin (north of Jordan) are known natural analogues of the degradation of cement by high-alkaline fluids. The pyrometamorphic rocks are similar to cements, which are hydraulic binders and are considered for the construction of the structure to store the radioactive wastes.

In Khushaym Matruk, travertines and marble breccias marked the marbles/bituminous marls interface reflecting the palaeo fluid circulations. The actual waters are characterized by a high-alkalinity, a Ca-sulfate saturation and high concentration in trace elements. The decarbonation and deshydration processes, due to the metamorphism, allowed the liberation of trace metals which are re-incorporated in the newly formed mineral retrograde and prograde phases. The high-alkaline groundwaters provide to the leaching of the cements/marbles (Khoury, 2011).

5. CONCLUSIONS AND OUTLOOKS

The pyrometamorphic facies present in scattered outcrops in central Jordan testify to the palaeo-combustion of the organic-rich rocks of different compositions that were deposited in restricted marine environments, local basins, during the Maastrichtian to Early Eocene. These deposits were locally oxidized during phases of uplift, erosion and faulting that allowed the ignition of the organic-rich protoliths. Limestones, clayey limestones and shales have suffered an important temperature increase up to 1500°C leading to the respective increasing temperature formation of marbles, calc-silicate rocks and paralavas. The oxidation of the organic matter allowed the decarbonation of the rocks. The marbles, which were formed by lower temperature combustion of limestones, mainly comprise calcite, carbonate-fluorapatite, anhydrous carbonated calcium silicates (spurrite) as well as retrograde hydrated mineral

phases such as ettringite and bultfonteinite. Clayey limestones and marls have been affected by higher temperature metamorphism to form melilite in the black and green calc-silicate rocks. Their phosphates have been totally decarbonated to form fluorapatite. Calcium silicate hydrates (tobermorite) and aluminum silicate hydrates (zeolites) were formed during the retrograde phase. The highest temperature combustion affecting the non-bituminous shale, which is clayey and siliceous, led to the formation of paralavas composed of pyroxenes, feldspars and numerous vacuoles of magnesium silicates, feldspars and calcite.

Several analytic methods can be used to compare these pyrometamorphic occurrences with the others known in the Arabian Peninsula. Fission track studies on apatites could be to date the pyrometamorphic event and compare it with the other occurrences in Israel. This method is based on the disintegration of ^{238}U which naturally splits and leads the deformation of the apatite lattice and the liberation of particles responsible to the tracks. The count of these fission tracks allows the formation age of the mineral to be determined. Kolodny and Gross (1971, 1973) dated the metamorphic rocks to 13.6 ± 2 Ma, Miocene age, about 55 Ma after the deposition of the parent sedimentary rocks. It will be interesting to date the metamorphic rocks of central Jordan to compare with the Israel examples. Bentor et al. (1972) show that the Israeli metamorphic rocks present an enrichment in light isotopes ^{13}C and ^{18}O , reflecting a correlation between the temperature and the mineralogy. This C enrichment should be due to a ^{12}C - CO_2 exchange, where CO_2 is enriched during the oxidation of the organic matter and by the partial decarbonation produce by the heating. The isotopic enrichment is correlated with the petrography of the rocks: the non metamorphic rocks have an isotopic composition typical of the marine carbonates, the metamorphic rocks have higher ^{12}C and ^{16}O contents (^{13}C and ^{18}O decrease) which increase toward the spurrite composition. The carbonated rocks have a ^{18}O content which increase compared with the metamorphic and non-metamorphic rocks and ^{13}C which increase compared with the spurrite facies, and decrease compared with the parent rocks (Kolodny and Gross, 1974). Growth curves and P-T diagrams should allow us to specify the condition of formations of the metamorphic minerals. Laboratory tests could be allowed to follow the evolution of the process for different protoliths. The study of the marble breccias and the travertines should be permit to determine the nature of the fluids, and the P-T conditions by microthermometric analyses.

REFERENCES

- Alexander, W.R., Dayal, R., Eagleson, K., Eikenberg, J., Hamilton, E., Linklater, C.M., McKinley, I.G., Tweed, C.J., 1992. A natural analogue of high pH cement pore waters from the Maqarin area of northern Jordan. II: results of predictive geochemical calculations. *J. Geochem. Explor.* 46, 1, 133-146.
- Alexander, W.R., and Smellie, J.A.T., 1998. Maqarin natural analogue project (synthesis report). Unpublished Nagra internal report, Nagra, Wettingen, Switzerland.
- Al-Zoubi, A., Avraham, Z.B., 2002. Structure of the earth's crust in Jordan from potential field data. *Tectonophysics* 346, 45-59.
- Bardez, I., 2004. Etude des caractéristiques structurales et des propriétés de verres riches en terres rares destinés au confinement des produits de fission et éléments à vie longue. Univ. Pierre et Marie Curie, Paris VI. Thèse, 265 p.
- Bentor, Y.K., Gross, S., Heller, L., 1963. Some unusual minerals from the 'Mottled Zone' complex, Israel. *Am. Mineral.* 48, 924-930.
- Bentor, Y.K., Gross, S., Kolodny, Y., 1972. New Evidence on the Origin of the High-Temperature Mineral Assemblage of the "Mottled Zone" (Israel). 24th IGC, Ottawa, Section 2, 267-275.
- Burg, A., 1990. The geology of the Hatrurim Formation. M.Sc. Thesis. The Hebrew University, Jerusalem (in Hebrew, with English abstract), and *Isr. Geol. Surv., Rep. GSI/18/91*.
- Burg, A., Strarinsky, A., Bartov, Y., Kolodny, Y., 1991. Geology of the Hatrurim Formation ("Mottled Zone") in the Hatrurim Basin. *Isr. J. Earth Sci.* 40, 107-124.
- Burg, A., Kolodny, Y., Lyakhovsky, V., 1999. Hatrurim-2000: The "Mottled Zone" revised, forty years later. *Isr. J. Earth Sci.* 48, 209-223.
- Burnham, C.W., 1959. Contact metamorphism of magnesium limestones at Crestmore, Calif.: *Bull. Geol. Soc. Am.* 70, 879-920.

Clark, B.H., Peacor, D.R., 1992. Pyrometamorphism and partial melting of shales during combustion metamorphism: mineralogical, textural, and chemical effects. *Contrib. Mineral. Petrol.* 112, 558-568.

Cosca, M.A., Essene, E.J., Geissman, J.W., Simmons, W.B., Coates, D.A., 1989. Pyrometamorphic rocks associated with naturally burned coal beds, Powder River Basin, Wyoming. *Am. Mineral.* 74, 85-100.

Elie, M., Techer, I., Trotignon, L., Khoury, H., Salameh, E., Vandamme, D., Boulvais, P., Fourcade, S., 2007. Cementation of kerogene-rich marls by alkaline fluids released during weathering of thermally metamorphosed marly sediments. Part II: Organic matter evolution, magnetic susceptibility and metals (Ti, Cr, Fe) at the Khushaym Matruk natural analogue (central Jordan). *App. Geochem.* 22, 1311-1328.

DeKayser, W.L., 1955. Reactivity in the Solid State between oxides of the cement system: IVA, Roy. Swed. Acad. Sci. of Eng. Sciences 26, 292-309.

Folkman, Y., Yuval, Z., 1976. Israel aeromagnetic map, scale, 1:250,000, Inst. Petrol. Res. Geophys. (now Geophys. Inst. Isr., Holon).

Fourcade, S., Trotignon, L., Boulvais, P., Techer, I., Elie, M., Vandamme, D., Salameh, E., Khoury, H., 2007. Cementation of kerogene-rich marls by alkaline fluids released during weathering of thermally metamorphosed marly sediments. Part I: Isotopic (C, O) study of the Khushaym Matruk natural analogue (central Jordan). *App. Geochem.* 22, 1293-1310.

Grapes, R., 2006. *Pyrometamorphism*. Springer-Verlag Ed., Berlin Heidelberg, 276 p.

Grapes, R., Zhang, K., Peng, Z., 2009. Paralavas and clinker products of coal combustion, Yellow River, Shanxi Province, China. *Lithos* 113, 831-843.

Gross, S., 1977. The mineralogy of the Hatrurim Formation, Israel. *Geol. Surv. Israel Bull.* 70. 80 p.

Grossman, L., Denton, S.E., Simon, S.B., 2002. Formation of refractory inclusions by evaporation of condensate precursors. *Geochim. Cosmochim. Acta* 66, 145-161.

Gur, D., Steinitz, G., Kolodny, Y., Strainsky, A., McWilliams, M., 1995. $^{40}\text{Ar}/^{39}\text{Ar}$ dating of combustion metamorphism ("Mottled Zone", Israel). *Chem. Geol.* 122, 171-184.

Harker, R.I., 1959. The synthesis and stability of Tilleyite, $\text{Ca}_5\text{Si}_2\text{O}_7(\text{CO}_3)_2$. *Am. J. Sci.* 257, 656-667.

Heimbach, W., Rosch, H., 1980. Die Mottled Zone in Zentraljordanien. *Geologisches Jahrbuch* 40, 3-17.

Khesin, B.E., Itkis, S.E., 2002. Revision of aeromagnetic data: Ground magnetic investigation of altered sedimentary rocks (Hatrurim Basin, Israel). *Proceedings of the Estonian Academy of Sciences-Geology* 51, 1, 16-32.

Khesin, B., Feinstein, S., Vapnik, Y., Itkis, S., Leonhardt, R., 2005. Magnetic study of metamorphosed sedimentary of the Hatrurim formation, Israel. *Geophys. J., Int.* 162, 49-63.

Khesin, B., Feinstein, S., Itkis, S., 2007. Possible sources of magnetic anomalies over thermally metamorphosed carbonate rocks of the Mottled Zone in Israel. In G.B. Stracher, Ed., *GSA Rev. Eng. Geol. XVIII: Geology of Coal Fires: Case studied from around the world*, 177-197. *Geol. Soc. Am., Boulder, Colorado.*

Khoury, H., Milidowski, A., 1992. High temperature metamorphism and low temperature retrograde alteration of spontaneously combusted marls. The maqarin cement analogue. *Water Rock Interaction*, Kharaka & Maest Eds, Rotterdam, 1515-1518.

Khoury, H., 2011. 10th International conference of Jordanian geologists association in association with the 7th international symposium on Middle East geology. 3-5 april 2011. *Energy and mineral resources, a base for economic development.*

Kolodny, Y., Bar, M., Sass, E., 1971. Fission track age of the 'Mottled Zone event' in Israel. *Earth Planet. Sc. Lett.* 11, 269-272.

Kolodny, Y., Gross, S., 1973. Hazeva formation sediments affected by Mottled Zone event. *Isr. J. Earth Sci.* 22, 185-193.

Kolodny, Y., Gross, S., 1974. Thermal metamorphism by combustion of organic matter, isotopic and petrological evidence. *J. Geol.* 82, 489-506.

Kolodny, Y., 1979. Natural cement factory. A geological story. In: "Physics and Chemistry of Cement", eds J. Skalny, Plenum Press, N.Y., 203-216.

Linklater, C.M., Albinsson, Y., Alexander, W.R., Casas, I., McKinley, I.G., Sellin, P., 1996. A natural analogue of high-pH cement pore water from the Maqarin area of northern Jordan: Comparison of predicted and observed trace-element chemistry of uranium and selenium. *J. of Cont. Hydrol.* 21, 1-4, 59-69.

Mader, U., Adler, M., Langer, V., Degnan, P., Milodowski, A., Smellie, J., Salameh, E., Khoury, H., Griffault, L., and Trotignon, L., 2001. The Maqarin natural analogue study of a cement-buffered hyperalkaline groundwater plume structural model and flow systems. In: Cidu, R. (editor) *Water-Rock Interaction 2001*. Swets & Zeitlinger, Lisse (publishers), 185-188.

Matthews, A., Nathan, Y., 1977. The decarbonation of carbonate-fluorapatite (francolite). *Am. Mineral.* 62, 565-573.

Matthews, A., Kolodny, Y., 1978. Oxygen Isotope Fractionation in Decarbonation Metamorphism: "The Mottled Zone Event". *Earth Planet. Sci. Lett.* 39: 179-192.

Matthews, A., Gross, S., 1980. Petrologic evolution of the 'Mottled Zone' (Hatrurim) metamorphic complex of Israel. *Isr. J. Earth Sci.* 29, 93-106.

Mendoza, C., 2010. Caractérisation et comportement sous irradiation de phases powellites dopées terres rares – Application au comportement à long terme des matrices de confinement des déchets nucléaires. Univ. Lyon. Thèse, 263 p.

Pitty, A.F., (Ed.), 2009. A natural analogue study of cement buffered, hyperalkaline groundwaters and their interaction with a repository host rock IV: an examination of the Khushaym Matruk (central Jordan) and Maqarin (northern Jordan) sites. NDA Technical Report, NDA, UK (in press).

Ron, H., Kolodny, Y., 1992. Paleomagnetic and rock magnetic study of combustion metamorphic rocks in Israel. *J. Geophys. Research.* 97, 6927-6939.

Rosa, D.F., Martin, R.F., 2010. A spurrite-, merwinite- and srebrodolskite- bearing skarn assemblage, west Clearwater lake impact crater, northern Quebec. *Can. Mineral.* 48, 6, 1519-1532.

Sharygin, V.V., Sokol, E.V., Vapnik, Ye., 2008. Minerals of the pseudobinary perovskite-brownmillerite series from combustion metamorphic larnite rocks of the Hatrurim Formation (Israel). *Russian Geol. Geophys.* 49, 709-726.

Sokol, E.V., Maksimova, N.V., Nigmatulina, E.N., Sharygin, V.V., Kalugin, V.M., 2005. *Combustion Metamorphism*. Novosibirsk, Russia, Publishing in House of the Siberian Branch of the Rus. Acad. Sci., 286 p.

Sokol, E.V., Volkova, N.I., 2007. Combustion metamorphic events resulting from natural coal fires. In G.B. Stracher, Ed., *GSA Rev. Eng. Geol. XVIII: Geology of Coal Fires: Case studied from around the world*, 97-115. Geol. Soc. Am., Boulder, Colorado.

Sokol, E.V., Novikov, I., Vapnik, Ye, Shagam, R., Kozmenko, O., 2010. Combustion metamorphic as indicators of fossil mud volcanism: New implications for the origin of the Mottled Zone, Dead Sea rift area. *Basin Research*. 22, 414-438.

Stein, M., 1979. Behavior of uranium during calcinations of phosphates rocks. M. Sc. Thesis, Hebrew Univ. Jerusalem.

Techer, I., Khoury, H., Salameh, E., Rassineux, F., Claude, C., Clauer, N., Pagel, M., Lancelot, J., Hamelin, B., Jacquot, E., 2006. Propagation of high-alkaline fluids in an argillaceous formation : Case study of the Khushaym Matruk natural analogue (central Jordan). *J. Geochem. Exploration*. 90, 1-2, 53-67.

Turner, F.J., 1967. Thermodynamic Appraisal of steps in progressive metamorphism of siliceous dolomite limestones. In: *Jahrbuch f. Mineralogie. Monatshefte* 1, 1-22.

Vapnik, Ye., Sharygin, V.V., Sokol, E.V., Shagam, R., 2007. Paralavas in a combustion metamorphic complex: Hatrurim Basin, Israel. In G.B. Stracher, Ed., *GSA Rev. Eng. Geol. XVIII: Geology of Coal Fires: Case studied from around the world*, 133-153. Geol. Soc. Am., Boulder, Colorado.

Appendix IV. Major and trace element concentrations of the metamorphic rocks.

Samples	Marbles										Black calc-silicate rocks					Green calc-silicate rocks			Paralavas	
	JRD10-62	JRD10-64	JRD10-84A	9502-22	9510-15	JRD10-39A	JRD10-39B	JRD10-44	JRD10-46	JRD10-47	JRD10-54	JRD10-55	JRD10-60	JRD10-61	JRD10-32	JRD10-35	9536-22			
<i>Major and minor elements (wt%)</i>																				
SiO ₂	0.64	3.98	10.21	6.28	7.88	7.68	4.68	4.75	2.72	4.98	36.31	33.79	41.33	40.31	51.82	61.86	54.22			
Al ₂ O ₃	0.17	1.01	3.09	2.61	3.21	3.12	1.71	0.54	0.95	1.57	6.42	6.23	8.61	8.27	8.98	7.39	9.18			
ThO ₂	0.01	0.04	0.13	0.11	0.12	0.12	0.07	0.03	0.04	0.07	0.26	0.23	0.38	0.35	0.41	0.36	0.43			
Fe ₂ O ₃	0.07	0.36	0.93	0.88	1.34	0.81	0.64	0.30	0.38	0.48	1.92	1.78	3.11	2.96	2.92	2.62	3.14			
K ₂ O	0.00	0.00	0.03	0.00	0.00	0.04	0.04	0.00	0.00	0.02	0.17	0.16	1.07	0.47	5.24	1.63	6.02			
MgO	0.98	0.47	0.77	0.65	0.69	0.54	0.47	0.27	0.52	0.64	1.60	1.59	1.75	1.70	4.22	1.91	7.74			
MnO	0.00	0.00	0.00	0.01	0.01	0.01	0.00	0.00	0.00	0.00	0.01	0.00	0.01	0.01	0.01	0.00	0.01			
CaO	54.10	53.82	52.47	53.20	50.04	54.19	55.29	55.14	54.19	54.21	44.94	45.50	35.21	36.96	13.44	13.99	10.55			
Na ₂ O	0.00	0.08	0.16	0.05	0.07	0.12	0.11	0.00	0.06	0.11	0.13	0.11	0.66	0.59	0.13	0.80	0.14			
P ₂ O ₅	2.82	20.17	13.92	2.52	3.96	5.09	3.94	0.95	3.42	7.76	5.40	5.06	4.81	5.09	1.84	1.82	1.91			
PF	39.26	14.44	12.71	32.19	nd	26.50	31.53	36.83	35.33	26.58	2.85	5.83	3.31	3.62	10.78	7.74	6.89			
Total	98.04	94.37	94.43	98.49	67.32	98.22	98.49	98.81	97.61	96.42	100.01	100.29	100.24	100.32	99.78	100.12	100.22			
CO ₂ tot	39.43	14.09	9.31	28.01	23.52	23.61	30.96	36.00	34.55	25.47	0.21	0.38	0.09	0.22	4.53	4.57	0.67			
TOC	0.01	0.01	0.01	0.01	0.02	0.04	0.02	0.01	0.01	0.01	0.01	0.01	0.01	0.01	0.01	0.01	nd			
TS	0.05	0.23	0.48	0.45	1.11	0.17	0.15	0.05	0.19	0.30	0.14	0.32	0.01	0.03	0.01	0.02	nd			
F	0.34	2.35	1.77	0.30	0.45	0.76	0.57	0.11	0.46	0.97	0.52	0.43	0.42	0.45	0.24	0.14	nd			
CaCO ₃	89.51	31.88	21.01	63.62	53.32	53.36	70.24	81.70	78.41	57.76	0.47	0.86	0.20	0.49	10.29	10.38	-			
TOC/TS	0.20	0.04	0.02	0.02	0.02	0.24	0.13	0.20	0.05	0.03	0.07	0.03	1.00	0.33	1.00	0.50	-			
<i>Trace elements (ppm)</i>																				
As	20.10	68.69	22.09	16.75	113.90	9.64	21.34	2.94	8.83	7.80	12.40	7.70	2.91	5.61	4.73	22.09	0.00			
Ba	25.36	868.90	269.70	2362.00	242.00	330.80	206.90	84.06	59.09	193.20	57.56	55.37	70.82	70.77	374.90	42.30	285.70			
Bi	0.00	0.00	0.58	0.00	0.00	0.00	0.27	0.00	0.00	0.29	0.00	0.00	0.00	0.00	0.11	0.00	0.00			
Cd	101.30	136.90	406.60	0.17	1.57	5.93	46.18	0.30	35.70	563.30	51.50	31.06	8.40	28.54	15.93	83.46	6.90			
Co	0.80	1.59	2.77	2.63	6.65	3.03	1.75	1.17	1.21	1.62	4.01	3.85	6.98	6.69	6.49	5.19	6.45			
Cr	119.90	1069.00	2019.00	702.80	900.30	818.60	951.70	156.10	618.00	1236.00	692.00	701.70	881.90	925.60	627.10	451.10	653.60			
Cu	17.77	67.86	277.50	69.47	130.60	85.10	87.16	36.39	84.64	137.30	88.66	88.66	158.90	172.10	33.89	77.84	160.40			
Mo	5.53	13.17	30.77	9.03	426.40	63.88	17.32	0.00	9.89	13.14	177.60	155.70	153.60	268.30	40.15	948.50	82.69			
Ni	37.97	375.80	456.60	179.10	584.70	365.00	252.70	78.11	229.30	323.40	195.60	199.60	370.40	391.50	200.40	182.20	241.60			
Pb	0.90	7.35	16.68	2.11	4.21	0.94	9.97	0.00	0.00	14.09	1.99	1.54	1.30	2.45	5.79	6.95	3.90			
Sr	941.60	1707.00	1381.00	1682.00	1569.00	1449.00	1533.00	1055.00	1337.00	1586.00	1318.00	1222.00	1352.00	1599.00	1802.00	695.70	1211.00			
Th	0.13	0.75	3.67	1.54	1.76	1.77	1.14	0.32	0.68	1.01	3.58	3.34	4.70	4.65	4.15	2.25	4.21			
U	7.90	67.58	133.60	25.16	104.80	57.33	34.61	3.00	33.18	39.99	41.06	38.19	43.77	45.09	23.07	458.80	30.82			
V	107.70	687.50	706.00	154.90	980.40	189.80	235.90	34.39	247.70	304.10	717.40	638.90	792.90	731.00	287.80	332.80	318.20			
Zn	263.00	1878.00	2351.00	514.10	2344.00	1134.00	806.40	154.30	854.30	1260.00	893.20	856.20	1528.00	2040.00	692.50	424.30	549.40			

Chapter V

Supergene uranium mineralization

This section is devoted to the superficial weathering of the rocks and to the associated uranium mineralization in the Belqa Group (MCM) in central Jordan to determine the processes causing the formation of the uranium-enrichment mineralization in the weathered zone. The weathered carbonate rocks are not quartz-feldspar clasts cemented by a carbonate precipitate, but correspond to partly decarbonated limestones showing sometime calcite recrystallization. The profiles in the weathered carbonates are not comparable to the classical Namibian or Australian calcretes.

1. SUPERGENE MINERALIZATION IN CENTRAL JORDAN

1.1. Previous studies

Pleistocene uranium calcrete type was reported by Dill (2011) in the north and central Jordan and in Syria. Hexavalent uranium minerals (carnotite $K_2(UO_2)_2(VO_4)_2 \cdot 3H_2O$, tyuyamunite $Ca(UO_2)_2(VO_4)_2 \cdot H_2O$, bayleyite $Mg_2(UO_2)(CO_3)_3 \cdot 18(H_2O)$, rauvite $Ca(UO_2)_2(V_{10}O_{28}) \cdot 16H_2O$, zellerite $Ca(UO_2)(CO_3)_2 \cdot 5H_2O$, autunite $Ca(UO_2)_2(PO_4)_2 \cdot 10-12H_2O$, saleeite $Mg(UO_2)_2(PO_4)_2 \cdot 10H_2O$) have also been described to the North of the Negev and the Judean desert in Israel (Gross and Ilani, 1987; Ilani and Strull, 1988). Gross and Ilani (1987) consider that the Senonian-Palaeocene phosphated formations are the source rocks of these minerals. The leaching of these rocks by meteoric waters would have allowed the transport of uranium and its reconcentration by evapotranspiration in a similar way as in the calcrete type uranium deposits.

1.2. Localisation

The uranium mineralization in central Jordan extends over 40 km². The mineralization is preferentially located on the lower topographical slope of the marbles of the MCM Formation which form topographic highs because of their better resistance to weathering. 10 samples of mineralized rocks have been selected (Fig.V.1). Four samples (JRD10-41/92/9542-5/9542-9) come from the NRA (Natural Resources Authority) trench which is the reference trench for this government agency and AREVA Company. Three samples (JRD10-89/90/91) were collected in the T21 trench (Fig.V.2), and three samples (JRD10-95/94/93) were collected in the T07 trench (Fig.V.3), both along vertical profiles up to 3 m deep.

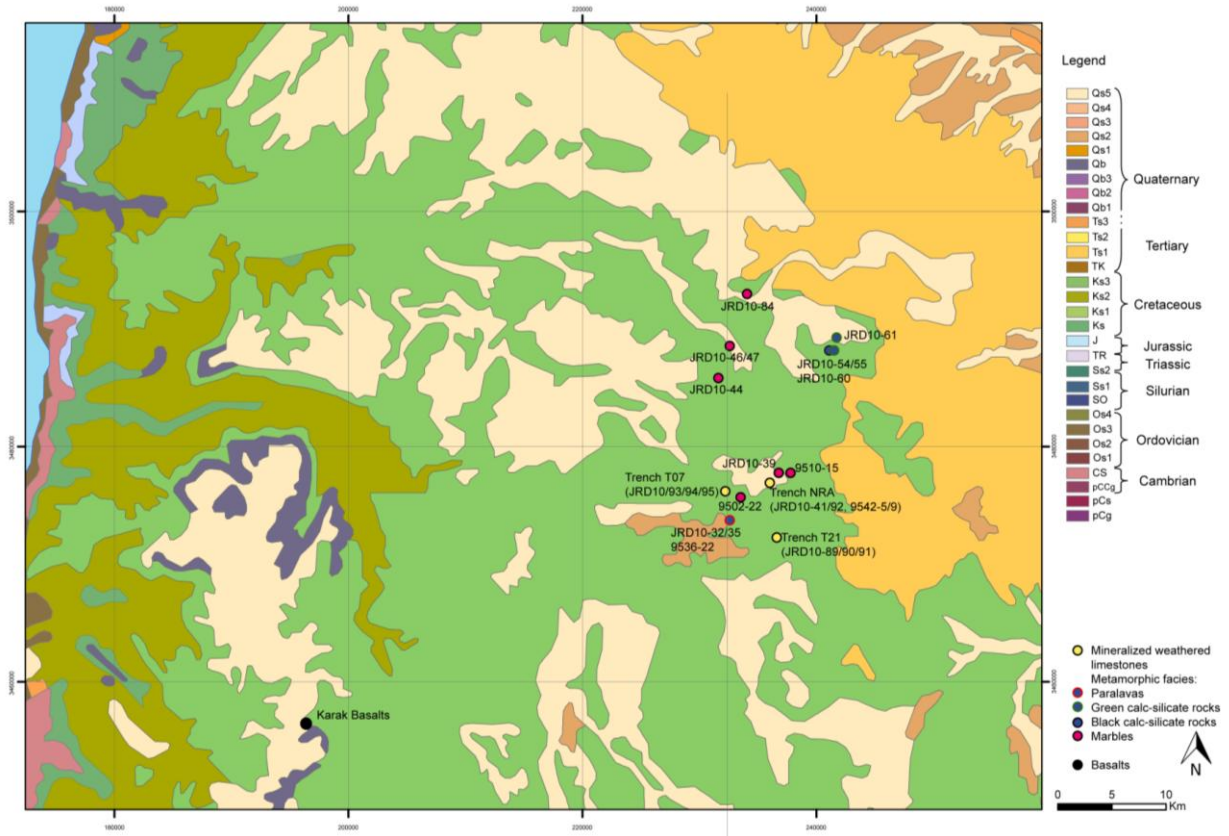


Figure V. 1. Geological map of the study area and location of the supergene samples against the metamorphic facies



Figure V. 2. Trench T21 (L:200m, w:1.5, d:3m)



Figure V. 3. Trench T07 (L:200m, w:1.5, d:3m)

2. MINERALIZED LITHOLOGICAL UNITS

2.1. Petrography

The lithological units hosting the mineralization correspond to weathered beige-grey fine-grained limestones (Fig.V.4a,b). They are highly porous and permeable. The friability and the softness of these rocks does not permit easy preparation of thin sections. They are mainly represented by altered corroded calcite (irregular surfaces and xenomorphic phases) (Fig.V.4) and some altered phosphates associated with clay minerals of smectite type. Altered phosphates, carbonate-fluorapatite, occur as aggregates of small crystals showing corrosion features, sometimes surrounded by clay minerals (Fig.V.4c,d,e). Newly formed minerals are crystallized in the porosity of the rock: calcite, fluorite, sulfato-phosphates, uranyl vanadates (tyuyamunite and strelkinite), and some gypsum. Fluorite crystals (Fig.V.4f,g,h) are associated with the secondary calcite crystals or occur in the porosity of the dissolved calcite crystals. Also fibrous fluorite is finely associated with micro fibrous uranyl vanadates of strelkinite type with some trace of Ca (Fig.V.4i,j,k). Other uranyl vanadates (pure strelkinite or tyuyamunite with some Na traces) occur as independent fibrous aggregates forming circular masses in the porosity (Fig.V.4l,m,n). Newly formed phosphates are acicular idiomorphic crystals of Na-sulfato phosphates forming rosettes (Fig.V.4o). Barite occurs as aggregate of prismatic crystals associated with uranyl vanadates (Fig 4p). Some clayey aggregates contain clasts of ilmenite, rutile, quartz, calcite and micrograins of florencite and ilmenite. Fe-Ti-V oxides occur in association with clay minerals in the porosity of calcite as micrograins aggregates (Fig.V.4q). Also, this phase occurs as independent micrograins disseminated in clay minerals.

X-ray diffraction analyses have shown the presence in some samples of quartz (JRD10-89/90/91/95), ettringite (JRD10-92/94), palygorskite ($(\text{Mg};\text{Al})_2\text{Si}_4\text{O}_{10}(\text{OH})^2_4\text{H}_2\text{O}$, fibrous magnesian clay), kaolinite, illite, chlorite, dolomite (Mg-carbonate), ankerite (CaFe-carbonate), antigorite/chrysotile (Mg-silicate), albite (JRD10-95).

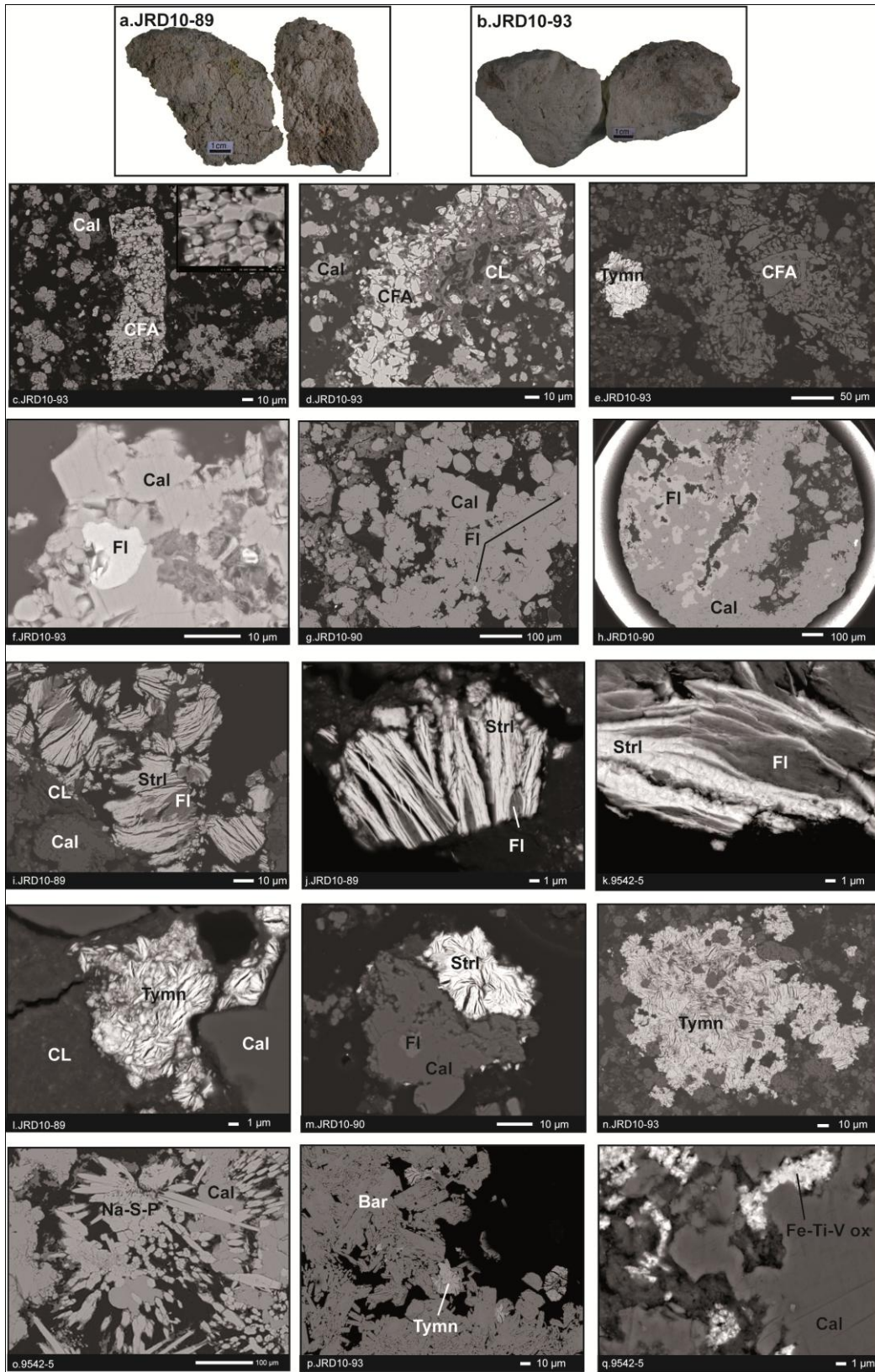


Figure V. 4. Macroscopic and microscopic views of the weathered limestones (Bar: barite, Cal: calcite, CFA: carbonate-fluorapatite, CL: clay minerals, Fl: fluorite, Na-S-P: Na-sulfato-phosphates, Tymn: tyuyamunite, Strl: strelkinite).

2.2. Geochemistry

2.2.1. Major and trace elements

Whole rock element analyses are given in appendix V. (p. 182).

The ternary diagrams in figure V.5 show the chemical compositions of the weathered limestones and the evolution of their compositions along the two trench profiles. Calcium carbonate ($62.51 < \text{CaCO}_3 < 80.85$ wt %) is the main constituent of the weathered limestones which are located near the calcite end member in the ternary diagrams. The presence of some alumina ($1.32 < \text{Al}_2\text{O}_3 < 3.42$ wt %) reflects the presence of small amounts of montmorillonite-illite \pm palygorskite confirmed by their high silica content ($4.97 < \text{SiO}_2 < 13.29$ wt %). Silica is also present in other phases such as rare silicates (Al; Mg) and quartz. The phosphate concentrations are low and variable ($0.31 < \text{P}_2\text{O}_5 < 3.36$ wt %) similar to those of the limestones and some of the marbles, but lower than some pyrometamorphic rocks in the area which can have up to 20.17 wt % P_2O_5 . The high Ignition Loss ($35.69 < \text{LOI} < 40.65$ wt %) is due to the presence of Ca-carbonates, the organic matter content being very low in these limestones ($0.02 < \text{C}_{\text{org}} < 0.06$ wt %). Sulphur ($0.07 < \text{S} < 1.34$ wt %) and fluorine ($0.11 < \text{F} < 1.12$ wt %) are respectively hosted by the sulfato-phosphates and sulfates (barite and gypsum), and fluorite crystals.

The weathered limestones are still significantly enriched in redox sensitive elements: Cr ($40 < \text{Cr} < 443$ ppm), Cu ($20 < \text{Cu} < 156$ ppm), Ni ($35 < \text{Ni} < 430$ ppm), U ($10 < \text{U} < 1046$ ppm), V ($53 < \text{V} < 430$ ppm), and Zn ($92 < \text{Zn} < 1251$ ppm). All these concentrations are higher than those of the limestones except for Cr.

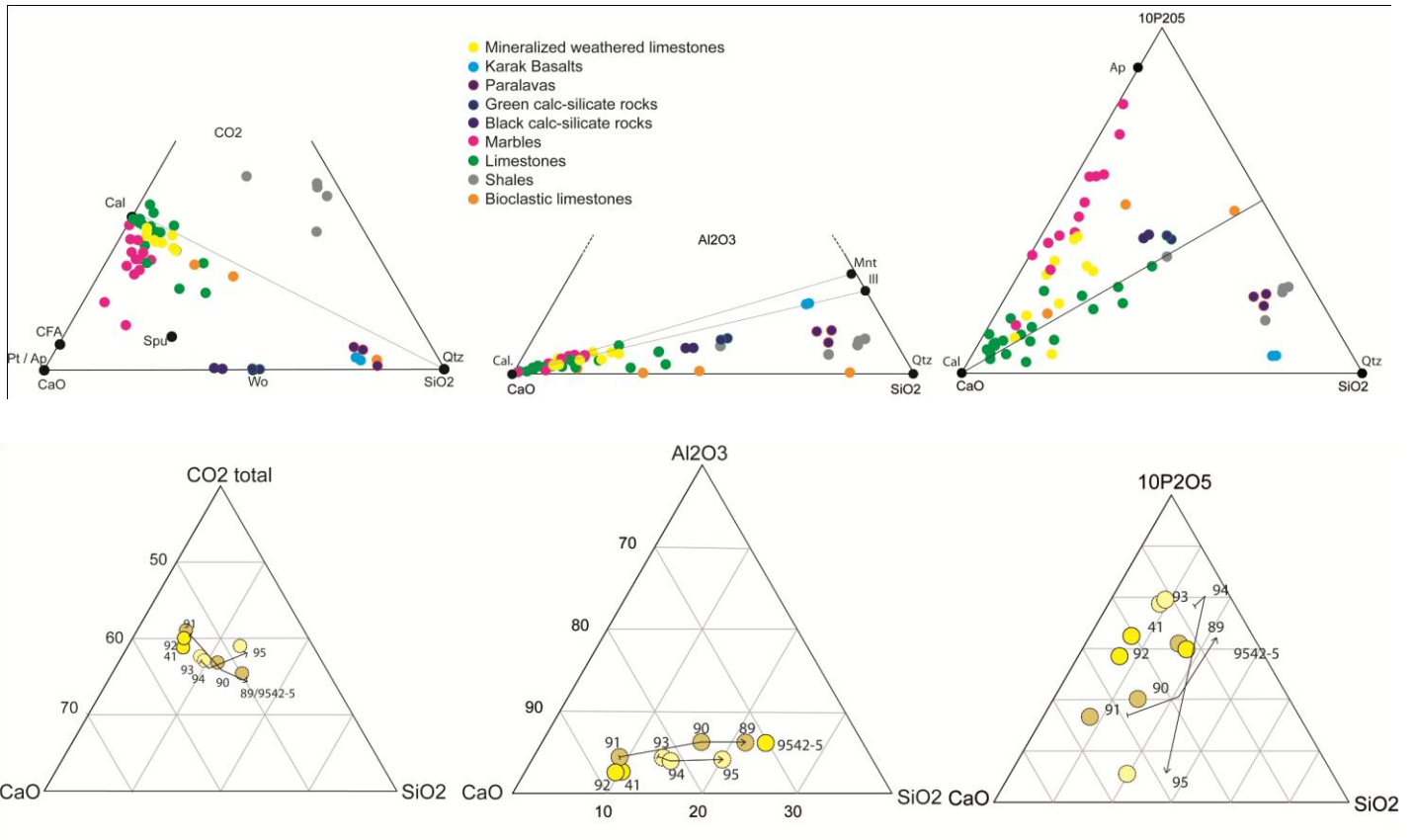


Figure V. 5. General ternary diagrams and diagrams showing the evolution of samples of two trenches T21 (top to bottom: JRD10-89/90/91) and T07 (top to bottom: JRD10-95/94/93). See Appendix V for sample depths. (Ap: apatite, Cal; calcite, CFA: carbonate-fluorapatite, Ill: illite, Mnt: montmorillonite, Qtz: quartz, Spu: spurrite, Wo, wollastonite).

2.2.2. Rare earth elements

The average non altered limestone-normalized REE patterns of the weathered limestones show different types of patterns (Fig.V.6). All the weathered limestones have higher REE contents than the average of the non altered facies. JRD10-41/92 and 9542-5 from the NRA trench present the same pattern with reverse fractionation ($0.76 < \text{LaN/YbN} < 0.78$) and a significant cerium anomaly ($0.79 < \text{Ce/Ce}^* < 0.87$), despite their normalization to the average non weathered limestone. This means that these samples have been enriched more strongly in the heaviest REE during the alteration with an enhancement of the cerium anomaly.

The samples from the two trenches show opposite behaviors. In the trench T21, the three samples present non fractionated patterns relative to the non-altered protolith reflecting the same REE fractionation that is seen in the non-altered limestones. JRD10-89, at the top of the profile, presents the highest global REE enrichment relative to the average non-weathered limestone, and JRD10-91, at the base, shows the lowest REE enrichment. In the trench T07, the patterns are more fractionated and present a reverse fractionation. JRD10-95, at the top of the profile, have the lowest REE content, except for cerium which presents an important positive anomaly ($Ce/Ce^*=1.42$) and present a normal fractionation ($LaN/YbN=1.29$). JRD10-93, at the base of the profile, shows a reverse fractionation ($LaN/YbN= 0.67$) with a negative cerium anomaly ($Ce/Ce^*=0.76$). JRD10-94, in intermediate position, presents a pattern similar to that the basal weathered limestone JRD10-93, with also a similar cerium anomaly of 0.78 and LaN/YbN of 0.75.

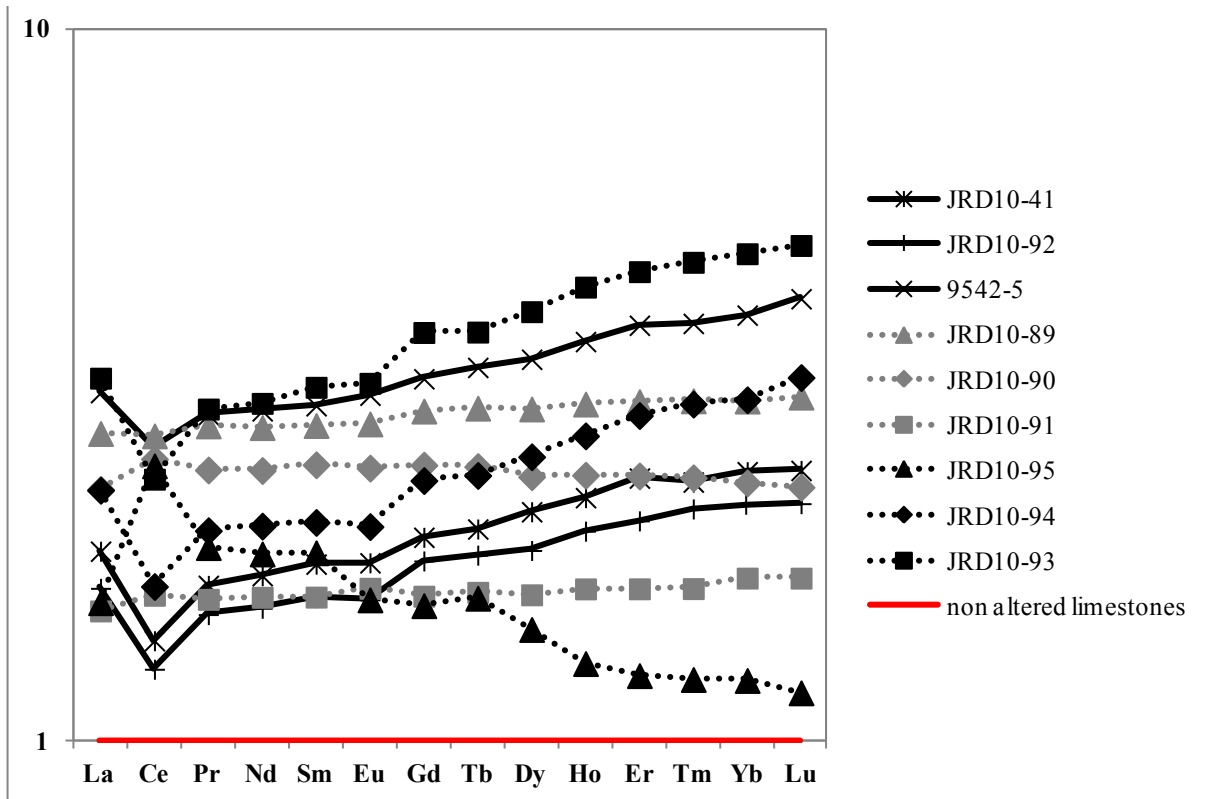


Figure V. 6. Average non altered limestones-normalized spectra of the weathered limestones.

2.2.3. Evolution along the trench profiles T21 (JRD10-89/90/91) and T07 (JRD10-95/94/93)

The diagrams in figure V.5 and V.7 show the evolution of the major and traces elements across the profile T21. The decrease of calcium (46→43→41 wt %) and CO₂ (36→30→29 wt %) contents from the bottom to the top of the trench T21 reflects a significant dissolution of the carbonates. Higher sulphur contents (JRD10-89/90) reflect the new formation of gypsum as observed in JRD10-89 (top of the trench) and especially in JRD10-90 (from intermediate depth), which contain also subidiomorphic to idomorphic secondary calcite crystals. Phosphates (1←1.30←2.4 wt %), and fluorine (0.15←0.43←0.61 wt %) are enriched toward the surface. Fluorite and carbonate-fluorapatite are more abundant toward the surface. The upward increase in alumina (2.30←3.38←3.42wt %) and silica (5←9←12 wt %) reflects the enrichment in clay minerals. Uranium (25<172<600 ppm) and barium also show an upward increase of their concentrations indicating an important crystallization of uranyl vanadates at the top of the trench in association with barite. Arsenic, copper and zinc increase too but we have no specific mineral phases illustrating this trend; these elements are probably associated with clay minerals. The variation in metals possibly reflects original variations in the protoliths.

As shown in the previous section, the REE concentrations are the highest at the top of the profile and decrease toward the base of the profile.

Across the T07 profile (Fig.V.5 and V.8), calcium and alumina concentrations are nearly constant. Silica increases (7,7<8<12 wt%) toward the surface, in contrast with the phosphate (3,35>3,36>0,31 wt% P₂O₅) and the fluorine (0.64>1.12>0.11 wt% F) which shown an important decrease of concentration from intermediate depth to the top. Contrary to the T21 trench profile, uranium (1046→24→10 ppm) and vanadium (430→205→53 ppm) concentrations decrease from the base to the top of the profile reflecting higher uranyl vanadates and Cu, Cr, Mo, Ni, REE at the base of the profile whereas barium which is concentrated to the top of the profile as barite crystals.

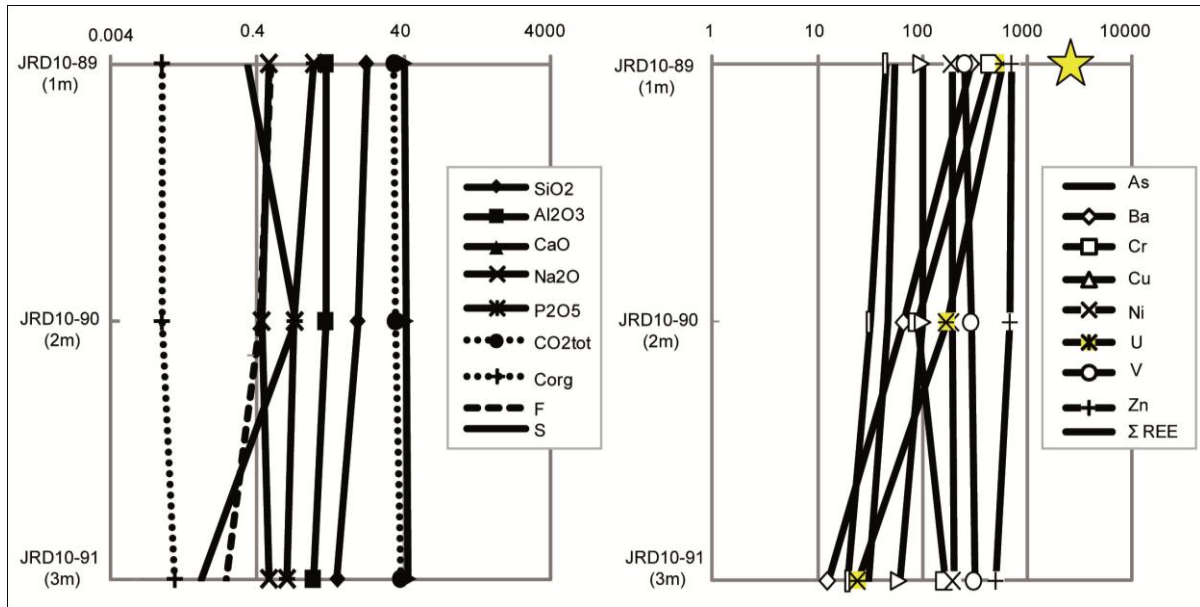


Figure V. 7. Profile of geochemical evolution for trench T21 (JRD10-89/90/91).

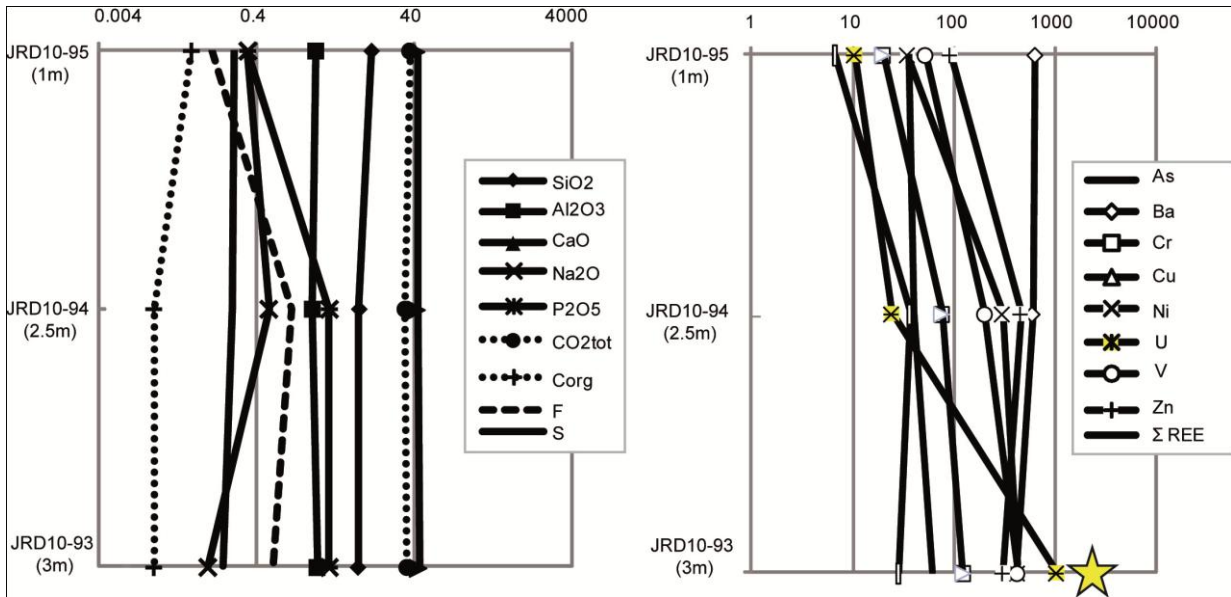


Figure V. 8. Profile of geochemical evolution for trench T07 (JRD10-95/94/93).

3. MINERALIZATION OF THE SUPERGENE LIMESTONES

3.1. Petrography

The uranium minerals have a variable composition between the tyuyamunite ($\text{Ca}(\text{UO}_2)_2\text{V}_2\text{O}_8 \cdot 5-8(\text{H}_2\text{O})$) and the strelkinite ($\text{Na}_2(\text{UO}_2)_2\text{V}_2\text{O}_8 \cdot 6(\text{H}_2\text{O})$) end members (Fig.V.9), with some traces of a carnotite component (up to 1.35 wt % K_2O). Strelkinite occurs as splinters or fibrous aggregates finely associated to fluorite. Tyuyamunite occurs as amassed fibrous aggregates associated with the clay minerals or simply around the calcite in the porosity of the weathered limestones. In the trench T21, the top of the profile (JRD10-89) has the higher U content present under the both form. In the trench T07, the base of the profile (JRD10-93) has the highest U content occurring as tyuyamunite aggregates. The figure 9 shows that the mineralization of the weathered limestone 9542-5 (which contain the Na-sulfato phosphates) has the closest composition to the Na_2O pole reflecting the presence of only strelkinite associated with fluorite. These observations show the correlation between strelkinite crystallization and fluorite which require the availability of Ca, and prevent the tyuyamunite formation. The tyuyamunite had incorporated Ca which has prevented the fluorite formation.

Uranium ($47.22 < \text{U} < 56.82$ wt %) and vanadium ($11.53 < \text{V} < 13.53$ wt %) contents show a positive correlation (Fig.V.10). The uranyl vanadates have higher V and U contents than the pure poles ($11.03 < \text{V} < 11.3$ wt %, $51.52 < \text{U} < 52.77$ wt %). Uranyl vanadates in classical calcrete deposits, are close to the potassium oxide end member, carnotite (Fig.V.11).

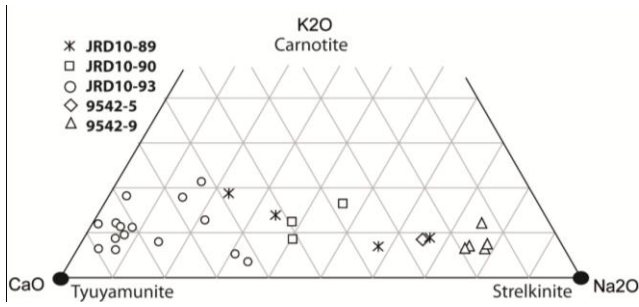


Figure V. 9. K₂O-CaO-Na₂O diagram.

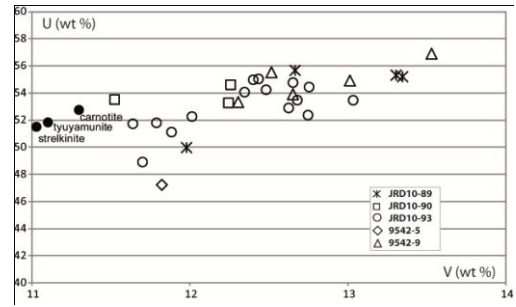


Figure V. 10. U – V diagram.

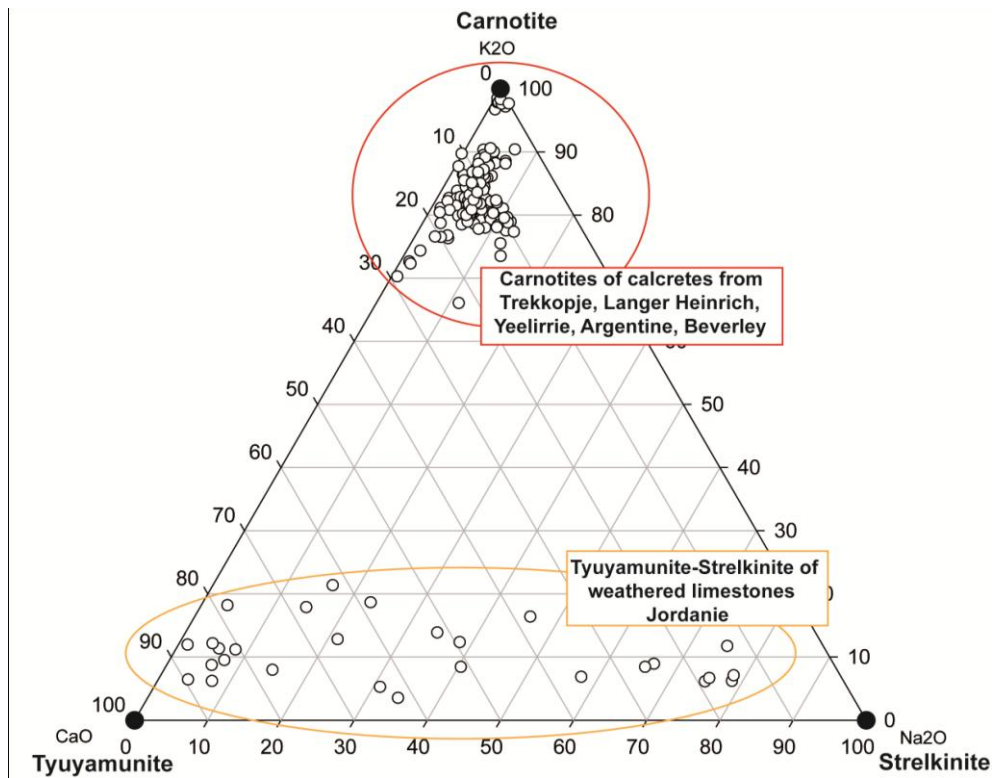


Figure V. 11. K₂O-CaO-Na₂O diagram. Comparison with the calcrete mineralization.

3.2. U and REE content

Uranyl vanadates have been analyzed by LA-ICP-MS to determine their REE contents. The whole rocks-normalized patterns of uranyl vanadates (Fig.V.12) are different from those of their weathered hosts. The REE patterns of the uranyl vanadates are more fractionated, richer in heavy REE ($0.005 < \text{LaN/YbN} < 0.8$) and are poorer in light REE except for cerium. All

the uranyl vanadates present a positive cerium anomaly ($3.78 < Ce/Ce^* < 314$). The highest REE content are observed in the uranyl vanadates from the weathered limestones JRD10-93 (ΣREE maximum= 436 ppm) and 9542-9 (ΣREE maximum= 341 ppm). These two host rocks have a slightly higher REE contents but mostly higher U concentrations (respectively 1046 and 1007 ppm U).

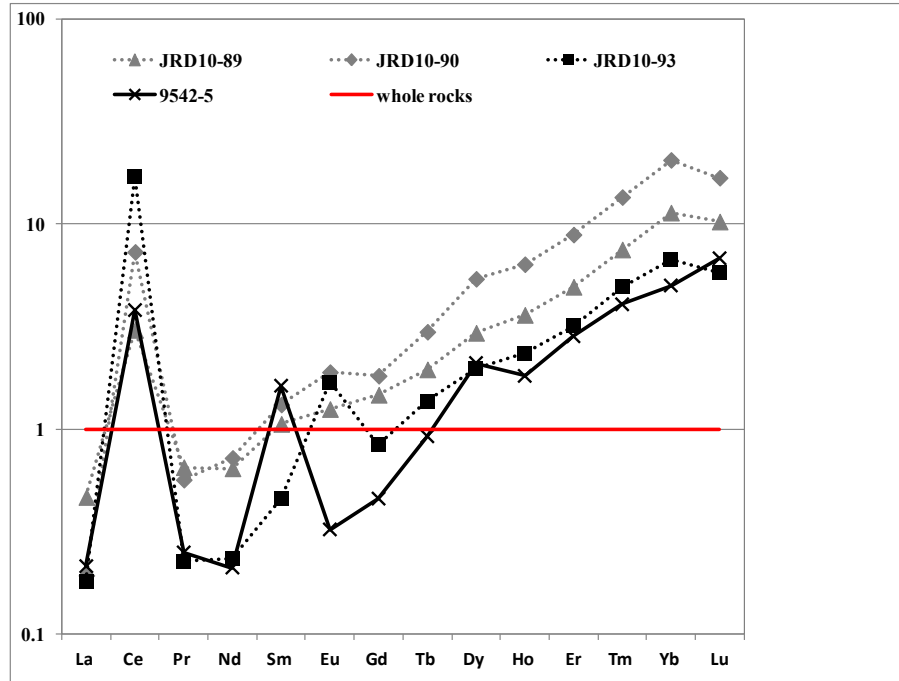


Figure V. 12. Whole rocks-normalization patterns of the U mineralizations.

4. VOLUME LOSS / MASS BALANCE

The isocon diagram is a simple graphical solution to the Gresen's equation (1967) rewritten by Grant (1986). This method permits to estimate the changes of mass, volume or concentration in mass transfer. The equation $Ca_i = (Mo/Ma) Co_i + \Delta C_i$ allows us to construct the diagram by plotting an altered composition (Ca) against an original composition (Co). C represents the concentration (wt% or ppm), i: the element, a: the altered rock, o: the referent rock, M: mass, ΔC : concentration change of the element i. The immobile elements during the process define the isocon 1:1 which is a straight line through the origin. The concentration variation (% gain or loss) corresponds to the difference between the element of coordinates (Co, Ca) and the isocone 1:1. Isocon diagrams permit to show the evolution of the elements along the alteration profile of the two sampled trenches T21. Numerous tests made to find the

adequate protolith allowed to select two referent rocks: the limestone JRD10-23 for the trench T21, and the limestone JRD10-58 for the trench T07. The immobile elements chosen for the isocons are Al_2O_3 , TiO_2 , Th, and Ta.

4.1. Trench T21 (JRD10-89/90/91)

The different isocon diagrams in figure V.13 show the elementary evolution along the vertical profile up to 3 m of depth. The 3 samples collected have immobile elements concentrations consistent with themselves along the profile and with the hypothetical protolith chosen. The profile presents a constant volume for the basal horizon (JRD10-91), in contrast with the intermediate and the upper horizons (JRD10-90/89) which show a volume loss about 50-70 % corresponding to the dissolution of the carbonates. The redox sensitive elements (mainly Zn and Cr), U, Y, and REE are more enriched at the top of the profile. However, the REE are not mobile, not fractionated, and stay along the isocon which confirm the REE patterns in figure V.6.

horizon to the reverse of the preceding profile. All the REE are enriched at the base of the profile except Ce and this increase is higher for the heavy REE. The basal horizon (JRD10-93) presents florencite crystals (REE, aluminium-phosphate) which may result from the leaching of the REE from the top of the profile.

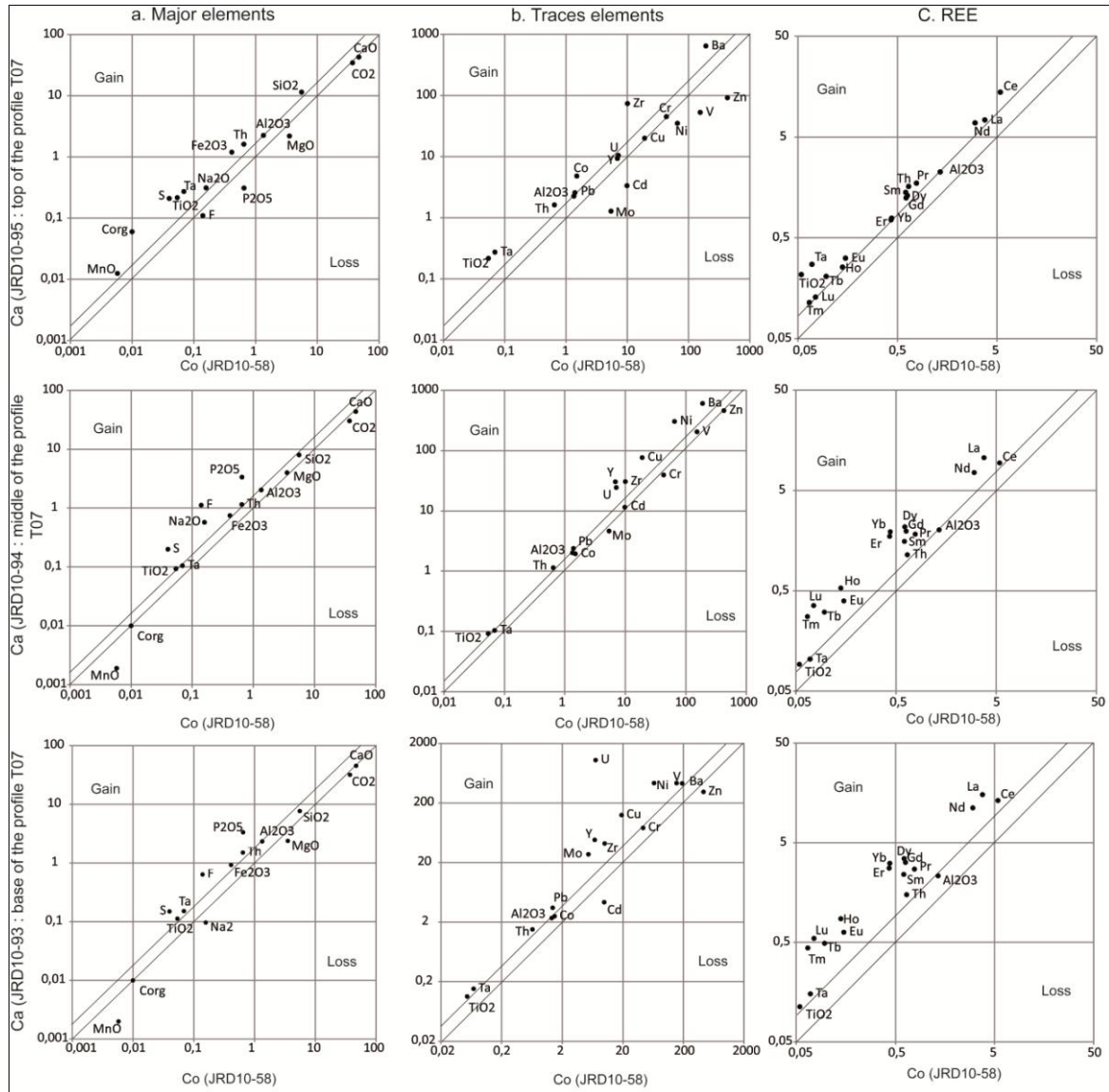


Figure V. 14. Isocons of the trench T07.

To summarize, these two trenches show opposite behavior, probably corresponding to two fluid circulation types. The trench T21 presents a loss of carbonate and an enrichment of trace elements and REE toward the surface. This phenomenon was probably controlled by capillary ascension of the solution and by evaporation as in classical calcretes ('per ascensum

mechanism’?; Goudie, 1983). In trench T07, the elements were gradually concentrated by leaching from the upper horizons to enrich the lower horizons (‘per descensum mechanism’?). The diagrams in figure V.15 illustrate these two opposite behaviors. It would have been interesting to have had the possibility to study more profiles to evaluate the frequency of each type of profile or if they represent different levels of erosions in a thicker alteration profiles.

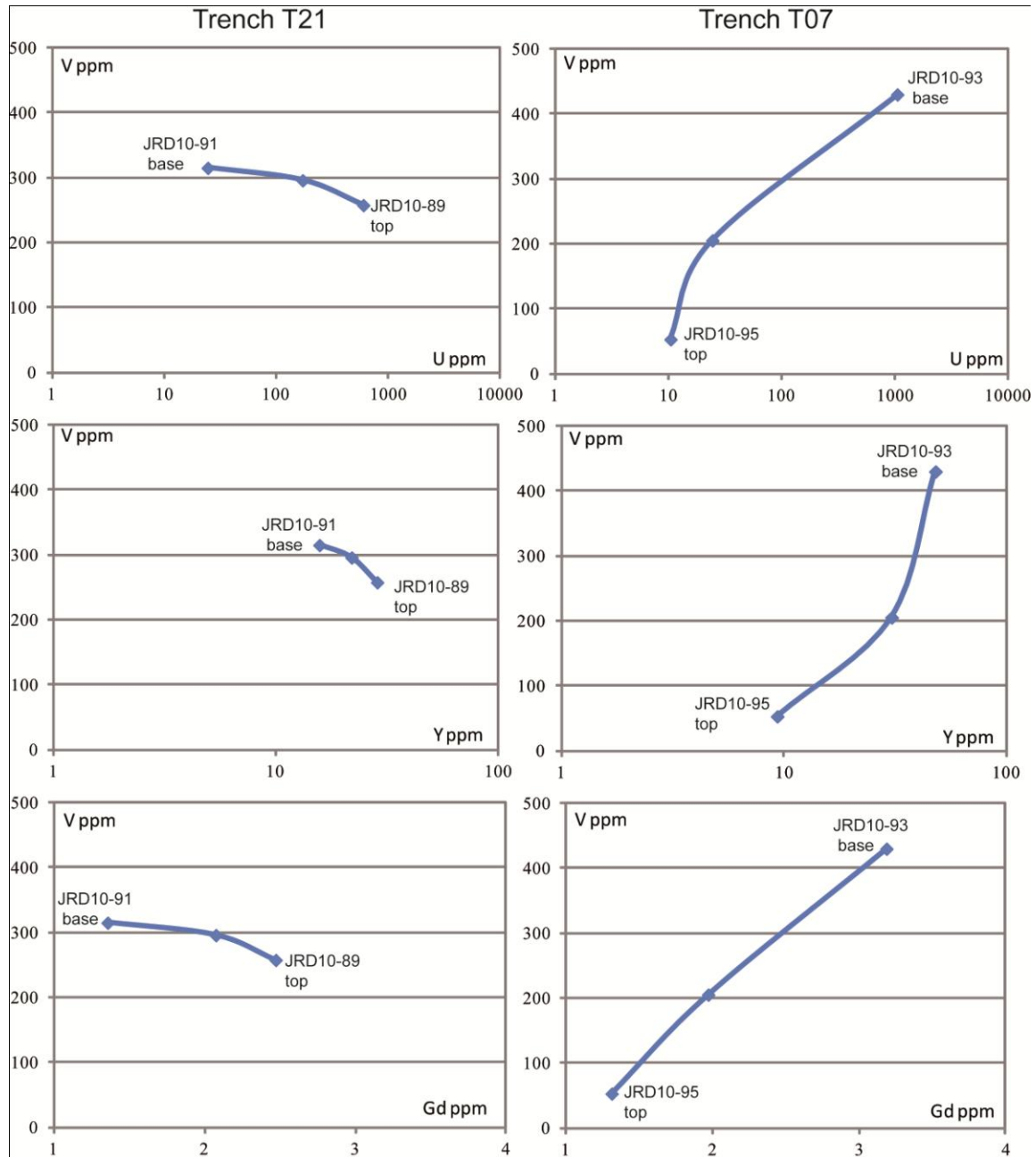


Figure V. 15. V - U, Mo, Gd. Example of the compositional evolution along the two vertical profiles T21 and T07.

5. FORMATION PROCESS OF THE SUPERGENE MINERALIZATION

5.1. Origin of the uranium mineralization

5.1.1. Uranium source

Several uranium sources have been identified in the Siwaqa area:

(i) The largest amount of uranium is associated with the phosphates which are present in variable concentration in most of the lithologies. Uranium substituted for calcium in the lattice of the biogenic carbonate-fluorapatites (CFA) formed by absorption of P present in the ocean by marine organisms to be decomposed at their death and deposited on the sea floor. Phosphogenesis was promoted by the great upwelling event at the southern margin of the Neo-Tethys Ocean during the Late Cretaceous (Chapters 2 and 3). However, the liberation of uranium from apatite needs the alteration of the apatite structure, which has occurred by several processes,

(ii) U was also formed as U-oxides adsorbed on the clay minerals and organic matter in the black shales deposited in restricted anoxic basins. The uranium content can be very high and is easily leachable, because it is mostly hosted as uranium oxides. However, the volume of these rocks which may have been exposed in the Siwaqa area is probably very limited.

(iii) The pyrometamorphism induced by the combustion of organic-rich layers led the decarbonation of the rocks, and to the destabilization of the CFA structure and finally to the liberation of U from the apatite structure. This uranium is reconcentrated in the form of micrometric uranium oxides crystals which represent an additional possible U source for the surficial deposits.

(iv) Weathering processes of the apatite from the different lithologies have been outlined in the Chapter 3. The supergene alteration of the carbonate-fluorapatites also led the liberation of U(4) oxidized in U(6) with the new formation of Na-sulfato-apatite and fluorite.

5.1.2. Vanadium source

Shales (up to 1041 ppm V) and metamorphic rocks (up to 980 ppm V) are the richest in vanadium, but the carbonates may have also up to 358 ppm V. In shales, vanadium is associated with organic matter, Fe oxides, probably clay minerals and can be present as traces in the phosphates. The marbles show a positive correlation P₂O₅-V (Fig.V.16) reflecting that

this element is probably at least partly carried by the carbonate-fluorapatite as for uranium. Carbonate-fluorapatite of the marbles contain between 0.047 to 0.50 wt% V as determined by electron microprobe analyses. However, no vanadium has been determined by LA-ICP-MS and no vanadiferous phase has been identified in these rocks. Hence, the alteration of CFA can be a source of vanadium and uranium. However, the main vanadium source is probably the bituminous layers where vanadium, like uranium, is disseminated in association with the organic matter.

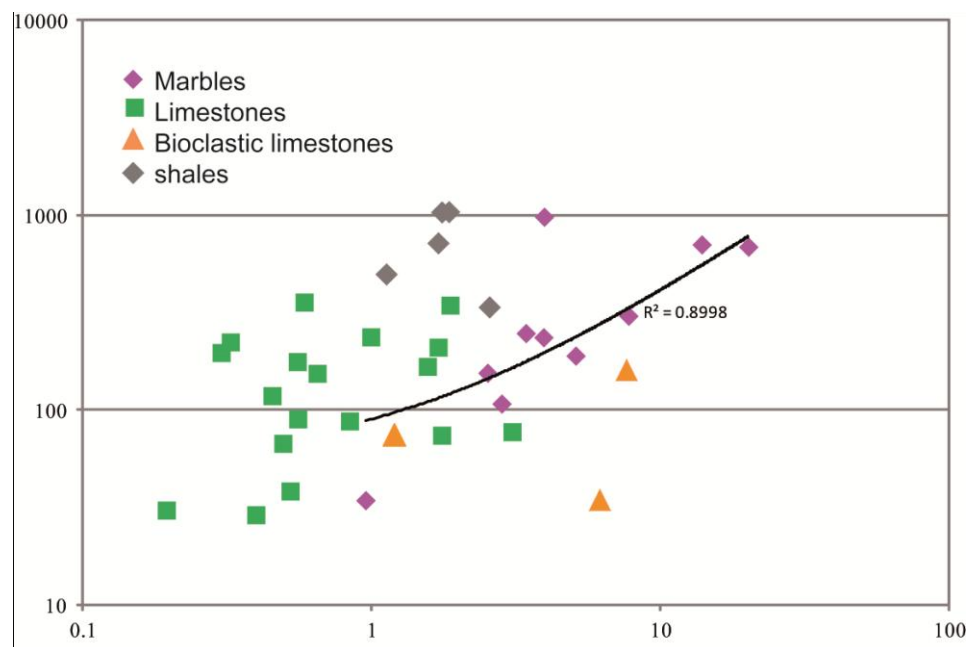


Figure V. 16. V- P₂O₅ diagram. Marbles present a coefficient correlation of 0.9 (without the sample with the higher V content).

5.1.3. Uranium and vanadium transport and deposition

As shown in Chapters 2 and 3, uranium is initially dominantly hosted by the carbonates-fluorapatites of the Maastrichtian-Palaeocene phosphatic limestones of the Belqa Group and by the organic matter and clay minerals of the shales. The pyrometamorphism and the supergene alteration allowed his liberation from the apatite structure and its reconcentration as micrometric inclusions of uranium oxides. Then, the uranium and vanadium from topographically higher marbles have been leached by meteoric waters which have migrated to the porous units.

The speciation of U and V depends of the oxidation state (fO_2) of the fluid, its pH and the nature of the available ligands. To understand the transport and the deposition of uranyl vanadates it is necessary to know the speciation of uranium and vanadium, the nature of the fluid, its pH and its oxidation state.

In the case of the surficial mineralization of the Siwaqa area, the conditions were the following:

- Low temperature meteoric water;
- Initially in equilibrium with the oxygen of the atmosphere and therefore highly oxidized, with redox conditions above the hematite-magnetite buffer conditions;
- In these conditions, uranium occurs as the hexavalent uranyl ion UO_2^{2+} (Fig.V.17a);
- Carbon dioxide from the atmosphere was dissolved in the water giving a slightly acidic pH (5,65 for $pCO_2=3,5$).

In the Siwaqa area, meteoric fluids have leached the different lithologies from which uranium was available and especially the marble which contain carbonate-fluorapatite. The figure V.17b show that the phosphate-bearing rocks may improve the transport of U^{6+} because of the PO_4^{2-} , CO_3^{2-} , F, Cl ions may have acted for complexing the UO_2^{2+} . But all these anions do not complex the uranyl ions in the same pH conditions.

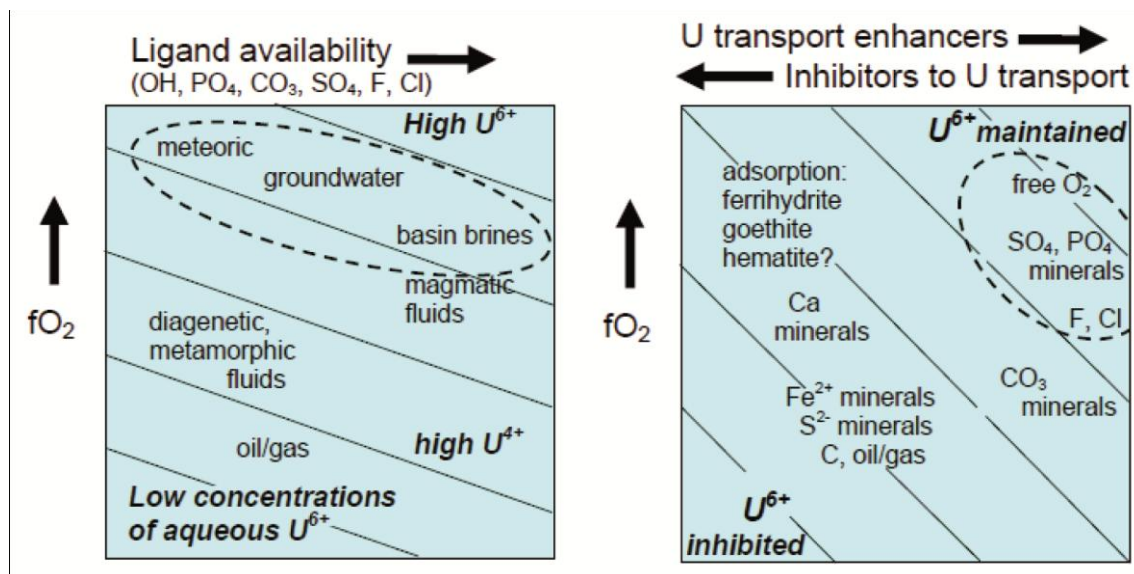


Figure V. 17. Parameters on U solubility. a. Fluid source parameters, b. fluid pathway parameters (Skirrow et al., 2009).

In oxidizing fluids and low temperatures, the nature of the uranyl complexes depend of the fluid pH (Fig.V.18): uranyl sulfate UO_2SO_4 for acidic conditions, uranyl phosphate $UO_2(HPO_4)_2$ for near neutral pH, and carbonates $UO_2(CO_3)_3^{4-}$ for alkaline fluids.

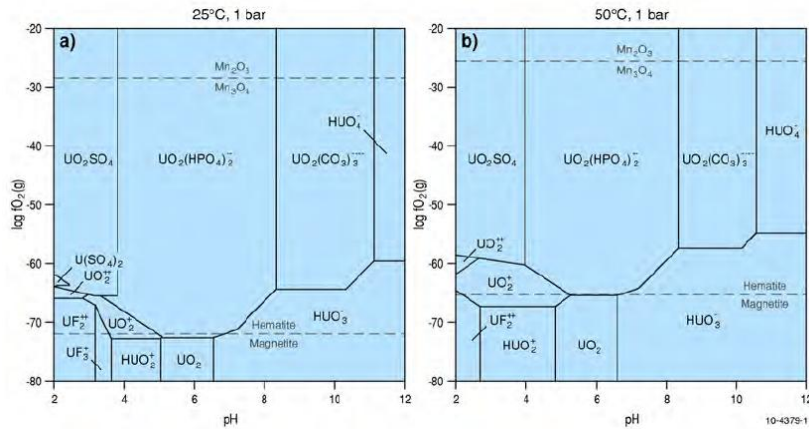


Figure V. 18. Log fO_2 -pH diagrams. Diagrams show dominant aqueous species of uranium in atmospheric conditions. Dashed lines marked Mn_3O_4/Mn_2O_3 and Hematite/Magnetite show the position of fO_2 buffers (Bastrakov et al., 2010).

The speciation of vanadium (Fig .V.19) depends also of the oxidation state and the pH of the fluid. For a oxidized meteoric fluid, vanadyl sulfate $VOSO_4$ (tetravalent) is dominant for acidic pH, hydroxyl vanadate VO_3OH^- (pentavalent) is the dominant complex for neutral to alkaline pH, and $H_2VO_4^{4-}$ is dominant species for intermediate for pH of 4 to 7.

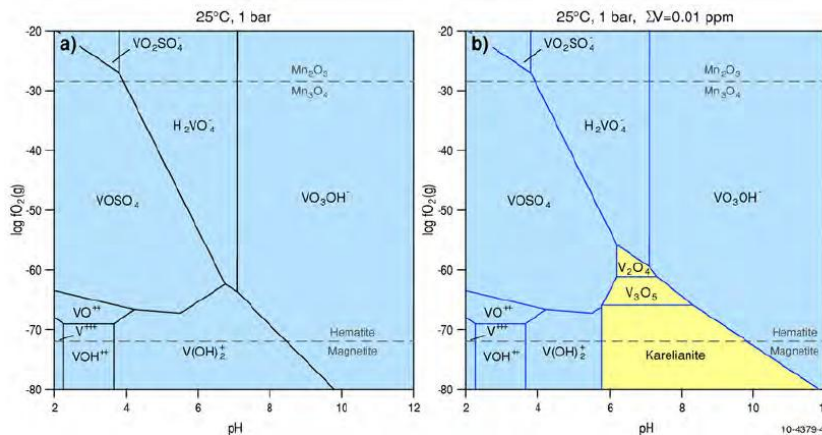


Figure V. 19. Log fO_2 -pH diagrams. The diagrams show dominant aqueous species of vanadium. Dashed lines marked Mn_3O_4/Mn_2O_3 and Hematite/Magnetite show the position of fO_2 buffers. Bastrakov et al., 2010.

The meteoric waters were slightly acidic in equilibrium with the atmospheric CO₂. The sulfides oxidation of the metamorphosed carbonated facies penetrated by the meteoric fluids allowed the production of sulfuric acid and the decrease of pH helping the dissolution of the uranium oxides liberated from the phosphates. These fluids have quickly evolved to alkaline pH by reaction with the metamorphic rocks of clinker type (Linklater et al., 1996; Techer et al., 2006; Fourcade et al., 2007; Elie et al., 2007). Hexavalent uranium solubility is considerably increased in highly alkaline waters. Thus, pyrometamorphism has not only permitted the liberation of uranium from the apatite structure, but has also facilitated the dissolution of uranium in surficial water for its transportation.

In these alkaline conditions the most probable uranyl complexes in solution were uranyl phosphates and/or carbonates, whereas the vanadium complex was probably vanadium hydroxyl. But the transport of these phases was short because of the evaporation and the presence of the V, led to the precipitation of uranyl vanadates which are the less soluble species of hexavalent uranium.

In the arid conditions prevailing in the Siwaqa area evaporation of surficial fluids leads to an increase of the concentration of the dissolved species in solutions and thus leads to the crystallization of the uranyl vanadium in subsurface conditions as in the calcrete deposits.

Uranyl vanadates being the less soluble hexavalent uranium minerals in near neutral conditions (Langmuir, 1978) will be the first to precipitate. But, precipitation of these minerals requires near neutral pH conditions. Hence, the highly alkaline fluids emerging from the pyrometamorphic have to have suffered a decrease of pH. The oxidation of the sulfides in the weathered limestones may have allowed the decreased pH favoring the uranium minerals precipitation in this trap.

After Langmuir (1978), the solubility of tyuyamunite is higher than that of the carnotite, with a minimum solubility at pH=6,5-7 (at 25°C) (Fig.V.20). But after Tokunaga et al., (2010), tyuyamunite has a lower solubility than carnotite (Fig.V.21).

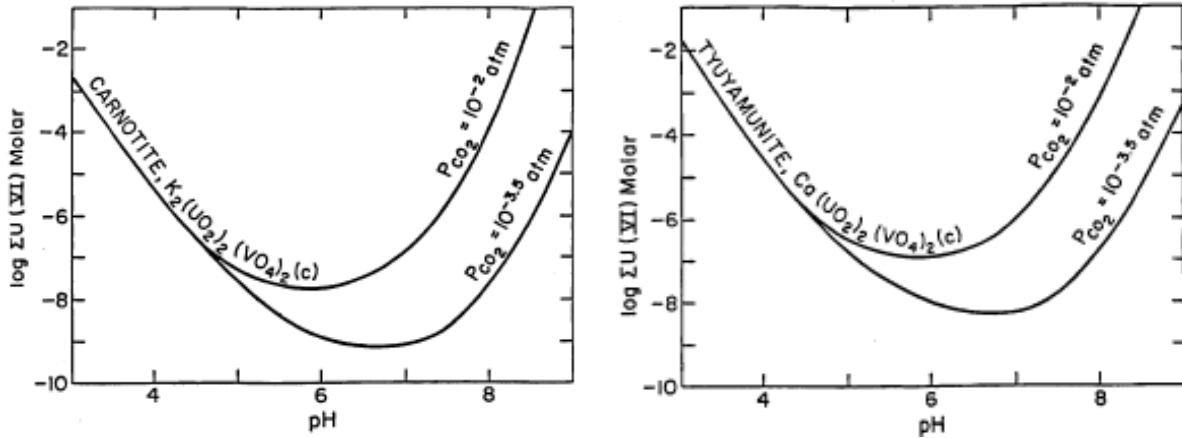


Figure V. 20. Carnotite and tyuyamunite – pH diagrams (25°C) (Langmuir, 1978).

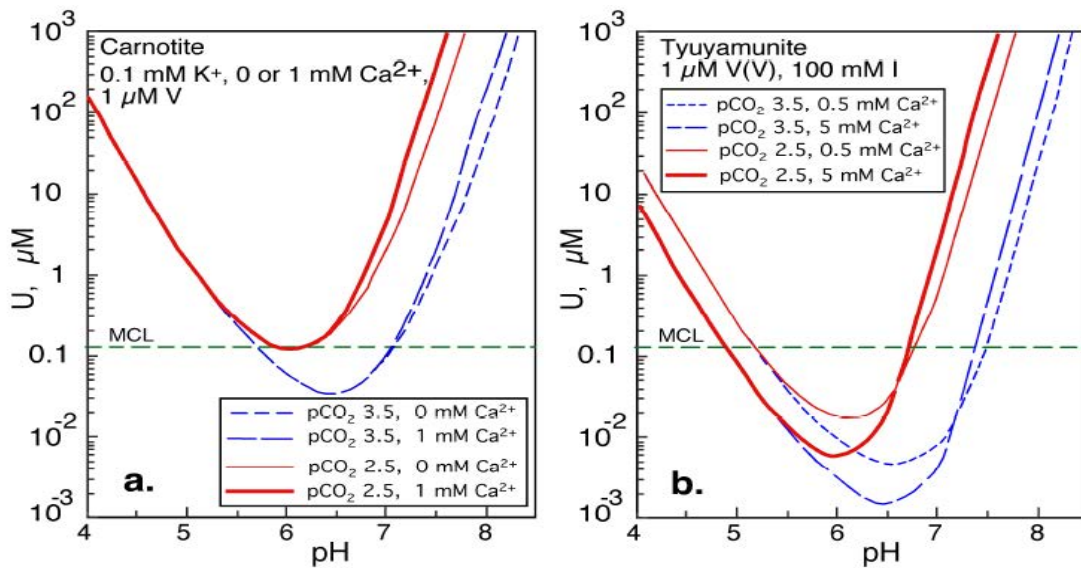


Figure V. 21. Carnotite and Tyuyamunite solubility – pH diagrams (Tokunaga et al., 2010).

The complex with the lowest solubility will be the first to precipitate. In an environment with a high K activity, carnotite can precipitate. But the surficial conditions in Siwaqa area, the absence of silicoclastic rocks and the predominance of carbonated rocks, have induced a very low K activity and a high Ca activity in the fluid, which have prevented the precipitation of carnotite, but favoured the crystallization of tyuyamunite.

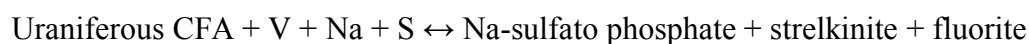
Beside tyuyamunite, the formation of Na-uranyl vanadates (strelkinite) and Na-sulfato phosphates require the availability of sodium in the fluids. The carbonates rocks being

extremely poor in sodium, this element most probably derives from saline waters typically generated by evaporation processes in arid climates. The source of sulfur for the Na-sulfato-phosphates can be easily found in the sulfides from the limestones or the marbles or from the sulfates which are derived from their oxidation in the marbles in minerals such as ettringite ($\text{Ca}_6\text{Al}_2(\text{SO}_4)_3(\text{OH})_{12} \cdot 26(\text{H}_2\text{O})$), and hashemite ($\text{Ba}(\text{Cr,S})\text{O}_4$), or from the oxidation of the sulfides in surficial conditions. Furthermore, the alteration of the carbonate-fluorapatite leads to the liberation of fluorine which crystallizes as fluorite by combining with calcium largely available in the carbonated host rocks. Fluorite is soluble from pH 7, which coincides with the minimum pH for the formation of the uranyl vanadates. Fluorite is intimately associated with the uranyl vanadates, indicating that the chemical reactions leading to the crystallization of these two minerals are probably synchronous.

Alteration and mineralization of the weathered limestones are illustrated by the following reaction:



Alteration, mineralization and Na-sulfato-phosphates crystallization have been formed in respect with the following reaction:



6. COMPARISON OF THE JORDANIAN MINERALIZATION WITH THE URANIFEROUS CALCRETES OF NAMIBIA AND AUSTRALIA

The two main calcrete deposits in the world, Yeelerrie (Western Australia) and Trekkopje (Namibia), share some similarities with the surficial uranium mineralization from central Jordan, but also present considerable differences:

- (i) In the major calcrete deposits, the main host of the mineralization is poorly sorted silicoclastic rocks mainly deriving from the erosion of granites with very poor to no hydrolysis of feldspars which are mostly preserved;
- (ii) The carbonates occur as concretion in these silicoclastic rocks deposited by evapotranspiration processes;

(iii) The uranium minerals are mainly carnotite, whereas those of the Siwaqa area are tyuyamunite and strelkinite reflecting the absence of silicoclastic rocks for providing the potassium necessary to crystallize carnotite, and the presence of carbonated lithologies largely predominating in the Belqa Group, providing the calcium for tyuyamunite;

(iv) The uranium and vanadium source rocks are carbonated rocks enriched in U-bearing phosphates and their pyrometamorphic equivalent, and to a lesser extent the black shales, whereas the source of U for the classical calcretes is predominantly uranium-rich granites (for example: the granitoids of the Yilgarn block in Yeelirrie are the U and K source, greenstones are the V source; Butt et al., 1984);

(v) The carbonates in classical calcretes are precipitated from evaporation-transpiration processes, whereas in the Siwaqa area the carbonates represent the initial host lithologies;

(vi) In the Siwaqa area the carbonates tend to be dissolved with a volume decrease in the whole rocks, whereas in the calcretes, carbonates are added to the system and precipitated in the porosity of the siliciclastic rock. Carlisle (1983) proposed that the calcrete region is only one authigenic deposit resulting of the loss of CO_2 , an increase in pH and $\text{CO}_3^{2-}/\text{HCO}_3^-$, but with constant or higher Ca^{2+} and Mg^{2+} evaporative concentration along the drainage and from the encounter between Ca, Mg carbonate waters and Ca, Mg sulfates and chloride brines in evaporative zone;

(vii) In the classical calcretes, uranium is transported in phreatic waters along valleys over large distance and these waters mix somewhere with vanadium bearing solution for the precipitation of uranyl vanadates. In contrast, in the Siwaqa area, the source of uranium and vanadium occur in the same lithologies and consequently uranium cannot migrate very far and is dominantly found at the foot of the marble ridges which represent the major source of uranium and vanadium.

The REE contents of carnotites of different deposits (Langer Heinrich, Trekkopje, Namibia, Yeleerie, Beverley) have been analyzed by LA-ICP-MS. REE patterns of the uranyl vanadates from calcrete type mineralizations tend to be less fractionated ($0 < \text{LaN}/\text{YbN} < 0,05$) and present a lower content in heavy REE than the uranyl vanadates of the weathered limestones from the Siwaqa area in central Jordan ($0,01 < \text{LaN}/\text{YbN} < 0,02$) but they typically also have the positive cerium anomaly (Fig.V.22).

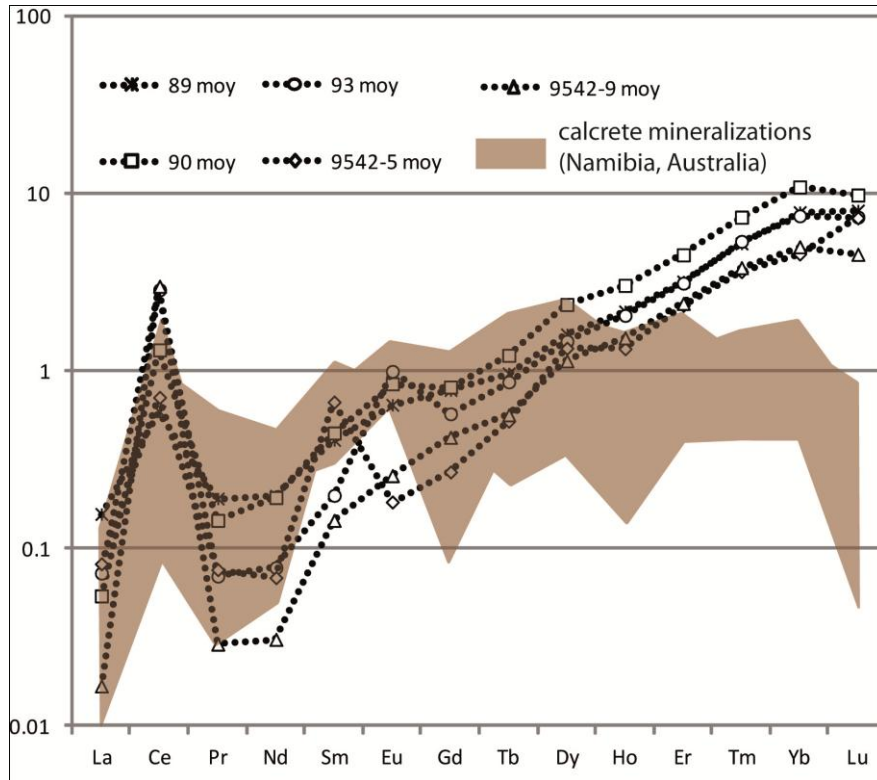


Figure V. 22. PAAS-normalization (McLennan, 1989) patterns of the uraniumiferous mineralizations of central Jordan and others occurrences.

7. GLOBAL BUDGET OF URANIUM MINERALIZATION

To evaluate the amount of uranium possibly involved for the formation of the surficial uranium mineralization, it is necessary to evaluate:

(i) The amount of U liberated by the alteration of the carbonate-fluorapatite:

The average U in the apatite from the non altered carbonates (shale, bioclastic limestones, marbles) is 172 ppm, the average U contained by the apatite from altered limestones is 21 ppm. But its amount corresponds to an average apatite, so it is necessary to calculate at the amount of uranium possibly leached out at the scale of a given mass of rock taking into account its phosphate content. The non altered carbonated rocks contain an average of 7.31 wt % P₂O₅, and their apatites have an average P₂O₅ content of 32.39 wt%. The altered rocks have an average phosphate content of 2.29 wt % P₂O₅, and their apatites have an average content of 31.35 wt %.

$(172 * 7.31) / 32.39 = 39$ ppm U bearing by the phosphates of the non altered rocks.

$(21 * 7.31) / 31.35 = 4.9$ ppm U bearing by the phosphate of the weathered rocks.

Hence, the amount of U liberated by the surficial alteration is $39 - 4.9 = 34.1$ ppm. The non altered carbonates analyzed have an average U content of 478 ppm, which is further evidence that uranium is present in others phases such as in the U micrograins disseminated in the matrix of the shales and the poikilitic uranium minerals in the marbles (Chapter II). The average U content of the weathered mineralized limestones in which the phosphates have been analysed is about 742 ppm U. This result shows that the leaching of the carbonate-fluorapatites is not the only source for the uranium accumulation in the porous limestones; it is necessary to consider the vertical transport mechanisms.

(ii) The U proportion in the shales, non-located in the phosphates:

The average U content of the oil shale (JRD10-12B, in which phosphates have been analyzed) is 3839 ppm, the average U content measured in its contained phosphates is 732 ppm. The phosphates of the shale present an average phosphate content of 29,55 wt % P₂O₅. The whole rock contents 1,70 wt % P₂O₅. The uranium content bearing by all the phosphates of the rock is $(732 * 1,70) / 29,55 = 42$ ppm U. The U proportion non located in the phosphate is $3839 - 42 = 3797$ ppm U.

(iii) The amount of U present in the weathered mineralized limestones (3 m of depth) for a square of 1km²:

The two trenches sampled in the Siwaqa area present an average uranium content of 313 ppm (265 ppm for T21, and 360 for T07). The density of the weathered mineralized limestones, about 1.4, was measured on cores by the AREVA's exploration geologists. The U tonnage (T, m³) on a area of 1 km² * 3m depth with a content of 313 ppm U is:

$$T = 1000 * 1000 * 3 * 1,4 * 313.10^{-6} = 4,2.10^{-6} * 313.10^{-6} = 1315 \text{ t U.}$$

The mineralized weathered limestones extend over 40 km² in central Jordan, that is a total tonnage of 52600 t U. But this estimated tonnage is a maximum value, and should be treated with great caution because the lateral continuity of the mineralization is probably not systematic, and furthermore, this evaluation has been made from the analysis of a very limited

number of samples (six). Only an evaluation based on systematic drilling over a wide area with high density depth and areal sampling can give a more realistic estimation.

8. CONCLUSIONS

The surficial uranium mineralization associated with the pyrometamorphism of the Belqa Group in the Dabba-Siwaqa area occurs as tyuyamunite and strelkinite, in the form of disseminated aggregates of splinter and also as fibrous minerals associated with fluorite in the pore space of the weathered limestones or in association with clay minerals. The weathered surficial limestones have been mineralized by meteoric waters that leached U and related metals from the marbles and which were transported to the more porous weathered zones in the adjacent limestones. Evaporation of the pore water fluids has promoted the concentration of the uranophile elements. The marbles, initially enriched in uranium mainly located in the carbonate-fluorapatite and destabilized by pyrometamorphism, represents the U source. Shales, rich in vanadium, are probably the main V sources. The percolation of metal-enriched alkaline groundwater through the metamorphic hills resulted in an increase in pH, and favored the uranyl and vanadate transport to the porous limestones beneath. The alteration of sulfides these weathered rocks led to a decrease of the pH permitting the complexation of U and V to form uranyl vanadates. The uranium enrichment of the porous supergene carbonates is due to three processes: (i) the leaching of the uraniferous rocks by lateral supply from the marbles, (ii) the leaching of the upper horizons of the weathered limestones to enrich the lower horizons (per descensum mechanism) or the capillary ascension and the evaporation (per ascensum mechanism) to enrich the upper horizons, and (iii) the volume loss of these weathered carbonates.

REFERENCES

- Bastrakov, E.N., Jaireth, S., Mernagh, T.P., 2010. Solubility of uranium in hydrothermal fluids at 25° to 300°C: Implications for the formation of uranium deposits. *Geoscience Australia Record* 2010/29. 91p.
- Butt, C.R.M., Mann, A.W., Horwitz, R.C., 1984. Regional setting, distribution and genesis of surficial uranium deposits in calcretes and associated sediments in western Australia. Division of Mineralogy, CSIRO, Wembley, Australia. IAEA, Vienna, 322, 121-128.
- Carlisle, D., 1983. Concentration of uranium and vanadium in calcretes and gypcretes. *Geol. Soc. London. Spec. Publ.* 11, 185-195.
- Dill, H.G., 2011. A comparative study of uranium-thorium accumulation at the western edge of the Arabian Peninsula and mineral deposits worldwide. *Arab. J. Geosci.* 4, 1, 123-146.
- Elie, M., Techer, I., Trotignon, L., Khoury, H., Salameh, E., Vandamme, D., Boulvais, P., Fourcade, S., 2007. Cementation of kerogene-rich marls by alkaline fluids released during weathering of thermally metamorphosed marly sediments. Part II: Organic matter evolution, magnetic susceptibility and metals (Ti, Cr, Fe) at the Khushaym Matruk natural analogue (central Jordan). *App. Geochem.* 22, 1311-1328.
- Fourcade, S., Trotignon, L., Boulvais, P., Techer, I., Elie, M., Vandamme, D., Salameh, E., Khoury, H., 2007. Cementation of kerogene-rich marls by alkaline fluids released during weathering of thermally metamorphosed marly sediments. Part I: Isotopic (C, O) study of the Khushaym Matruk natural analogue (central Jordan). *App. Geochem.* 22, 1293-1310.
- Goudie, A.S., 1983. Calcrete. In: A.S. Goudie and K. Pye (Eds.), *Chemical Sediment and Geomorphology*. London, Academic Press, 93-131.
- Grant, J.A., 1986. Isocon analysis: A brief review of the method and applications. *Phys. Chem. Earth* 30, 997-1004.
- Gresen, R.L., 1967. Composition-volume relationships of metasomatism. *Chem. Geol.* 2, 47-55.
- Gross, S., Ilani, S., 1987. Secondary uranium minerals from the Judean Desert and northern Negev, Israel. *Uranium* 4, 147-158.

Ilani, S., Strull, A., 1988. Uranium mineralization in the Judean Desert and in the northern Negev, Israel. *Ore Geol. Rev.* 4, 305-314.

McLennan, S.M., 1989. Rare earth elements in sedimentary rocks: Influence of provenance and sedimentary processes. *Geochemistry and mineralogy of the rare earth element. Rev. Mineral. Geochem.* 21, 169-200.

Langmuir, D., 1978. Uranium solution-mineral equilibria at low temperatures with applications to sedimentary ore deposits. *Geochim. Cosmochim. Acta* 42, 547-569.

Linklater, C.M., Albinsson, Y., Alexander, W.R., Casas, I., McKinley, I.G., Sellin, P., 1996. A natural analogue of high-pH cement pore water from the Maqarin area of northern Jordan: Comparison of predicted and observed trace-element chemistry of uranium and selenium. *J. Cont. Hydrol.* 21, 1-4, 59-69.

Skirrow, R.G., Jaireth, S., Huston, D.L., Bastrakov, E.N., Schofield, A., Van der Wielen, S.E., Barnicoat, A.C., 2009. Uranium mineral systems: Processes, exploration criteria and a new deposit framework. *Geoscience Australia Record* 2009/20, 44p.

Techer, I., Khoury, H., Salameh, E., Rassineux, F., Claude, C., Clauer, N., Pagel, M., Lancelot, J., Hamelin, B., Jacquot, E., 2006. Propagation of high-alkaline fluids in an argillaceous formation: Case study of the Khushaym Matruk natural analogue (central Jordan). *J. Geochem. Exploration.* 90, 1-2, 53-67.

Tokunaga, T.K., Kim, Y., Wan, J., 2010. Potential remediation approach for uranium-contaminated groundwaters through potassium uranyl vanadate precipitation. *Environ. Sci. Technol.* 43(14), 5467-5471.

Appendix V. Major and trace element concentrations of the supergene mineralized limestones.

depth Samples	NRA trench			Trench T21			Trench T07		
	JRD10-41	JRD10-92	9542-5	1 m JRD10-89	2 m JRD10-90	3 m JRD10-91	1 m JRD10-95	2.5 m JRD10-94	3 m JRD10-93
<i>Major and minor elements (wt%)</i>									
SiO ₂	5.73	5.34	13.29	12.27	9.38	4.97	11.50	7.99	7.70
Al ₂ O ₃	1.39	1.32	3.35	3.42	3.38	2.30	2.26	2.03	2.34
TiO ₂	0.07	0.07	0.16	0.15	0.15	0.10	0.22	0.09	0.11
Fe ₂ O ₃	0.59	0.60	1.31	1.39	1.19	0.79	1.20	0.75	0.93
K ₂ O	0.00	0.00	0.03	0.00	0.03	0.00	0.17	0.00	0.00
MgO	1.12	1.23	2.04	1.69	1.06	2.21	2.20	3.99	2.39
MnO	0.00	0.00	0.00	0.00	0.00	0.00	0.01	0.00	0.00
CaO	48.16	48.01	39.22	40.98	42.55	46.46	43.07	43.63	45.54
Na ₂ O	0.38	0.43	0.80	0.58	0.46	0.58	0.31	0.57	0.10
P ₂ O ₅	2.58	2.11	2.22	2.37	1.30	1.02	0.31	3.36	3.35
PF	39.64	39.34	36.11	35.67	36.63	40.65	38.23	36.87	35.59
Total	99.66	98.46	98.54	98.52	96.13	99.08	99.47	99.28	98.05
CO ₂ tot	34.01	35.42	27.56	29.02	30.14	35.66	34.70	30.28	31.96
TOC	<0.02	<0.02	0.02	<0.02	0.02	0.03	0.06	<0.02	<0.02
F	0.95	0.67	1.01	0.61	0.43	0.15	0.11	1.12	0.64
TS	0.11	0.15	0.36	0.30	1.34	0.07	0.21	0.20	0.15
CaCO ₃	77.18	80.39	62.51	65.83	68.38	80.85	78.42	68.70	72.52
<i>Trace elements (ppm)</i>									
As	27.1	32.94	70.06	45.22	31.52	19.71	6.809	37.14	28.9
Ba	58.03	49.26	937.6	299	67.59	12.66	647.4	605.8	425.4
Bi	0	0	0	0.239	0	0	0	0	0
Cd	11.77	12.29	39.56	16.68	14.14	10.56	3.346	11.54	4.315
Co	1.534	1.706	3.158	3.356	2.817	2.808	4.812	1.952	2.509
Cr	128.3	49.49	227.8	443.1	89.99	164.5	45.13	39.6	76.07
Cu	88.51	93.43	155.7	99.65	102.9	60.88	20.01	76.83	125
Mo	9.722	10.04	6.666	5.638	2.754	1.618	1.28	4.659	27.48
Ni	210.6	223.2	252.5	191.6	192.3	198.6	35.08	304.6	430.3
Pb	1.4985	0.9245	6.3993	9.4453	4.9873	1.7151	2.5668	2.4003	3.478
Sb	2.867	5.271	5.875	4.345	2.49	1.701	0.598	3.428	1.685
Sr	598.8	378.5	467.1	496.8	420.9	521.8	703.7	569.9	468.8
Ta	0.095	0.088	0.212	0.196	0.19	0.116	0.273	0.105	0.152
Th	0.971	0.894	1.971	1.826	1.695	1.116	1.619	1.148	1.511
U	587.3	304.1	1007	599.3	172.1	24.51	10.47	24.46	1046
V	338	250.3	379.4	257.8	296	315.1	52.98	205.4	430.1
Y	23.9	21.71	37.29	28.6	21.95	15.74	9.324	30.44	47.89
Zn	194	603.5	1251	723.7	699.9	511.8	92.1	460.9	306.5
Zr	23.8	23.08	53.33	33.45	33.74	19.55	73.89	30.72	41.7
<i>Rare Earth elements (ppm)</i>									
Ce	7.925	7.226	14.83	15.38	14.27	9.181	13.96	9.445	13.37
Dy	1.824	1.609	2.988	2.544	2.043	1.394	1.246	2.179	3.486
Er	1.431	1.246	2.347	1.833	1.441	1	0.755	1.752	2.792
Eu	0.354	0.314	0.609	0.555	0.481	0.326	0.314	0.398	0.633
Gd	1.642	1.521	2.743	2.471	2.074	1.357	1.316	1.973	3.187
Ho	0.438	0.393	0.726	0.593	0.471	0.326	0.256	0.535	0.866
La	8.743	7.753	14.61	12.8	10.68	7.206	7.401	10.65	15.31
Lu	0.265	0.238	0.462	0.336	0.251	0.187	0.129	0.358	0.549
Nd	6.451	5.806	11	10.42	9.068	6.015	6.922	7.574	11.27
Pr	1.543	1.404	2.682	2.586	2.242	1.475	1.744	1.842	2.731
Sm	1.363	1.223	2.276	2.135	1.88	1.225	1.414	1.56	2.416
Tb	0.259	0.238	0.437	0.383	0.317	0.211	0.207	0.308	0.49
Tm	0.216	0.198	0.361	0.281	0.219	0.153	0.114	0.278	0.44
Yb	1.541	1.383	2.558	1.937	1.486	1.092	0.784	1.945	3.121
ΣREE	34.00	30.55	58.63	54.25	46.92	31.15	36.56	40.80	60.66

Conclusions générales

Les roches sédimentaires carbonatées du Groupe Belqa de la région de Siwaqa-Khan Azzabib (Campanien-Paléocène) se sont formées pendant des périodes de transgressions marines associées à un réchauffement climatique et un upwelling de grande envergure. Les shales et une partie des calcaires, enrichis en matière organique, se sont déposés en eaux suboxiques à anoxiques profondes dans des bassins limités par des failles normales. Les autres calcaires, pauvres en matière organique, ont été déposés dans des conditions de faible productivité primaire et/ou avec de faibles conditions de préservation de la matière organique, en milieu moins profond. Les protolithes des marbres se sont formés dans les mêmes conditions d'anoxie ce qui a permis de préserver la matière organique qu'ils contiennent. Ces circonstances ont permis un enrichissement synsédimentaire en éléments sensibles aux conditions redox (U, Cu, Co, Mo, Sb, V). Cet enrichissement résulte d'une précipitation directe à partir de l'eau de mer ou à travers leur incorporation dans les organismes marins (via leur métabolisme). D'autres éléments également sensibles aux conditions redox (Cr, Ni, Cd, Zn) sont enrichis au-delà des concentrations classiques observées dans les shales. Un flux exogénique attribué à l'altération d'ophiolites obductées à la fin du Crétacé lors de la collision entre la plaque arabe et le continent européen est proposé.

La combustion de la matière organique fortement enrichies dans certains niveaux de carbonates est responsable du pyrométamorphisme. Ce métamorphisme de très haute température (jusqu'à 1500°C) et très basse pression a entraîné la formation de minéraux originaux et rares, typiques des ciments de type Portland et clinkers. Les facies pyrométamorphiques sont observés dans un large domaine mais sont très localisés et inégalement répartis en Jordanie centrale, ce qui témoigne de la nature éparse du phénomène d'oxydation et de combustion touchant des horizons bitumineux locaux comme ceux mis en place en bassins restreints. Les différents facies métamorphiques observés attestent de la présence de protolithes de natures distinctes et de différents degrés de métamorphisme. Les marbres, qui présentent encore de la calcite et de la carbonate-fluorapatite, se sont formés à partir d'une calcination incomplète de calcaires plus ou moins phosphatés. Les facies métamorphique noirs et verts se sont probablement formés à partir de roches plus argileuses (calcaires argileux/ marnes) et ont subi une combustion complète entraînant la décarbonatation totale des carbonate-fluorapatites et la formation de silicates de calcium anhydres en proportions plus importantes. Les paralavas ont été formés par pyrométamorphisme de shales, plus siliceux et plus alumineux, entraînant la formation de

pyroxènes et silicate de magnésium. Le pyrométamorphisme est responsable d'un enrichissement en éléments majeurs peu mobiles et en traces par perte de volume résultant à la fois des réactions de décarbonatation et de la combustion de la matière organique par perte de CO₂.

Les phosphates, initialement sous forme de carbonate-fluorapatites d'origine sédimentaire/diagénétique, ont été marqués par les événements affectant la plate-forme carbonatée de Jordanie centrale (à partir du Miocène), et peuvent servir de marqueurs de l'évolution des différentes lithologies. Ces carbonate-fluorapatites, ayant une signature semblable à celle l'eau de mer à cette époque, se sont formés grâce à la concomitance de différentes conditions exceptionnelles (réchauffement des latitudes, augmentation du niveau marin, upwelling) sur la marge sud de l'océan Téthys au Campanien-Eocène. Le pyrométamorphisme a entraîné la déstabilisation de ces carbonate-fluorapatites, ce qui a permis la libération de l'uranium présent dans leur structure, initialement incorporé par substitution au calcium. Le pyrométamorphisme a également provoqué une décarbonatation de certaines carbonate-fluorapatites se transformant alors en fluorapatite, accompagné d'un fractionnement des terres rares entraînant un enrichissement des terres rares légères. L'altération supergène des carbonate-fluorapatites et le milieu évaporitique riche en sulfate et sodium a permis la formation d'apatite sulfato-phosphatées. Les terres rares des carbonate-fluorapatites supergènes altérées sont fractionnées, enrichies en terres rares légères, et les sulfato-apatites supergènes néoformés sont appauvris en terres rares.

Les sources de l'uranium sont donc principalement l'uranium mis à disposition lors du pyrométamorphisme dans les marbres, et celui libéré lors de l'altération supergène des carbonate-fluorapatites. Les marbres, formant des collines à cause leur nature plus résistante à l'érosion, et les oxydes d'uranium reconcentrés dans les carbonate-fluorapatites qu'ils contiennent, ont été lessivés par les fluides météoriques légèrement acides qui ont percolé jusqu'aux calcaires altérés en contrebas. La perte de volume de ces calcaires correspond à une dissolution des carbonates par les eaux météoriques qui leur confèrent une forte porosité dans laquelle les vanadates d'uranyles de Ca et Na (tyuyamunite et strelkinite) ont précipité via des processus d'évapo-transpiration, avec des transports latéraux limités car le vanadium était disponible sur place aussi bien dans les marbres que les carbonates. Ces processus verticaux semblent avoir opéré 'per ascensum' et 'per descensum'. Le mécanisme 'per ascensum' a contrôlé l'enrichissement des calcaires supergènes poreux par ascension capillaire et

évaporation directe, alors que le mécanisme 'per descensum' a entraîné un enrichissement graduel des facies pulvérulents par lessivage des horizons supérieurs vers les horizons inférieurs.

Ce modèle génétique présente donc de larges différences avec celui des grands gisements de type calcrète : les roches porteuses des minéralisations sont des carbonates ayant subi une dissolution importante leur conférant une très forte porosité, contrairement aux minéralisations de type calcrète qui sont portées par des conglomérats silicoclastiques dérivant de l'érosion de granites, et cimentés par des carbonates. Les minéraux uranifères rencontrés en Jordanie centrale sont de la tyuyamunite et strelkinite, contrairement à la carnotite rencontrée dans les calcrètes. Cela témoigne de l'absence de roches siliclastiques, source de potassium favorisant la précipitation de carnotite. Les sources d'uranium et de vanadium sont les carbonate-fluorapatites des roches carbonatées et de leurs équivalents pyrométamorphiques où se sont formées les uraninites, et très localement des shales. Les fluides porteurs d'U et V n'ont alors pas eu besoin de migrer sur de longues distances et ont permis la précipitation des uranyl vanadates au pied des collines. Contrairement aux minéralisations de type calcrète, où les nappes phréatiques ont transporté l'uranium jusqu'à leur mélange avec des fluides riches en vanadium, permettant alors la précipitation des uranyl vanadates. Ce phénomène de minéralisation supergène concerne de faibles profondeurs (entre 1 et 5m) mais s'étend cependant sur de larges surfaces (40 km²).

Appendix

Surficial uranium mineralization of calcretes

1. CALCRETES

1.1. Definition

Calcretes are conglomerates cemented by carbonates, accumulated in continental environment on a host rock from the introduction and cementation of carbonates during evapotranspiration processes and variations of the groundwater level. Pedogenic calcretes are formed in vadose area by vertical processes leading the loss of H₂O and CO₂, and from an authigenic cement. Most time, they have nearly the same composition and the same texture that the non pedogenic calcretes (Carlisle, 1983). These non pedogenic calcretes are formed on altered basement with lateral transport of the elements, in contrast with an evaporitic system which have a vertical distribution. Calcretes present different morphologies (pulverulent, nodular, pisolitic, tubular, lamellar) which can be combined and complexified the system (Wright and Tucker, 1991; Alonso-Zarza, 2003). Calcretes are also characterized by microstructures: “alpha-calcretes” are abiogenic and present typical phenomenon of precipitation/dissolution with mosaic structure,” beta-calcretes” are mostly biogenic and show biological textures such as pisoids, roots and microcodiums (Zhou and Chafetz, 2009).

1.2. Uraniferous calcretes

The surficial uranium deposits are defined following several parameters and different classifications. Toens and Hambleton-Jones (1984), divided them in three main environments (Fig.A.1): 1. Fluvatile, 2. Lacustrine/playa, 3. Pedogenic. In this classification, calcrete belongs to the pedogenic category because they are formed from a parent rock directly on the altered substratum (authigenic) or on soils formed from fluvatile or eolian material (allogenic). Dahlkamp (1993) defined the surficial mineralizations following four categories: 1. Duricrust (fluvatile, valley-fill / lacustrine, playa) to which belongs the calcrete, 2. Peat bog where uranium is associated to organic matter, 3. Karstic caverns which could be similar to te calcretes but without evapotranspiration, 4. Pedogenic and fill structure where U occurs as uranyl phosphates or reducing uranium minerals, this type is not well known and presents weathering of primary uranium such as the deposit of Schlaginweit located in the granitic batholith of Achala, Argentina. More common U sources are the uraniumiferous granites altered in arid to semi-arid climate. U is transported as hexavalent uranyl carbonates by acid oxidizing fluids which become alkaline during the percolation (Mann & Deutscher, 1978).

The uranyl carbonates complexes are dissociated and U can be associated with V to form uranyl vanadate like carnotite which is the less soluble form.

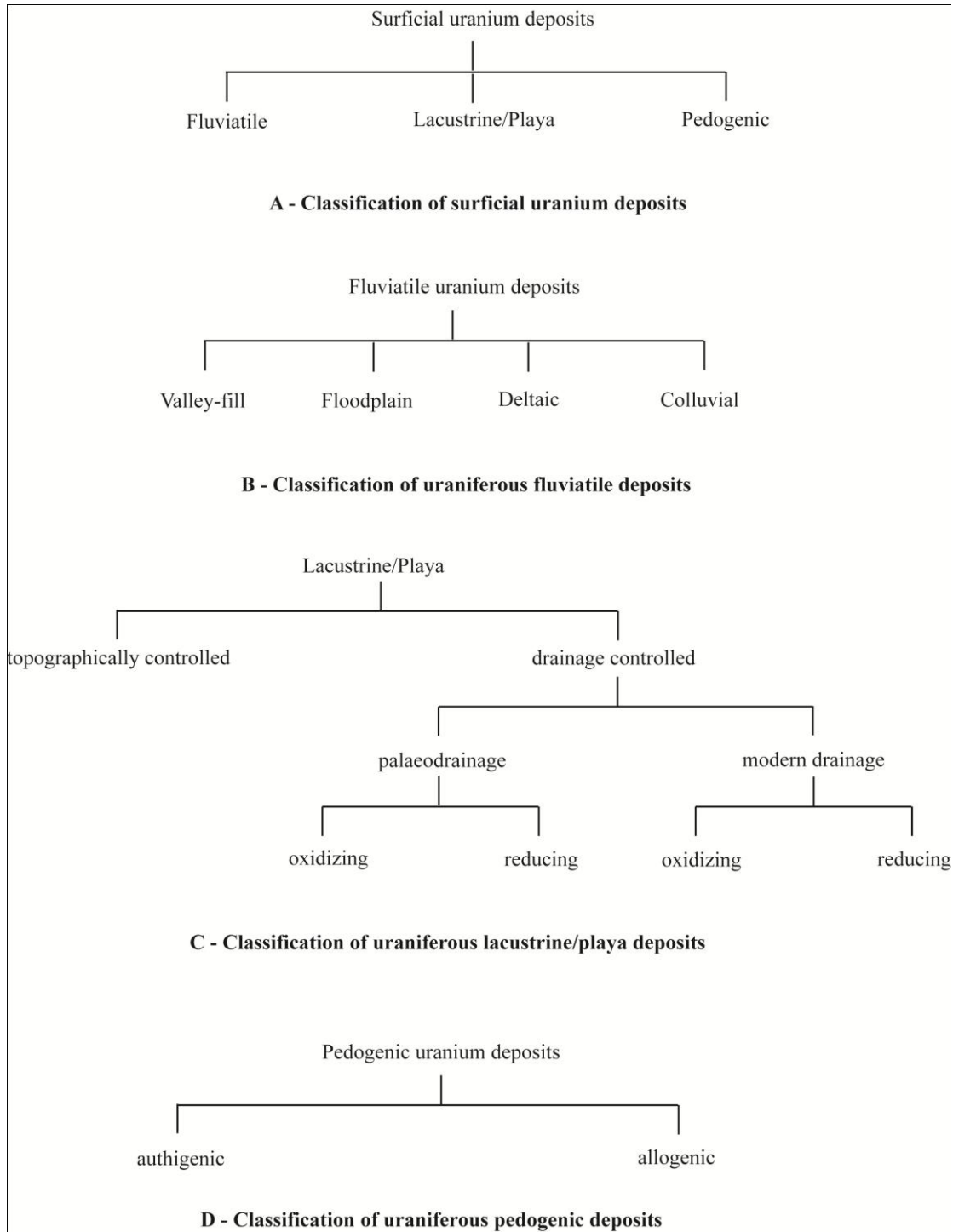


Figure A. 1. Classification of the surficial uranium deposits after Toens and Hambleton-Jones (1984).

2. URANIUM SURFICIAL MINERALIZATION OF AUSTRALIA AND NAMIBIA: URANIFEROUS CALCRETES

2.1. Knowledge statement

The most well-known uranium surficial deposits are the calcrete mineralizations of Yeelirrie in Australia and Langer Heinrich/Trekkojpe in Namibia.

Yeelirrie (Australia) is the most important surficial uranium deposits in the world. These mineralizations have been formed in a catchment area constituted of Archean uranium-rich granites and vanadium-rich green rocks, with an arid climate setting during the Late Tertiary-Quaternary (Fig.A.2) (Mann & Deutscher, 1978; Cameron, 1984; Galloway & Hobday 1996).

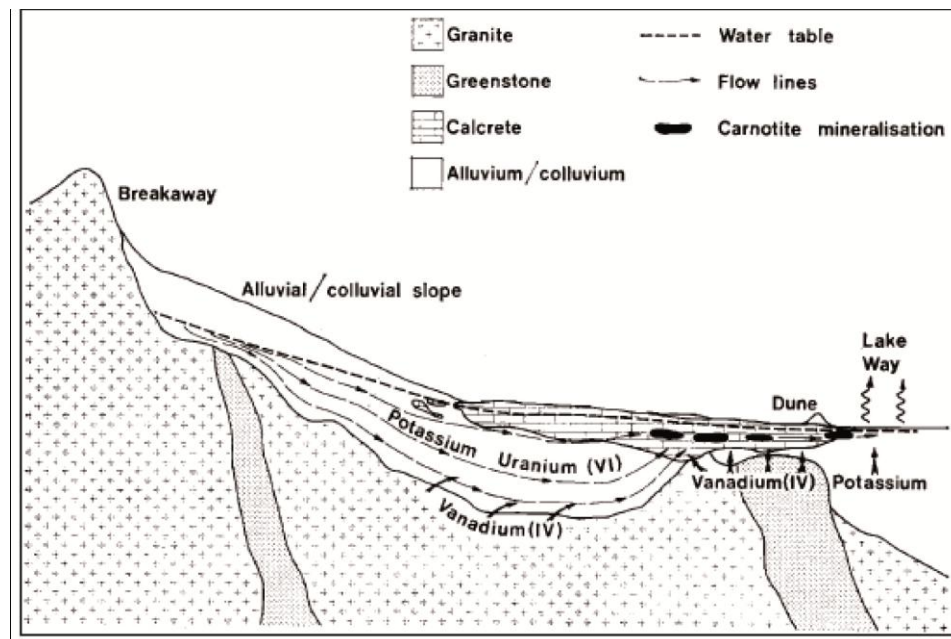


Figure A. 2. Idealized section along the representative catchment showing the postulated redox controlled genesis of carnotites in calcrete. Mann and Deutscher (1978).

The mineralization is located in the valley-fill calcretes along drainage channels and occurs as lense of carnotite coating the cavities and the fissures. The salinity, pH, Ca, Mg, K, U, V concentrations increase toward the basin with the drainage direction. The deposit of the calcrete depends of severals paremeters (Carlisle, 1983): (i) The CO_2 loss simultaneous with the pH increase and the $\text{CO}_3^{2-}/\text{HCO}_3^-$ ratio; (ii) The equal or more Ca^{2+} and Mg^{2+} evaporative

concentration; (iii) The meeting between the ions precipitation where Ca/Mg of the carbonates, carrying by water and the ions brine of salted lakes. Uranium was transported by groundwaters as uranyl carbonate. Then, this complex was dissociated allowing the liberation of U^{6+} and his association with vanadium (oxidized 4→5) to form the carnotite. This mineralization is enable by three principal driving mechanisms (Mann & Deutscher 1978): evaporation, decomplexation, redox.

Langer Heinrich and **Trekkopje** (Namibia) are ones of the most important surficial ore deposits discovered since the discovery of Yeelirrie in 1972. They are located in upper Cretaceous-lower Tertiary palaeovalleys (Hambleton-Jones, 1984). The depositional environment is fluvial-type. The sediments are composed of basement clasts and authigenic calcite. Uranium mainly occurs as carnotite. The source rocks are Proterozoic migmatites, pegmatites, alaskites, granites and marbles (Carlisle et al. 1978). Tardi-granites of Spitzkoppe are the last source rocks of the Trekkopje deposit (Bowell et al., 2009). Several mechanisms have been identified: the evaporation of the groundwater, the uranyl carbonates decomplexation, the redox conditions and the vanadium adsorption (Hambleton-Jones, 1984). Carnotites have been deposited during the flash flooding of the palaeochannels, as coating of the grains and filling the cavities. Uraniferous granites have been eroded and oxidizing alkaline saline solutions have transported uranium. The carbonated fluids permitted the mobilization of hexavalent uranium. Bowell et al. (2009) proposed that the carnotites are a secondary mineralization from upstream primary carnotites by the uranyl-carbonate decomplexation.

2.2. Geochemical and mineralogical characterization

2.2.1. Langer Heinrich

Five on six samples (LHU1/2/3/4/6) are very immature microconglomeratic arkoses. They are constituted by quartz, often smoky, pink potassic feldspars, plagioclases, micas clasts cemented by carbonates. The sample LHU-2 present yellow uraniferous mineralizations (U^{6+}) (Fig.A.3). LHU-5 is a fine-grained sandstone with a weak consolidation and some carbonates traces (Fig.A.4).



Figure A. 3. Mineralized sample LHU-2 showing the heterogeneous granulometry of the rock, and the yellowish hexavalent uranium minerals.



Figure A. 4. Sample LHU-5 corresponding to a relatively well sorted sandstone.

Clays (Fig.A.5) of LHU-1 are mainly detritic illite-muscovite types which have low specific surfaces limiting the uranium adsorption. LHU-2, mineralized and rich in carbonates, presents some illite, illite/chlorite interstratified and vermiculites which have a higher specific surface allowing the uranium adsorption. LHU-5, poor in carbonates, is the richest in clays occurring as illite, illite/chlorite interstratified and smectites. All samples contain muscovite and biotite.

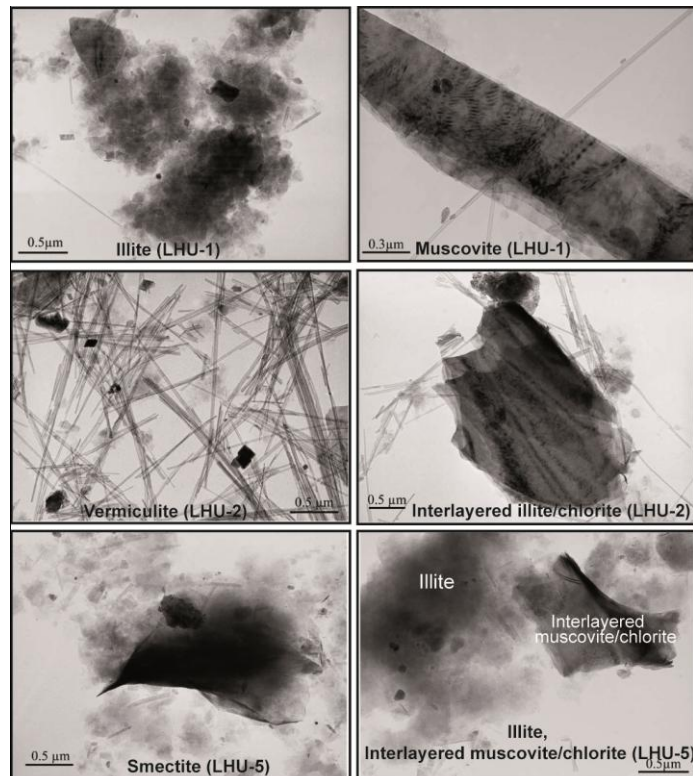


Figure A. 5. TEM views of the clay minerals.

The Q-P diagram (Fig.A.6) presents the quartz proportion (Q) and the albite, potassic feldspars (P). Calcium is mainly carried by carbonates, and some plagioclases. LHU-1 and LHU-2 are the poorest in quartz with a low Q (41 et 42,5 %wt) due to the important content in carbonates (23,8 et 25,5 %wt). Feldspars have an intermediate albite-K feldspar distribution. The other four samples have high silica content (jusqu'à 74,6 %wt) and show feldspars with compositional variations. LHU-5 is rich in albite whereas the three other (LHU-6/4/3) are rich in K-feldspars, respectively enriched toward plagioclases with similar quartz contents.

The A-Q diagram (Fig.A.7) presents the quartz proportion and the alumina proportions in clays which is not integrated in the feldspar structures (A). LHU-5 are rich in albite and clays which not result from the alteration of plagioclases but probably from detritic origin. LHU-1 and 2, richest in carbonates, have the lower A parameter indicating that they are the poorer in clay. The carbonate precipitation is probably due to the low clay content which not decreases the rock porosity. Moreover, the important carbonate contents of these rocks cannot possible in the initial porosity of the arkoses. A increase of volume or a quartz dissolution (photo) have probably permitted to liberate space for the carbonate formation. LHU-2 is the richer in uranium with 1047 ppm, the other samples have uranium content from 2 to 42 ppm.

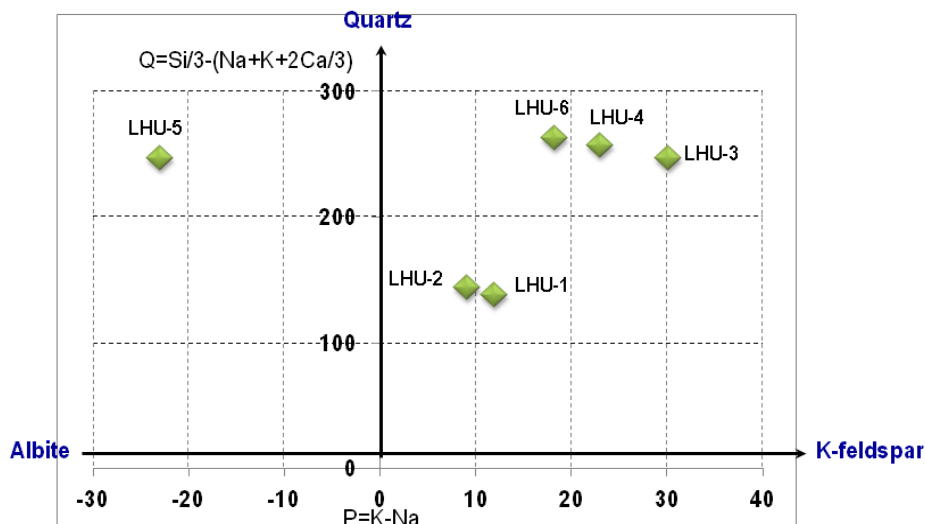


Figure A. 6. Q-P diagram. Relative proportions of quartz – albite – K-feldspar in the sediments of Langer Heinrich in a Q'-P' chemical-mineralogical diagram.

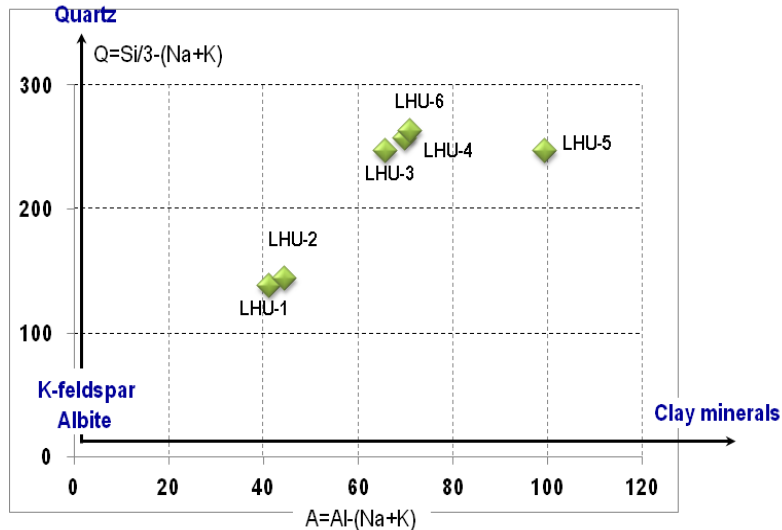


Figure A. 7. A-Q diagram representing the variations of the proportions of quartz and clay minerals in the Langer Heinrich sediments.

2.2.2. Trekkopje

The visit of ‘Midi Pit’ of the Klein Trekkopje deposits permitted to see the basement constituted of granites, pegmatites, marbles, schistes and dolerite which outcrop at the base of the sediments. Immature and poor-sorted conglomerates filled the valley. This filling consists in clasts of variable sizes (centimetric to pluricentimetric, up to 85 cm) and different nature reflecting the basement: pegmatites, marbles, weathered dolerite. These clasts are not oriented. They are cemented by calcium carbonates. The yellow uraniferous mineralizations are mainly located within the fractures and heterogeneously disseminated in the conglomerates (Fig.A.8).

Calcretes are beige-light brown conglomerates constituted of quartz, feldspars, plagioclases, biotite and muscovite clasts cemented by a thin clayey carbonate phase.

Finally, the calcretes of Trekkopje, Langer Heinrich and Yeelirrie are conglomerates with a thin clay-carbonate mixed to cementing varied size and nature clasts eroded from the underlying basement. This calcrete mineralization present secondary uranium occurring as fine splinter thinly linked with the clay phase.



Figure A. 8. Fluvial conglomerate with carnotite mineralization in Midi Pit, Trekkopje, Namibia.

2.2.3. Uraniferous mineralizations of the Australian and Namibian calcretes

The mineralization occurs as idiomorphic carnotite, tyuyamunite and mix between these two poles (Fig.A.9), associated with clayey matrix (Fig.A.10) rounding the clasts.

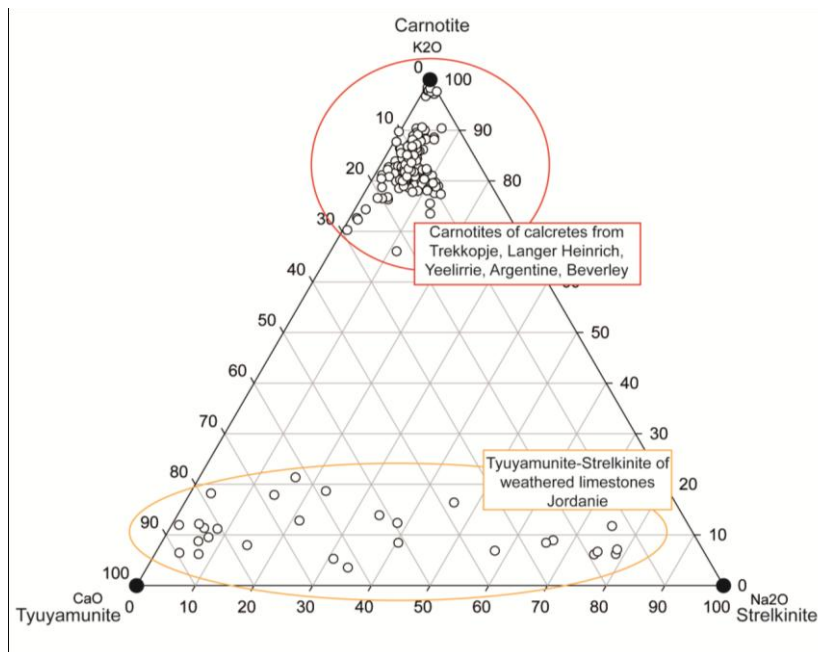


Figure A. 9. 10CaO-10Na₂O-K₂O ternary diagram of the uranyl vanadates.

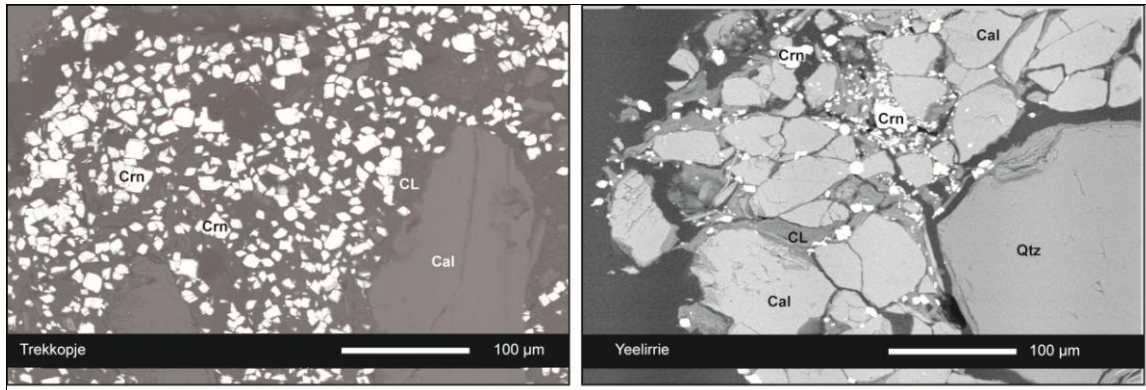


Figure A. 10. SEM views of the carnotite mineralization in calcretes (Cal: calcite, CL: clay minerals, Crn: carnotite, Qtz: quartz).

3. CONCLUSION

The petrographical, mineralogical, geochemical studies of 6 samples of the Langer Heinrich uranium deposit leads to the following main conclusions:

- (i) Five samples correspond to highly immature microconglomeratic arkoses. Two samples (LHU-1 and 2) are very rich in carbonates (about 45 wt %). One sample (LHU-2) is clearly mineralized with visible hexavalent U minerals.
- (ii) One sample (LHU-5) corresponds to a fine grained weakly indurated sandstone, relatively well sorted.
- (iii) Sample LHU-1 which is barren and rich in carbonate contains mostly detrital clay minerals : illite and muscovite.
- (iv) Sample LHU-2 which is mineralized and rich in carbonates also presents detrital clay minerals (illite), but also some newly formed clay minerals represent by interlayered illite/chlorite and vermiculites which have both a much larger specific surface and therefore a larger capacity of adsorption of uranium which may decrease the leacheability of U during the extraction processes.
- (v) Sample LHU-5 which is barren, but is the richest in clay minerals and poor in carbonates. It also presents detrital clay minerals (illite), but also interlayered chlorite/illite and smectite which also have both a much larger specific surface.

(vi) Two samples (LHU-1 & 2) are poor in quartz and very rich in carbonates. The four other samples are rich in quartz with variable proportions of K-feldspar and albite. LHU-5 is the richest in albite, despite its high clay content indicating that the clay minerals do not result from plagioclase alteration.

(vii) The two samples rich in carbonates (LHU-1 and 2) are the less clay rich. Their important carbonate contents (about 45 wt%) largely exceeds the possible initial porosity of the sandstone suggesting that either there has been an increase in volume of the rock, or dissolution of the detrital quartz (observed in thin section).

(viii) The carbonates are pure calcite and the most mineralized sample is the richest in carbonate underlying the importance of evapotranspiration processes for both carbonate and U deposition.

(ix) All the samples have similar Rare Earth Elements (REE) patterns typical of post-Archean sedimentary rocks.

(x) Samples LHU-1 and 2 present a negative Ce anomaly whereas LHU-6 which may reflect a provenance of the material of some of the sediments from a dismantled lateritic profile.

(xi) The uranium minerals from sample LHU-2 correspond to a mixture of Carnotite and Tyuyamunite with nearly all the intermediate compositions.

REFERENCES

- Alonzo-Zarza, A.M., 2003. Palaeoenvironmental signification of palustrine carbonates and calcretes in the geological record. *Earth Sci. Rev.* 60, 261-298.
- Bowell, R.J., Barnes, A., Grogan, J., Dey, M., 2009. Geochemical controls on uranium precipitation in calcrete palaeochannel deposits in Namibia. A paper presented at the 24th International Applied Geochemistry Symposium, Fredericton Canada, 1st - 4th June 2009.
- Cameron, E., 1984. The Yeelirrie calcrete uranium deposits, western Australia. IAEA, Vienna, 322, 157-164.
- Carlisle, D., Merifield, P.M., Orme, A.R.R., Kohl, M.S., Kolker, O., 1978. The distribution of calcretes and gypcretes in southwestern United States and their uranium favourability based on a study of deposits in Western Australia and South West Africa (Namibia), US Dept. Of Energy. GJBX-29(78), 274 p.
- Carlisle, D., 1983. Concentration of uranium and vanadium in calcretes and gypcretes. *Geol. Soc. London. Spec. Publ.* 11, 185-195.
- DAHLKAMP, F.J., 1993. Uranium ore deposits. – Springer-Verlag Ed., 1-460.
- Galloway, W.E., and Hobday, D.K., 1996. Terrigenous clastic depositional systems: applications to fossil fuel and groundwater resources, 2nd ed. Springer, 1-489.
- Hambleton-Jones, B.B., 1984. Surficial uranium deposits in Namibia. IAEA, Vienna, 322, 205-216.
- Toens, P.D., and Hambleton-Jones, B.B., 1984. Definition and classification of surficial uranium deposits. IAEA, Vienna, 322, 9-14.
- Mann, A.W., and Deutscher, R.L., 1978. Genesis principles for the precipitation of carnotite in calcrete drainages in western Australia. *Econ. Geol.* 73, 1724-1737.
- Wright, V.P., Tucker, M.E. 1991. Calcretes. *Int. Ass. Sedim., Reprint Series*, 2, 1-352.
- Zhou, J., Chafetz, H.S., 2009. Biogenic caliche in Texas: the role of organisms and effect of climate. *Sed. Geol.* 222, 207-225.

TABLE DES FIGURES

Introduction

Figure 1. Carte géologique de la péninsule arabique (Le Nindre et al., 2003).....	15
Figure 2. Colonne stratigraphique de Jordanie (d'après Harshbarger (1966), Powell (1988), Eraifej (2006), Jarra et al. (2003), Sawarieh (2005)).	17
Figure 3. Cartes géologiques de la Jordanie. La carte a situe la Jordanie dans la péninsule arabique. La carte b présente les différentes provinces et la zone d'étude, la carte c présente un zoom avec la localisation des échantillonnages (d'après Alsharhan and Nairn, 2003; Bender, 1975; Föster et al., 2010; Parlak and Roberston, 2004, Sawarieh, 2005).....	18

Chapitre II

Figure II. 1. Schematic structural map of the western Arabain Plate. The dotted frame marks the figure II.2. (after Föster et al., 2010; Parlak and Roberston, 2004).....	37
Figure II. 2. Generalized geology of the Dead Sea Transform area (modified after Sokol et al., 2011), and geological detailed map (after Bender, 1975) of the studied area, with location of samples and outcrops of the Mottled Zone Complexes in Jordan and Israel.	38
Figure II. 3. Chrono-lithostratigraphic column of central Jordan, with stratigraphic location of samples, and macrophotos of one of each lithologic group.	42
Figure II. 4. a) Microphotograph, Plane Polarized Light. Bioclastic limestones 9502-18; SEM images: b) shale JRD10-14A; c) shale JRD10-12B; d) limestone JRD10-22; e) limestone JRD10-09; f) marble JRD10-44; g) marble JRD10-47; h) marble JRD10-84A. Bar: barite, Blt: bultfonteinite, Brw: brownmillerite, Cal: calcite, CaSi: calcium silicate, Cd Sp: cadmium-rich sphalerite, CFA: carbonate-fluorapatite, CL: clay mineral, Dol: dolomite, Ett: ettringite, Fe ox: iron oxide, Hcl: hydrocalumite, Hsh: Hashemite, o: ooid of phosphate, OM: organic matter, Py: pyrite, S: sulfur, Se: selenium, Srb: srebrodolskite, sk P: phosphate skeleton, Uox: uranium oxide.....	46
Figure II. 5. Ternary diagrams: a) CaO-SiO ₂ -5Al ₂ O ₃ ; b) CaO-SiO ₂ -10P ₂ O ₅ ; c) CaO-SiO ₂ -CO ₂ total. Grey square: bioclastic limestones, triangle: shales, white square: limestones, black square: marbles. Ap: apatite, AS: average shale (Wedepohl, 1971, 1991), Cal: calcite, CFA: carbonate-fluorapatite, Ill: illite, Kln: kaolinite, Mnt: montmorillonite, Qtz: quartz.	54
Figure II. 6. Enrichment factor (EF) of major, minor, and trace elements of each lithologic group, and OC-rich sediments (modified after Brumsack, 2006).	55
Figure II. 7. PAAS-normalized (McLennan, 1989) rare earth elements patterns of the Belqa Group lithologies: a) average REE patterns of each lithologic group; b)REE patterns of the	

marbles; c) REE patterns of the limestones; d) REE patterns of the shales; e) REE patterns of the bioclastic limestones.....	58
Figure II. 8. Al+P – REE diagram.....	59
Figure II. 9. TS-TOC diagram. The dashed line represents the average S/C ratio of normal marine sediments (2.8) beneath oxygenated seawater. (Berner, 1982, 1983).....	60
Figure II. 10. Schematic diagram of the sedimentation conditions and the chemical processes on the shelf. Without scale. (RSE: redox sensitive elements).....	62
Figure II. 11. U-O diagram.....	65

Chapitre III

Figure III. 1. Paleogeographic map of the upwelling belt along the southern Tethys margin during the Late Campanian and Early Maastrichtian, (after Parish and Curtis 1982, Ashckenazi-Polivoda et al., 2011). Star marks the location of central Jordan.....	85
Figure III. 2. Microscopic and SEM views of the bioclastic limestones and its phosphates. ag: carbonate-fluorapatite aggregate, Cal: calcite, O: ooid of carbonate-fluorapatite, Sk CFA: skeleton of carbonate-fluorapatite.....	89
Figure III. 3. Microscopic views of the phosphates in the shale JRD10-12B. ag: CFA: aggregate, Sk CFA: skeleton of carbonate-fluorapatite.	90
Figure III. 4. Microscopic views of the marbles and its phosphates. Cal: calcite, CFA: carbonate-fluorapatite, Ett: ettringite, Hcl: hydrocalumite, Jn: jennite, U ox: uranium oxide, Spu: spurrite.	91
Figure III. 5. Microscopic views of the phosphates in black calc-silicate rock (a) and in green calc-silicate rock (b). FAp: fluorapatite, Mel: melilite, Pmp: pumpellyite, Wo: wollastonite.	92
Figure III. 6. Microscopic views of the weathered phosphates (a, b) and of the newly formed supergene phosphates (c). Cal: calcite, CFA: carbonate-apatite with low fluorine content, Na-S-P: Na-sulfato phosphate.....	93
Figure III. 7. RAMAN spectrum of a carbonate-fluoroapatite hosting by a marble.....	96
Figure III. 8. LA-ICP-MS spectrum. a: carbonate-fluorapatite (bioclastic limestone 9502-17). U=78 ppm; b: carbonate-fluorapatite (marble JRD10-84A).	97
Figure III. 9. PAAS-normalized (McLennan, 1989) rare earth elements patterns of the different apatites of the lithologies of the Belqa Group.	99
Figure III. 10. Whole rocks-normalized rare earth elements detailed for each phosphate type of each rock. a) sedimentary carbonate-fluorapatites, b) metamorphic carbonate-fluorapatites	

of the marbles, c) metamorphic idio to subidiomorphic fluorapatites of the calc-silicate rocks, d) weathered and newly formed supergene phosphates.	101
Figure III. 11. U - Σ REE.	103
Figure III. 12. wt% P ₂ O ₅ - Σ REE of the phosphate normalized to the whole rocks Σ REE. ..	103
Figure III. 13. U - P diagram (after Fleurance et al., 2013; see Chapter II).	105
Figure III. 14. U contents of the whole rocks with the range of U content of the phosphates from each rock.	105
Figure III. 15. F - CO ₃ diagram.	107
Figure III. 16. 2PO ₄ +Ca versus 2CO ₃	109
Figure III. 17. 2PO ₄ versus CO ₃ +SiO ₄ diagram.	109
Figure III. 18. PO ₄ +Ca versus CO ₃ +Na diagram.	109
Figure III. 19. SO ₄ +Na versus PO ₄ +Ca diagram.	110

Chapitre IV

Figure IV. 1. Location of the metamorphic complexes (coloured in red) and the studied area (red square) (after Techer et al., 2006; Grapes, 2006).	125
Figure IV. 2. Macroscopic (a, b) and SEM views (c to n) of the marbles. (Blt = bultfonteinite, Brm = brownmillerite, Cal = calcite, CFA = carbonate-fluorapatite, Ett = ettringite, Hcl = hydrocalumite, Hsh = hashemite, Jn = jennite, Py = pyrite, Spu = spurrite, Sr = Srebrodolskite).	129
Figure IV. 3. Macroscopic and microscopic views of the black calc-silicate rocks (Chr = chromite, Cls = celestine, FAp = fluorapatite, Fe-Prv = Fe-perovskite, Mel = melilite, Pmp = pumpellyite, Pw = powellite, Tbm = tobermorite, Wo = wollastonite).	130
Figure IV. 4. Macroscopic and microscopic views of the green calc-silicate rocks (FAp = fluorapatite, Mel = melilite, Tbm = tobermorite, Zeo = zeolites, Wo = wollastonite).	132
Figure IV. 5. Macroscopic and microscopic views of the paralavas (Cal = calcite, Fds = feldspar, Px = pyroxene).	133
Figure IV. 6. Paragenetic sequences for the formations of the marbles (a), the calc-silicate rocks (b), and the paralavas (c).	136
Figure IV. 7. (SiO ₂ +P ₂ O ₅)-(Al ₂ O ₃ +Fe ₂ O ₃)-(CaO+MgO) diagram. (After the ternary diagram of Grapes (2006). However, the fields enclosed rock analyses from the Mottled Zone (Israel) have been corrected for carbonate content by substrating and amount of CaO equivalent to	

CO₂ (after Matthews and Gross, 1980). Our Jordanian samples have not been corrected in the same way, but it is not impact the ratio SiO₂+P₂O₅/(Al+Fe)₂O₃..... 139

Figure IV. 8. Ternary diagrams. a: CaO-SiO₂-CO₂. b: CaO-SiO₂-Al₂O₃. c: CaO-SiO₂-P₂O₅. 140

Chapitre V

Figure V. 1. Geological map of the study area and location of the supergene samples against the metamorphic facies..... 157

Figure V. 2. Trench T21 (L:200m, w:1.5, d:3m) 157

Figure V. 3. Trench T07 (L:200m, w:1.5, d:3m) 157

Figure V. 4. Macroscopic and microscopic views of the weathered limestones (Bar: barite, Cal: calcite, CFA: carbonate-fluorapatite, CL: clay minerals, Fl: fluorite, Na-S-P: Na-sulfato-phosphates, Tymm: tyuyamunite, Strl: strelkinite). 159

Figure V. 5. General ternary diagrams and diagrams showing the evolution of samples of two trenches T21 (top to bottom: JRD10-89/90/91) and T07 (top to bottom: JRD10-95/94/93). See Appendix V for sample depths. (Ap: apatite, Cal; calcite, CFA: carbonate-fluorapatite, Ill: illite, Mnt: montmorillonite, Qtz: quartz, Spu: spurrite, Wo, wollastonite)..... 161

Figure V. 6. Average non altered limestones-normalized spectra of the weathered limestones. 162

Figure V. 7. Profile of geochemical evolution for trench T21 (JRD10-89/90/91)..... 164

Figure V. 8. Profile of geochemical evolution for trench T07 (JRD10-95/94/93)..... 164

Figure V. 9. K₂O-CaO-Na₂O diagram. 166

Figure V. 10. U – V diagram..... 166

Figure V. 11. K₂O-CaO-Na₂O diagram. Comparison with the calcrete mineralization. 166

Figure V. 12. Whole rocks-normalization patterns of the U mineralizations. 167

Figure V. 13. Isocons of the trench T21..... 169

Figure V. 14. Isocons of the trench T07..... 170

Figure V. 15. V - U, Mo, Gd. Example of the compositional evolution along the two vertical profiles T21 and T07. 171

Figure V. 16. V- P₂O₅ diagram. Marbles present a coefficient correlation of 0.9 (without the sample with the higher V content). 173

Figure V. 17. Parameters on U solubility. a. Fluid source parameters, b. fluid pathway parameters (Skirrow et al., 2009).	174
Figure V. 18. Log fO_2 -pH diagrams. Diagrams show dominant aqueous species of uranium in atmospheric conditions. Dashed lines marked Mn_3O_4/Mn_2O_3 and Hematite/Magnetite show the position of fO_2 buffers (Bastrakov et al., 2010).	175
Figure V. 19. Log fO_2 -pH diagrams. The diagrams show dominant aqueous species of vanadium. Dashed lines marked Mn_3O_4/Mn_2O_3 and Hematite/Magnetite show the position of fO_2 buffers. Bastrakov et al., 2010.	175
Figure V. 20. Carnotite and tyuyamunite – pH diagrams (25°C) (Langmuir, 1978).	177
Figure V. 21. Carnotite and Tyuyamunite solubility – pH diagrams (Tokunaga et al., 2010).	177
Figure V. 22. PAAS-normalization (McLennan, 1989) patterns of the uraniferous mineralizations of central Jordan and others occurrences.	180

Annexe

Figure A. 1. Classification of the surficial uranium deposits after Toens and Hambleton-Jones (1984).	193
Figure A. 2. Idealized section along the representative catchment showing the postulated redox controlled genesis of carnotites in calcrete. Mann and Deutscher (1978).	194
Figure A. 3. Mineralized sample LHU-2 showing the heterogeneous granulometry of the rock, and the yellowish hexavalent uranium minerals.	196
Figure A. 4. Sample LHU-5 corresponding to a relatively well sorted sandstone.	196
Figure A. 5. TEM views of the clay minerals.	196
Figure A. 6. Q-P diagram. Relative proportions of quartz – albite – K-feldspar in the sediments of Langer Heinrich in a Q'-P' chemical-mineralogical diagram.	197
Figure A. 7. A-Q diagram representing the variations of the proportions of quartz and clay minerals in the Langer Heinrich sediments.	198
Figure A. 8. Fluvial conglomerate with carnotite mineralization in Midi Pit, Trekkopje, Namibia.	199
Figure A. 9. $10CaO-10Na_2O-K_2O$ ternary diagram of the uranyl vanadates.	199
Figure A. 10. SEM views of the carnotite mineralization in calcretes (Cal: calcite, CL: clay minerals, Crn: carnotite, Qtz: quartz).	200

TABLE DES TABLEAUX

Chapter II

Table II. 1. Synthetic stratigraphic nomenclature: lithostratigraphy, lithology and depositional environments of the studied area. Fm.: Formation, Mb: Member. (Compiled data from Abed, 1982; Abed and Kraishan, 1991; Powell and Moh'd, 2011; Pufahl et al., 2003).	39
Table II. 2. Concentrations of major, minor, trace and rare earth elements of the Belqa Group lithologies.	50

Chapter III

Table III. 1. U, P ₂ O ₅ and ΣREE contents of the different rocks of the Belqa Group.	93
Table III. 2. Major elements and U contents of the different phosphates types (a), ions numbers and CO ₃ contents (b).	94
Table III. 3. Excess fluorine calculations	107

Chapter IV

Table IV. 1. Minimum temperatures of appearance of the minerals in the metamorphic rocks.	143
Appendix IV. Major and trace element concentrations of the metamorphic rocks.	153

Chapter V

Appendix V. Major and trace element concentrations of the supergene mineralized limestones.	185
--	-----

Résumé: Les différentes lithologies sédimentaires du Groupe Belqa présentent un enrichissement en P et en toute une série d'éléments sensibles aux conditions redox. Il est montré que l'enrichissement en U, Cu, Co, Mo, V résulte d'un dépôt syn-sédimentaire sous conditions suboxiques. Par contre, les éléments Cr, Ni, Cd, Zn sont beaucoup plus enrichis et requièrent un flux exogénique de métal probablement relié à l'altération de roches ultrabasiques obductées à la même période au nord de cette région, lors de la collision de la plaque arabo-africaine avec la plaque eurasiennne. Les phosphates représentent le principal hôte de l'uranium et des terres rares. L'analyse des apatites par ablation laser ICP-MS a permis de montrer leur évolution, depuis le stade sédimentaire-diagénétique, puis pyrométamorphique, jusqu'à l'altération supergène. La libération de l'uranium de la structure de l'apatite lors du pyrométamorphisme et de l'altération supergène permet sa mise à disposition pour la formation de minéralisations. Le pyrométamorphisme, dû à une combustion des niveaux riches en matière organique, est responsable de la déstabilisation des apatites, et de la formation de roches de compositions semblables à des ciments clinker/Portland. L'uranium a également été libéré de la structure de l'apatite par altération supergène. L'altération météorique et les fluides évaporitiques ont permis le lessivage et le transport des éléments (U, V) des roches carbonatées métamorphiques, et des carbonates puis a conduit au dépôt des vanadates d'uranyles dans les carbonates pulvérulents ayant subi une dissolution importante.

Mots clés: Jordanie centrale, Groupe Belqa, Maastrichtien-Paléocène, éléments sensibles aux conditions redox, phosphates, uranium, pyrométamorphisme, carbonate-fluorapatite, calcaires supergènes altérés, tyuyamunite, strelkinite.

Abstract: The different lithologies of the Belqa Group present an enrichment in P and various redox sensitive elements. The U, Cu, Co, Mo, V enrichment results from synsedimentary deposition in suboxic conditions. However, the higher Cr, Ni, Cd, Zn enrichment requires an exogenic metal flux probably related to the terrestrial leaching of ultrabasic rocks obducted during the collision between African-Arabian and Eurasian plates to the north of the study region, at the same time. Phosphates are the main host lithology for uranium and rare earth elements. The analysis of the apatites by laser ablation ICP-MS shows their evolution along the sedimentary-diagenetic and pyrometamorphic stages, up to the supergene weathering. The uranium liberation from the apatite structure during the pyrometamorphism and surficial weathering led to its availability as supergene ore mineralization. Pyrometamorphism resulted from the combustion of organic-rich layers and caused the destabilization of the apatites, and the formation of rocks which have compositions similar to clinker/Portland cements. Uranium has been also released from the structure of the apatite by supergene alteration. Meteoric weathering and the evaporitic groundwater resulted in the leaching and the transport of the elements (U, V) from the metamorphic carbonated hills, and from the surrounding permeable limestone which has undergone dissolution in the near surface zone.

Key words: central Jordan, Belqa Group, Maastrichtian-Paleocene, redox sensitive elements, phosphates, uranium, pyrometamorphism, carbonate-fluorapatite, weathered supergene limestones, tyuyamunite, strelkinite.